Papers Presented to the

INTERNATIONAL
COLLOQUIUM
ON
VENUS

AUGUST 10–12, 1992

PASADENA, CALIFORNIA

PAPERS PRESENTED TO THE

INTERNATIONAL COLLOQUIUM ON VENUS

August 10–12, 1992
Pasadena, California

PREFACE

This volume contains short papers that have been accepted for the International Colloquium on Venus, August 10–12, Pasadena, California. The Program Committee consisted of R. Stephen Saunders (*Jet Propulsion Laboratory*) and Sean C. Solomon (*Massachusetts Institute of Technology*), chairmen; Raymond Arvidson (*Washington University*); Valery L. Barsukov, Mikhail Yu. Zolotov, Alexander T. Basilevsky (*Vernadsky Institute*); Vassily Moroz (*Institute for Space Research*); Donald B. Campbell (*Cornell University*); Thomas Donahue (*University of Michigan*); James W. Head III (*Brown University*); Pamela Jones (*Lunar and Planetary Institute*); Mona Jasnow, Andrew Morrison, Timothy Parker, Jeffrey Plaut, Ellen Stofan, Tommy Thompson, Cathy Weitz (*Jet Propulsion Laboratory*); Gordon Pettengill (*Massachusetts Institute of Technology*); and Janet Luhmann (*University of California, Los Angeles*).

TABLE OF CONTENTS

Papers Presented to the
International Colloquium on Venus

Papers Presented to the
International Colloquium on Venus

N93-14289

VENUS RADAR MAPPING FROM THE VENERA 15 AND 16 SPACECRAFTS: RESULTS AND RESTRICTIONS. E. L. Akim[1], A. I. Zakharov[2], and A. P. Krivtsov[2], [1]Institute of Applied Mathematics, Russian Academy of Sciences, Russia, [2]Institute of Radioengineering and Electronics, Russian Academy of Sciences, Russia.

This report contains a description of the results of the Venus northern hemisphere radar survey in 1983–1984 from the Venera 15 and 16 spacecrafts. In addition, we discuss some peculiarities in the function of the radar equipment that defined the technology of SAR data processing. Among these peculiarities are insufficient calibration of SAR and radar altimeter and erroneous automatic gain control data transmission from the spacecrafts.

As a result, the procedure of image synthesis and mosaicking contained multistage image brightness corrections. This led to the fact that the average image brightness in a spot 100 km in diameter was constant everywhere in the mosaics.

Twenty-seven radar mosaics in the Lambert-Hauss conic projection with 1–2-km spatial resolution covering 25% of the surface of Venus have been produced.

A Venus surface roughness map was constructed by joint processing of SAR and altimeter data. The mutual calibration of the SAR and altimeter was made in the special radar session, when the SAR and altimeter were declined from the local vertical at the same angle.

The possibility of estimating relative variations in surface reflection properties over a tens-of-kilometers interval from Venera images is still being considered.

Joint analysis of the coordinates of small features on the Venera and Magellan images is one more approach being used to refine the period of rotation for Venus.

N93-14290

LOCAL-TIME ASYMMETRIES IN THE VENUS THERMO-SPHERE. M. J. Alexander[1], A. I. F. Stewart[1], and S. W. Bougher[2], [1]Laboratory for Atmospheric and Space Physics, University of Colorado, Boulder CO 80309, USA, [2]Lunar and Planetary Laboratory, University of Arizona, Tucson AZ 85721, USA.

Our current understanding of the global structure and dynamics of the Venus thermosphere is embodied in models such as the Venus Thermospheric General Circulation Model (VTGCM, [1]) and empirical composition models such as VIRA [2] and VTS3 [3]. To first order the thermosphere is symmetrical about the axis through the subsolar and antisolar points. Solar radiation at extreme ultraviolet and infrared wavelengths heats the dayside thermosphere and drives a subsolar-to-antisolar (SS-AS) circulation pattern with strong winds (250–300 m/s) across the terminator. This circulation advects low mass atoms (H and He) and heat from the dayside to the nightside. The forcing provided by the solar heating is strong, such that the VTGCM has had to include a prescribed wave drag term to slow the winds and match diurnal variations in temperature and O and CO.

This simple symmetric picture is modified by a thermospheric "superrotation," i.e., the thermospheric winds also have a westward (in the same direction as the lower atmosphere rotation) zonal

component with a magnitude of approximately 50–75 m/s. Since the thermospheric winds have never been measured directly, this has been inferred from nightside density and nightglow distributions that have been associated with the nightside convergence point of the SS-AS circulation. Hydrogen and He peak in density on the nightside, but not at the antisolar point. Their density peaks are shifted into the early morning hours at 5 a.m. and 3 a.m. respectively. Nightglow emissions from NO that are also associated with the antisolar convergence of the winds have been observed to peak at 2 to 3 a.m. local time. The current VTGCM includes this superrotation with an asymmetric Rayleigh drag prescription.

We have completed an analysis of ultraviolet images of Venus at 130 nm acquired by the Pioneer Venus Orbiter Ultraviolet Spectrometer (PVOUVS). This emission originates from oxygen atoms in the Venus thermosphere. Oxygen is one of the main constituents at these altitudes, and so with careful modeling we can infer important information about the structure of the thermosphere from these data. *In situ* measurements of thermospheric densities [4] were only accomplished at low latitudes and near the maximum in solar activity, while the PVOUVS images show latitudes from 60°S to the north pole and now span an entire solar activity cycle. We have examined 97 images spanning the 10-year period between 1980 and 1990, and have developed a technique for global radiative transfer modeling with which we create synthetic models of each image analyzed [5,6]. The models incorporate our current understanding of the thermosphere described above. We study the ratio of data and model images to remove observational geometry artifacts. In these ratio images we have found a persistent pattern in 130-nm brightness that is present in every image analyzed. It appears as an asymmetry in local time with lowest values at the morning terminator and relatively high values in the late afternoon. To examine the average structure of these patterns, we map each ratio image into latitude and local time, and average them to create a map of solar-locked features. Figure 1 shows the result. We can relate these solar-locked brightness patterns directly to variations in atomic oxygen, and find that the a.m. to p.m. densities differ by up to a factor of 2 where the VTGCM predicts only a 5% variation. The asymmetry is present only at latitudes poleward of 30°, and so was not observed in the *in situ* measurements taken at equatorial latitudes.

We have developed a hypothesis for understanding the persistent local-time asymmetry observed in Fig. 1 as a signature of vertically propagating internal gravity waves interacting with the thermospheric SS-AS cirulation. If the source for these waves is presumed to be in the upper cloud deck or just above, and if they saturate in the thermosphere, they will create a striking asymmetry in eddy diffusion with local time. Experiments we have conducted with the VTGCM suggest that such variations in eddy diffusion can account for the oxygen variations we observe in the PVOUVS data. We use a parameterization first developed by Lindzen [7] to study variations in eddy diffusion with local time. The magnitude of the eddy diffusion K is a strong function of the difference between the mean zonal wind speed and the phase speed of the wave,

$$K \propto |\bar{u} - c|^4$$

So waves with predominantly westward phase speeds—like those forced in the upper clouds—will interact very differently with the

AVG OF 56 INBOUND ORBITS

AVG OF 42 PERIAPSIS ORBITS
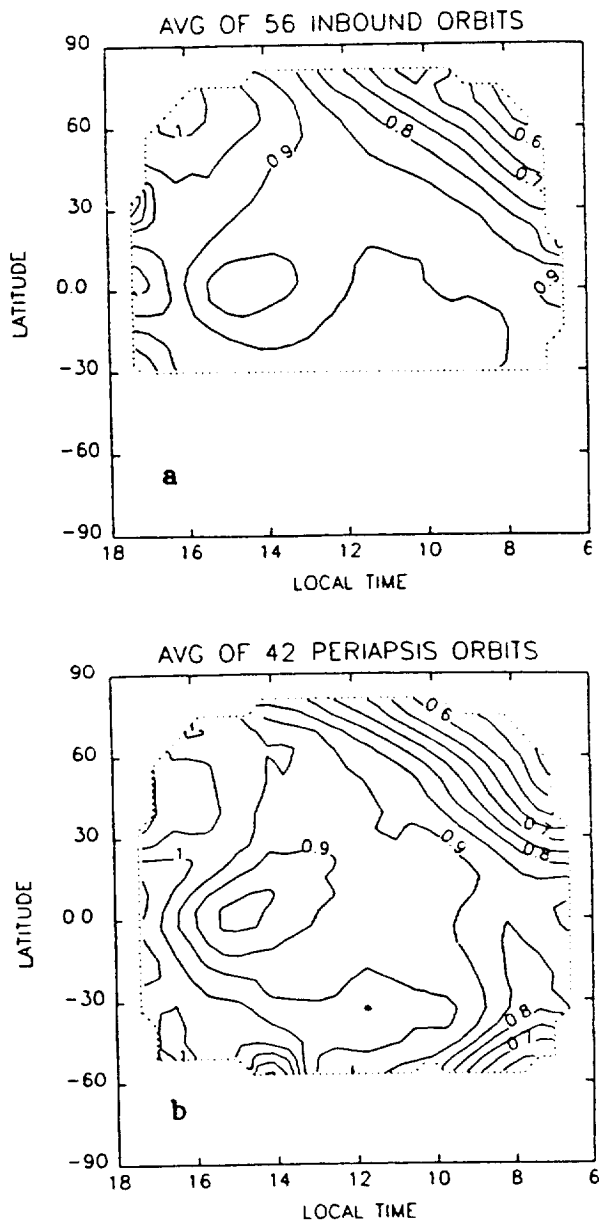
Fig. 1. Contours of brightness ratio (data/model) of the 130-nm emission displaying the local-time asymmetry (see text). The brightness ratio patterns can be thought of as anomalous patterns in O. (a) and (b) are derived from two different types of PVOUVS data: (a) contains more data, so it better displays the northern hemisphere pattern, but in (b) we can see to more southerly latitudes. The northern hemisphere pattern is mirrored there.

Fig. 2. Eddy diffusion coefficients characteristic of 8 a.m. and 4 p.m. wind profiles derived with the Lindzen parameterization [7]. Also shown are the VTGCM and von Zahn et al. [8] one-dimensional photochemical model K for reference.

References: [1] Bougher et al. (1988) *Icarus*, 73, 545–573. [2] Keating et al. (1986) *Adv. Space Res.*, 5, 117–171. [3] Hedin et al. (1983) *JGR*, 88, 73–83. [4] Niemann et al. (1980) *JGR*, 85, 7817–7827. [5] Meier R. R. and Lee J.-S. (1982) *Planet. Space Sci.*, 30, 439–450. [6] Alexander et al. (1991) *Bull. AAS*, 23, 1194. [7] Lindzen R. S. (1981) *JGR*, 86, 9707–9714. [8] von Zahn et al. (1980) *JGR*, 85, 7829–7840.

N93 - 14291

RINGED IMPACT CRATERS ON VENUS: AN ANALYSIS FROM MAGELLAN IMAGES.

Jim S. Alexopoulos and William B. McKinnon, Department of Earth and Planetary Sciences and McDonnell Center for the Space Sciences, Washington University, St. Louis MO 63130, USA.

We have analyzed cycle 1 Magellan images covering ~90% of the venusian surface and have identified 55 unequivocal peak-ring craters and multiringed impact basins. This comprehensive study (52 peak-ring craters and at least 3 multiringed impact basins) complements our earlier independent analysis of Arecibo and Venera images and initial Magellan data [1,2] and that of the Magellan team [3].

Peak-ring craters are characterized by an outer, well-defined radar-bright rim, and an inner bright ring defined by a concentric arrangement of isolated and sometimes clustered peaks. The general appearance of venusian peak-ring craters, including their inner rings and crater rims, is morphologically similar to equivalent structures on the Moon, Mars, and Mercury. Some venusian peak rings, however, are distorted in shape (noncircular outline of inner ring) and off-center. Ejecta morphologies around peak-ring craters vary from regular and symmetric, including those due to oblique impact, to irregular and asymmetric. Many peak-ring craters exhibit outflow channels. The outflows emanate from within the crater and breach the crater rim (e.g., Cleopatra), while others extend away from the distal end of the ejecta blanket or have been incorporated within the main ejecta deposit (e.g., Cochran). The interiors of most peak-ring craters are radar-dark or smooth (similar to surrounding plains), although some are bright. A few larger craters are completely flooded and show no interior structure or inner ring (e.g., Koidula, ~70 km in diameter, and Alcott, ~65 km in diameter). The radar-smooth signature of the interior is likely due to postimpact resurfacing, either volcanism or (possibly differentiated) impact

westward afternoon winds than with the eastward morning winds. Figure 2 shows some example eddy diffusion profiles calculated with this method. Early morning a.m. values are typically a factor of 10 or more larger than corresponding p.m. values. These local-time asymmetries will be discussed in more detail in the context of several scenarios for the middle atmosphere wave forcing. This same mechanism can also give rise to asymmetric wave drag forces that have the potential for generating the thermospheric superrotation. The mechanism for *in situ* forcing of the thermospheric superrotation is still considered a mystery, so this corollary provides strong support to our cloud-level wave source hypothesis.

melt. Many peak-ring craters also exhibit radar-bright returns associated with rough material around peaks. Numerous central-peak structures and peak-ring craters also show darker regions at the periphery of the crater floor. These are probably areas of localized flooding, or possibly pools of impact melt. A few structures also exhibit radar-bright regions near the periphery of the floor that may represent slumped material from the crater rim. Fractures (or ridges) associated with some structures (i.e., Isabella, ~170 km in diameter, and Mona Lisa, ~81 km in diameter) exhibit a radial and concentric pattern interior to the inner ring. This tectonic fabric is the possible manifestation of stresses associated with viscous relaxation.

A plot of crater-rim to peak-ring diameter ratio against crater diameter (Fig. 1) shows that this ratio is relatively large (~5) at the transition diameter from central-peak craters and declines to less than 2 at larger diameters. The onset diameter to peak-ring forms on Venus is ~40 km [1], although peak-ring craters as small as ~30 km in diameter have now been identified (Fig. 1). The inner rings of these smaller structures are usually comprised of small, isolated, and concentrically arranged peaks, and thus are not as distinct as the coherent ring mountains of larger peak-ring craters. These smaller peak-ring forms represent transitional forms between complex craters with central and multiple peaks and well-developed peak-ring craters. The fact that ratios are larger at the transition and that ring ratios decrease with crater size is consistent with peak-ring crater formation being an extension of the process of central peak formation. Specifically, peak rings may form by hydrodynamic uplift and subsequent collapse of an increasingly unstable central peak. Upon collapse, excess material may be redistributed around the central collapse area, forming a cluster of multiple peaks or a small ring of concentrically arranged peaks. At larger scales, complete peak collapse may allow for a relatively wider redistribution of material, leading to smaller ring diameter ratios. Lending support to this argument may be the radar-bright returns associated with, and sometimes surrounding, the concentrically arranged peaks and with the central peak or peak complexes of larger complex craters. This brighter zone may be rougher material (at radar wavelength scales) associated with the central peak collapse process. On the other hand, no craters with both a peak ring and central peak have been identified, in contrast with the Moon, Mercury, and Mars. The scatter in ring ratios at a given crater diameter (Fig. 1) is real. A possible explanation is that the degree of hydrodynamic collapse of the central peak and subsequent modification, for a given crater size, depends on differences in regional postshock target rock properties (specifically, the effective viscosity and yield strength).
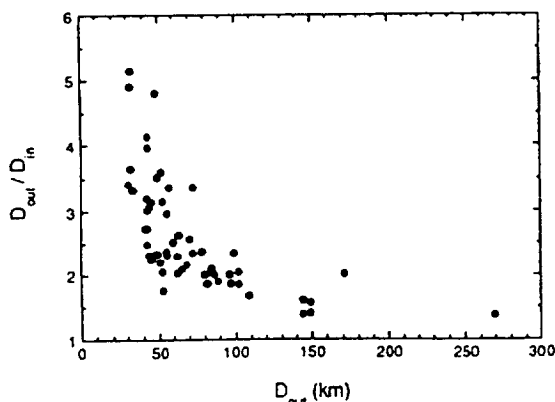
The declining ring ratio with diameter trend in Fig. 1 is similar to that observed for peak-ring craters on Mercury [1,2], albeit over a smaller-scale range. Most of the larger ringed craters with ratios of ~2 or less are similar in appearance to the smaller peak-ring forms. They exhibit an inner ring of isolated and concentrically arranged massifs (e.g., Marie Celeste, ~97 km in diameter, and Bonnevie, ~84 km in diameter), i.e., they have a distinct peak ring. However, others (e.g., Mona Lisa) exhibit very bright radar returns from continuous ridgelike portions of the inner ring that may actually be scarps. Scarplike inner rings may represent a new class of impact structure, intermediate between peak-ring craters and true multiringed basins, or the degree of floor uplift may simply be pronounced for the largest peak-ring craters. The fact that the ejecta deposits extend away from the rim of Mona Lisa means that the inner ring probably formed within the present crater rim. This is unlike venusian multiringed basins, where ejecta deposits can be seen to extend away from the first ring interior to the outer ring, implying that the outer ring formed outside what would approximate the crater rim in a smaller complex crater.

The transition from central-peak to peak-ring forms occurs at a range of diameters on the terrestrial planets that are determined mainly by surface gravity and postshock material properties [2,4]. The observed average onset diameter of ~40 km is consistent with our previous study [2] and, along with the transitions on the other terrestrial planets, supports our conclusion that the effective viscosity of cratered rubble during the modification stage is linearly proportional to crater diameter.

Of the four largest ringed craters yet identified on Venus, three appear to be multiringed impact basins. Klenova (~144 km in diameter), Lise Meitner (~148 km in diameter), and Mead (~270 km in diameter) are morphologically different from peak-ring craters, but similar to larger multiringed basin forms on the Moon, specifically Orientale. Our initial classification [1,2] of Klenova as a multiringed basin was based on the scarplike appearance of its outer rings as identified in Venera images. The Magellan image of Klenova confirms our initial interpretation. Klenova exhibits three distinct rings: an inner ring of concentrically arranged peaks (peak-ring) analogous to Orientale's Inner Rook, and two outer rings (main and intermediate) that we interpret to be possible fault scarps similar to Orientale's Cordillera ring and Outer Rook respectively. The ejecta blanket, not as evident in Venera images, is distinct and symmetrical and shows fields of secondary craters beyond the continuous ejecta deposits.

The Arecibo image of Lise Meitner exhibits two distinct radar-bright rings that we interpret to be scarplike and thus similar to Orientale's Cordillera ring and Outer Rook. The interior of Meitner is uniformly radar dark, implying a likely smooth floor of postimpact volcanic deposits. Meitner also exhibits an outer, radar-bright feature, which is at the correct spacing to be a possible partial ring, and a feature, ~9 km in width, interior to the inner ring that may be another ring or, more likely, a terrace similar to that produced by slumping of complex craters (Fig. 2). Analysis of the cycle 2 Magellan image of Meitner should better reveal the nature of these structural elements.

The largest impact structure identified on Venus, Mead, is comprised of two distinct rings. The radar-bright returns associated with each ring and an initial topographic evaluation indicate that the two rings are possible fault scarps analogous to Orientale's Cordillera ring and Outer Rook. The radar appearance of the ejecta deposits around Mead is suppressed relative to and not as distinct as that of peak-ring craters, but ejecta do occur between the two rings and extend across the outer one. The uniform radar returns associ-

Fig. 1.

Outer or Transitional Ring material
Main Ring material
Inner Ring material
Bench material
Ejecta
Interior and surrounding plains

75 km
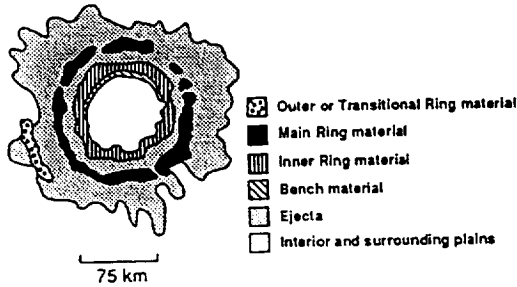
Fig. 2.

ated with Mead's interior probably indicate flooding of the topographically lower and relatively flat basin floor, with fracturing (mainly toward the center) producing locally radar-bright returns.

Isabella, with a diameter of ~170 km, is a ringed crater of the same scale, but its interior has been extensively flooded. A partially concentric arrangement of isolated peaks defines the remnants of an inner ring and a possible intermediate ring, both within the well-defined crater rim. The diameter ratio of the crater rim to the inner ring of peaks is roughly 2. If the intermediate ring, or a remnant thereof, can be shown to be scarplike in nature, then Isabella would also be a multiringed basin as interpreted here.

The ring diameter ratios of the three unequivocal multiringed impact basins are distinctly different from peak-ring craters (Fig. 1), although they follow the trend of decreasing ring ratios with increasing diameter. The ring diameter ratios for the two most distinct rings for Klenova, Meitner, and Mead are ~1.6, ~1.6, and ~1.4 respectively. Also, ring ratios for Klenova's intermediate ring to peak ring is ~1.4, as is Meitner's partial ring to main ring. These ring ratios are close to the $\sqrt{2}$ ratio suggested for Orientale and other lunar multiring basins, thus supporting the multiringed basin analogy. Finally, theoretical arguments [1,2] support the formation of multiringed basins on Venus at these scales (>100–150-km diameter).

References: [1] Alexopoulos J. S. et al. (1991) *LPSC XXII*, 13–14. [2] Alexopoulos J. S. and McKinnon W. B. (1992) *Icarus*, submitted. [3] Schaber G. G. et al. (1992) *JGR*, submitted. [4] Melosh H. J. (1989) *Impact Cratering: A Geologic Process*, Oxford, New York, 245 pp.

N93-19292

IS ISHTAR TERRA A THICKENED BASALTIC CRUST?
Jafar Arkani-Hamed, Department of Geological Sciences, McGill University, Montreal, Canada, H3A 2A7.

The mountain belts of Ishtar Terra and the surrounding tesserae are interpreted as compressional regions [1,2,3]. The gravity and surface topography of western Ishtar Terra suggest a thick crust of 60–110 km [4,5] that results from crustal thickening through tectonic processes. Underthrusting was proposed for the regions along Danu Montes [6] and Itzpapalotl Tessera [7]. Crustal thickening was suggested for the entire Ishtar Terra [8]. In this study, three lithospheric models with total thicknesses of 40, 75, and 120 km and initial crustal thicknesses of 3, 9, and 18 km are examined. These models could be produced by partial melting and chemical differentiation in the upper mantle of a colder, an Earth-like, and a hotter Venus having temperatures of respectively 1300°C, 1400°C, and 1500°C at the base of their thermal boundary layers associated with mantle convection. The effects of basalt-granulite-eclogite trans-

formation (BGET) on the surface topography of a thickening basaltic crust is investigated adopting the experimental phase diagram [9] and density variations through the phase transformation [10].

Figure 1a shows the thermal evolution of the lithosphere of the cold Venus model with a linear crustal thickening of 0.5 km/m.y. followed by an exponential thickening for only 20 m.y. starting at 100 m.y. with a characteristic time of 20 m.y. (the main results are not very sensitive to these values; see below). Figure 1b shows the stability field of different phases that basalt enters. The BGET begins when the crust reaches a thickness of 7 km, and eclogite appears when the crust thickens beyond 70 km. Geologically speaking, the BGET is assumed to be instantaneous. Ahren and Schubert [11] suggested that cold basalt may take several tens of millions of years to transform to eclogite, and based on this suggestion Vorder Bruegge and Head [5] proposed that Maxwell Montes are 65 m.y. old. However, the recent crater distribution obtained from Magellan data suggests that the average age of Ishtar Terra is similar to that elsewhere on Venus, 500 m.y. [12,13]. To assess the effects of the time lag in the phase change, the crustal thickening is halted at 120 m.y. and the crust is allowed to reach thermal equilibrium for the next 80 m.y. The temperature increase does not significantly reduce the volume proportion of eclogite.
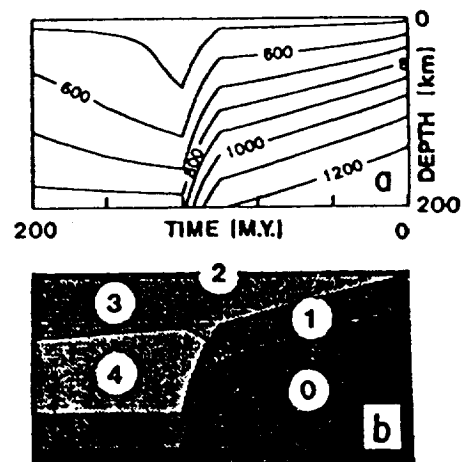
Fig. 1. Thermal evolution of the cold Venus model with a thickening crust. The numbers on the curves are temperatures in °C. Figure 1b shows the existing phases. 0 = undepleted peridotite, 1 = depleted peridotite, 2 = basaltic crust, 3 = granulite, and 4 = eclogite.

The surface topography produced by crustal thickening is determined assuming Airy isostasy with a compensation depth at 150 km as suggested for the western part of Ishtar Terra [14]. Figure 2 shows the resulting topography with (curve 1) and without (curve 2) taking into account the BGET. The density of basalt is 2900 kg/m³ at room temperature. That of granulite increases linearly and reaches ~3500 kg/m³ when eclogite appears. Also taken into account is the density decrease with temperature. The constant density model in Fig. 2 is similar to that of Bindschadler et al.'s [8] at steady-state condition, taking into account the density differences of the two models. However, in a more realistic model with the BGET, the surface topography attains a maximum of 1.8 km with a total crustal thickness of 38 km, beyond which the topography decreases due to sinking of the denser assemblages into the mantle. Halting the crustal thickening causes a rebound of the crust, but not enough

and (4) total thickness of the crust. Figure 2 shows the surface topography produced by lithospheric models assuming linear thickening of the crust. There are three sets of curves in each figure. Sets 1, 2, and 3 show the effects of the initial temperature distributions corresponding to lithospheres 100, 200, and 300 m.y. old. Within a given set, the curves a, b, and c are for thickening rates of 0.5, 0.25, and 0.167 km/m.y. respectively. In 1a and 2a the thickening was halted after 100 m.y., and in 1b after 200 m.y., allowing the lithosphere to reach thermal equilibrium. Curve 4 shows compensation at 200 km depth. None of these factors have a significant effect on the maximum height of the surface topography. The controlling factor, however, is the total thickness of the basaltic crust. The maximum topographic height is achieved when the crust reaches its critical thickness of ~38 km, beyond which the crustal shortening actually depresses the surface due to creation of high-density granulite and eclogite in the deeper parts that readily sink into the mantle. The crust of the cold Venus model requires significant thickening before it reaches the critical thickness, whereas those of the Earth-like and especially the hot Venus models need less thickening. Consequently, the cold Venus model produces a surface topography that is ~1.5 times higher than that of the Earth-like Venus model and ~3 times higher than that of the hot Venus model.

Lakshmi Planum is higher than 4 km above the mean surface of Venus and Maxwell Montes stand ~6 km higher. These prominent features are ~2-6 times higher than the maximum height that could be achieved by thickening a basaltic crust, no matter which lithospheric model is used. These features probably contain relatively less dense materials and represent analogues of continental masses on Earth.

References: [1] Solomon S. C. and Head J. W. (1984) *JGR, 89,* 6885–6897. [2] Vorder Bruegge R. W. and Head J. W. (1989) *GRL, 16,* 699–702. [3] Kiefer W. S. and Hager B. H. (1991) *JGR, 96,* 20967–20980. [4] Morgan P. and Phillips R. J. (1983) *JGR, 88,* 8305–8317. [5] Vorder Bruegge R. W. and Head J. W. (1991) *Geology, 19,* 885–888. [6] Janle P. and Jansen D. (1984) *Earth Moon Planets, 31,* 141–155. [7] Solomon S. C. and Head J. W. (1990) *GRL, 17,* 1393–1396. [8] Bindschadler D. L. et al. (1990) *GRL, 17,* 1345–1348. [9] Ito K. and Kennedy G. C. (1971) *Am. Geophys. Union Mon., 14,* 303–314. [10] Green D. H. (1967) *The Poldervaart Treatise on Rocks of Basaltic Composition, Vol. 1* (H. H. Hess and A. Poldervaart, eds.), Wiley-Interscience, New York. [11] Ahren T. J. and Schubert G. (1975) *Rev. Geophys. Space Phys., 13,* 383–400. [12] Schaber G. G. et al. (1992) *JGR,* in press. [13] Phillips R. J. et al. (1992) *JGR,* in press. [14] Sjogren W. L. et al. (1984) *GRL, 11,* 489–491.

N93-1 P 9

CONSTRAINTS ON THE THERMAL EVOLUTION OF VENUS INFERRED FROM MAGELLAN DATA.

J. Arkani-Hamed[1], G. G. Schaber[2], and R. G. Strom[3], [1]Department of Geological Sciences, McGill University, Montreal, Canada, H3A 2A7, [2]U.S. Geological Survey, Flagstaff AZ 86001, USA, [3]Department of Planetary Sciences, University of Arizona, Tucson AZ 85721, USA.

A surface topography produced through viscous deformation of a mantle by internal loadings correlates with the resulting gravity anomaly if the mantle has an almost uniform viscosity [1]. The high correlation over low-degree spherical harmonics of surface topography and gravity anomalies of Venus and the greater apparent depth of compensation of the topography imply a high-viscosity upper mantle for Venus [2] that probably results from dehydration effects of the high surface temperature [3] and from the colder interior of

Fig. 2. The surface topography produced by the crustal shortening of the cold Venus model with (curve 1) and without (curve 2) taking the BGET into account. Point B approximates Bindschadler et al.'s [8] model and point M is the approximate height of Maxwell Montes.

Fig. 3. The surface topography produced by the crustal thickening of the cold (1300), the Earth-like (1400), and the hot (1500) Venus models. The curves a, b, and c denote the thickening rates of 0.5, 0.25, and 0.167 km/m.y., respectively. The compensation depths are at 150 km, except for the curve 4 whose compensation depth is at 200 km.

rebound to produce a significant surface elevation. Not only is it impossible to produce a high plateau, but it is quite possible to produce a basin.

The factors that could affect the surface topography of a thickening crust are (1) the initial temperature distribution in the lithosphere, (2) thickening rate of the crust, (3) depth of compensation,

Venus [4]. The convecting mantle that is tightly coupled to the high-temperature weak lithosphere through the high-viscosity upper mantle [2] may strongly deform the lithosphere, producing a mobile and semifree boundary layer on top of the convecting mantle.

The thermal convection models of a mantle that convects under a stress-free surface boundary condition [5] and is mostly heated from within, as favored for Venus by many investigators [e.g., 3,4,6], develop a strong thermal boundary layer at the surface but a weaker one at the base [7]. Strong instabilities in the near-surface boundary layer result in downwelling of cold plumes, whereas the upwelling zones are relatively diffused [8]. Such a mantle convection may not create sharp oceanic-type ridge systems, but it may result in distinct compressional features at the surface associated with the downwellings. The lack of distinct ridge systems on Venus, and the almost axisymmetric geometry of Lakshmi Planum and surrounding mountains that are interpreted as thickened crust over downwelling mantle convection [6], are in good agreement with the surface expressions of a convecting mantle that is mainly heated from within.

Another major characteristic of the mantle convection models is their time dependence. A time-dependent oscillatory convection at high Rayleigh numbers reduces to a steady-state slow convection as the Rayleigh number is decreased below a critical value. In Venus' mantle the local Rayleigh number probably decreases with depth due to decrease in the thermal expansion coefficient with depth [4,7]. The secular cooling of the core decreases the temperature drop across the mantle, and the secular cooling of the mantle increases its effective viscosity. It is therefore possible that the Rayleigh number decreases with time as the mantle cools. This would increase the thickness of the thermal boundary layers, especially the lower one, decrease the heat flux out of the core, and hamper the instability of the lower layer. The mantle becomes more like one that is heated mainly from within. The Rayleigh number may decrease below the critical value and a time-dependent, vigorous convection may suddenly change to a quasisteady and slow circulation [4].

The impact craters with diameters from 1.5 to 280 km compiled from Magellan observations indicate that the crater population on Venus has a completely spatially random distribution [9] and the size/density distribution of craters with diameters ≥35 km is consistent with a "production" population with an age of 500 ± 250 m.y. [10]. The similarity in size distribution from area to area indicates that the crater distribution is independent of crater size. Also, the forms of the modified craters are virtually identical to those of the pristine craters. These observations imply that Venus reset its cratering record by global resurfacing 500 m.y. ago, and resurfacing declined relatively fast. The fact that <40% of all craters have been modified and that the few volcanically embayed craters are located on localized tectonic regions [11] indicate that only minor and localized volcanism and tectonism have occurred since the latest vigorous resurfacing event ~500 m.y. ago and the interior of Venus has been solid and possibly colder than Earth's. This is because the high-temperature lithosphere of Venus would facilitate upward ascending of mantle plumes and result in extensive volcanism if Venus' upper mantle were as hot as or hotter than Earth's [12]. Therefore, the present surface morphology of Venus may provide useful constraints on the pattern of that vigorous convection, and possibly on the thermal state of the Venus' mantle.

We examine this possibility through numerical calculations of three-dimensional thermal convection models in a spherical shell with temperature- and pressure-dependent Newtonian viscosity, temperature-dependent thermal diffusivity, pressure-dependent thermal expansion coefficient, and time-dependent internal heat pro-

duction rate. Both rigid and free boundary conditions are considered at the surface, whereas the boundary condition at the core/mantle boundary is assumed free as long as the core has not become completely solidified. Otherwise it is assumed to be rigid. The lateral dependence of the governing equations of motion, heat transfer, and continuity is resolved through spherical harmonic representations of field variables and the resulting radially dependent differential equations are solved numerically using the Green function method [4]. Among all parameters affecting the pattern of convection circulations, the free boundary condition at the surface and the secular decrease of temperature at the core/mantle boundary have by far the most dominant effects. These two factors result in fast cooling of the mantle and sharp reduction in its effective Rayleigh number, so that oscillatory vigorous convection circulations could become quasisteady and slow. A strong thermal boundary layer is developed near the surface, whereas that near the core/mantle boundary is relatively weak. Consequently, major lateral variations in temperature exist in the upper mantle, but they are subdued near the core/mantle boundary.

References: [1] Richards M. A. and Hager B. H. (1984) *JGR, 89,* 5987–6002. [2] Phillips R. J. (1990) *JGR, 95,* 1301–1316. [3] Kaula W. M. (1990) *Science, 247,* 1191–1196. [4] Arkani-Hamed J. and Toksoz M. N. (1984) *PEPI, 34,* 232–250. [5] Schubert G. et al. (1990) *JGR, 95,* 14105–14129. [6] Bindschadler D. L. et al. (1990) *GRL, 17,* 1345–1348. [7] Leitch A. M. and Yuen D. A. (1991) *JGR, 96,* 15551–15562. [8] Jarvis G. T. and Peltier W. R. (1989) in *Mantle Convection: Plate Tectonics and Global Dynamics* (W. R. Peltier, ed.), 479–595, Gordon and Breach. [9] Phillips R. J. et al. (1992) *JGR,* submitted. [10] Schaber G. G. et al. (1992) *JGR,* submitted. [11] Strom R. G. et al. (1992) *LPSC XXIII,* 1065–1066. [12] Erickson S. G. and Arkani-Hamed J. (1992) *GRL,* in press.

N93 - 14189+2

SURFACE PROCESSES ON VENUS. R. E. Arvidson, McDonnell Center for the Space Sciences, Earth and Planetary Sciences, Washington University, St. Louis MO 63130, USA.

Magellan synthetic aperture radar (SAR) and altimetry data were analyzed to determine the nature and extent of surface modification for venusian plains in the Sedna Planitia, Alpha Regio, and western Ovda Regio areas. Specific cross sections derived from the SAR data were also compared to similar data for dry terrestrial basaltic lava flows (Lunar Crater and Cima volcanic fields) and playas (Lunar and Lavic Lakes) for which microtopographic profiles (i.e., quantitative roughness information) were available. In Sedna Planitia, where clear stratigraphic relations can be discerned among volcanic flow units, the youngest unit has planform and microwave characteristics indicative of pahoehoelike flows. The second youngest flow exhibits cross-section values similar to fresh a'a flows at the Lunar Crater and Cima fields. Older flows have the same planform shapes as the youngest a'a flow, but exhibit backscatter signatures similar to degraded terrestrial flows. We suggest that flows with a variety of surface textures have been emplaced at Sedna Planitia and elsewhere and that initial properties have been removed by surface processes for the older units. Degradational effects of ejecta are directly evident in deposits from the nearby impact crater Lind mantle sections of the Sedna flows. Differences in cross sections between mantled and unmantled flows are consistent with ejecta thicknesses of centimeters. Similar thicknesses are inferred for the extensive parabolic ejecta deposit from Stuart Crater, which is located on plains to the east of Alpha Regio. Ejecta deposits are inferred to accumulate during impact events and to be dispersed

over geologic time by aeolian activity. The widespread distribution of thin ejecta deposits indicates that the rate of aeolian erosion is low, perhaps only a fraction of a micrometer per year. We thus conclude that most flow degradation in locations such as Sedna Planitia is due to *in situ* weathering. In addition, elevation-dependent weathering is inferred in western Ovda Regio, where plains above 6054 km radius have enhanced reflection coefficients (>0.20) as compared to adjacent plains at lower elevations. Furthermore, the presence of deposits with normal reflection coefficients blown in from lower elevation plains indicates that the conversion to high dielectric materials occurs at a slower rate than the rate of sediment accumulation by winds. Combined vertical rates of surface modification of meters over hundreds of millions of years are inferred from the extent of surface modification for plains and the impact crater abundance. This rate is orders of magnitude lower than the terrestrial value and suggests that it will be possible to constrain relative ages of surfaces on the basis of degree of preservation of volcanic landforms and microwave signatures.

N93-12295

SHIELD FIELDS: CONCENTRATIONS OF SMALL VOLCANIC EDIFICES ON VENUS.

J. C. Aubele and L. S. Crumpler, Department of Geological Sciences, Box 1846, Brown University, Providence RI 02912, USA.

Observations: Pre-Magellan analysis of the Venera 15/16 data indicated the existence of abundant small volcanic edifices, each ≤20 km diameter, interpreted to be predominantly shield volcanos [1,2] and occurring throughout the plains terrain, most common in equidimensional clusters. With the analysis of Magellan data, these clusters of greater than average concentration of small volcanic edifices have been called "shield fields" [3,4]. A typical shield field consists of volcanos numbering ≈10^2 and ranging in density from 4 to 10 edifices per 10^3 km^2 within an area that covers ≥10^4 km^2. Most of these fields are roughly equant in outline, but a small percentage are elongate or consist of diffuse concentrations of edifices over larger areas. Typical field diameters mostly range from 50 to 350 km, with a mode from 100 to 150 km (Fig. 1). The cumulative size distribution (Fig. 2) of shield fields more closely follows the trend of coronae/arachnoids/novae (features assumed to be dominantly intrusive) than features assumed to be dominantly extrusive (such as large or intermediate-sized volcanos); this similarity apparently reflects reservoir and source dimensions. The volcanic edifices within an individual shield field are generally ≤10 km in diameter, and are predominantly radar-bright and shield-shaped in profile with a single summit pit [5]. A small number of fields are composed predominantly of a less common edifice type such as radar-dark shields, edifices with radar-bright aureoles or
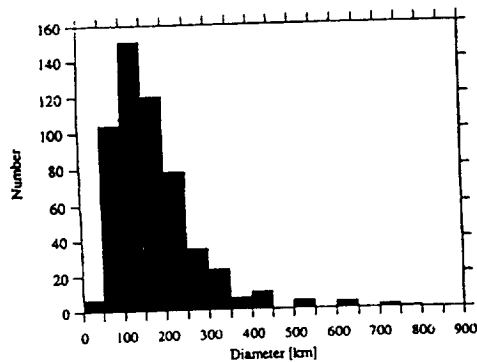
Fig. 1.
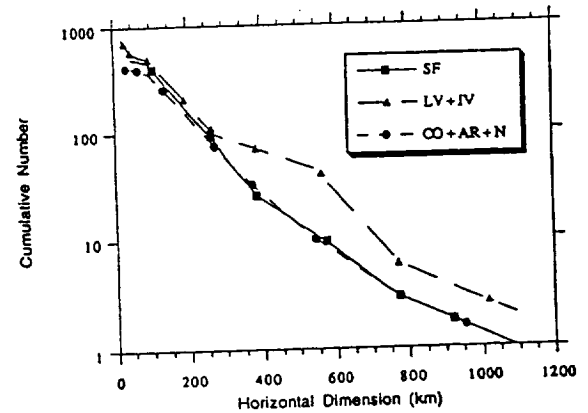
Fig. 2.

halos, elongated small shields with bright radial flow patterns ("anemones"), or domical or conical profile edifices [5]. The radar-bright or radar-dark material locally surrounding shield field edifices, which sometimes covers local structural lineaments, is interpreted to represent associated volcanic material, probably thin lava flow units, although minor amounts of ash or cinder may produce a very thin local veneer in some areas [5]. If the visible flow fields associated with some shield fields are of average size, then the area of resurfacing associated with a shield field appears to be comparable to that of the area of a single large volcano. Shield formation did not apparently occur planetwide as a single event, as there appears to be a range of shield field ages in relation to the surrounding regional plains units based on stratigraphic relationships. A few vents within a shield field may be aligned along dominant structural trends, and summit pits frequently occur along dominant structural trends; however, the clustering characteristics of edifices within a shield field appear to be most similar to that of terrestrial cinder cone fields lacking in well-defined structural vent control.

Distribution: At the conclusion of cycle 2 coverage, 556 shield fields (Fig. 3) have been identified in the catalog of volcanic features [3,6] prepared for the Magellan Science Analysis Team, Volcanism Working Group; shield fields are the most abundant single category type of volcanic or magmatic features. Approximately 70% of shield fields occur on 50% of the surface of Venus. Shield fields are somewhat more distributed over the surface than are large single magmatic or volcanic features such as coronae or large volcanos [3,6,7]; however, Magellan global analysis has confirmed the previous observation made from the Venera dataset [1] of at least one and possibly two dominant global concentrations. The region of greatest concentration, which also shows high concentrations of all other volcanic features [4,8,9], has been informally named the Beta-Atla-Themis or "BAT" region, centered at longitude 250°. Density of shield fields within this region ranges from 2 to 7 fields per 10^6 km^2 and high density of shield fields appears to define the margins of the BAT area. Magellan has also confirmed the previous observation based on Venera data [1] that small volcanos do not occur in large numbers in the areas dominated by ridge belts or in the very lowest or very highest elevations on the planet. Approximately 59% of shield fields occur in elevations between mean planetary radius and 2 km above MPR, 36% occur in regions below MPR in elevation, and only 5% occur in regions greater than 2 km above MPR. When normalized for percentage of surface area at these elevations, 76% of shield fields occur in regions 1 to 2 km above MPR. Fields are commonly spatially associated
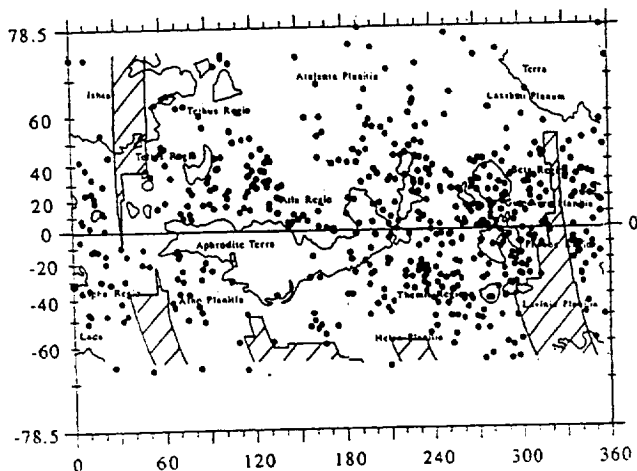
Fig. 3.

with larger volcanic features. Shield fields frequently occur within the inner rings of coronae; those asociated with large volcanos often occur around the distal edges of, and occasionally are surrounded by, the radial lava flows forming the volcano flanks, but they also occur near the summit of a few large volcanos.

Implications: Although individual small shields can and do occur almost everywhere on the plains terrain of Venus, they most commonly occur in fields that are well-defined, predominantly equant, clusters of edifices. Major questions include why the edifices are concentrated in this way, how they relate to the source of the eruptive material, and what the possible relationship of shield fields to plains terrain is. There are three possible models for the origin of fields and small shields: (1) a field represents an "island" of higher topography subsequently surrounded by later plains material; (2) a field represents the area of a region of anomalous melting; or (3) a field represents the area of a magma reservoir. Model 1 would imply that the fields represent portions of a stratigraphic "layer" of small edifices produced globally in an earlier period of greater small shield productivity and that there has been a change in eruption style with plains formation occurring predominantly after the production of the small edifices. If the shield fields are isolated "islands" surrounded by flooded plains, the equant aspect of most fields could be explained; however, some fields show associated flows superimposed on surrounding plains and the manner in which shield fields appear to cover local structural patterns suggests that they are associated with plains-forming material themselves. In addition, local stratigraphic relationships show that there is a range of shield field ages in relation to the surrounding regional plains units and the associated larger volcanic features, implying that shield formation did not occur planetwide as a single event. Models 2 and 3 imply that the fields represent areas of melting anomalies. Model 2 implies that the area of the field is controlled by the extent of the region of melting. A variation of Model 2 uses small reservoirs to explain local groups and alignments of edifices or differences in edifice type due to variations in eruptive style or melt chemistry. Model 3 implies that the area of the field is controlled by the areal extent of a magma reservoir. The areal shape and density of most shield fields could be explained by postulating a shallow regional reservoir or trap located between the melt source region and the surface and approximately equal in size to the areal extent of the field. Given the stratigraphic evidence of the range of shield field ages, models 2 and 3 are favored over model

1 for most cases. Whether the shape and size of a field reflects the area of the melt anomaly or the area of a reservoir is difficult to determine. The formation of a field of small volcanos, rather than a single large volcano, must imply a difference in magma rates or reservoir/source area characteristics. The reservoir or source area characteristics of shield fields can apparently be related to the scale of the feature, as has previously been postulated for coronae [7]. An associated question is the relationship of shield fields to plains terrain. This can be expressed as four possibilities, some of which are also related to the model of origin of the "fields" described above. The possibilities are as follows: (1) The edifices may be the source of lava flows that form or resurface the plains, which would imply that the extrusive volume from each edifice is greater than the visible volume of the edifice and that the plains terrain is created from a stratigraphic sequence of edifices and associated flows; (2) the edifices and plains may be formed simultaneously, which would imply that the edifices are localized point sources within a large extrusive mechanism that creates plains; (3) the edifices may predate the plains, which would imply an early global edifice-building stage and subsequent change in eruption style and heat flow to large-volume-flow field-type eruptions; or (4) the edifices may postdate the plains, which would imply a change in eruption style to late-stage localized small-volume extrusions or hot-spot-type anomalies.

Detailed studies of several shield fields are continuing in an attempt to answer these fundamental questions and to select appropriate models for understanding shield fields and their role in volcanic resurfacing processes and crustal volume contributions.

References: [1] Aubele and Slyuta (1990) *Earth Moon Planets, 50/51,* 493–532. [2] Garvin and Williams (1990) *GRL, 17,* 1381–1384. [3] Head et al. (1992) *JGR,* special Magellan issue, submitted. [4] Aubele J. C. et al. (1992) *LPSC XXIII,* 47–48; Aubele et al. (1992) *Eos, 73,* 178. [5] Guest et al. (1992) *JGR,* special Magellan issue, submitted. [6] Crumpler et al. (1992) *LPSC XXIII,* 277–278; Crumpler et al. (1992) in preparation. [7] Stofan E. R. et al. (1992) *JGR,* special Magellan issue, submitted. [8] Head et al. (1992) *LPSC XXIII,* 515–516. [9] Crumpler and Aubele (1992) *LPSC XXIII,* 275–276.

N93-14298

THE GEOLOGY OF THE VENERA/VEGA LANDING SITES. A. T. Basilevsky[1] and C. M. Weitz[2], [1]Vernadsky Institute of Geochemistry and Analytical Chemistry, Russian Academy of Sciences, Moscow 117975, Russia, [2]Jet Propulsion Laboratory, California Institute of Technology, Pasadena CA 91109, USA.

We have performed a photogeological analysis of the Venera/Vega landing sites using Magellan radar images. These seven sites are the only places on Venus where geochemistry measurements were taken. In this study, the updated coordinates of the landing sites are used and the landing circle has a radius with an admissable error of about 150 km [1].

Photogeologic Description of the Landing Sites: Venera 8 landed on the equatorial plains within a small local topographic rise eastward of Navka Planitia. The coordinates of the landing site are $10.70°S, 335.25°E$. Gamma-spectrometric analysis showed that the surface material contains relatively high contents of K, U, and Th [2,3]. A comparison with terrestrial K_2O-U-Th analogs of this material suggests that it may represent evolved subalkaline magmatic rock of intermediate silica content [4,5] or alkaline basalt [6,7,8,9], particularly lamprophyres [10].

Analysis of Magellan data shows that there are two plain-forming volcanic complexes within the landing circle. The older mottled plain and the younger plains complex both consist of radar-bright, -intermediate, and -dark subunits. Because some of these subunits have a flowlike morphology, we believe that these units are lava flows. The older mottled plain is dissected by northwest-trending swarms of fractures while the younger plain complex in the western half of the landing circle is not affected by these fractures.

In the northern part of the landing circle is a steep-sided pancake dome, approximately 22 × 25 km in diameter. Radar foreshortening measurements indicate a height of about 270 m and a slope of 12.6°. The dome is similar to other steep-sided volcanic domes described by Head et al. [11] and Pavri et al. [12]. Some smaller steep-sided domes, many small gentle-sloped domes, and a possible filled caldera can also be found within the landing circle.

Venera 9 landed on the northeastern slope of Beta Regio rise. The landing circle is centered at 31.01°N, 291.64°E. This slope of Beta rise, as well as the other slopes, is made up of tessera and plain embaying the tessera. Within the landing site, the plain predominates while tessera occupies less than 10% of the area. The plain is mostly fractured with a radar-bright fracture system extending eastward from Rhea Mons. The slopes of the east-west-trending fractures are radar-bright because of surface roughness from scarps and rock fragments. Small (a few kilometers across) gentle-sloped volcanic domes can also be seen in the vicinity of the landing site. No pancake features resembling the Venera 8 dome have been found at the Venera 9 site [13].

The Venera 9 spacecraft landed on a steep (~30°) slope covered with platelike decimeter-sized rock fragments and soil between these rock fragments [14]. This panorama is probably showing a slope on one of the numerous fractures seen in the Magellan imagery of the landing circle. The gamma ray spectrometer measured low contents of K, U, and Th, which suggests a tholeiitic basaltic composition for the sample [3].

Venera 10 landed on the lowland near the southeastern edge of Beta Regio rise. The landing circle is centered at 15.42°N, 291.51°E. The geology of this area includes large massifs of tessera and mottled plain that embays the tessera. The center of the landing site is on the plain about 30 km south of the tessera. The plain occupies 60–65% of the landing circle, while the tessera occupies the remaining 35–40%. Adjacent to the southern boundary of the landing site is a 60-km-diameter gently sloped volcano with lava flows emanating radially from it and entering into the landing circle. A few wind streaks, implying a west to northwest direction of aeolian transportation, are seen behind some small volcanic domes [13].

The television panorama of the site shows that the Venera 10 spacecraft landed on the plain and not on the tessera. The plain is covered with soil in local lows between the layered bedrock. The outcrops of bedrock are spaced a few meters from each other and are about 10 to 15 cm above the soil-covered lows. This implies that the soil thickness in the lows is not more than about 0.5 m [14]. Gamma ray spectroscopy measurements of K, U, and Th are very close to those measurements taken at the Venera 9 landing site [3].

Venera 13 landed at Navka Planitia on the eastern end of Phoebe Regio rise. The landing circle is centered at 7.55°S, 303.69°E. The landing site is dominated by radar-dark plain transected in its southwestern part by a northwest-southeast-trending fracture belt. The southeastern portion of the site is affected by part of a 200-km coronalike feature. This feature has radial lava flows emanating from it that enter the landing circle in the southeast. Northeast-southwest-trending subtle wind streaks can be seen behind some

topographic obstacles, inferring a southwest downwind direction.

Just outside the landing site circle are four pancake volcanic domes and a steep-sloped volcano with a summit caldera [13]. Two of these steep-sided domes are located about 300 km southwest of the estimated landing point. The flat-topped pancake dome (25 × 30 km diameter) formed first and the steep-sided conical volcanic edifice with a summit crater (15 × 20 km diameter) formed on the western flank of the pancake dome. These domes are approximately 2.2 km in elevation above the surrounding plain. The flat-top dome located 200 km southeast of the estimated landing point is 35 × 45 km in diameter and rises 1.5 km above the surrounding plain. This dome lies on top of the southeastern portion of the coronalike feature. The two other pancake domes are a 15 × 20 km dome located 230 km northeast of the estimated landing point and a 12 × 15 km dome located 320 km east of the estimated landing point.

The television panoramas of the site show a landscape similar to that seen at the Venera 10 site: soil in local lows and layered bedrock outcrops at local highs [15]. X-ray fluorescence spectroscopy indicated a composition close to subalkaline (4% K₂O) basalt [16].

Venera 14 landed in southern Navka Planitia, about 800 km southeast of the Venera 13 landing site. The landing circle is centered at 13.05°S, 310.19°E, on the eastern flank of a 75-km-diameter gentle-sloped volcano. The landing site is dominated by lava flows from the volcano. There is much variation in the backscatter cross sections for the different lava flows, most likely related to the surface roughness of the flows. The flow lengths range from tens to several hundreds of kilometers. The western side of the volcano is heavily fractured by a northwest-southeast-trending fracture zone that also dissects the radar-dark plain at the Venera 13 landing site [17]. Inside the landing circle are some patches of complex fractured terrain embayed by lava flows. No steep-sided volcanic features resembling those observed in the vicinities of the Venera 8 and 13 sites are seen inside the Venera 14 landing circle. There is, however, a 12 × 17 km diameter complex volcanic dome, 165 km north of the Venera 14 landing site. The bright radar-illuminated western side and the darkened eastern side suggest radar foreshortening from steep slopes. Because the dome is small, isolated, and outside the landing circle, it is unlikely that the dome could have influenced the geochemistry measurements made at the landing site. Instead, we believe that the geochemistry inside the landing circle represents the lava flows from the gentle-sloped 75-km-diameter volcano.

Television panoramas of the Venera 14 site show a plain dominated by layered bedrock and a minor amount of soil in local lows. If the soil were removed from the Venera 10 and 13 sites, then the Venera 10, 13, and 14 panoramas would look remarkably similar. X-ray fluorescence spectroscopy indicates a composition close to tholeiitic basalt [16].

Vega 1 landed on Rusalka Planitia, north of Aphrodite Terra rise and about 1000 km west of Sapas Mons. The landing circle is centered at 8.10°N, 175.85°E. The landing site is dominated by a radar-dark plain with a network of narrow and low sinuous ridges. In some places, the plain looks brighter and the boundaries of these brighter spots are very diffuse. Outside the landing circle, there are vast areas of radar-bright plains. The ridges continue from the darker unit into the brighter unit. Near the center of the landing center is a radar-bright, gentle-sloped volcanic dome about 10–12 km in diameter. The dome has a radar-bright, fan-shaped wind streak indicating a preferential direction of aeolian transportation to the southeast. A few smaller volcanic domes, usually associated with bright spots, are also seen in the landing circle. No television panoramas were taken at the landing site. Gamma ray spectroscopy

measurements indicate low contents of K, U, and Th, typical for tholeiitic basalts [18,4].

Vega 2 landed at the transitional zone between Rusalka Planitia and the eastern edge of Aphrodite Terra rise. The landing circle is centered at 7.14°S, 177.67°E, about 1500 km south of the Vega 1 landing site. Most of the landing site consists of a densely fractured radar-bright plain with radar-dark plain to the northeast. The southwestern portion of the site has ridges and fractures associated with a 300-km-diameter coronalike feature. No television panoramas were made at the site but both gamma ray spectroscopy and X-ray fluorescence spectroscopy measurements were taken. The gamma ray measurements of K, U, and Th and the X-ray fluorescence spectroscopy measurements of bulk chemistry indicate a composition close to tholeiitic basalt [18,4].

Discussion: We have shown that within all the Venera/Vega sites the dominant type of terrain is plains. These plains include (1) mottled (Venera 8, 10, and Vega 1), (2) homogeneously dark (Venera 13), (3) dominated by prominent lava flows (Venera 14), and (4) fractured (Venera 9 and Vega 2). The plains are associated with coronalike features (Venera 8(?), 13, 14, and Vega 2), fracture belts and swarms (Venera 8, 13), and tesserae (Venera 8(?), 9, 10). This diversity reflects the global diversity of the venusian plains.

For the two sites (Venera 8 and 13) where nontholeiitic compositions of the surface material were determined, the steep-sided domes resembling those described by Head et al. [11] and Pavri et al. [12] have been found. For the five sites where geochemical signatures of tholeiitelike basalts were identified (Venera 9, 10, 14, and Vega 1, 2), these steep-sided domes have not been observed inside the landing circle. We believe that this correlation favors a nontholeiitic origin for these steep-sided domes.

The television panoramas from the Venera 9, 10, 13, and 14 landers show a microlandscape with characteristics that correlate well with the Magellan observations. At these four sites, the panoramas all showed bedded outcrops. Before the Magellan mission, these bedded rocks were considered as either basaltic tuffs or lavas [14,15]. Magellan imagery does not resolve the lava vs. tuff issue, although the presence of prominent lava flows at the Venera 14 site favors a lava interpretation of the bedded rocks. The very low bulk density of these rocks estimated from Venera 13 and 14 overload measurements (1.5 g/cm³) favors the tuff interpretation. Therefore, the origin of these bedded rocks still remains an enigma.

Conclusion: Joint analysis of Magellan and Venera/Vega data on the Venera/Vega landing sites has shown that the panoramas and geochemistry measured by the landers agree well with the morphology seen in Magellan imagery of the site. This observation suggests that it is possible to extrapolate our geochemical and morphologic results to the remaining Magellan imagery of Venus.

References: [1] Akim E. L. and Stepanyantz V. A. (1992) *Astronomichesky Vestnik* (in Russian), in press. [2] Vinogradov et al. (1973) *Icarus, 20,* 253–259. [3] Surkov et al. (1976) *Kosmicheskeye Issledovaniz, 14 (5),* 704–709 (in Russian). [4] Surkov et al. (1986) *Proc. LPSC 17th,* in *JGR, 91,* E215-E218. [5] Nikolaeva O. V. (1990) *Earth Moon Planets, 50/51,* 329–342. [6] Surkov Yu. A. and Fedoseev G. A. (1978) in *Advances in Space Research in Soviet Union,* 313–351, Nauka, Moscow (in Russian). [7] Taylor S. R. and McLennan S. M. (1985) *The Continental Crust: Its Composition and Evolution,* Blackwell, Oxford, 312 pp. [8] Taylor S. R. (1989) *Tectonophysics, 161,* 147–156. [9] Taylor S. R. (1991) *Nature, 350,* 376–377. [10] Basilevsky et al. (1992) *JGR,* in press. [11] Head et al. (1992) *JGR,* in press. [12] Pavri et al. (1992) *JGR,* in press. [13] Basilevsky A. T. and Weitz C. M. (1992) *LPSC XXIII,* 67–68. [14] Florensky et al. (1977) *Bull. GSA, 88,* 1537–1545. [15] Basilevsky et al. (1985) *Bull. GSA, 96,* 137–144. [16] Surkov et al. (1984) *Proc. LPSC 14th,* in *JGR, 89,* B393-B402. [17] Ivanov M. A. (1992) *LPSC XXIII,* 579–580 [18] Barsukov et al. (1986) *Geokhimia, 3,* 275–288 (in Russian).

N93-14297 *P. 3*

GLOBAL DEFORMATION ON THE SURFACE OF VENUS.

Frank Bilotti, Chris Connors, and John Suppe, Department of Geological and Geophysical Sciences, Princeton University, Princeton NJ 08544, USA.

Large-scale mapping of tectonic structures on Venus shows that there is an organized global distribution to deformation. The structures we emphasize are linear compressive mountain belts, extensional rifted zones, and the small-scale but widely distributed wrinkle ridges. Ninety percent of the area of the planet's compressive mountain belts are concentrated in the northern hemisphere whereas the southern hemisphere is dominated by extension and small-scale compression [1,2]. We propose that this striking concentration of fold belts in the northern hemisphere, along with the globe-encircling equatorial rift system, represents a global organization to deformation on Venus. A great circle that connects the northernmost branches of a globe-encircling rift system roughly separates the tectonic hemispheres [1] (Fig. 1). South of this tectonic equator [1] there are a few well-formed fold belts at the edges of small crustal blocks within the global rift system, but the globally significant deformation is the rift system and the wrinkle ridges.

Compressional structures on Venus can be divided into two major styles: linear fold belts and wrinkle ridges. Figure 2 shows that the major difference between these two styles is the distribution and localization of strain. Wrinkle ridges represent deformation that is distributed over thousands of kilometers whereas fold belts show concentrated deformation along narrow bands. Venus is the only terrestrial planet other than Earth that has linear compressive mountain belts [3]. Venusian fold belts, similar to those at plate margins of the Earth, are the dominant compressional structures in the northern tectonic hemisphere. They are typically about 100 km wide and thousands of kilometers long. The relatively small amount of erosion on Venus allows us to image fault-related folds forming over regionally extensive decollement horizons within the belts [4]. This supports the notion that these mountain belts are analogous to the thin-skinned fold-and-thrust belts of Earth. Wrinkle ridges are the dominant style of compressional deformation in the southern
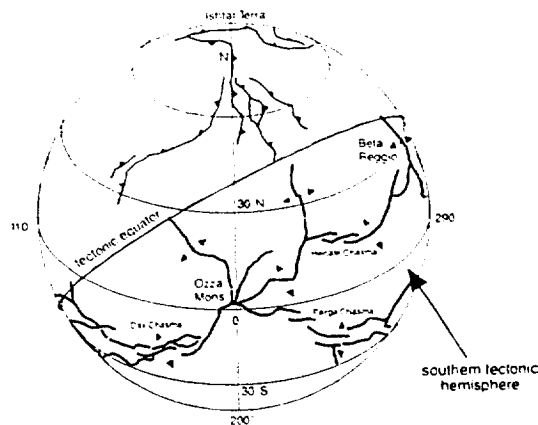
Fig. 1. Generalized tectonic map of Venus after [3]. Rift zones are indicated by the heavy black lines. Ninety percent of the area of foldbelts lies in the northern hemisphere while the southern tectonic hemisphere is dominated by extension and small-scale compression in the form of wrinkle ridges.
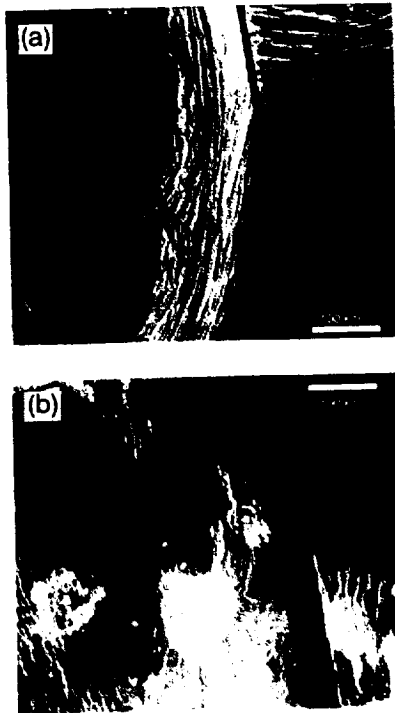
Fig. 2.   Magellan SAR images showing (a) the northeastern edge of the Artemis Chasma foldbelt and (b) wrinkle ridges from the southern plains. Note the concentration of strain in the foldbelt when compared with the distributed strain of the wrinkle ridges.

Fig. 3.   Latitudinal distributions of foldbelts on Venus. Note the dominant concentration in the northern hemisphere and the poleward increase in the normalized plot.

hemisphere. Those that can be adequately resolved with the Magellan SAR are comprised of angular folds and/or an outcropping thrust-fault.

The plains fold belts, termed ridge belts on Venus [5,6], are concentrated between 150° and 250° longitude in the northern hemisphere and show a strongly north-south (longitudinal) trend [7,8]. Ridge belts cover 3.6×10^6 km², almost 1% of the venusian surface. Another 0.6% of the surface of Venus is covered by fold belts along the borders of major crustal blocks or structures such as coronae, novae, tesserae highlands, and the high plateau of Lakshmi Planum. The surface area covered by fold belts increases with latitude in the northern hemisphere as shown in Fig. 3a. If we normalize by the latitudinal area (Fig. 3b) we find that the percent

area of fold belts very strongly increases poleward in the northern hemisphere. This observation agrees with previous tectonic models [9,8] that propose an internally deforming lithospheric shell that converges toward the north pole. These models call upon an equatorial rift system to generate the new crust that balances this compressive deformation. If we assume modest shortening within the northern hemisphere fold belts (≈100%), we find that relatively small amounts of rifting (≈150-km one-way extension) are necessary to produce all the obvious compressional deformation in the northern hemisphere.

The distribution of wrinkle ridges in the southern hemisphere is being mapped (Fig. 4); the most striking result is the strongly coherent pattern of orientation over many thousands of kilometers.
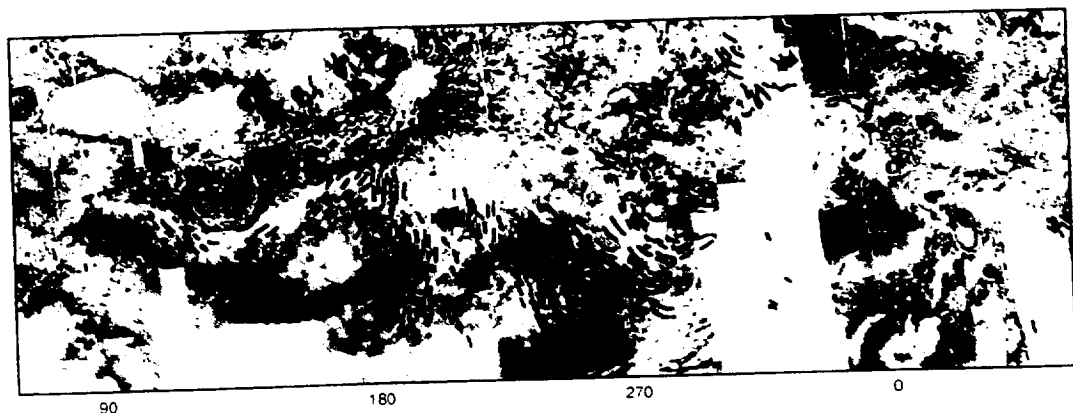
Fig. 4.   Trends and relative densities of wrinkle ridges (black lines) in the southern plains mapped onto mercator projection of topography. Note the high correlation between topography and the deformational trends.

Furthermore, there is a high correlation between wrinkle ridge trends and long-wavelength topography. Within these trends we observe quite regular interridge spacing of 15–30 km. Preliminary studies of wrinkle ridges reveal that individual structures may accommodate up to 1.5 km of shortening. Therefore the distributed shortening in the southern plains that is accommodated by wrinkle ridges is about 1–5%. A higher-resolution investigation of wrinkle ridges is necessary to refine these results and gain a better understanding of the stresses involved in wrinkle ridge formation on Venus. Thus the low-intensity wrinkle ridge deformation of the plains has consistent patterns that approach a global scale.

References: [1] Suppe J. and Connors C. (1991) *Workshop on Mountain Belts on Venus and Earth.* [2] Bilotti F. and Suppe J. (1992) *LPSC XXIII,* 102. [3] Solomon S. C. and Head J. W. (1991) *Science, 252,* 252–260. [4] Suppe J. and Connors C. (1992) *JGR, 97,* in press. [5] Solomon S. C. et al. (1992) *JGR, 97,* in press. [6] Squyres S. W. et al. (1992) *JGR, 97,* in press. [7] Frank S. H. and Head J. W. (1990) *Earth Moon Planets, 50/51,* 421–470. [8] Suppe J. and Connors C. (1992) *LPSC XXIII,* 1389–1390. [9] Morgan W. J. and Morgan J. P. (1991) *AGU Progr. w/Abstr., 72,* 284.

N 9 3 - 1 4 2 8 8

COLDSPOTS OR HOTSPOTS? THE ORIGIN OF PLATEAU-SHAPED HIGHLANDS ON VENUS.

D. L. Bindschadler, Department of Earth and Space Sciences, University of California, Los Angeles CA 90024, USA.

A compelling question for the terrestrial planets is the origin of the highland regions on Venus. Data on the topography, gravity signature, and surface morphology returned by the Pioneer Venus, Venera 15/16, and Magellan spacecraft represent a basis for dividing these highlands into two distinct groups: volcanic rises and plateau-shaped highlands [1]. Volcanic rises are generally thought to be due to mantle upwellings in the form of large mantle plumes [2] and are thus similar in origin to terrestrial hotspots. There is less agreement as to the origin of plateau-shaped highlands (PSH) [1,3,4]. Coldspot mantle downwelling can lead to the formation of a highland region under Venus conditions [3], and previous to Magellan some PSH (particularly W. Ishtar Terra and Ovda and Thetis Regiones) were suggested to be compressionally deformed regions of thickened crust created by mantle downwelling [5,6,7].

A hotspot model proposes that such regions are formed by magmatism and tectonism related to the near-surface ascent of either the diapir-shaped large mantle plume [8] or a solitary disturbance propagating up a plume conduit [9]. The intent of this abstract is to (1) briefly review the characteristics of both volcanic rises and plateau-shaped highlands on Venus and the models for their formation and (2) consider tests that may help to make clear which model best explains the plateau-shaped highlands.

Characteristics of Venus Highlands: Highlands on Venus can be divided into volcanic rises and plateau-shaped highlands (PSH) on the basis of their topography, long-wavelength gravity-topography relationships, and geologic features (Table 1). Volcanic rises are characterized by roughly circular topographic rises with domical cross sections, relatively large geoid-topography ratios (GTRs), and the presence of large volcanic constructs, widespread flows, and extensional tectonism (commonly manifested as radially trending rifts). They include Beta, Atla, Bell, Imdr, and Western and Central Eistla Regiones. Plateau-shaped highlands (PSH) are so named for their shape in cross sections and are characterized in plan view by a variety of shapes, by steep margins and rugged interiors, by lower GTRs than volcanic rises, and by surfaces dominated by the heavily deformed complex ridged terrain (or tessera). They generally appear to share a common sequence of tectonism: shortening (commonly margin-parallel) followed by relatively small amounts (<10%?) of extension [1]. These regions include Ovda, Thetis, Alpha, Tellus, and Phoebe Regiones, Fortuna and Laima Tesserae, and W. Ishtar Terra [1]. The inclusion of W. Ishtar Terra is arguable given its large apparent depth of compensation (ADC) [10] and GTR values as well as the presence of extensive volcanic plains and two large volcanic constructs (see Table 1). For the purposes of this work, W. Ishtar Terra is considered a PSH on the basis of its topography and the overwhelmingly compressional tectonics manifested in its orogenic belts.

Models for Plateau-shaped Highlands: Observations that must be explained by a successful model for PSH include topography, long-wavelength gravity anomalies, and surface morphology. The latter includes the abundant deformational features that dominate their surfaces. A successful model should therefore explain the style(s) of deformation (i.e., compression, extension, etc.) and the relative ages and geometries of these various structural features, information that can be derived from Magellan images because of

TABLE 1.   Characteristics of Venus highlands.

Characteristic	Volcanic Rises	Plateau-shaped Highlands
Topographic cross section	Domical	Steep-sided, rugged interior
Topographic planform	Circular to elongate	Circular to polygonal
Gravity anomaly	Positive, centrally located	Positive or negative, offset from center
GTR/ADC values	~20–35 m/km ~150–300 km	~10–15 m/km ~30–90 km
Volcanic features	Shield volcanos, extensive plains, and flows	Minor plains, flows, and domes
Extensional tectonics	Rifts, numerous graben, and fractures	Small (<10 km), late-stage graben
Compressional tectonics	Largely absent	Broad (10–20 km) ridges, marginal belts
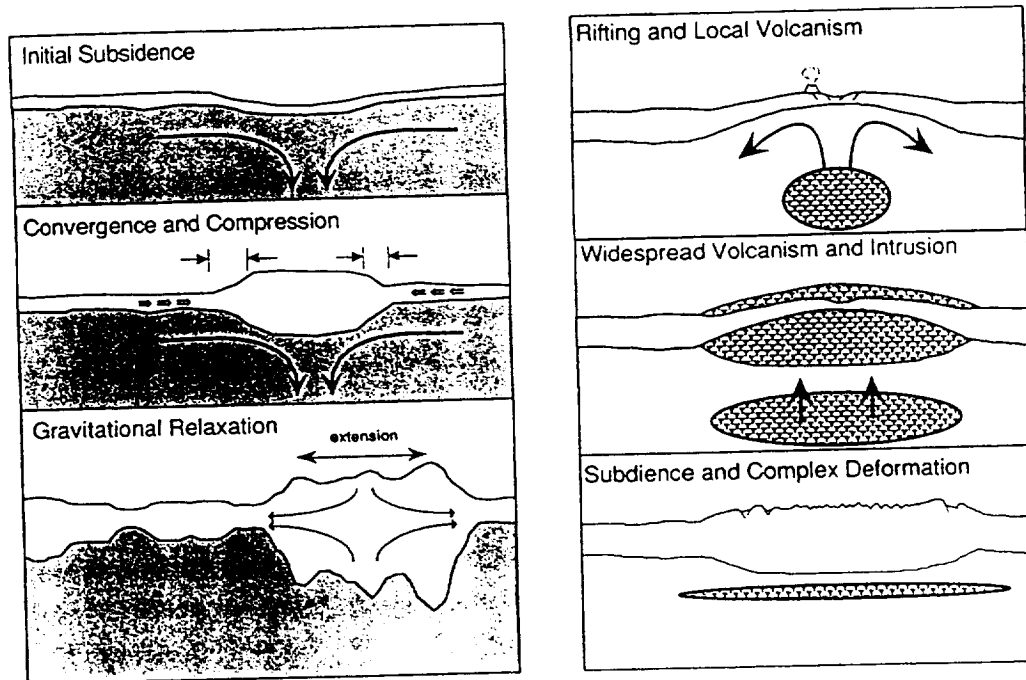
Fig. 1. Sketches illustrate the sequence of events in proposed coldspot (left), and hotspot (right) models for the formation of plateau-shaped highlands on Venus. Hotspot sketch adapted from [8].

their high spatial resolution (120–300 m) [11]. Three models have been suggested as explanations for all or parts of these observations: (1) coldspot tectonics, (2) hotspot tectonics, and (3) asperity tectonics.

Coldspot models [1,5,6] hold that PSH form over mantle downwellings, which are an expected feature of any convecting system, and are thought to represent the highest velocities and strain rates at the top of a convecting mantle [12]. The basic evolution of a PSH (Fig. 1) includes initial subsidence, crustal thickening, and tectonic deformation, which leads to formation of a highland, followed eventually by relaxation and spreading of the highland once downwelling ceases. A necessary condition for this process to operate is that the effective viscosities of the lower crust and upper mantle be sufficiently small and sufficiently similar in magnitude for crustal thickening to proceed within geologically reasonable timescales (<0.5 Ga). This condition appears to be satisfied for Venus conditions and compositions [5,13], but flow laws for crustal material remain a major source of uncertainty. Hotspot models hold that PSH form by magmatism and tectonism caused by the near-surface approach of large volumes of hot, plume-related material (Fig. 1) and are described in more detail elsewhere [8,3,4]. An asperity tectonics model suggests that any crustal plateau (however formed) represents a lithospheric strength discontinuity ("asperity"), which causes the plateau to act as a "magnet" to strain [10,14]. This occurs because the crustal plateau is relatively weak and is thought to deform more easily than stronger, surrounding provinces.

Test of Models: Significant questions of each of the three above models remain unanswered. To understand the formation of PSH it is necessary to answer the following questions:

1. Under what conditions can coldspot models produce gravity and topography that provide acceptable fits to Magellan and/or Pioneer Venus data? Are these conditions plausible, given our knowledge of Venus?

2. What are the detailed kinematics of a coldspot-produced PSH? Do the predicted style, sequence, and relative geometry of tectonic features match Magellan observations?

3. Can hotspot-related tectonic processes (including gravitational spreading/sliding, membrane compression due to subsidence, and deformation related to thermoelastic stresses) qualitatively match observed PSH deformation? Can these processes quantitatively produce enough surface deformation to explain complex ridged terrain?

4. What are the relevant timescales for hotspot tectonic processes and are they geologically reasonable?

5. Can an asperity tectonics model focus sufficient strain into a crustal plateau to explain the observed disparity between PSH and surrounding lowlands in terms of their degree of deformation?

Items (1) and (2) are currently under study and any progress will be reported at the colloquium.

References: [1] Bindschadler D. L. et al.(1992) *JGR*, in press. [2] Phillips R. J. and Malin M. C. (1983) In *Venus* (D. M. Hunten et al., eds.), 159–214, Univ. of Arizona, Tucson. [3] Phillips R. J. et al. (1991) *Science, 252*, 651–658. [4] Grimm R. E. et al. (1992) *LPSC XXIII*, 453–454. [5] Bindschadler D. L. and Parmentier E. M. (1990) *JGR, 95*, 21329–21344. [6] Bindschadler D. L. et al. (1990) *GRL, 17*, 1345–1348. [7] Bindschadler D. L. and Head J. W. (1991) *JGR, 96*, 5889–5907. [8] Herrick R. R. and Phillips R. J. (1990) *GRL, 17*, 2129–2132. [9] Kiefer W. S. and Hager B. H. (1991) *JGR, 91*, 403–419. [10] Grimm R. E. and Phillips R. J. (1991) *JGR, 96*, 8305–8324. [11] Bindschadler D. L. et al. (1992) *JGR*, submitted. [12] Bercovici D. et al. (1989) *GRL, 16*, 617–620. [13] Lenardic A. et al. (1991) *GRL, 18*, 2209–2212. [14] Solomon S. C. et al. (1992) *JGR*, submitted.

MONTE CARLO MODELING OF THE RESURFACING OF VENUS.

M. A. Bullock[1], D. H. Grinspoon[1], and J. W. Head[2], [1]Laboratory for Atmospheric and Space Physics and the Department of Astrophysical, Planetary and Atmospheric Sciences, University of Colorado, Boulder CO 80309, USA, [2]Department of Geological Sciences, Brown University, Providence RI 02912, USA.

The observed size-frequency distribution of impact craters on Venus is consistent with a production surface that is approximately 0.5 to 1.0 Gy old [1]. However, widespread volcanism on the surface suggests that some regions may be significantly younger than this, and the question of whether the surface is in production or equilibrium remains open. Recent results from the Magellan mission to Venus show that only a small number of impact craters are modified by volcanism [2]. Furthermore, statistical analyses of the placement of impact craters on the surface of Venus suggest a completely spatially random distribution [1]. The existing distribution of impact craters on Venus may be explained by three possible equilibrium models:

1. Global scale resurfacing occurred at some time in the past, followed by much reduced volcanic activity [2]. Impact craters would have accumulated since this time, and the surface of Venus would be of a single production age.

2. Resurfacing occurs on a regional level, with a characteristic length scale that is less than the scale of randomness of the crater population [3].

3. Volcanic activity is responsible for a slow vertical accumulation of lava, resulting in the eventual removal of craters [1].

We have developed a three-dimensional model of venusian resurfacing that employs Monte Carlo simulations of both impact cratering and volcanism. The model simulates the production of craters on Venus by using the observed mass distributions of Earth- and Venus-crossing asteroids and comets [4]. Crater rim heights are calculated from a power law fit to observed depth/diameter ratios. The growth of a variety of volcanic features is simulated in the model. The areal extent of shield fields, large volcanos, and lava floods is determined in the simulations by sampling the appropriate distributions for the feature type from Magellan data. Since a greater number of modified craters is found in the Atla-Beta-Themis region, the spatial distribution of volcanic activity is skewed in the model to represent regions of greater or lesser volcanism. Lava flows are modeled by an energy minimization technique to simulate the effects of local topography on the shape and extent of flows. Some mixture of the three endmember models described may be necessary to adequately explain the observed paucity and distribution of partially embayed impact craters. The model is run under a wide range of assumptions regarding the scale and time evolution of volcanism on Venus. Regions of the parameter space that result in impact crater distributions and modifications that are currently observed will be explored to place limits on the possible volcanic resurfacing history of Venus.

References: [1] Phillips R. J. et al. (1991) *JGR*, special Magellan issue, submitted. [2] Schaber G. G. et al. (1992) *JGR*, special Magellan issue, submitted. [3] Phillips R. J. et al. (1991) *Science, 252*. [4] Shoemaker E. M. et al. (1989) *Reports of the Planetary Geology and Geophysics Program: 1988*.

DEBRIS AVALANCHES AND SLUMPS ON THE MARGINS OF VOLCANIC DOMES ON VENUS: CHARACTERISTICS OF DEPOSITS.

M. H. Bulmer[1], J. E. Guest[1], K. Beretan[2], G. Michaels[2], and S. Saunders[2], [1]University of London Observatory, University College London, NW7 2QS, UK, [2]Jet Propulsion Laboratory, Mail Stop 230-225, Pasadena CA 91109, USA.

Modified volcanic domes, referred to as collapsed margin domes, have diameters greater than those of terrestrial domes and were therefore thought to have no suitable terrestrial analogue. Comparison of the collapsed debris using the Magellan SAR images with volcanic debris avalanches on Earth has revealed morphological similarities. Some volcanic features identified on the seafloor from sonar images [1,2] have diameters similar to those on Venus and also display scalloped margins, indicating modification by collapse.

Examination of the SAR images of collapsed dome features reveals a number of distinct morphologies to the collapsed masses. Ten examples of collapsed margin domes displaying a range of differing morphologies and collapsed masses have been selected and examined. Of these, five have more than one failure on their flanks. The aprons have distinct radar characteristics that reveal lobate boundaries, large radar-bright blocks, and hummocky terrain, features typical of landslide deposits [3], making them distinct from lava flows, which show a more constant radar backscatter and irregular boundaries. The morphologies vary (Fig. 1), from those that spread only toward their terminus to those that spread very early in their course and have a large lateral extent. Similar morphologies, seen in GLORIA images of landslides on the seafloor off the Hawaiian Ridge [1], are suggested to be two types, debris avalanches and slumps. The slumps are slow moving during emplacement, wide, and thick, with transverse blocky ridges and steep toes, while debris avalanches are fast moving, elongate, and thinner. While it is difficult to see small-scale surface detail from the SAR images, the comparison seems justified.

The distance the aprons have traveled from the base of the dome ranges from 8.6–68.8 km, making their runout distances comparable to large terrestrial volcanic debris avalanches, pyroclastic flows, and lahars. Data on the travel distance of the venusian avalanches (Table 1) as a function of vertical drop height (H/L), plotted against terrestrial mass movement features, demonstrates the great mobility of a number of them.

TABLE 1. Measurements of seven debris aprons from collapsed margin domes on Venus.

A	B	C	D	E
Name	Volume km³	Height km (H)	Length km (L)	H/L
-26.3, 296.8		1.4	62	0.022
-29.7, 183.7	220	0.9	38.5	0.023
-16.8, 244.8	150	3.7	25.7	0.14
-7.6, 255	135	1.6	19	0.08
-25.4, 308		1.6	10	0.16
-25.4, 308		1.6	8.6	0.19
-0.2, 284.9		0.14	23	0.0061

Fig. 1. Mapped outlines of slump and debris avalanche aprons. The outline in the bottom right is that of a possible lava flow from the collapsed margin dome on Sapas Mons.

On Earth, landslides on volcanic edifices can be triggered by a number of different processes, including those occurring as a result of aseismical crustal deformation, such as oversteepening of slopes due to deformation (possibly resulting from dyke emplacement of magma rise), overloading of the slope (by lavas), excess weight at the top of the slope (due to a large cone or a large area of summit lava), removal of support by explosions on the flanks, and caldera collapse. Failure occurring coseismically can result from structural alteration of the constituent parts of the slope leading to failure, dislodgement of otherwise stable slopes, and fault movement resulting in an increased slope angle [4]. Seismic pumping may also be a major control on slope stability during an earthquake [5].

On Venus, similar processes may operate. The high ambient temperatures may result in development of a weak carapace, which in turn may allow relatively rapid dome growth to occur. If the effusion rates are high, as suggested by the size of the features, then oversteepening would be a likely consequence resulting in failure and collapse. Landslide scars may be modified by continued dome growth. The existence of fractures around the base of some of the collapsed domes and of debris aprons cut by fractures suggests that

there has been seismic activity and surface deformation occurring during the period of modification of the dome.

References: [1] Moore J. G. et al. (1989) *JGR, 94,* 17465–17484. [2] Holister C. D. et al. (1978) *EPSL, 41,* 405–418. [3] Siebert L. (1984) *J. Volcanol. Geotherm. Res., 22,* 163–197. [4] Guest J. E. et al. (1984) *J. Volcanol. Geotherm. Res., 21,* 1–23. [5] Murphy B. (1992) Ph.D. thesis, University of London.

N93-14701

MIXED-VALENCE IRON MINERALS ON VENUS: Fe^{2+}-Fe^{3+} OXIDES AND OXY-SILICATES FORMED BY SURFACE-ATMOSPHERE INTERACTIONS. Roger G. Burns and D'Arcy W. Straub, Department of Earth, Atmospheric and Planetary Sciences, Massachusetts Institute of Technology, Cambridge MA 02139, USA.

Background: The oxidation state and mineralogy of iron on the hot surface of Venus are poorly understood [1–3], despite qualitative *in situ* measurements of oxygen fugacity during the Venera 13/14 missions [4], some reflectance spectral data derived from the

Venera 9/10 and Venera 13/14 missions [5], numerous equilibrium thermodynamic calculations [e.g., 3,6,7], and several experimental studies of rock and mineral assemblages heated in air [5,8–10,11] or CO_2-dominated atmospheres [2,12]. Inferences from these investigations are that Fe^{3+}-bearing minerals such as hematite (α-Fe_2O_3), magnesioferrite ($MgFe^{3+}_2O_4$), acmite ($NaFe^{3+}Si_2O_6$), and epidote ($Ca_2Fe^{3+}Al_2Si_3O_{12}(OH)$) are thermodynamically unstable [3], and that magnetite (Fe_3O_4 or $Fe^{2+}Fe^{3+}_2O_4$) is the predominant mixed-valence iron oxide mineral on Venus. Recently, the Fe^{2+}-Fe^{3+} silicate mineral laihunite (with ideal endmember composition $Fe^{2+}Fe^{3+}_2Si_2O_8$), earlier suggested to occur on oxidized surfaces of terrestrial planets [10], was proposed to be a reaction product of olivine with the venusian atmosphere [3]. This possibility is discussed further here. We suggest that other mixed-valence Fe^{2+}-Fe^{3+}-O_2-OH^- silicates could also result from surface-atmosphere interactions on Venus. Such minerals include oxy-amphiboles (e.g. $Ca_2(Mg,Fe^{2+},Fe^{3+})_5$ $Si_8O_{22}(OH,O)_2$)], ilvaite ($CaFe^{2+}_2Fe^{3+}$ Si_2 $O_8(OH)$], oxy-biotites [e.g. $K(Mg,Fe^{2+},Fe^{3+})_{2-3}(Si_3AlO_{10})(OH,O)_2$], and babingtonite ($Ca_2Fe^{2+}Fe^{3+}Si_5O_{14}(OH)$].

Conversion of Hematite to Magnetite: Spectroscopic observations, which correlated spectrophotometric data of the Venera 9/10 and 13/14 missions with laboratory reflectance spectra of hematite, suggested that this ferric oxide phase might exist metastably on the venusian surface [5]. However, a kinetic study of the conversion of hematite to magnetite [12] showed that, although coatings of magnetite on hematite crystallites may partially inhibit the decomposition of Fe_2O_3, complete conversion of hematite to magnetite is sufficiently rapid at venusian surface temperatures so as to dismiss the existence of metastable hematite on Venus. Thus, magnetite appears to be the dominant oxide mineral accommodating ferric iron on Venus. However, a number of other opaque mixed-valence silicate minerals also host Fe^{3+} ions and could exist on the surface of Venus.

Stability of Laihunite: The occurrence of ferrifayalite, consisting of intergrowths of fayalite (stoichiometric $Fe^{2+}_2SiO_4$) and laihunite (nonstoichiometric $Fe^{2+}_xFe^{3+}_ySiO_4$), in terrestrial metamorphic [13], plutonic, and extrusive igneous rocks [14–17] suggested that such Fe^{3+}-bearing olivines might also exist on other terrestrial planets [10], including Venus [3]. Ferrifayalites have also been produced experimentally by aereal oxidation in the temperature range 400°–800°C of Mg-Fe and Mn-Fe olivines [8–10, 16,18,19]. These natural and experimentally induced oxidation products of olivine, including the granulite-facies laihunite (intergrown with magnetite) from metamorphic rocks at the type-locality in China [13], consist of a variety of superstructure olivine polytypes [16,17,20,21]. Maghemite (γ-Fe_2O_3 or nonstoichiometric spinel) was also identified in oxidized fayalites [8–10]. However, at elevated temperatures, ferrifayalite-maghemite assemblages decompose to hematite, leading to the suggestion [9] that a laihunite-maghemite-quartz oxygen fugacity buffer more oxidizing than the (stoichiometric) fayalite-magnetite-quartz buffer could exist at temperatures below 600°C. Such a Fe^{3+}-bearing assemblage would be relevant, therefore, to the surface of Venus.

More recently, the stability of laihunite has been questioned, based on heating experiments above 300°C at various oxygen fugacities [18,19]. Laihunite synthesized from fayalite was transformed to hematite, magnetite, and amorphous silica under a CO_2 atmosphere. In a CO_2/H_2 (ratio 1000:1) atmosphere, laihunite decomposed to fayalite, magnetite, and amorphous SiO_2. Similar reaction products were obtained for laihunites synthesized from Mg-Fe and Mn-Fe olivine solid-solutions. It was concluded [19]

that at 1 bar atmospheric pressure and temperatures exceeding 300°C, laihuinite has no stability field under any oxygen fugacity. These findings conflict with the numerous terrestrial occurrences of laihunite [13–17] and earlier thermodynamic calculations for the system Fe_2O_3-FeO-SiO_2 at 15 kb [22] that showed laihunite to be stable at granulite-facies temperatures (600°–700°C). Therefore, if laihunite does occur on Venus [3], it may be metastable in the venusian atmosphere at $P \leq 95$ bar and $T < 475°C$.

The Possible Existence of Oxy-Amphiboles and Oxy-Micas on Venus: Early thermodynamic calculations of chemical interactions between basaltic rocks and the atmosphere of Venus indicated that amphiboles such as glaucophane ($Na_2Mg_3Al_2Si_8O_{22}(OH)_2$) and tremolite ($Ca_2Mg_5Si_8O_{22}(OH)_2$), together with epidote, magnetite, and phlogopite ($KMg_3Si_3AlO_{10}(OH)_2$), are stable assemblages [1,6,23]. However, the suggestion that these hydroxyl-bearing minerals, as well as other amphiboles, micas, and clay silicates, are stable on Venus has been hotly debated (see [3]). The problem centers on estimated water-dissociation pressures of common OH^--bearing minerals, which render them unstable in the venusian atmosphere. On the other hand, fluorine-bearing amphiboles and micas, in which F^- ions replace OH^- in the crystal structures, may be stable on Venus [3,7].

Dehydroxylated amphiboles and micas formed by intracrystalline redox reactions could also be stable phases on Venus. Such dehydroxylated minerals are well known as oxy-hornblendes and oxy-biotites in terrestrial volcanic rocks, where they occur as primary magmatic phases or were formed by oxidation of extrusive amphiboles and micas at the Earth's surface.

When Fe^{2+}-bearing amphiboles and micas are heated in a vacuum or inert gas, an internal oxidation-reduction reaction occurs in the mineral crystal structures, resulting in an oxy-amphibole or oxy-mica component [24,25]

$$Fe^{2+} + OH^- = Fe^{3+} + O^{2-} + \tfrac{1}{2}H_2$$
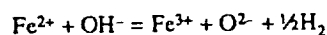
In an oxidizing atmosphere, the reaction becomes

$$Fe^{2+} + OH^- + \tfrac{1}{4}O_2 = Fe^{3+} + O^{2-} + \tfrac{1}{2}H_2O$$
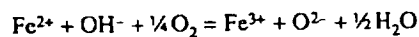
The overall result of both of these reactions is to convert the structural OH^- ions to O^{2-} anions, which are retained in the amphibole or mica crystal structure to charge-balance the Fe^{3+} ions produced by oxidation of Fe^{2+} cations [26,27]. Similar Fe^{2+}-Fe^{3+}-O^{2-}-(OH^-)-bearing amphiboles and micas would be thermally stable on the surface of Venus. Thus, oxy-hornblendes and oxy-biotites should be recognized as candidate mixed-valence iron minerals on Venus.

Other Mixed-Valence Fe^{2+}-Fe^{3+} Silicates Likely to Exist on Venus: Calcite and magnetite are predicted to be stable over almost the entire surface of Venus [3]. On Earth, these two minerals coexist with a variety of Ca-Fe silicates in skarn deposits that formed by contact metamorphism when magma intruded ferruginous limestones or siliceous dolomites [28,29]. Minerals present in progressive decarbonation sequences away from such plutons range from high-temperature pyroxene (e.g., hedenbergite, $CaFe^{2+}Si_2O_6$) and garnet (e.g., andradite, $Ca_3Fe^{3+}_2Si_3O_{12}$) assemblages to ilvaite ($CaFe^{2+}_2Fe^{3+}Si_2O_8(OH)$) and babingtonite ($Ca_2Fe^{2+}Fe^{3+}Si_5O_{14}(OH)$], which formed at lower temperatures. In the CO_2-saturated environment during skarn formation, ilvaite-bearing assemblages become stable when temperatures and oxygen fugacities fall below about 500°C and 10^{-25} bar respectively [30,31]. At compa-

rable temperatures, the crystallization of babingtonite requires more hydrous conditions, lower CO_2, and slightly higher O_2 fugacities in the fluid phase than ilvaite. Since similar temperatures, CO_2 pressures, and oxygen fugacities induced within skarn deposits exist on Venus, ilvaite and perhaps babingtonite could have also formed on the surface of this planet by the interaction of the venusian atmosphere with extruded basaltic rocks. One factor that might mitigate against the formation of these calcic Fe^{2+}-Fe^{3+} silicates on Venus, however, are the high abundances of Mg and Al measured during the Venera 13/14 [32] and Vega 2 [33] missions. The Mg^{2+} and Al^{3+} cations are not accepted into the crystal structures of ilvaite and babingtonite.

Discussion: Although magnetite is generally regarded to be the predominant ferric-bearing mineral on Venus, other mixed-valence Fe^{2+}-Fe^{3+} minerals known to exist on the surface of Earth could be stable in the venusian atmosphere. Thus, in addition to laihunite (which is probably metastable) and ilvaite and babingtonite (both of which may be found in rocks depleted of Mg and Al), oxy-amphiboles and oxy-micas may also be major constituents of the venusian surface. The opacities and high electrical conductivities of such mixed-valence Fe^{2+}-Fe^{3+} silicate minerals, the properties of which resemble magnetite [34], may also contribute to high radar-reflectivity regions in the highlands of Venus [35].

References: [1] Volkov V. P. et al. (1986) *Adv. Phys. Geochem.*, 6, 136–190. [2] Gooding J. L. (1986) in *The Solar System Observations and Interpretations* (M. G. Kivelson, ed.), 208–299, Prentice-Hall. [3] Fegley B. Jr. et al. (1992) *Proc. LPSC, Vol. 22*, 3–19. [4] Florensky C. P. et al. (1983) *LPSC XIV*, 203–204. [5] Pieters C. M. et al. (1986) *Science, 234*, 1379–1383. [6] Barsukov V. L. et al. (1982) *Proc. LPSC 13th*, in *JGR, 87*, A3–A9. [7] Nozette S. and Lewis J. S. (1982) *Science, 216*, 181–183. [8] Bartels K. S. and Burns R. G. (1986) *Eos, 44*, 1270. [9] Bartels K. S. and Burns R. G. (1989) *Intl. Geol. Congr., 28*, 9293. [10] Bartels K. S. and Burns R. G. (1989) *LPSC XX*, 44–45. [11] Straub D. W. et al. (1991) *JGR, 96*, 18819–18830. [12] Straub D. W. and Burns R. G. (1992) *LPSC XXIII*, 1375–1376. [13] Zhang R. et al. (1981) *Tscher. Mineral. Petrog. Mitt., 28*, 167–187. [14] Schaefer M. W. (1983) *Nature, 303*, 325–327. [15] Schaefer M. W. (1985) *Am. Mineral., 70*, 729–736. [16] Kondoh S. et al. (1985) *Am. Mineral., 70*, 737–746. [17] Banfield J. F. et al. (1990) *Contrib. Mineral. Petrol., 106*, 110–123. [18] Iishi K. et al. (1989) *Neues Jahrb. Mineral. Mh., H6*, 245–254. [19] Iishi K. et al. (1989) *Neues Jahrb. Mineral. Mh., H8*, 345–356. [20] Kitamura M. et al. (1984) *Am. Mineral., 69*, 154–160. [21] Shen B. et al. (1986) *Am. Mineral., 71*, 1455–1460. [22] Wang S.-Y. (1980) *Geochimica (Chinese), 3*, 31–42. [23] Khodakovsky I. L. et al. (1979) *Icarus, 39*, 352–363. [24] Barnes V. E. (1930) *Am. Mineral., 15*, 393–417. [25] Phillips M. W. et al. (1988) *Am. Mineral., 73*, 500–506. [26] Phillips M. W. et al. (1989) *Am. Mineral., 74*, 764–773. [27] Popp R. K. et al. (1990) *Am. Mineral., 75*, 163–169. [28] Burt D. M. (1971) *Annu. Rept. Geophys. Lab. Yearb., 70*, 189–197. [29] Burt D. M. (1971) *Soc. Mining Geol. Japan, Spec. Issue 3*, 375–380. [30] Gustafson H. J. (1967) *J. Petrol., 15*, 455–496. [31] Gole M. J. (1981) *Can. Mineral., 19*, 269–277. [32] Surkov Y. A. et al. (1984) *Proc. LPSC 14th*, in *JGR, 89*, B393–B402. [33] Surkov Y. A. et al. (1986) *Proc. LPSC 16th*, in *JGR, 91*, E215–E218. [34] Burns R. G. (1991) in *Mixed-Valence Systems: Applications in Chemistry, Physics and Biology* (K. Prassides, ed.), 175–200, NATO ASI-C Ser., Math. Phys. Sci., 343, Plenum. [35] Research supported by NASA grant number NAGW-2049.

THERMAL BUOYANCY ON VENUS: PRELIMINARY RESULTS OF FINITE ELEMENT MODELING.

J. D. Burt and J. W. Head, Department of Geological Sciences, Brown University, Providence RI 02912, USA.

Introduction: Enhanced surface temperatures and a thinner lithosphere on Venus relative to Earth have been cited as leading to increased lithospheric buoyancy. This would limit [1] or prevent [2] subduction on Venus and favor the construction of thickened crust through underthrusting. Underthrusting may contribute to the formation of a number of features on Venus. For example, Freyja Montes, a linear mountain belt in the northern hemisphere of Venus, has been interpreted to be an orogenic belt [3] and a zone of convergence and underthrusting of the north polar plains beneath Ishtar Terra, with consequent crustal thickening [4]. Such mountain belts lie adjacent to regions of tessera and contain evidence of volcanic activity. Tessera is also considered to consist of thickened crust [5] and crustal underthrusting is one possible mode for its formation [4]. Models for the formation of the mountain belts and associated features must then explain compressional deformation and crustal thickening, as well as melt production.

In order to evaluate the conditions distinguishing between underthrusting and subduction, we have modeled the thermal and buoyancy consequences of the subduction end member. This study considers the fate of a slab from the time it starts to subduct, but bypasses the question of subduction initiation. Thermal changes in slabs subducting into a mantle having a range of initial geotherms are used to predict density changes and thus their overall buoyancy. Finite element modeling is then applied in a first approximation of the assessment of the relative rates of subduction as compared to the buoyant rise of the slab through a viscous mantle.

Subduction Model: In the model, slabs, having a thickness set by 90% of the basalt solidus, subduct at a 45° angle into the mantle. The initial geotherms match surface thermal gradients of 10°C/km, 15°C/km, and 25°C/km [6]. Slabs heat via conduction, crustal radioactivity, phase changes, and adiabatic compression. Phase changes involving the conversion of basalt to eclogite at depths of 60 to 160 km and then enstatite to forsterite plus stishovite between 260 and 360 km generate 0.13×10^{-5} ergs/cm^3 s and 0.36×10^{-5} ergs/cm^3 s respectively [7]. The slab radiogenic heat production is 2.63×10^{-7} ergs/g s [8]. Adiabatic compression adds 0.5°C per kilometer of depth. Convergence rates ranged from 5 mm/yr to 100 mm/yr.

The thermal evolution of the slab is followed using a finite difference technique [7,9]. The model region measures 800 km horizontally by 400 km deep. Processing ends when the slab tips reach a 300-km depth, implying time intervals of 10 m.y. to 100 m.y. Slab density changes derive from the thermal results through calculation of the thermal expansion ($a_v = 3 \times 10^{-5}$/°K [8]) and the effects of pressure ($b = 1 \times 10^{-3}$/kbar [8]) on initial densities set for zero pressure and temperature. The assumed initial density structure includes a 10-km or 25-km basaltic crust (density = 3.0 g/cm^3), a corresponding 25-km or 65-km-thick depleted mantle zone (density = 3.295 g/cm^3), and an underlying undepleted mantle (density = 3.36 g/cm^3). Density changes due to the phase transitions are also included. Results take the form of density distributions within the model region.

Finite element modeling is then employed to gauge the rate at which a slab having the density structure derived above will move through a viscous mantle. Buoyancy body forces are applied to a slab having a viscosity of 10^{21} Pa s surrounded by a mantle with a

viscosity of 10^{19} Pa s. Zero stress boundary conditions are applied to all sides of the model region, while no motion perpendicular to region boundaries are allowed except at the top.

Results: Figure 1 shows a typical result of the computations modeling the density changes. Density contours (0.1 g/cm^3 spacing) clearly delineate the slab and its crustal layer. In this case (10°C/km geotherm, 25 km crust, subduction rate of 5 km/m.y.) the net slab densities in the region above the basalt-eclogite phase transition are lower than their mantle surroundings (the phase change is set for the density analysis at 110 km depth). Above the 110-km depth densities in the crustal portion of the slab are lower than in the mantle outside the slab. This causes the net slab density to be less than that in the surrounding mantle. Below the basalt-eclogite phase change, net slab densities exceed those in the neighboring mantle. Net slab buoyancy remains positive until the slab has lengthened to about 275 km. Thereafter, slabs become negatively buoyant.

Initial finite element results indicate that the positively buoyant slabs will rise through the mantle at a rate of 5 to 10 km/m.y. This analysis considers only the instantaneous velocity of the slab and does not incorporate the full results of the density modeling or the dynamics of slab subductive descent.

Discussion: Qualitatively, subduction is likely to be enhanced by negatively buoyant slabs or hindered by slabs that are positively buoyant. Positive net buoyancy is found above the basalt-eclogite phase change, tending to oppose subduction. Negative net slab buoyancy for the full-length slab was found for all conditions, while neutral buoyancy was achieved for slabs at a length of about 275 km. Thus, the slab must penetrate deeply into the mantle before negative buoyancy can help drive subduction. The rate of the slab's buoyant rise through the mantle is then important in determining whether the slab may descend deeply enough to become negatively buoyant.

Preliminary results of finite element modeling indicate the slab may rise at rates between 5 and 10 km/m.y. Thus, subducting slabs will tend to rise into an underthrusting position if their subduction rate is slow. However, it may be that moderate to high rates of subduction will overwhelm the buoyant rise of a slab. This could lead to slabs being forced through the basalt-eclogite phase transition and to great enough depths to become negatively buoyant, thus possibly producing a self-sustaining subduction system.

These initial results must be considered in light of the presumption of subduction made in undertaking the analysis. Some process still must be found that would carry the slab downward despite its initial positive buoyancy. Further work will model more closely the dynamics of the subductive motion of the slab and the effects of the slab density evolution on slab buoyancy, its rate of rise through the mantle, and the continuance of subduction.

These results indicate that for all cases of assumed Venus geotherm a lithospheric slab whose subduction has been initiated will instead be forced to underthrust the overriding lithosphere if the

Fig. 1.   Final density distribution for 10°C/km geotherm, 25 km crust, and 5 km/m.y. subduction rate. Contours have a 0.1 g/cm^3 spacing.

subduction rate is slow. This could then lead to crustal thickening, melting, and volcanism, and possibly provide one model to explain the association of compressional mountain belts and blocks of high-standing tessera, with apparent flexural rises and foredeeps, and with large volumes of volcanic deposits.

References: [1] Phillips R. J. and Malin M. C. (1982) in *Venus* (D. M. Hunten et al., eds.), 159–214, Univ. of Arizona, Tucson. [2] Anderson D. L. (1981) *GRL, 8*, 309–311. [3] Crumpler L. S. et al. (1986) *Geology, 14*, 1031–1034. [4] Head J. W. (1990) *Geology, 18*, 99–102. [5] Vorder Bruegge R. W. and Head J. W. (1989) *GRL, 16*, 699–702. [6] Hess P. C. and Head J. W. (1989) *Abstracts of the 28th International Geological Congress*, 2–55. [7] Minear J. W. and Toksoz M. N. (1970) *JGR, 75*, 1397–1419. [8] Turcotte D. L. and Schubert G. (1982) *Geodynamics: Applications of Continuum Physics to Geological Problems*, Wiley, New York, 450 pp. [9] Gerald C. F. (1978) *Applied Numerical Analysis, 2nd edition*, Addison-Wesley, Reading, Massachusetts.

N92-10703

EROSION VS. CONSTRUCTION: THE ORIGIN OF VENUSIAN CHANNELS.   D. B. J. Bussey and J. E. Guest, University of London Observatory, University College London, London NW7 2QS, UK.

Lava channels are a common feature in the volcanic regions of the Moon, and have now been observed on Venus [1]. There has been much debate about the origin of lunar channels: Are they the result of erosional (either thermal or mechanical) or constructional processes? It is necessary to determine the criteria to distinguish between the different types of channels. The clearest evidence is that the presence of levees indicates that the channel experienced a constructional phase for a period.

Greeley [2] has proposed that Hadley Rille, on the Moon, was formed as a leveed channel and lava tube system. Evidence for this is its location along the crest of a ridge. In addition, Hadley Rille and other lunar mare sinuous rilles are discontinuous, suggesting that their origin was, in part, a lava tube that has subsequently undergone partial roof collapse. Carr [3] and Head and Wilson [4] have argued that these rilles were produced by lava erosion. For lunar highland channels, which tend to be larger than their mare counterparts, mechanical erosion of the megaregolith is a possible process.

Channels of several different types have been observed on the surface of Venus [1]. They are probably formed by more than one process. They range in size from a few kilometers to over 6800 km [1]. The relatively short ("tadpolelike") channels [5] (e.g., 24 S 347) appear similar to lunar mare sinuous rilles in morphology. They are so like certain constructional terrestrial channels (e.g., Kalaupapa, Hawaii [6]) that it appears reasonable to say that they too are constructional channels or collapsed lava tube systems.

However, the long sinuous channels referred to by Baker et al. [1] as "canali" pose a different problem in the understanding of their formation. One example of a channel of this type in the southeast region of Aphrodite Terra appears to show both erosional and constructional characteristics. This channel is represented in Fig. 1. It is approximately 700 km long with an average width of about 1 km. It drops a distance of 700 m from beginning to end, which means that the average slope is 0.06°. Its source may have been a graben situated at the northwest end of the channel. It appears to have different origins along its length.

The lack of levees near the source suggests that the channel is erosional in this region. An inferred profile is shown as AA' in Fig. 1.
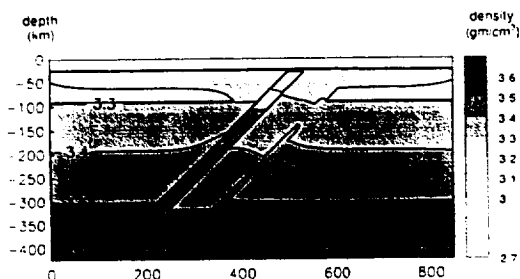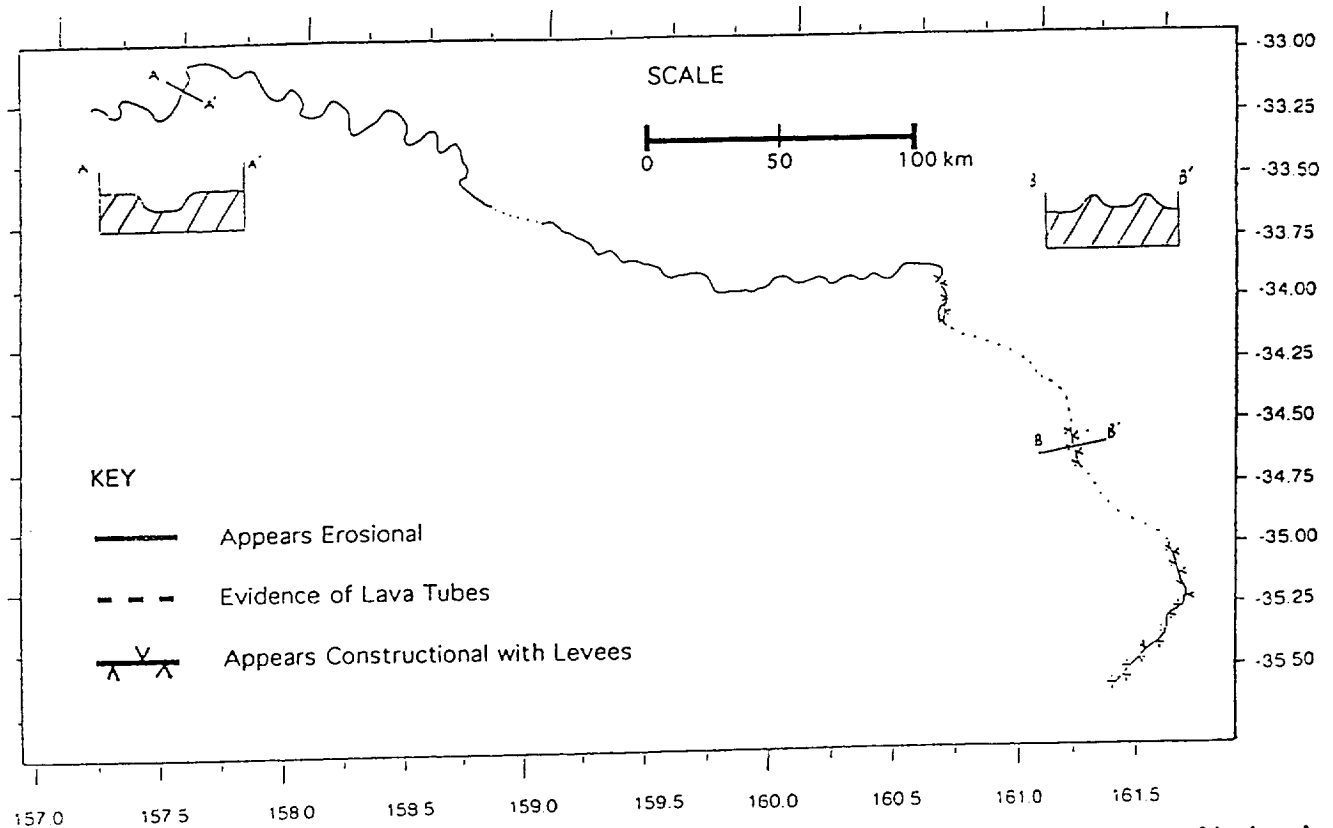
Fig. 1. A channel in southeast Aphrodite Terra. Evidence for erosion or construction obtained by analysis of north-south sections of the channel.

The presence of levees indicates that a constructional phase has occurred. These are formed by lava repeatedly splashing over the channel sides and solidifying. Evidence of levees is seen further away from the source. A possible profile is shown in BB' in Fig. 1. However, the presence of levees does not mean that the lava was not also eroding and deepening the channel. BB' could just as credibly be redrawn with the level of the channel floor below the level of the surrounding terrain.

Thus, in conclusion, our example channel is very sinuous and there is evidence of erosion. There may also have been overflow here. In its middle reaches it roofs over and has the characteristics of a lava tube. In the lower reaches there is strong evidence for the presence of levees indicating construction.

On Earth, limited amounts of erosion may occur in basaltic lava channels [7], although not nearly on the same scale as on the planets just mentioned. For lava erosion on Earth to occur to a comparable extent, excessive eruption times are required. However, low-viscosity komatiite lava may erode to a larger extent and there is direct evidence that carbonatite lava erodes when the underlying strata is also carbonatite [8].

Previously it has always been assumed that for thermal erosion to occur the flow must be turbulent [9]. Recent findings [8] indicate that this may be a false assumption and that laminar flow may be effective in eroding the substrate.

References: [1] Baker V. R. et al. (1992) *JGR*, in press. [2] Greeley R. (1971) *Science, 172*, 722–725. [3] Carr M. H. (1974) *Icarus, 22*, 1–23. [4] Head J. W. and Wilson L. (1981) *LPSC XII*, 427–429. [5] Head J. W. et al. (1991) *Science, 252*, 276–288. [6] Wood C. A. and Kienle J. (1990) *Volcanoes of North America*, 330–331, Cambridge. [7] Peterson D. W. and Swanson D. A. (1974)

In *Studies in Speleology, Vol. 2*, 209–222. [8] Pinkerton H. et al. (1990) *LPSC XXI*, 964–965. [9] Hulme G. (1973) *Mod. Geol., 4*, 107–117.

N92-11304

POLARIZATION PROPERTIES AND EARTH-BASED RADAR MEASUREMENTS OF VENUS IN THE POST-MAGELLAN ERA. D. B. Campbell, Department of Astronomy, Cornell University, Ithaca NY 14853, USA.

Studies of the polarization properties of reflected radar signals provide information about wavelength-scale surface and subsurface irregularities and can place constraints on the scattering models used to explain anomalously high backscatter cross sections, such as those measured for the surfaces of the icy Galilean satellites. The JPL aircraft-mounted synthetic aperture radars (SAR) provide cross-section and polarization information for terrestrial terrain types. Comparison of these measurements with results from the Magellan mission is helping to relate volcanic flow types on Venus to terrestrial equivalents [1]. Unfortunately, the Magellan SAR transmits and receives a single linear polarization so that information concerning the polarization properties is dependent on past and future observations from the Earth, primarily with the 12.6-cm wavelength (the same as Magellan) radar system on the Arecibo telescope.

Early radar observations of Venus discovered several areas on the planet that had both high backscatter cross sections and high circular polarization ratios (i.e., the ratio of the received power in the same sense as that transmitted to that in the opposite sense). Most prominent among these were Alpha and Beta Regiones and

Maxwell Montes. At the then achievable spatial resolutions of about 100 km, the measured ratios for Alpha and Beta were approximately 0.5 while that for Maxwell Montes was closer to unity. More recent measurements with the Arecibo system in 1983 and 1988 indicate that the ratios for parts of Maxwell Montes are very close to unity and may exceed unity in some areas. Very high cross sections and inverted polarization ratios have been observed for the icy Galilean satellites and the south polar region on Mars. All models attempting to explain the phenomenon invoke internal scattering in a very low-loss ice medium.

Results from the Pioneer-Venus [2] and Magellan missions [3] showed that Theia and Rhea Montes in Beta Regio and Maxwell Montes are areas with low thermal emissivities and high Fresnel reflectivities. Pettengill et al. [3] invoked the presence of very high dielectric constant material and Muhleman [4] has pointed out that volume scattering could play an important role. However, if further analysis of the current data and future measurements confirm that the polarization ratio exceeds unity, then the current models to explain the low emissivities and high reflectivities will need to be revised.

With no new missions currently planned, the only method to obtain additional data for the surface of Venus in the post-Magellan era will be with groundbased telescopes. Improvements to the Arecibo radar system currently underway will increase its sensitivity for radar mapping of Venus by about a factor of 7, allowing high-quality imaging at 1- to 2-km resolution over approximately 40% of the surface. This resolution and sensitivity are more than adequate for mapping of the polarization properties of selected areas aimed at studies such as the wavelength-scale roughness properties of volcanic flows for comparison with terrestrial data and the understanding of the high-emissivity/low-reflectivity areas.

References: [1] Campbell B. A. (1992) *JGR*, in press. [2] Pettengill G. H. et al. (1988) *JGR, 93*, 14881–14892. [3] Tyler G. L. et al. (1991) *Science, 252*, 265–270. [4] Muhleman D. O., personal communication.

N93-10305

BRIGHT CRATER OUTFLOWS: POSSIBLE EMPLACEMENT MECHANISMS.

D. John Chadwick[1], Gerald G. Schaber[1], Robert G. Strom[2], and Darla M. Duval[3], [1]U.S. Geological Survey, Flagstaff AZ 86001, USA, [2]Department of Planetary Sciences, University of Arizona, Tucson AZ 85721, USA, [3]University of North Dakota, Grand Forks ND 58202, USA.

Lobate features with a strong backscatter are associated with 43% of the impact craters cataloged in Magellan's cycle 1 (Fig. 1). Their apparent thinness and great lengths are consistent with a low-viscosity material. The longest outflow yet identified is about 600 km in length and flows from the 90-km-diameter crater Addams. There is strong evidence that the outflows are largely composed of impact melt, although the mechanisms of their emplacement are not clearly understood. High temperatures and pressures of target rocks on Venus allow for more melt to be produced than on other terrestrial planets because lower shock pressures are required for melting [1].

The percentage of impact craters with outflows increases with increasing crater diameter. The mean diameter of craters without outflows is 14.4 km, compared with 27.8 km for craters with outflows. No craters smaller than 3 km, 43% of craters in the 10- to 30-km-diameter range, and 90% in the 80- to 100-km-diameter range have associated bright outflows. More melt is produced in the
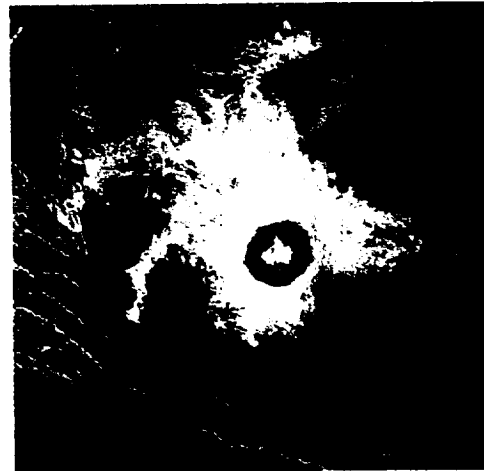
Fig. 1. Hellman, 35 km in diameter. Note position of outflows downrange of missing segment of ejecta.

more energetic impact events that produce larger craters [2]. However, three of the four largest craters have no outflows.

Outflow occurrence is also correlative with impact incidence angle. Fifty-nine percent of Venus' craters have bilaterally symmetric ejecta: a large concentration on one side and little or none on the other. Such craters were probably formed by oblique impacts; more pronounced asymmetry in the ejecta reflecting a lowering impact angle [3]. Of craters with asymmetric ejecta, those with outflows are more numerous than those without above about 15 km in diameter. This transition occurs in craters with symmetric ejecta patterns above about 35 km, which suggests that oblique impacts are much more efficient at producing outflows than those with higher-angle trajectories. Forty-eight percent of asymmetric-ejecta craters have outflows, compared with only 34% of those with symmetric ejecta. Schultz [3] observed a relation between decreasing impact angle and increasing length and areal coverage of outflows. More impact melt is not expected to be generated in oblique impacts relative to high-angle impacts due to lower energy deposition in the target [4]. Rather, oblique impacts may be more efficient at removing the outflow materials from the crater and may also incorporate a higher percentage of the projectile in the outflows.

Of the 227 venusian craters with outflows and asymmetric ejecta, about 26% have outflow sources centered on the downrange axis, and 87% have outflows originating from within 90° in azimuth of this axis (Fig. 1). These relations suggest that the outflows are transported downrange during the impact. Popigai, a 100-km-diameter Asian impact crater, has an asymmetric distribution of melt glass attributed to oblique impact [5]. This downrange distribution is evident in flows from fresh lunar craters as well [6].

In the following paragraphs we present four possible mechanisms for the emplacement of bright outflows. We believe this "shotgun" approach is justified because all four mechanisms may indeed have operated to some degree.

Model 1: Emplacement by Jetting: There are apparently two types of bright outflows: those deposited after emplacement of the crater rim materials and a rarer form that appears to have been deposited before. Jetting is a very early process that occurs before ejecta emplacement, and jets have velocity usually higher than that of the projectile [4]. Therefore, any jetted materials that remain in the vicinity of the crater would lie stratigraphically below the rest

of the ejecta. Impact velocities as low as 1–2 km per second may be sufficient to produce jetting [7].

As impact angle decreases, the speed of the jet increases and the amount of jetted material decreases to conserve momentum [4]. It is unclear whether atmospheric drag could slow the jet enough for local deposition.

Model 2: Emplacement as Lavalike Flows: In this model, impact melt and solid fragments are transported out of the transient crater within a turbulent, radially expanding gas cloud and deposited in a discrete layer atop the crater rim deposits. This same mechanism was proposed to explain the aerodynamic sculpturing and lack of sorting of melt bombs in suevite deposits at Ries Crater [8]. At Ries, glass constitutes about 15% of the suevite volume. Calculations by Basilevsky and Ivanov [9] and Ivanov et al. [10] suggest that a 26-km-diameter crater such as Ries would produce 20% to 50% more melt on Venus; thus a venusian suevite layer may be composed of over 20% melt.

With high melt volumes and inefficient cooling of the melt by hot incorporated clasts, venusian suevites may remobilize after emplacement to form laminar, lavalike outflows. Many outflows are observed to contain sinuous, leveed channels that commonly have complex tributary and distributary systems. Channels in outflows are usually best developed close to the crater, giving way to broad, unchannelized distal lobes. Similar transitions occur in Hawaiian lava flows, apparently due to increasing viscosity of the flows with distance from the source.

Additional evidence for a slow, lavalike emplacement of the outflows is their common inability to surmount topographic obstacles (exceptions are described below). Small volcanic cones surrounded by flows have commonly retained their circular shape; flows of higher velocity would be expected to submerge part of one side of these cones. Alternatively, it is not yet clear whether the melt could remain molten long enough to produce the more lengthy flows.

Model 3: Emplacement by Turbulent Flow: This model requires a low-viscosity fluid similar to that of model 1, but emplacement is at a much higher velocity in a turbulent gas/solid/melt mixture, similar to terrestrial pyroclastic surges. This model would best explain the outflows if the channels observed within many of them are erosional, although it is not clear whether a surgelike mechanism would produce the intricate networks of leveed tributaries and distributaries that are observed.

Some outflows show a marked ability to climb slopes. At Cochran, flow directions follow topographic contours except on the northwestern side of the crater. Here the flow appears to climb as much as 300 m into an elevated tessera region [11]. The northwestern side of the crater is interpreted to be in the downrange direction, so this observation is consistent with a turbulent flow being driven forward along the impactor trajectory. The driving force may be the momentum of the impact itself or a strong drafting created by the impactor wake as suggested by Schultz [3].

Terrestrial pyroclastic flows have been analyzed by using the energy-line model that gives the potential head of a flow along its runout distance [12,13]. For the gravitational collapse of a debris column, H/L is the ratio of column height to runout distance and determines the slope of the energy line. H represents the initial potential energy of the material converted to kinetic energy, which is dissipated as the flow moves along the surface. The vertical distance between the energy line and the subjacent topography is used to calculate the velocity at a given distance from the crater. It

is possible for the flows to travel up slopes if they lie below the energy line [12].

Values of H/L for large terrestrial pyroclastic deposits fall in the range of 0.1 to 0.2. These values, coupled with the longest L value (measured at Addams), result in column heights of 60 to 120 km. Using the height of origin for Addams and neglecting the subjacent topography, we derive an initial velocity of the 600-km-long outflow at the crater edge of about 1 to 1.5 km/s. This value exceeds the sonic velocity of the venusian atmosphere. However, the values of H/L in Venus' dense atmosphere are probably quite different from those on Earth. Values of H/L of less than 0.02 are required if the initial velocity of the outflow at Addams were to be below the sonic velocity of Venus' atmosphere.

Kinetic energy may be imparted to the flow by the energy of the impact in lieu of a collapsing column. This is possibly a more likely scenario because of the tendency of the flows to be directed downrange.

Model 4: Slow Ejection of Molten Transient-Crater Lining: Features similar to the venusian outflows, albeit much smaller, are the small flows and ponds on ejecta near the rims of relatively fresh lunar craters. Hawke and Head [6] interpreted these materials to be impact melt that originally lined the transient crater and was ejected at low velocities from the crater interior by rebound and wall slumping during the modification stage of crater formation. This model is supported by the great number of outflows that appear to originate very high on the ejecta blankets of Venus' craters, commonly at the rims. This relation was also noted by Edmunds and Sharpton [14]. The backscatter tone of the floors of many outflow craters indicates that the floors are much smoother than the flows themselves, however, possibly indicating that they are not the same material.

It is possible that a combination of models 2 and 3 may best explain the longer outflows. Schultz [3] observed a significant population of outflows (38% of 253 craters) in which a combination of laminar and turbulent emplacement styles was evident. Thus these flows may have been given initially high velocities by the impact and may have behaved as turbulent, ground-hugging surges. Upon degassing, the solid-melt fraction of the flow would have settled to the surface and continued to flow in a slow, laminar fashion. Secondary flowage of this type has been observed in terrestrial rheomorphic tuffs [15], which probably have a much lower melt fraction than the outflows.

References: [1] Vickery A. M. and Melosh H. J. (1991) *LPSC XXII*, 1443–1444. [2] Grieve R. A. F. et al. (1977) In *Impact and Explosion Cratering* (D. J. Roddy et al., eds.), 791–814, Pergamon, New York. [3] Schultz P. H. (1992) *JGR*, submitted. [4] Melosh H. J. (1989) *Impact Cratering: A Geologic Process*, Oxford, New York. [5] Masaitis V. L. and Mashchak M. S. (1980) *LPSC XI*, 674–675. [6] Hawke B. R. and Head J. W. (1977) In *Impact and Explosion Cratering* (D. J. Roddy et al., eds.), 815–841, Pergamon, New York. [7] Kieffer S. W. (1977) In *Impact and Explosion Cratering* (D. J. Roddy et al., eds.), 751–769, Pergamon, New York. [8] Hörz F. (1982) *GSA Spec. Pap. 190*, 39–54. [9] Basilevsky A. T. and Ivanov B. A. (1990) *GRL*, *17*, 175–178. [10] Ivanov B. A. et al. (1992) *JGR*, submitted. [11] Moore H. J. (1992) *LPSC XXIII*, 929–930. [12] Sheridan M. F. (1979) *GSA Spec. Pap. 180*, 125–136. [13] Malin M. C. and Sheridan M. F. (1982) *Science, 217*, 637–640. [14] Edmunds M. S. and Sharpton V. L. (1992) *LPSC XXIII*, 329–330. [15] Wolff J. A. and Wright J. V. (1981) *J. Volc. Geotherm. Res., 10*, 13–34.

N93-14308

IMAGE PROCESSING AND PRODUCTS FOR THE MAGELLAN MISSION TO VENUS. Jerry Clark, Doug Alexander, Paul Andres, Scott Lewicki, and Myche McAuley, Magellan Image Data Processing Team, Jet Propulsion Laboratory, Mail Stop 168-514, 4800 Oak Grove Drive, Pasadena CA 91109, USA.

The Magellan mission to Venus is providing planetary scientists with massive amounts of new data about the surface geology of Venus. Digital image processing is an integral part of the ground data system that provides data products to the investigators. The mosaicking of synthetic aperture radar (SAR) image data from the spacecraft is being performed at JPL's Multimission Image Processing Laboratory (MIPL). MIPL hosts and supports the Image Data Processing Subsystem (IDPS), which was developed in a VAXcluster environment of hardware and software that includes optical disk jukeboxes and the TAE-VICAR (Transportable Applications Executive-Video Image Communiation and Retrieval) system. The IDPS is being used by processing analysts of the Image Data Processing Team to produce Magellan image data products. Data arrive at the IDPS via the fiber optic Imaging Local Area Network from the SAR Data Processing Subsystem that correlates raw SAR data into image data. The input SAR image swaths, called F-BIDRs (Full-resolution Basic Image Data Record), are long, thin swaths of imagery covering an area on the surface about 20 km in width by about 17,000 km in length, extending from the north pole to near the south pole of Venus. Systematic procedures were written for the automatic mosaicking of multiple orbits of data into image frames covering predetermined regions of the planet. Algorithms were developed to perform such functions as the correction of radiometric differences at the edges of adjacent orbits and the automatic tiepointing of overlapping data to correct for navigational errors between orbits. After mosaicking, the images are contrast enhanced, annotated, and masked to create photo products for scientific analysis. Other versions of mosaics are created from reduced resolution image swaths. Depending on the product, the data are output from the MIPL as archive tapes; working WORM (Write-Once-Read-Many) optical disks; premastered tapes for stamping, by a vendor, of CD-ROMs (Compact-Disc-Read-Only-Memory) that are used to distribute mosaics and ancillary data to the scientific community; and exposed film that is used for the production of prints and copy negatives. Numerous special products have been made at the request of the investigators, including SAR mosaics merged with non-SAR data (such as altimetry and radiometric emissivity data) that are displayed as color composites and stereo anaglyphs that use SAR data collected at different look-angles to view surface topography through stereo parallax. In addition, mosaicked data are used to make other products, including terrain rendering that shows SAR mosaics combined with digital elevation data in perspective views and videos that use thousands of incremented rendered scenes to create simulated flights over the surface of Venus.

(This work is being performed at JPL, California Institute of Technology, under contract with NASA.)

N93-14307

THE THERMOSPHERE AND IONOSPHERE OF VENUS. T. E. Cravens, Department of Physics and Astronomy, University of Kansas, Lawrence KS 66045, USA.

Our knowledge of the upper atmosphere and ionosphere of Venus and its interaction with the solar wind has advanced dramatically over the last decade, largely due to the data obtained during the Pioneer Venus mission and to the theoretical work that was motivated by this data. Most of this information was obtained during the period 1978 through 1981, when the periapsis of the Pioneer Venus Orbiter (PVO) was still in the measurable atmosphere. However, solar gravitational perturbations will again lower the PVO periapsis into the upper atmosphere in September 1992, prior to the destruction of the spacecraft toward the end of this year. The physics and chemistry of the thermosphere and ionosphere of Venus will be reviewed in this paper. The book entitled *Venus Aeronomy* [1] contains several chapters that together provide a good overview of this subject.

The neutral atmosphere is primarily composed of carbon dioxide, but for altitudes above about 160 km atomic oxygen, which is produced via photodissociation of CO_2 by solar photons, becomes the dominant neutral species. The PVO neutral mass spectrometer has provided most of our information on the composition of the Venus thermosphere. The thermosphere of Venus is quite cold in comparison with Earth's thermosphere with an exospheric temperature on the dayside of $T_{ex} \approx 300$ K, whereas at Earth $T_{ex} \approx 1500$ K. The nightside thermosphere of Venus is extremely cold with $T_{ex} \approx 100$ K; it has been suggested, in fact, that this region of the atmosphere be called the "cryosphere" rather than the thermosphere. It is not fully understood why the upper atmosphere of Venus is so cold, although part of the answer is contained in the CO_2 15-μm cooling mechanism and also in the nature of the thermosphere dynamics. Thermospheric wind speeds of several hundred meters per second have been theoretically calculated for altitudes above about 150 km, and indirect observational evidence, such as compositional gradients, supports the validity of these calculations.

The exobase of Venus is located at about 180 km; above this altitude, in the exosphere, neutral atoms and molecules largely follow ballistic trajectories. Both atomic oxygen and atomic hydrogen are abundant in the Venus exosphere. The H density is about 10^5 cm^{-3} on the dayside and about 10^7 cm^{-3} on the nightside. Two populations of exospheric H exist at Venus: (1) a cold thermal component and (2) a hot (i.e., an effective temperature of ≈ 1200 K) nonthermal component. The hot hydrogen is thought to be mainly produced by the charge exchange of hot H^+ ions with neutral H and O atoms. Both cold and hot populations of atomic oxygen also exist in the Venus exosphere, and the nonthermal hot population has a larger density than the cold population for altitudes above about 300 km. The hot oxygen corona, as it is called, was observed by the ultraviolet spectrometer onboard PVO via resonantly scattered solar 130.4-nm photons. The major source of hot oxygen is the dissociative recombination of ionospheric O_2^+ ions. Hot oxygen plays an important role in the solar wind interaction with Venus, because photoionization of oxygen atoms that are present out in the Venus magnetosheath creates heavy ions that "mass load," and thus slow down, the solar wind flow.

The ionosphere of Venus forms due to the ionization of neutrals. Photoionization by solar extreme ultraviolet (EUV) photons is the main ionization process, although some contribution is also made by electron impact ionization by photoelectrons on the dayside and by "auroral" electrons on the nightside. It should be noted that superthermal electrons appear to be precipitating into the nightside atmosphere of Venus, generating emissions observed by the PVO ultraviolet spectrometer and also creating ionization. However, the Venus aurora is very weak in comparison with the terrestrial aurora, and is thought to be caused by relatively low energy electrons (i.e., energies of ≈ 100 eV or less, whereas auroral electrons at Earth have energies of thousands of eV).

The ionization process for the major neutral species, CO_2 and O, in the ionosphere of Venus can be represented by the reactions

$$hv + CO_2 \rightarrow CO_2^+ + e$$
$$\rightarrow CO + O^+ + e$$
$$hv + O \rightarrow O^+ + e$$
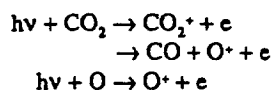
where hv represents an ultraviolet photon. h is Planck's constant and v is the photon frequency. hv must exceed the ionization potential of the molecule for these photochemical reactions to proceed.

A peak electron density in the Venus ionosphere of $\approx 6 \times 10^5$ cm^{-3} was observed on the dayside by the Pioneer Venus radio occultation experiment, as well as by the radio occultation experiments on other missions. The altitude of the peak is located at $z \approx 140$ km. The major ion species in the lower ionosphere of Venus was observed by the PVO ion mass spectrometer and by the retarding potential analyzer experiments to be O_2^+ and not CO_2^+, even though the abundance of neutral O_2 in the atmosphere of Venus is negligible, because of the following rapid ion-neutral reaction

$$CO_2^+ + O \rightarrow O_2^+ + CO$$
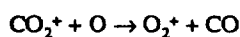
The O_2^+ ions are removed from the ionosphere by means of the following dissociative recombination reaction with ionospheric electrons

$$O_2^+ + e \rightarrow O + O$$
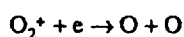
The neutral oxygen atoms produced by this reaction have energies of a few eV and are the source of the hot oxygen corona. The major ion species observed by instruments on PVO for altitudes above ≈ 160 km is O^+. Many minor ion species, including H^+, CO^+, N_2^+, CO_2^+, NO^+, He^+, C^+, and N^+, were observed by the PVO ion mass spectrometer.

Electron and ion temperatures of several thousand degrees were observed in the ionosphere of Venus by the PVO electron temperature probe and by the retarding potential analyzer. Theoretical models indicate that most of the energy required to heat the ionospheric plasma to these temperatures, which greatly exceed the neutral temperature, is derived from the solar wind interaction with the ionosphere.

The nightside ionosphere of Venus is quite variable, both spatially and temporally, with peak densities typically observed to be about 10^4 cm^{-3}. The main source of nightside ionization is thought to be transport of ions from the dayside to the nightside. O^+ ions drift upward on the dayside, then flow horizontally with speeds of several kilometers per second above 200 km, and then subside to lower altitudes on the nightside. Large ion drift speeds near the terminator of Venus were measured by the PVO retarding potential analyzer. Auroral ionization also contributes to the nightside ionosphere, especially during time periods of large solar wind dynamic pressure, when it is known that the nightside ionosphere at higher altitudes virtually disappears. A variety of other nightside ionospheric phenomena have also been observed, such as tall rays, ionospheric clouds, and ionospheric holes.

The solar wind interacts very strongly with the ionosphere of Venus. In fact, two types of ionosphere exist: (1) unmagnetized and (2) magnetized. The former ionospheric state is observed to be present whenever the solar wind dynamic pressure is low, and in this case large-scale magnetic fields are excluded from the ionosphere, although small-scale magnetic structures called flux ropes were observed to be present in the ionosphere by the PVO magnetometer.

The boundary between the solar wind and ionosphere, called the ionopause, is rather narrow and is located at higher altitudes for unmagnetized ionosphere cases. However, the dayside ionosphere is observed to be permeated by large-scale magnetic fields during conditions of high solar wind dynamic pressure. In this case, electrical currents flow throughout the ionosphere and both the density structure and the dynamics of the ionosphere are strongly affected by the solar wind interaction. The ionopause in this case is located below about 300 km and is rather broad.

References: [1] Russell C. T., ed. (1991) *Venus Aeronomy,* Kluwer, Dordrecht.

N93-14308

NEAR-INFRARED OXYGEN AIRGLOW FROM THE VENUS NIGHTSIDE. D. Crisp[1], V. S. Meadows[2], D. A. Allen[3], B. Bezard[4], C. DeBergh[4], and J.-P. Maillard[5], [1]Jet Propulsion Laboratory, USA, [2]University of Sydney, Australia, [3]Anglo-Australian Observatory, [4]Observ. Paris-Meudon, France, [5]IAP Paris, France.

Groundbased imaging and spectroscopic observations of Venus reveal intense near-infrared oxygen airglow emission from the upper atmosphere [1,2] and provide new constraints on the oxygen photochemistry and dynamics near the mesopause (~100 km). Atomic oxygen is produced by the photolysis of CO_2 on the dayside of Venus. These atoms are transported by the general circulation, and eventually recombine to form molecular oxygen. Because this recombination reaction is exothermic, many of these molecules are created in an excited state known as $O_2(^1\Delta)$. The airglow is produced as these molecules emit a photon and return to their ground state. Connes et al. [1] found that the airglow intensity is comparable on the dayside (1.5×10^{12} photons/cm^2/s) and nightside (1.2×10^{12} photons/cm^2/s) of the planet. They concluded that the $O_2(^1\Delta)$ emission is spatially uniform, and that chemical reactions involving $O_2(^1\Delta)$ provide a major pathway for the recombination of oxygen atoms in the venusian atmosphere. The intensity and apparent uniformity of this emission has puzzled atmospheric chemists for more than a decade because these properties cannot be explained by existing models [3].

New imaging and spectroscopic observations acquired during the summer and fall of 1991 show unexpected spatial and temporal variations in the $O_2(^1\Delta)$ airglow [4,5]. High-resolution (0.4 cm^{-1}) spectra of selected regions of the dayside and nightside of Venus were obtained with the Fourier Transform Spectrometer on the Canada-France-Hawaii Telescope (Mauna Kea Hawaii) on 27 June and 1 July 1991 (Fig. 1). Individual oxygen emission lines of the $O_2(^1\Delta)$ band near 7880 cm^{-1} (1.269 μm) were resolved, allowing us to distinguish the airglow emission from the deep-atmosphere thermal emission peak near 7830 cm^{-1} (1.277 μm). The intensity of the nightside $O_2(^1\Delta)$ emission increased by a factor of 4 between 10N to 5S latitude on 27 June. The emission measured near 15S latitude on 1 July was almost six times brighter than that seen four days earlier, and about three times brighter than that reported by Connes et al. [1]. Comparisons of intensities of individual rotational transitions in the P and R branches of the emission spectrum indicate a rotational temperature of 186 ± 6 K (Fig. 2).

This temperature is comparable to that derived from the $O_2(^1\Delta)$ observations made in the mid 1970s [1]. When Pioneer Venus arrived in 1978, the Venus mesosphere was characterized by an anomalous thermal structure, with warm poles and a relatively cool equator. Dynamical models showed that this temperature structure was consistent with a rapid decrease in the amplitude of the cloud-
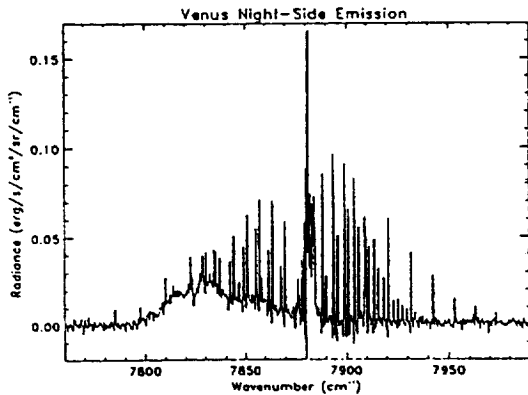
Fig. 1. High-resolution spectrum of the Venus nightside taken on 1 July 1991 at the Canada-France-Hawaii Telescope with the Fourier Transform Spectrometer. The broad emission peak centered near 7830 cm^{-1} (1.277 µm) is thermal emission from the lowest scale height (0–20 km) of the venusian atmosphere. The narrow emission lines and the sharp spike centered near 7880 cm^{-1} are $O_2(^1\Delta)$ airglow, which is produced in the upper mesosphere (~94 km).
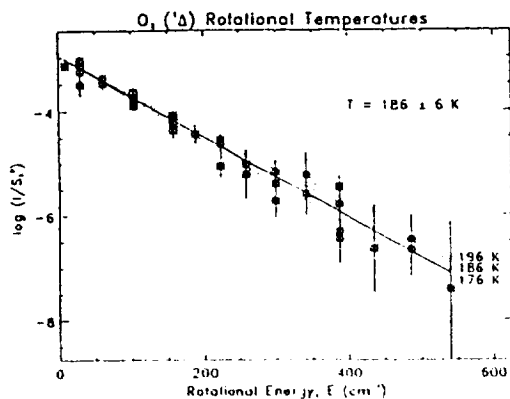
Fig. 2. The local kinetic temperatures can be inferred from the rotational energies of transitions in the P and R branches of the $O_2(^1\Delta)$ band. We find rotational temperatures of 186 ± 6 K.

Fig. 3. Images of the Venus nightside taken at wavelengths in the bright Q branch of the $O_2(^1\Delta)$ band on 19 and 20 September 1991. The intensity of the brightest region changed by about 20% between 20:39 and 21:54 U.T. This bright spot completely vanished the following day.

top superrotation at these altitudes [6]. Groundbased millimeter-wave observations indicate that this thermal structure may have changed dramatically in the mid 1980s, when low-latitude temperatures increased substantially in the upper mesosphere [7]. This warming may have produced tropical temperatures that were warmer than those at the poles, disrupting the anomalous thermal structure and allowing the high-speed cloud-top winds to extend throughout the mesosphere. If that change occurred, our recent $O_2(^1\Delta)$ observations suggest that the venusian mesosphere has since reverted to conditions like those seen in the late 1970s.

The first images of the Venus nightside at wavelengths within the narrow Q branch of the $O_2(^1\Delta)$ band were obtained with the InfraRed Imaging Spectrometer (IRIS) on the Anglo-Australian Telescope (Siding Spring Observatory) on 27 and 28 July 1991. Unlike the almost featureless deep-atmosphere thermal emission at 1.277 µm, the $O_2(^1\Delta)$ airglow occasionally has contrasts as large as 10:1 on the nightside. On 27 July, the brightest feature was centered between 30

and 40N latitude near the dark limb (3 a.m. meridian). The antisolar point was also relatively bright. Within one day, the locations and intensities of the airglow features had changed dramatically. Similar variations in the $O_2(^1\Delta)$ emission were seen on 19 and 20 September 1991 (Fig. 3). This transience and localized structure was not apparent in the earlier groundbased spectroscopic observations of $O_2(^1\Delta)$ emission [1], but similar features have been seen in Pioneer Venus Ultraviolet Spectrometer observations of NO emission [8], which is produced at much higher altitudes (~120 km). The implications of these observations for the composition and general circulation of the upper venusian atmosphere are not yet understood, but they provide important new constraints on comprehensive dynamical and chemical models of the upper mesosphere and lower thermosphere of Venus.

References: [1] Connes P. et al. (1979) *Astrophys. J., 229,* L29. [2] Crisp D. et al. (1991) *Science, 253,* 1263. [3] Yung Y. L. and Demore W. (1982) *Icarus, 51,* 199. [4] Crisp D. et al. (1991) *Bull. AAS, 23,* 1194. [5] Allen D. A. et al. (1992) *Nature,* submitted. [6] Taylor F. W. et al. (1980) *JGR, 85,* 7963. [7] Clancy T. and Muhleman D. (1991) *Icarus, 89,* 129. [8] Stewart A. I. F. et al. (1980) *JGR, 85,* 7861.

GLOBAL CORRELATION OF VOLCANIC CENTERS ON VENUS WITH UPLANDS AND WITH EXTENSION: INFLUENCE OF MANTLE CONVECTION AND ALTITUDE.

L. S. Crumpler, J. W. Head, and J. C. Aubele, Department of Geological Sciences, Brown University, Providence RI 02912, USA.

Introduction: In this paper the observed distribution of volcanism on Venus and its associations with geologic and tectonic characteristics are examined for significant global-scale tectonic, mantle, and volcanic influences. We find that volcanic centers are correlated geologically with zones of extension, infrequent in lowland regions, and infrequent in regions with evidence for tectonic shortening. In addition, volcanic centers are significantly concentrated in a broad region at least 10,000 km in diameter between Beta, Atla, and Themis Regiones. This area is nearly hemispheric in scale and coincides spatially with the area of greatest concentration of extensional characteristics. Our analysis suggests that the observed distribution patterns of volcanic centers reflect the regional patterns of extension, the origin of the extension and volcanism are closely related, and the hemispheric scale of both patterns implies a deep-seated origin such as large-scale interior mantle dynamic patterns. However, altitude-dependent effects on both the formation and preservation of volcanic centers could also strongly influence the observed distribution pattern.

Identification/Classification: The global survey of volcanism includes the area available for analysis from the first and second mission cycles [17], more than 90% of the surface area. The final volcanic catalog [4] identifies, describes, and locates to the nearest half-degree 1548 individual volcanic features larger than ~20 km in diameter. Volcanic features identified include large volcanos, intermediate volcanos, calderas, coronae, arachnoids, novae, shield fields, large lava channels, large lava flows and lava floods, and several other unusual volcanic features. Criteria for identification and classification of volcanic features on Venus [6,4] were carefully outlined and consistently used throughout the survey in order to reduce drift and biases in the classification systematics. The identification criteria selected are dependent on observed image characteristics of a large precursor dataset, were chosen to follow previous usages, and have been supplemented for additional rigor and reproducibility with the use of three size divisions of radial structure, five size divisions of concentric structure, and a concisely-organized identification flowchart. Details of the classification and related observations and reduction procedures are presented elsewhere [4]. In the following, the distribution characteristics and several models for the origin of the observed distribution are discussed in further detail.

Analysis of Distribution: The global distribution of volcanic centers on Venus is nonrandom both visually (Fig. 1) and from several spatial statistical measures. Areas of significant overabundance and underabundance correlate with several specific regional and global geologic characteristics.

Areal Distribution: The global distribution map (Fig. 1) shows that anomalous concentrations of volcanic centers occur at two scales; "global," with dimensions in excess of 10,000 km, and "regional," with dimensions in excess of a few thousand kilometers. Volcanic centers are prominently clustered in a circular region 10,000 to 12,000 km in diameter and centered near longitude 250° and encompassing the areas of Beta Regio, Atla Regio, and Themis Regio. Hereafter this anomaly is referred to as Beta-Atla-Themis, or BAT. A more diffuse clustering of moderate- to high-density areas may be present in the opposite hemisphere (Fig. 1), but in this
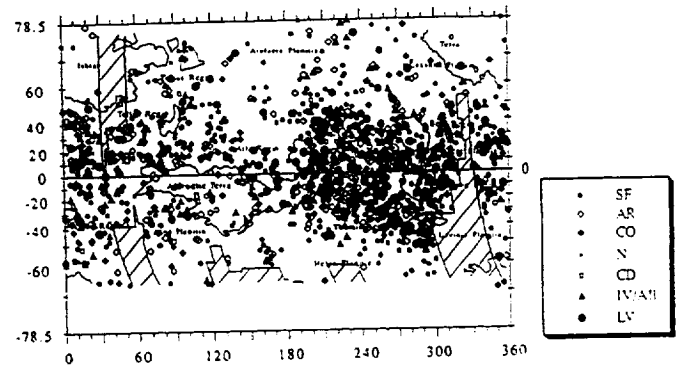
Fig. 1. Global map of the distribution of volcanic centers relative to significant highlands and prominent named surface areas. The highland outlines are represented by the 1.5-km contour. Mercator projection. Ruled areas are cycle 1 and 2 mission gaps.

discussion we focus on BAT in order to further assess some of the primary characteristics of areas bearing concentrated volcanic centers.

The average global areal abundance of volcanic centers (>20 km in diameter) is 3.5 ± 2.9 per 10^6 km^2, based on a sample of 361 equal areas 1000 km × 1000 km. The areal number density is contoured in Fig. 2 in order to show where significant departures (>1 std.dev.) occur relative to the global average density. Areas of moderate volcanic center abundance (>3 to 7 centers/10^6 km^2) attain their greatest contiguous areal extent in the Beta-Atla-Themis area. Several smaller areas (<3000 km across) of greater density (>10 centers /10^6 km^2) also occur locally within this cluster. Large areas of moderate (>3 to 7 centers/10^6 km^2) density also occur elsewhere in the equatorials regions, notably in the hemisphere centered about longitude ~70° trending from Alpha Regio northeast to Tethus Regio. Estimates of the relative areas over which significantly different densities occur show that moderate densities of >3 to 7 centers/10^6 km^2 occur over ~40% of the surface area. Approxi-
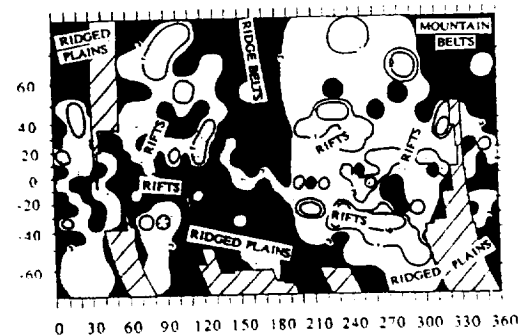
Fig. 2. Contour map of the observed global abundance of cataloged volcanic features on Venus. Contours (3, 7, and 10 volcanic centers per 10^6 km^2) selected to show the mean, mean +~1 s.d., and mean +~2 s.d. intervals. Background dots are volcanic center locations for reference. Areas with lower than nominal abundances occur primarily in association with tessera (for example, Aphrodite Terra) and in areas of lowland plains (for example, Atalanta and Helen Planitiae). The areas of higher abundance are generally associated with geological characteristics of extensional strain (for example, Beta-Atla-Themis Regiones).

mately 60% of the 40% of the surface area covered by moderate volcanic center abundance is accounted for by BAT; the other 40% lies in the broad region noted above just noted in the opposite hemisphere. Higher densities, between 7 and 10 centers/10^6 km^2, occur over ~10% of the surface area. Areas with the greatest densities (>15 centers/10^6 km^2) occur over less than 1% of the surface, mostly within BAT. The abundances over the remaining ~50% of the surface are less than the global mean.

Volcanic centers are primarily associated with regions lying at intermediate altitudes between MPR and 1 to 2 km above MPR. This includes primarily the areas known as uplands, and generally excludes most of the highlands and lowlands. Extreme high or low altitudes are underrepresented in the population. In the following, some of the significant geological associations that this distribution implies are discussed further.

Geological Relationships/Correlations: Areas of low density (fewer than 3 centers/10^6 km^2) occur mostly in lowlands and volcanic centers are strongly excluded from highlands. These areas include primarily extensive ridged lava plains and tesserae respectively. The distribution of tesserae have been mapped from Magellan data [9], appear widely distributed, and are frequently associated with prominent highlands. Where tesserae occur within broader areas of high regional volcanic center concentrations, the tesserae areas are manifest as anomalously vacant areas. Prominent "holes" in the concentration of volcanic centers occur in association with the tessera areas of Ovda, Thetis, Beta, and Phoebe regions.

Extreme high or low altitudes are underrepresented in the population. Areas with lowland characteristics are widespread but occur over relatively well-defined regions with either east-west orientation (Sedna, Niobe, Aino, and Helen) in midlatitudes or as north-south swaths ~30° wide along meridians centered at the longitudes of Eastern Aphrodite (Atalanta, Rusalka, Helen) (165°) and Eistla Regio (Guinevere, Lavinia) (345°).

Although volcanic centers are less abundant in areas of tessera, where there are through-going rifts and zones of extension, volcanic centers are relatively more abundant in tessera settings. In fact, many volcanic centers are clearly associated with regional riftlike patterns of extension. The greatest concentration of volcanic centers, BAT, is characterized by a variety of structural settings, but is mostly situated in a region characterized tectonically by uplift and extension, including that associated with magma emplacement and flank rifting [7,20]. Detailed maps of the location of fracture locations and trends [13], and the sites of several major intersecting rifts [21], show that graben, fractures, fracture belts, and riftlike patterns of extension occur primarily in the Beta-Atla-Themis Regiones and the Alpha-Tellus-Tethys region. We note that these areas of observed high fracture abundance correspond to the areas of greater volcanic center abundance reported here. Major rifts connect the larger volcanic centers within Eistla and Sappho Regiones [20,5], and a network of interlaced fractures connect local concentrations of volcanism to the north and south of Aphrodite Terra.

Geologically, most of the lowland plains appear to be the site of extensive lavas characterized by frequent large lava channels and a mosaic of linear mare-type ridge structural patterns generally interpreted to be the result of tectonic shortening of a few percent over large regions [23]. Ridges of this type are particularly abundant in the extensive lowland plains of eastern Aino and Helen Planitiae, and occur throughout the lowlands of Guinevere, Lavinia, Rusalka, Atalanta, and Snegurochka Planitae. Volcanic centers are also underabundant within the regions of mountain belts where there is evidence of intense shortening and regional compression [3,8,25]. Models for the origin of regional shortening associated with moun-

tain belts include both upwelling and downwelling [16,17,5,1,12,11], but the lowland plains, particularly where ridge belts are common, are most consistent with the characteristics of broad mantle downwelling [27,15]. Therefore, in contrast to areas of high volcanic center density where extension is pervasive, evidence for the sign of the strain in the extreme upper and lower altitudes frequently implies tectonic shortening, and may be associated with regional mantle downwelling.

Coronae, which are thought to represent the sites of intense mantle upwelling [23,24,10,22], are abundant throughout the region of abundant rifting associated with BAT, particularly in Themis Regio. In addition, the area of BAT includes several areas of large positive gravity anomalies thought to represent regions of significant dynamic mantle support and possibly associated with local mantle upwelling [11]. Overall the distribution pattern of coronae and related features may be interpreted as general maps of the global regions of mantle upwelling and surface extension.

Significance of Geologic Correlations: Interior Dynamics, Environment of Formation, or Age? Initial study of these relationships suggests that spatial variations in volcanic center density and global geological and geophysical characteristics are correlated with global structural patterns and styles of tectonism.

On the basis of (1) the observed correlation between areas of high volcanic center abundance and areas with geological evidence for extension and (2) the correlation of areas of low volcanic center abundance and areas with geological evidence for compression, we outline in the following a series of hypotheses for the observed distribution that may be tested.

1. The distribution is governed by the predicted influence of the high gradient in surface pressure with altitude on the occurrence and style of volcanic centers and intrusions on Venus [26]. This suggests that the absence of volcanic centers in lowlands could also be a primary result of the absence of shallow-depth magma reservoirs in lowlands. Shallow magma emplacement is a necessary characteristic of volcanic centers as it regulates the volume and rate of individual magma eruptions in a manner conducive to building local edifices. In the absence of shallow magma reservoirs, eruptions, when they do occur, would be from great depths, and large lava flood events, rather than local volcanic edifices, would be formed. Under this hypothesis, volcanic centers are underabundant in lowlands because the environment of formation does not favor their formation there.

2. Low volcanic center abundance occurs in the plains because these are areas of mantle downwelling. Volcanic centers are excluded from areas associated with mantle downwelling because these are areas of net regional compressional strain and locally cooler mantle. Areas of high volcanic center abundances might be primarily associated with characteristics of mantle upwelling, regional extensional strain, and relatively warmer mantle and associated increased regional partial melt production. The abundance of rifting and coronae in these areas supports this interpretation, but does not address the origin of the observed range in morphology of centers between the plains and uplands.

3. Because the regions of high volcanic center abundance are elevated areas, they are preserved as islands from surrounding lava plains-type flooding events. This hypothesis predicts that the surface where volcanic centers are most abundant should be older on average relative to areas of low volcanic center abundance. Initial correlation of volcanic center frequency with reported impact crater distribution [19,14] suggests that if such a correlation is present it is relatively weak.

Conclusions: On the basis of our initial analysis, we conclude that the observed pattern of volcanic features may be correlated with the distribution pattern of global physiographic and geologic characteristics. The distribution of volcanic centers and regional tectonic patterns suggests that volcanic features are generally excluded from lowlands and regions of tectonic shortening, and occur predominantly in upland regions characterized by geologic evidence for extension. Three hypotheses that may account for the observed distribution and geologic association may be categorized as (1) environment/elevation-related, (2) mantle dynamics-related, and (3) age-related. It is likely that all three influences occur, but on the basis of the global association of areas of high volcanic center abundance with tectonic characteristics of extension and the probable association of many individual volcanic centers with local mantle upwelling and plumes, we believe that the regional concentrations of volcanic centers may be primarily associated with regions of broad mantle upwelling phenomena. Although the broad-scale characteristics and association of the distribution of volcanic centers may be accounted for by the first hypothesis, details of the distribution and local associations may be strongly influenced by altitude and age-dependent effects.

References: [1] Bindschadler et al. (1990) *GRL, 17,* 1345. [2] Campbell et al. (1989) *Science, 246,* 373. [3] Crumpler et al. (1986) *Geology, 14,* 1031. [4] Crumpler et al. (1992) in preparation. [5] Grimm and Phillips (1991) *JGR, 96,* 8305. [6] Head et al. (1991) *GRL, 17,* 11337. [7] Head et al. (1991) *JGR,* submitted. [8] Head J. W. (1990) *Geology, 18,* 99. [9] Ivanov et al. (1992) *LPSC XXIII.* [10] Janes et al. (1992) *JGR,* submitted. [11] Kieffer and Hagar (1991) *JGR, 96,* 20967. [12] Lenardic et al. (1991) *GRL, 18,* 2209–2212. [13] Michaels et al. (1992) *LPSC XXIII,* 903. [14] Phillips et al. (1992) *JGR,* submitted. [15] Phillips et al. (1991) *Science, 252,* 651. [16] Pronin A. A. (1986) *Geotectonics, 20,* 271. [17] Roberts et al. (1991) *GRL, 17,* 1341. [18] Saunders et al. (1992) *JGR,* submitted. [19] Schaber et al. (1992) *JGR,* submitted. [20] Senske et al. (1992) *JGR,* submitted. [21] Senske and Head (1992) *LPSC XXIII,* 1269. [22] Squyres et al. (1992a) *JGR,* submitted. [23] Squyres et al. (1992b) *JGR,* submitted. [24] Stofan et al. (1992) *JGR,* submitted. [24] Stofan et al. (1991) *JGR, 96,* 20933. [25] Vorder Bruegge and Head (1989) *GRL, 16,* 699. [26] Head and Wilson (1992) *JGR, 97,* 3877. [27] Zuber (1990) *GRL, 17,* 1369–1372.

N93-14310

THE SPIN VECTOR OF VENUS DETERMINED FROM MAGELLAN DATA.

M. E. Davies[1], T. R. Colvin[1], P. G. Rogers[1], P. W. Chodas[2], and W. L. Sjogren[2], [1]RAND, USA, [2]Jet Propulsion Laboratory, California Institute of Technology, Pasadena CA 91109, USA.

A control network of the north polar region of Venus has been established by selecting and measuring control points on full-resolution radar strips. The measurements were incorporated into a least-squares adjustment program that improved initial estimates of the coordinates of the control points, pole direction, and rotation rate of Venus. The current dataset contains 4206 measurements of 606 points on 619 radar strips. The accuracy of the determination is driven by spacecraft ephemeris errors. One method used to remove ephemeris errors is to adjust the averaged orbital inclination and argument of periapsis for each orbit. A more accurate method that has been used with selected blocks of orbits incorporates optimally fitting measurements of additional points at all latitudes of the radar strips together with Earth-based spacecraft radiometric tracking measurements to compute new spacecraft ephemerides. The root-

mean-space (RMS) of the point measurement residuals in these improved ephemeris solutions is typically about 20 m in slant range, and 40 m in the along-track direction. Both the control network computations and the improved ephemeris solutions incorporate radii at the measured points derived from the Magellan altimetry dataset [1]. The radii of points north of 85° are computed in the least-squares adjustments.

An accurate estimate of the rotation period of Venus was obtained by applying the ephemeris improvement technique to the second cycle closure orbits 2166–2171 that overlaid the first cycle initial orbits 376–384. Sixty-four common points were measured on both orbit groups and improved ephemeris solutions computed over both blocks simultaneously, along with the rotation rate. A similar analysis was made using orbits 874–878 from cycle 1 and 4456–4458 from cycle 3. Fifty-two common points were measured on both orbit groups and the rotation period of 243.0185 ± 0.0001 was computed. This latter solution confirmed the initial solution, and was an improvement over the first closure solution because of the longer period between overlapping orbits.

The geodetic control network uses measurements of points on overlapping radar strips that cover the north polar region; these are only the even-numbered orbits. These strips were taken in the first cycle and encircle the pole except for three gaps due to the superior conjunction data loss, the reduced data due to occultation, and the area of ongoing work. Improved ephemeris solutions for 40 orbits (376–384, 520–528, 588–592, 658–668, 1002–1010, 1408–1412, 1746–1764, and 2166–2170) are included and fixed in the geodetic control computations, thus tying the network to the J2000 coordinate system. The argument of periapsis and orbital inclination of all remaining orbits were allowed to vary as part of the least-squares adjustment. The RMS of the point measurements is typically on the order of 75 m in both along-track and cross-track. The rotation period was fixed at 243.0185 days. The coordinates of the 606 measured points were determined and the solution for the direction of the north pole was $\alpha = 272.76° \pm 0.02°$, $\delta = 67.16° \pm 0.01°$ (J2000).

References: [1] Ford P. G. and Pettengill G. H. (1992) *JGR,* in press.

N93-14311

MONTE CARLO COMPUTER SIMULATIONS OF VENUS EQUILIBRIUM AND GLOBAL RESURFACING MODELS.

D. D. Dawson[1], R. G. Strom[1], and G. G. Schaber[2], [1]University of Arizona, Tucson AZ 85721, USA, [2]U.S. Geological Survey, Flagstaff AZ 86001, USA.

Two models have been proposed for the resurfacing history of Venus: (1) equilibrium resurfacing and (2) global resurfacing. The equilibrium model [1] consists of two cases: In case 1 areas ≤0.03% of the planet are spatially randomly resurfaced at intervals of ≤150,000 yr to produce the observed spatially random distribution of impact craters and average surface age of about 500 m.y., and in case 2 areas ≥10% of the planet are resurfaced at intervals of ≥50 m.y. The global resurfacing model [2] proposes that the entire planet was resurfaced about 500 m.y. ago, destroying the preexisting crater population and followed by significantly reduced volcanism and tectonism. The present crater population has accumulated since then, with only 4% of the observed craters having been embayed by more recent lavas.

To test the equilibrium resurfacing model we have run several Monte Carlo computer simulations for the two proposed cases. For case 1 we used a constant resurfacing area of 0.03% of the planet with a constant thickness and a constant 150,000-yr time interval
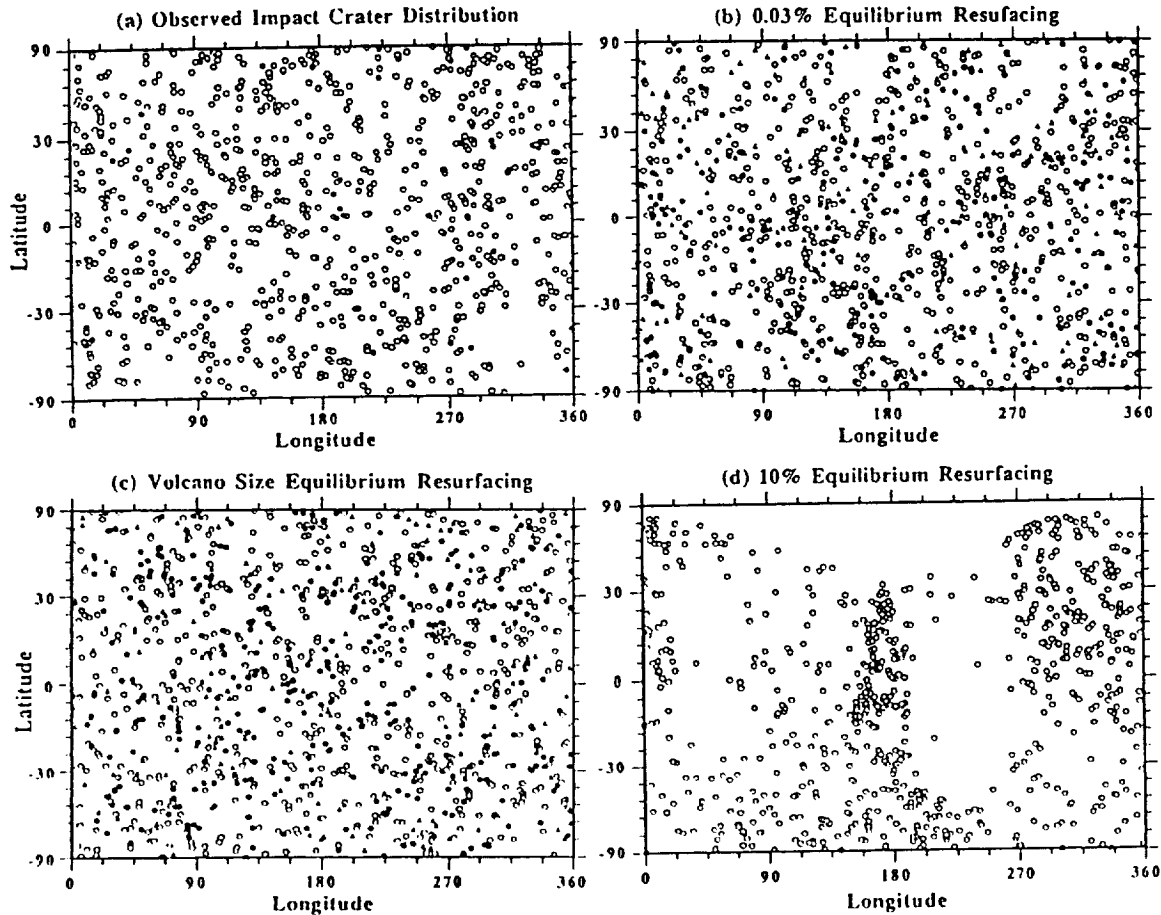
Fig. 1. (a) Observed Venus impact crater distribution. (b) 0.03% planet equilibrium resurfacing Monte Carlo simulation. (c) Observed volcano size distribution equilibrium resurfacing Monte Carlo simulation. (d) 10% equilibrium resurfacing Monte Carlo simulation. The unfilled circles are pristine craters, the solid circles are flooded craters, and the solid triangles are possibly flooded craters. Flooded craters not shown in (d).

between resurfacing events. Another more realistic simulation used the observed size distribution of volcanic features determined by Head et al. [3] and a variable time interval between resurfacing events that depended on the size of the event. Each simulation was run for a simulation period of 3 b.y. We took into account ejecta blankets by doubling the size of the craters. The center of each crater was marked with a dot, and the amount of the crater covered by resurfacing events was determined. Craters that were entirely covered by a single resurfacing event were considered destroyed. The minimum amount of flooded craters were those craters that had either not had their central point covered or had not had an area equal to 100% of their area covered. The maximum amount of flooded craters included the minimum amount and those craters that fulfilled both of the above criteria but had not been entirely covered by a single event. Some fraction of these latter craters may have been destroyed, but the others were probably intact and flooded. In fact, this category of crater only constituted about 15% of the total number of craters remaining after the simulations. Furthermore, a constant thickness resurfacing event is unrealistic and will produce more destroyed craters than a more realistic tapered event that will produced more partially flooded craters. For each simulation the input crater size-frequency distribution was the observed differential –0.2 slope for craters between 2 and 30 km diameter and the

observed differential –3 slope at diameters greater than 30 km. After the simulations, however, the size distribution had changed to a –2 slope at diameters greater than 30 km, because over the simulation time of 3 b.y. the smaller craters were preferentially erased relative to the large craters to produce the –2 slope. Therefore, it was necessary to input an artificial size-frequency distribution with a –4 slope for craters greater than 30 km diameter in order to arrive at a –3 slope at the end of the simulation.

For the case 1 equilibrium resurfacing model to be valid the resulting crater distribution should be spatially random and there should be only about 4% partially flooded craters. Figures 1b and 1c show the results of the simulations compared to the observed crater distribution (Fig. 1a). Although the crater spatial distribution appears to be random, the amount of flooded craters is a minimum of 24% and maximum of 40% in the 0.03% resurfacing model, and a minimum of 30% and maximum of 46% in the more realistic observed volcano size distribution model. This is between 6 and 10 times the amount of flooded craters observed. The computer simulations do not take into account the more than 300 splotches that are part of the impact record and are not embayed by lava. This would only exacerbate the problem by producing many more flooded impact events. Furthermore, the input size frequency distribution above 30 km diameter required to produce the observed distribution

is completely unlike any size distribution on the terrestrial planets. Therefore, the computer simulations strongly indicate that the case 1 equilibrium resurfacing model is not a valid explanation for the resurfacing history of Venus. The observed nonrandom distribution of volcanic features [3] and the noncorrelation of the density of impact craters and volcanic features in equal areas [2] are further arguments against the equilibrium resurfacing model.

Case 2 of the equilibrium resurfacing model (≥10% resurfacing areas) simply will not work, except at the 100% (global) resurfacing level. Figure 1d is a Monte Carlo simulation for constant 10% resurfacing areas with a constant 50-m.y. time interval between events. Clearly the crater distribution is completely nonrandom and totally different from the observed distribution. We have done simulations for 25% and 50% resurfacing areas with similar results. Therefore, the equilibrium resurfacing model is not a valid model for an explanation of the observed crater population characteristics or Venus' resurfacing history.

The global resurfacing model is the most likely explanation for the characteristics of Venus' cratering record. The amount of resurfacing since that event, some 500 m.y. ago, can be estimated by a different type of Monte Carlo simulation. In this simulation the cratering record begins 500 m.y. ago with the observed crater size distribution. Our first simulation randomly selects craters from this size distribution and resurfaces areas with volcanos randomly selected from the observed volcano size distribution. The time interval between volcanic events is chosen so that only 4% of the craters are flooded at the end of 500 m.y. To date, our initial simulation has only considered the easiest case to implement. In this case the volcanic events are randomly distributed across the entire planet and, therefore, contrary to observation, the flooded craters are also randomly distributed across the planet. This simulation results in a maximum resurfaced area of about 10% of the planet since the global event, and an obliteration of about 4% of the craters. Future simulations will take into account the observed nonrandom distribution of flooded craters and, therefore, the nonrandom distribution of volcanic events. These simulations will probably result in a lower percentage of planet resurfacing because volcanism will be concentrated in smaller areas.

References: [1] Phillips R. J. et al. (1992) *LPSC XXIII*, 1065–1066. [2] Schaber G. G. et al. (1992) *JGR*, special Magellan issue, in press. [3] Head J. W. et al. (1992) *JGR*, special Magellan issue, in press.

N93-14312

METHANE MEASUREMENT BY THE PIONEER VENUS LARGE PROBE NEUTRAL MASS SPECTROMETER.

T. M. Donahue[1] and R. R. Hodges Jr.[2], [1]University of Michigan, Ann Arbor MI 48109, USA, [2]University of Texas at Dallas, Richardson TX, 75083, USA.

The Pioneer Venus Large Probe Mass Spectrometer detected a large quantity of methane as it descended below 20 km in the atmosphere of Venus. Terrestrial methane and ^{136}Xe, both originating in the same container and flowing through the same plumbing, were deliberately released inside the mass spectrometer for instrumental reasons. However, the ^{136}Xe did not exhibit behavior similar to methane during Venus entry, nor did CH_4 in laboratory simulations. The CH_4 was deuterium poor compared to Venus water and hydrogen. While the inlet to the mass spectrometer was clogged with sulfuric acid droplets, significant deuteration of CH_4 and its H_2 progeny was observed. Since the only source of deuterium identifiable was water from sulfuric acid, we have concluded that we should

correct the HDO/H_2O ratio in Venus water from 3.2×10^{-2} to $(5 \pm 0.7) \times 10^{-2}$.

When the probe was in the lower atmosphere, transfer of deuterium from Venus HDO and HD to CH_4 can account quantitatively for the deficiencies recorded in HDO and HD below 10 km, and consequently, the mysterious gradients in water vapor and hydrogen mixing ratios we have reported. The revision in the D/H ratio reduces the mixing ratio of water vapor (and H_2) reported previously by a factor of 3.2/5.

We are not yet able to say whether the methane detected was atmospheric or an instrumental artifact. If it was atmospheric, its release must have been episodic and highly localized. Otherwise, the large D/H ratio in Venus water and hydrogen could not be maintained.

N93-14313

VISCOELASTIC RELAXATION OF VENUSIAN CORONAE AND MOUNTAIN BELTS: CONSTRAINTS ON GLOBAL HEAT FLOW AND TECTONISM.

I. Duncan and A. Leith, Department of Earth and Planetary Science, Washington University, St. Louis MO 63130, USA.

Venus differs from Earth in that water is essentially absent and its surface temperatures are about 470 K higher. The competing effects of high surface temperature and dry lithologies on the long-term history of surface topography have been studied using the finite-element method (Tecton) [1].

The relaxation history of surface topographic features, such as coronae and mountain belts, is a function of thermal gradient, crustal thickness and lithology, regional stresses, and basal tractions applied to the lithosphere. In this study we have examined the relative effects of these factors over a period of 500 Ma (presumed to be the mean age of the venusian surface) [2].

We assume that the venusian crust is composed of various combinations of diabase, gabbro, komatiite, and refractory lithologies such as anorthosite and websterite. Using appropriate thermal conductivities and surface heat fluxes scaled from Earth values (with and without a secular cooling contribution from the core) [3,4], thermal gradients ranging from about 20 K km^{-1} to 60 K km^{-1} are computed. We further assume that the thickness of a diabase crust is limited by the dry solidus. The models are dynamically isostatically balanced, using an elastic foundation.

Preliminary results of the study are shown in Fig. 1, in which a 2-km-high volcanic plateau has been instantaneously emplaced on the surface. For this model the crustal thermal gradient was 28 K km^{-1}. After the elastic response (essentially representing initial isostatic balance) the topography relaxes until the plateau is about 230 m above the surrounding region, and the slope from ridge crest to moat has been reduced from an initial 6° to about 2.5°. The values we obtain for our model plateau heights and slopes are in the observed range for venusian coronae. Thus we argue that coronae on Venus can be modeled as the product of elastoviscous relaxation of volcanic plateau. Although our starting models are oversimplifications, they do show all the critical morphological characteristics of venusian coronae. Matching the observed spectrum of corona morphology by varying the size, initial slope, and rheology of model plateaus enables constraints to be placed on plausible values for the venusian heat flux. We argue that the mean global heat flux must be significantly lower (~1/3) to be consistent with the observed spectrum of coronae topography.

We are presently examining models similar to those described above to investigate venusian mountain belts. Our models differ
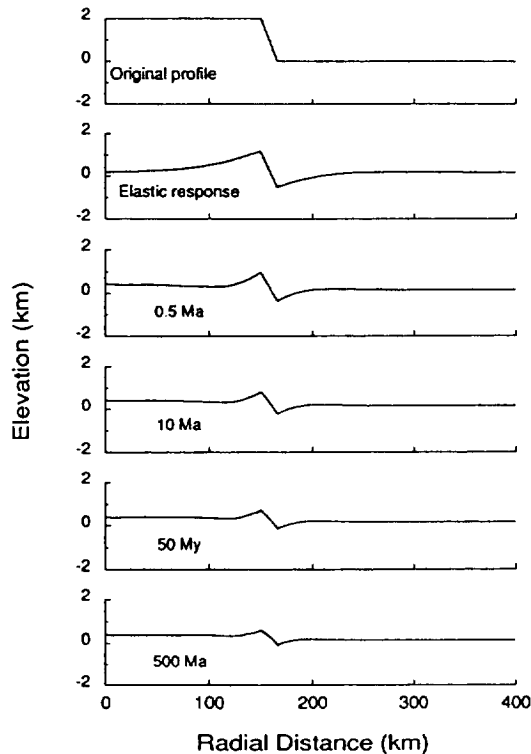
Fig. 1. Radial profiles across an initially 2-km-high and 150-km-radius plateau. The plateau and upper 2.5 km of the crust are of diabase composition and the lower 2.5 km of crust is of gabbro and overlies a peridotite mantle. The lithosphere is 33 km thick. The thermal gradient through the upper crust is 28 K km⁻¹. Topographic profiles are shown for the original plateau, the instantaneous elastic response to loading (isostatic balance), and for 0.5, 10, 50, and 500 Ma. Vertical exaggeration is x21.

from those of other workers in that (1) our thermal models are distinctive and we believe more realistic and (2) our models are dynamically isostatically balanced with both hydrostatic restoring forces and dynamic support by tectonic stress and basal tractions being modeled. The implications of our models' stress evolution for surface deformation can be tested against Magellan imagery.

References: [1] Melosh H. J. and Raefsky A. (1980) *Geophys. J. R. Astron. Soc.*, *60*, 333–354. [2] Phillips R. J. et al. (1992) *LPSC XXIII*, 1065–1066. [3] Solomon S. C. and Head J. W. (1984) *JGR*, *87*, 9236–9246. [4] Phillips R. J. and Malin M. C. (1984) *Annu. Rev. Earth Planet. Sci.*, *12*, 411–443.

N93-14314

FLEXURAL ANALYSIS OF UPLIFTED RIFT FLANKS ON VENUS.

Susan A. Evans, Mark Simons, and Sean C. Solomon, Department of Earth, Atmospheric, and Planetary Sciences, Massachusetts Institute of Technology, Cambridge MA 02139, USA.

Introduction: Knowledge of the thermal structure of a planet is vital to a thorough understanding of its general scheme of tectonics. Since no direct measurements of heat flow or thermal gradient are available for Venus, most estimates have been derived from theoretical considerations or by analogy with the Earth [1]. The flexural response of the lithosphere to applied loads is sensitive to regional thermal structure. Under the assumption that the yield strength as a function of depth can be specified, the temperature

gradient can be inferred from the effective elastic plate thickness [2]. Previous estimates of the effective elastic plate thickness on Venus range from 11–18 km for the foredeep north of Uorsar Rupes [3] to 30–60 km for the annular troughs around several coronae [4,5]. Thermal gradients inferred for these regions are 14–23 K km⁻¹ and 4–9 K km⁻¹ respectively [3,4]. In this study, we apply the same techniques to investigate the uplifted flanks of an extensional rift. Hypotheses for the origin of uplifted rift flanks on Earth include lateral transport of heat from the center of the rift, vertical transport of heat by small-scale convection, differential thinning of the lithosphere, dynamical uplift, and isostatic response to mechanical unloading of the lithosphere [6]. The last hypothesis is considered the dominant contributor to terrestrial rift flanks lacking evidence for volcanic activity, particularly for rift structures that are no longer active [6]. In this study, we model the uplifted flanks of a venusian rift as the flexural response to a vertical end load.

Tectonic Environment: We examine a linear rift system centered at 33°S, 92°E, in an area to the east of Aino Planitia. The feature appears as a linear ridge in Pioneer Venus altimetry and thus has been named Juno Dorsum. However, the increased resolution of Magellan images and topography has established that this feature is actually a linear rift with pronounced flanking highs. The rift is 100 km wide and 450 km long; it has a central depression 1–2 km deep and flanks elevated by as much as 1 km (Figs. 1 and 2). The rift connects a 1.5-km-high volcano on its western edge to two coronae, Tai Shan and Gefjun [7], to the east. Despite the presence of the volcano and coronae, both the center of the rift and the adjacent flanks appear to be free of volcanic flows. Juno Dorsum is at the end of a nearly continuous chain of coronae, rifts, and linear fractures that extends eastward and appears to terminate at the northwestern edge of Artemis Corona. The rift appears in Magellan images as numerous east-northeast-trending lineaments, which we interpret to be normal faults. To the north and south are smooth, radar-dark plains that stand very close to mean planetary elevation.

We use Magellan altimetric profiles from orbits 965–968 and 970–972 (Figs. 1 and 2). While topographic profiles perpendicular to the strike of the rift are preferable, the orbit tracks cross the rift
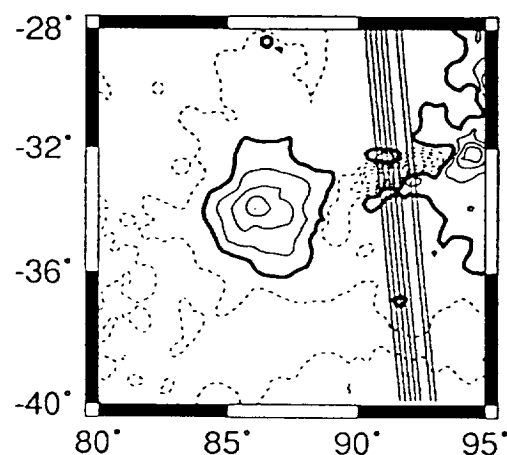
Fig. 1. Topographic contour map of the Juno Dorsum region. Thin solid lines denote positive elevation contours, thick solid lines zero elevation, and dashed lines negative elevations. The contour interval is 0.3 km, and the datum is mean planetary radius, 6051.9 km. The rift is located in the center right of the figure, with an unnamed volcano to its west. The north-south-trending lines indicate the tracks of orbits 965–968 and 971–972 (numbers increasing, eastward). The orbit tracks make an angle of approximately 75° with the strike of the rift.
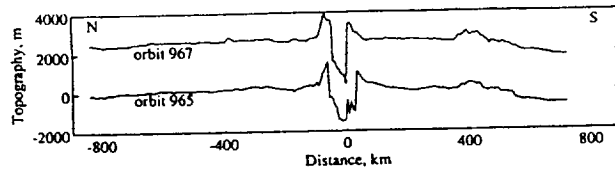
Fig. 2. Example orbit profiles over Juno Dorsum; see Fig. 1 for location. The rift flanks are elevated 800 to 1000 m above the surrounding plains, and interference from other regional topographic features is minimal. Orbit 967 has been offset vertically by 2500 m for clarity.

at an angle of approximately 75°, and we can easily make the geometrical correction for this small difference. Profiles from single orbits avoid errors introduced by interorbit offsets. As is evident in Fig. 2, the topography of the surrounding plains region is rather smooth, and the uplift of the flanks is quite distinct and easy to discern from other regional topography.

Model: We model the uplift of the rift flanks as the flexural response of a thin elastic plate overlying a fluid substratum [8]. We assume that the flexure is of the form

$$w = \exp\left(\frac{-x}{\alpha}\right)\left[A\cos\left(\frac{-x}{\alpha}\right) + B\sin\left(\frac{-x}{\alpha}\right)\right] \qquad (1)$$

where w is the vertical deflection of the plate from the regional datum, x is the distance along the profile, and α is the flexural parameter given by

$$\alpha = \left[\frac{E\,T_e^3}{3\,\rho_m\,g(1-v^2)}\right]^{\frac{1}{4}} \qquad (2)$$

where E is Young's Modulus (60 GPa), T_e is the elastic plate thickness, ρ_m is the mantle density (3300 kg m^3), g is the gravitational acceleration (8.87 m s^{-2}), and v is Poisson's ratio (0.25). The objective is to find the three parameters A, B, and α such that the root-mean-square (rms) misfit between the observed and calculated topographic profiles is a minimum. Since w depends nonlinearly on α, we first fix the value of α, then calculate the best-fitting values of A and B. The flexural parameter is then varied over a range corresponding to an elastic plate thickness of 1 to 50 km, and the procedure is repeated. From the parameters providing the best overall fit we calculate the plate curvature at the first zero-crossing. This curvature and the apparent elastic plate thickness are then used to estimate the thermal gradient from the curves in [3].

We model only the rift flanks, so we remove the central rift depression from the profiles and model each rift flank separately. The location of highest topography in the half profile defines the origin of the horizontal axis. We fit topography up to 350 km from the rift, to avoid modeling the small rise 400 km to the south of the rift (Figs. 1 and 2). We also remove the mean elevation and the best-fit linear trend from our profiles before fitting to prevent bias from long-wavelength regional topography.

Results: Of the 14 profiles obtained in orbits 965–968 and 971–972, we analyze 10 that have flanks rising 600–1200 m above the regional mean elevation. Four of these profiles are well fit by elastic plate thicknesses of 8–16 km. For each of these profiles, there
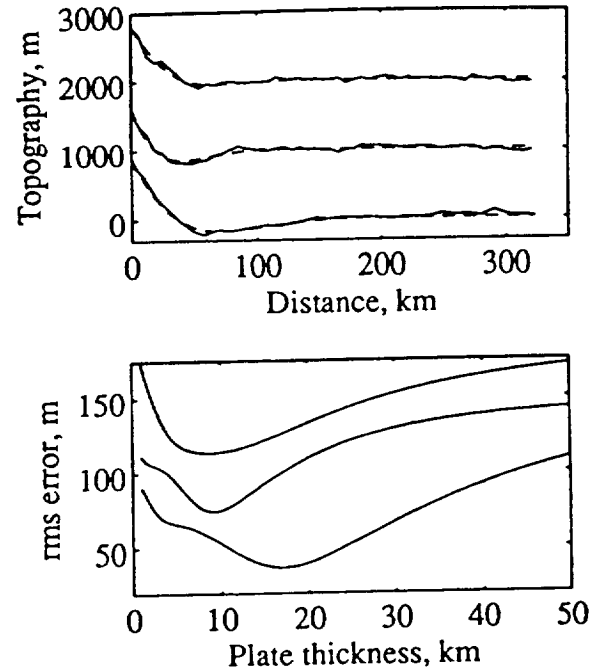
Fig. 3. Top: Topographic profiles (solid) and best-fit flexural profiles (dashed) for three half profiles; top to bottom are orbit 967, southern flank; orbit 968, southern flank; orbit 968, northern flank. Bottom: the rms error as a function of elastic plate thickness for the same profiles. Note that the top two profiles are best fit only over a small range of elastic plate thicknesses, whereas the bottom profile can be fit by a broader range of plate thicknesses. All profiles are consistent with elastic plate thicknesses in the range 8–20 km. For clarity, the upper two profiles at top have been vertically offset by 1000 m and 2000 m, respectively, and the corresponding error curves by 30 and 60 m.

is a narrow range of plate thicknesses for which the rms error is small, so the results are well constrained (Fig. 3). Three of these profiles produce best-fitting plate thicknesses of 8–9 km, suggesting that the true effective elastic plate thickness may be near the low end of this range. The remaining profiles generally contain more small-scale topographic variation of ±100 m in amplitude and are equally well fit by a range of plate thicknesses. The fits for all profiles, however, are consistent with elastic plate thicknesses of 8–20 km.

These effective plate thicknesses and the calculated curvatures imply thermal gradients of 15–30 K km^{-1} if the base of the mechanical lithosphere is limited by the ductile strength of olivine [3]. Because the values of elastic lithosphere thickness derived here are comparable to or less than the estimated crustal thickness beneath plains regions on Venus [9,10], the base of the mechanical lithosphere may lie within the crust and be limited by the flow law for lower crustal material. In such a situation, the thermal gradients would be less than the figures given above.

The effective elastic plate thicknesses we derive for the Juno rift structure (8–20 km) are comparable to those obtained for the North Polar Plains at Uorsar Rupes (11–18 km) and both regions involve flexure of the lithosphere beneath plains at elevations near the planetary mean. A general relationship between regional elevation and elastic plate thickness might be expected if regional elevation were controlled by lithospheric thermal structure [11], as in the

Earth's oceanic regions. Further analysis of flexure is warranted to determine if such a relationship holds for Venus.

References: [1] Solomon S. C. and Head J. W. (1982) *JGR*, *87*, 9236. [2] McNutt M. K. (1991) *JGR*, *89*, 11180. [3] Solomon S. C. and Head J. W. (1991) *GRL*, *17*, 1393. [4] Sandwell D. T. and Schubert G. (1992) *JGR*, in press. [5] Sandwell D. T. and Schubert G. (1992) *Science*, submitted. [6] Weissel J. K. and Karner G. D. (1989) *JGR*, *94*, 13919. [7] Stofan E. R. (1992) *JGR*, in press. [8] Turcotte D. L. and Schubert G. (1982) *Geodynamics*, 125–131. [9] Grimm R. E. and Solomon S. C. (1988) *JGR*, *93*, 11911. [10] Zuber M. T. and Parmentier E. M. (1990) *Icarus*, *85*, 290. [11] Morgan P. and Phillips R. J. (1983) *JGR*, *88*, 8305.

N93-14315

UNDERSTANDING THE VARIATION IN THE MILLIMETER-WAVE EMISSION OF VENUS.

Antoine K. Fahd and Paul G. Steffes, School of Electrical Engineering, Georgia Institute of Technology, Atlanta GA 30332, USA.

Recent observations of the millimeter-wave emission from Venus at 112 GHz (2.6 mm) have shown significant variations in the continuum flux emission [1] that may be attributed to the variability in the abundances of absorbing constituents in the Venus atmosphere. Such constituents include gaseous H_2SO_4, SO_2, and liquid sulfuric acid (cloud condensates). Recently, Fahd and Steffes [2,3] have shown that the effects of liquid H_2SO_4 and gaseous SO_2 cannot completely account for this measured variability in the millimeter-wave emission of Venus. Thus, it is necessary to study the effect of gaseous H_2SO_4 on the millimeter-wave emission of Venus. This requires knowledge of the millimeter-wavelength (MMW) opacity of gaseous H_2SO_4, which unfortunately has never been determined for Venus-like conditions.

We have measured the opacity of gaseous H_2SO_4 in a CO_2 atmosphere at 550, 570, and 590 K, at 1 and 2 atm total pressure, and at a frequency of 94.1 GHz. Our results, in addition to previous centimeter-wavelength results [4], are used to verify a modeling formalism for calculating the expected opacity of this gaseous mixture at other frequencies. This formalism is incorporated into a radiative transfer model to study the effect of gaseous H_2SO_4 on the MMW emission of Venus.

Experimental Configuration: The experimental setup used to measure the MMW opacity of gaseous H_2SO_4 atmosphere consists of a free-space transmission system as shown in Fig. 1. In this system, a glass cell contains the H_2SO_4/CO_2 gaseous mixture that is introduced prior to the measurement process. The glass cell is located inside a temperature-controlled chamber. A transmitting antenna is used to launch energy into the glass chamber. A receiving antenna is placed at the output of the glass cell in order to collect the outgoing signal. Using a precision variable attenuator, the resulting opacity of the gaseous mixture is measured.

Measurement Results: The measured absorptivity (dB/km) of H_2SO_4 at 94.1 GHz is shown in Fig. 2 where it is plotted as a function of temperature for 2 and 1 atm. The reported absorptivities in Fig. 2 are normalized to their respective mixing ratios. The measurements were performed at 550, 570, and 590 K in order to allow enough H_2SO_4 vapor pressure in the glass cell.

Although the measurements were performed at 94.1 GHz, care must be taken when projecting the absorption of H_2SO_4 at frequencies far from 94.1 GHz. As a result, we have developed an absorption model based on a Van Vleck-Weisskopf (VVW) formalism. In this formalism, we added the contributions from 2359 resonant lines of H_2SO_4 computed by Pickett et al. (private communication, 1991) that cover frequencies between 1.5 and 450 GHz.

In order to fully implement the VVW formalism, an appropriate broadening parameter must be determined. To solve this problem,
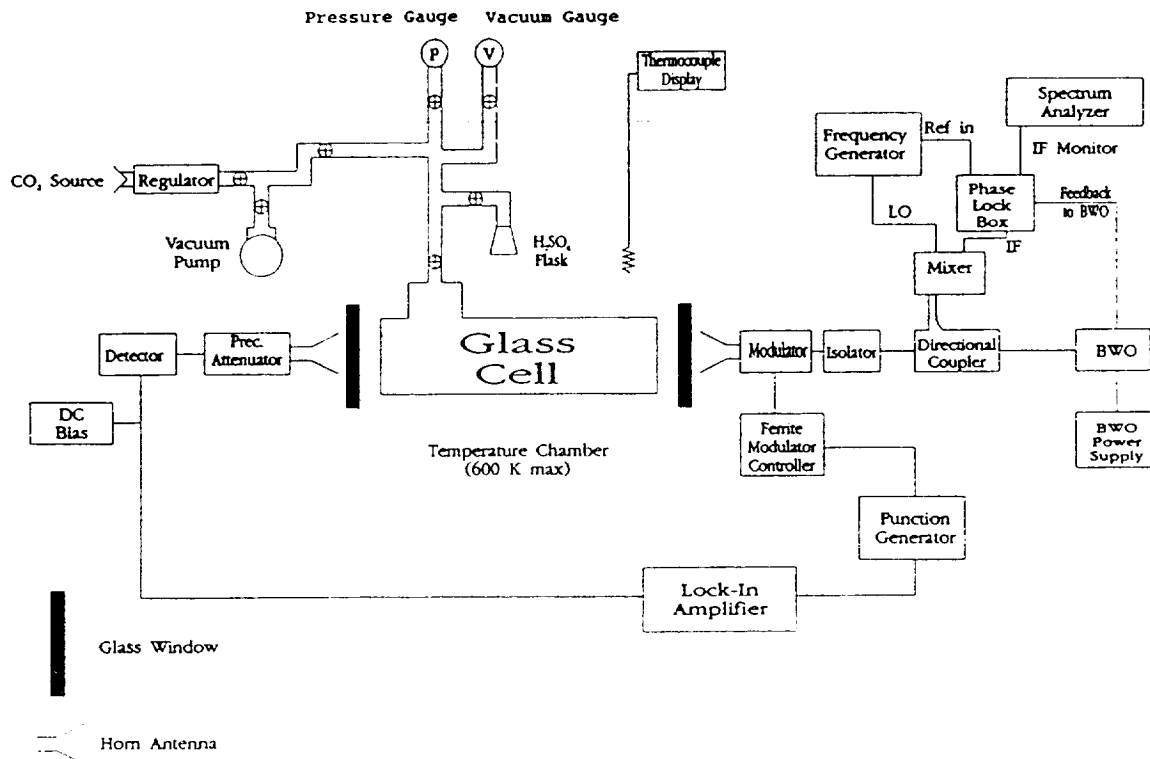
Fig. 1. Block diagram of the atmospheric simulator as configured for measurements of the millimeter-wave absorption at 94.1 GHz.
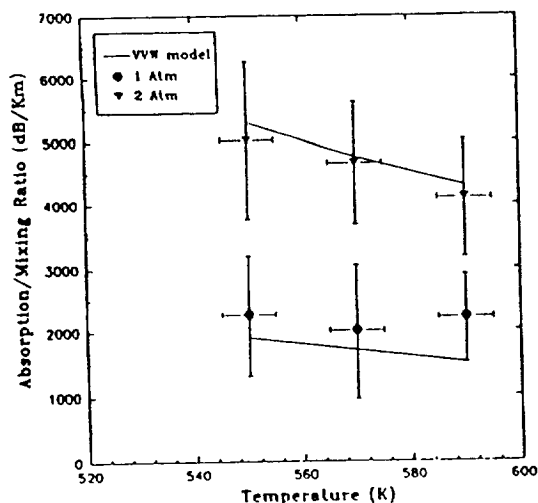
Fig. 2. Laboratory measurements of the normalized absorptivity (dB/km) of gaseous H_2SO_4 in a CO_2 atmosphere at 94.1 GHz. Solid curves are the theoretically calculated absorption from the VVW formalism.
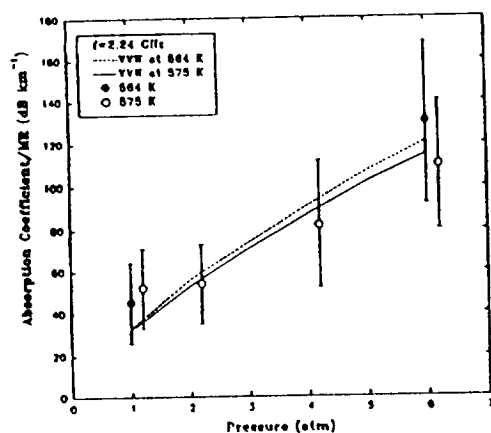
Fig. 3. Comparison between the measured absorption (normalized by mixing ratio) of H_2SO_4 [4] and the calculated absorption from the VVW formalism at 2.24 GHz.
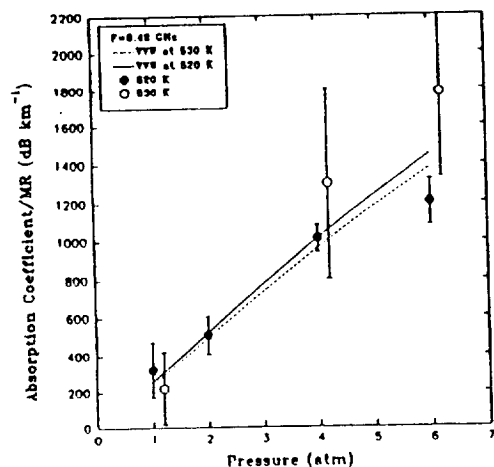
Fig. 4. Comparison between the measured absorption (normalized by mixing ratio) of H_2SO_4 [4] and the calculated absorption from the VVW formalism at 8.42 GHz.
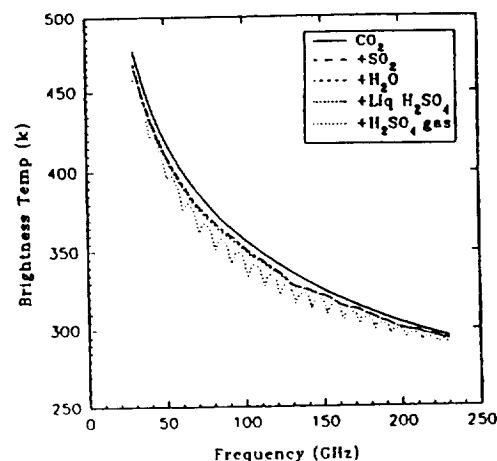
Fig. 5. Comparison of the effects of atmospheric constituents on the brightness temperature of Venus between 30 and 230 GHz.

we adjusted the broadening parameter so that the calculated opacity matches the measured absorptivity at 94.1 GHz and the microwave opacities at 2.24 and 8.42 GHz reported by Steffes [4]. Comparisons between the calculated and measured opacity of H_2SO_4/CO_2 are shown in Figs. 2, 3, and 4. A careful examination of these results indicates that the calculated opacities of H_2SO_4 using the VVW formalism with a broadening parameter of 1.55 MHz/Torr agree well with the measured microwave and millimeter-wave opacities of the gaseous mixture. This finding is quite important since it demonstrates for the first time that the VVW formalism can be used to accurately predict the opacity of H_2SO_4/CO_2 gaseous mixture over a wide frequency range.

Modeling of the Atmosphere of Venus: A radiative transfer model has been developed in order to investigate the effects of the atmospheric constituents of Venus on its MMW emission. Such constituents include gaseous SO_2, liquid sulfuric acid (cloud condensates), and gaseous H_2SO_4.

Sensitivity to Liquid H_2SO_4: Results from the radiative transfer model indicate that liquid H_2SO_4 does indeed affect the brightness temperature of Venus at millimeter wavelengths [3]. For instance, at 112 GHz a decrease in brightness temperature of 2 K is obtained for a uniform cloud layer between 48 and 50 km where droplets sizes of 25 μm and a bulk density of 50 mg/m³ are assumed. However, this decrease in brightness temperature is much less than the reported variation in the emission of Venus, which indicates that variations in the abundance of liquid H_2SO_4 are not the major source of the observed brightness temperature variation.

Sensitivity of SO_2: The effects of gaseous SO_2 on the computed MMW emission of Venus are well described in Fahd and Steffes [2]. Using an abundance profile of 62 ppm below an altitude of 48 km, we have found that the brightness temperature is decreased by approximately 5 K. Although this decrease is significant, it cannot completely account for the measured variation in emission.

Sensitivity to Gaseous H_2SO_4: Using the developed model for the absorption of gaseous H_2SO_4 in a CO_2 atmosphere, we have found that this gaseous mixture seems to have the biggest effect on the calculated brightness temperature of Venus. Specifically, at 112 GHz, a drop of 14 K is observed assuming an H_2SO_4 (g) abundance of 25 ppm between 48 and 38 km. This decrease in brightness

temperature is quite significant compared with the effects of gaseous SO_2 and liquid H_2SO_4. Thus, we can state that the variations observed by de Pater et al. [1] are most likely due to the variations in the abundance of gaseous H_2SO_4 and not to liquid H_2SO_4 or gaseous sulfuric dioxide as previously suggested.

A plot of the calculated millimeter-wave spectrum of Venus based on the presence of one or more constituents is shown in Fig. 5. The results reported in this figure show the effect that H_2SO_4 (g) has on the MMW spectrum of Venus. In addition, the results show that there are specific millimeter-wave frequencies that are especially sensitive to the abundance of H_2SO_4 vapor in the lower atmosphere of Venus.

References: [1] de Pater I. et al. (1991) *Icarus, 90,* 282–298. [2] Fahd A. K. and Steffes P. G. (1992) *Icarus,* in press. [3] Fahd A. K. and Steffes P. G. (1991) *JGR, 96,* 17471–17476. [4] Steffes P. G. (1985) *Icarus, 64,* 576–585.

N93-14316

RADAR SCATTERING PROPERTIES OF PANCAKELIKE DOMES ON VENUS.

P. G. Ford and G. H. Pettengill, Center for Space Research, Massachusetts Institute of Technology, Cambridge MA 02139, USA.

Magellan radar images have disclosed the presence of a large number of almost perfectly circular domes, presumably of volcanic origin, in many regions of Venus [1], several with diameters of 30 km or more. Their high degree of symmetry has permitted measurements of their shape, as determined by the Magellan altimeter [2], to be compared with models of dome production from the eruption of high-viscosity magmas [3].

In this work, we examine in detail the radar images of domes in Rusalka Planitia (2.8°S, 150.9°E) and Tinatin Planitia (12.2°N, 7.5°E), selected for their circular symmetry and apparent absence of modification due to large-scale slumping or tectonic rifting. Assuming that these domes are shaped according to the model of reference [3], we can orthorectify the available Magellan SAR image swaths (F-BIDRs: Full-Resolution Basic Image Data Records) to generate three-dimensional plots of the radar scattering cross-section σ_0 (r, θ, ϕ) as a function of distance from center of dome (r), scattering angle (θ), and azimuthal coordinate (ϕ).
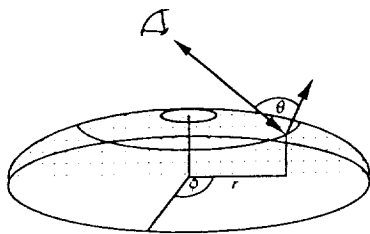
The behavior of σ_0 with respect to changes in θ has been determined from Pioneer Venus radar data for many broad classes of Venus surface type [4], and parameterized as a combination of a quasispecular scattering component σ_{qs} and a diffuse component σ_d:

$$\sigma_0(\theta) = \sigma_{qs}(\theta) + \sigma_d(\theta) =$$

$$\frac{\alpha C\rho}{2}(\cos^4\theta + C\sin^2\theta)^{-3/2} + (1-\alpha)\rho K\theta^\nu$$

where α represents the fraction of the surface that contributes to

quasispecular scattering, C is the Hagfors parameter [5], ρ is the Fresnel reflection coefficient, and K and ν are functions of small-scale surface roughness. Average values of C, ρ, and α over an entire dome are extracted from altimeter measurements.

Variations of σ_0 with respect to radial distance r are interpreted as changes in the small-scale roughness of the dome, which would be expected from the radial dependence of the cooling rate of the lava, perhaps enhanced by subsequent weathering. The result of aeolian processes may also be seen in the dependence of σ_0 on azimuth angle ϕ, since fine-grained surface material that contributes to σ_d may be emplaced or rearranged by the prevailing surface winds.

References: [1] Head J. W. et al. (1991) *Science, 252,* 276–288. [2] Ford P. G. and Pettengill G. H. (1992) *JGR,* in press. [3] McKenzie D. et al. (1992) *JGR,* in press. [4] Ford P. G. and Senske D. A. (1990) *GRL, 17,* 1361. [5] Hagfors T. (1970) *Radio Sci., 5,* 189.

N93-14317

SEQUENTIAL DEFORMATION OF PLAINS ALONG TESSERA BOUNDARIES ON VENUS: EVIDENCE FROM ALPHA REGIO.

M. S. Gilmore and J. W. Head, Department of Geological Sciences, Brown University, Providence RI 02912, USA.

Tesserae are regions of elevated terrain characterized by two or more sets of ridges and grooves that intersect orthogonally [1]. Tesserae comprise 15–20% of the surface of Venus, but the nature of their formation and evolution is not well understood; processes proposed to account for their characteristics are many and varied [2]. Two types of tessera boundaries have been described: Type I are generally embayed by plains; type II boundaries are characterized by being linear at the 100-km scale and often associated with steep scarps or tectonic features [2,3]. Margins such as the western edge of Alpha have been described by these authors as type II. Some of the tessera have boundaries that display deformation of both the edge of the tessera and the adjoining plains [2,3]. This study focuses on the western edge of Alpha Regio in an effort to characterize one occurrence of this type of boundary and assess the implications for the style in general. Using Magellan SAR imagery, lineament lengths, orientations, and spacings were measured for ten 50 × 60-km areas spanning 500 km of the western boundary. Structural characteristics and orientations were compared to stratigraphic units in order to assess the sequence and style of deformation.

Alpha Regio is a 1300 × 1500-km prominent radar-bright upland feature in the southern hemisphere of Venus that averages 1 km above the surrounding plains [4]. Ridges and troughs within Alpha average 33 km long 20 km apart in the north and 35 km long 17 km apart in the south; their prominent orientation is N20°E [4]. The ridges and troughs on the western edge of Alpha have an orientation of N15°E, but differ from the interior ridges as their average spacing is 4 km (Fig. 1). These lineaments are joined by a second set of lineaments and graben trending N55°W and extending into the plains. The deformation producing these northwest-trending lineaments has occurred over a period of time separated by several stages of plains emplacement. Two plains units have embayed the western edge of Alpha: a radar-dark plains unit (Pl$_1$) that embays the edge of the heavily deformed tesserae, and a radar-bright unit to the west that embays the radar-dark unit (Fig. 2). The plains unit closest to the tessera (Pl$_1$) has fewer lineaments than the tessera, but a greater number of lineaments (spaced at an average of 3 km apart) than the younger plains unit (Pl$_2$), which embays and covers unit Pl$_1$. The
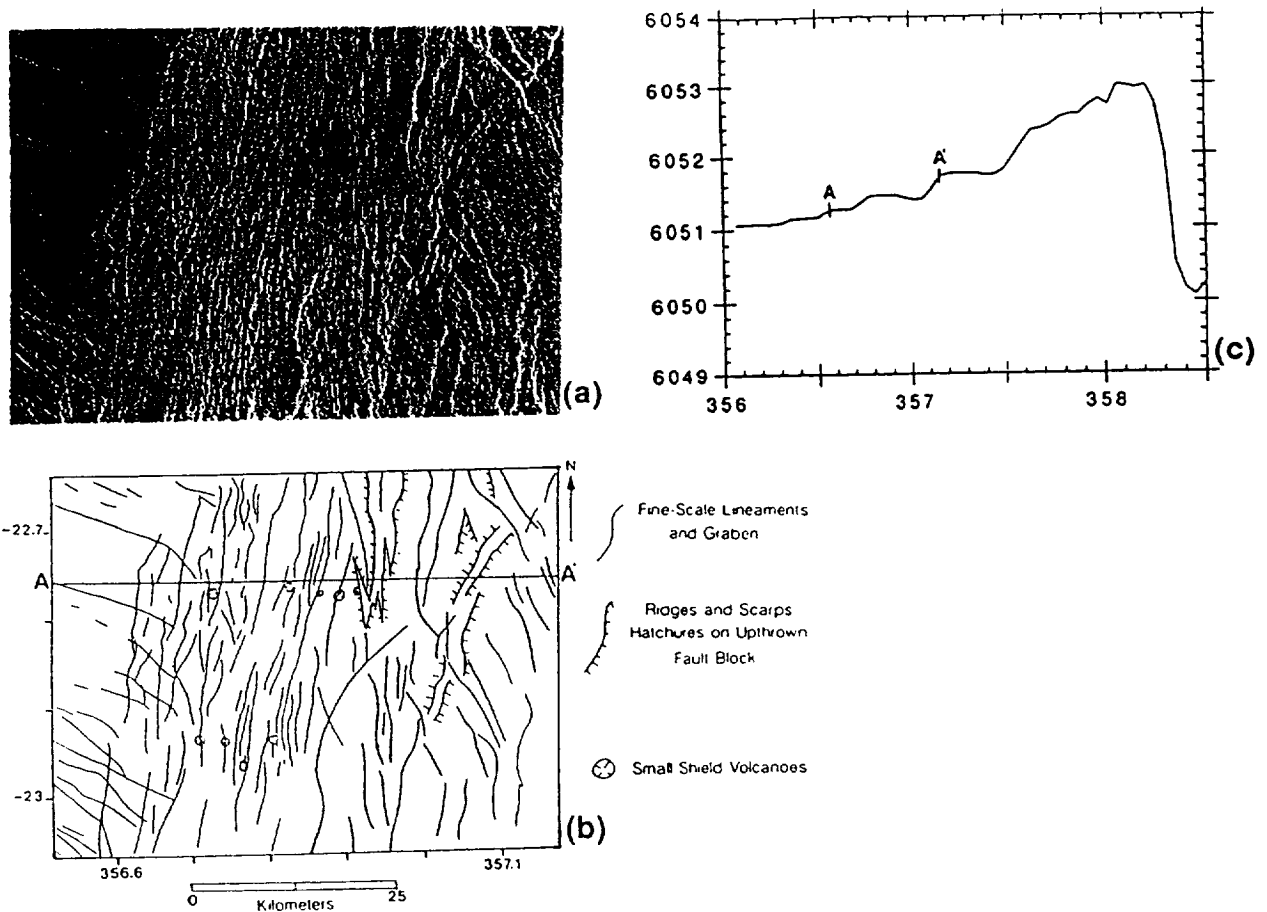
Fig. 1. (a) SAR image of portion of western Alpha Regio including plains, fine-scale lineaments, and ridges and troughs typical of Alpha tessera. The fabric of the fine-scale lineaments clearly differs from the more typical tessera fabric. (b) Sketch map of (a) emphasizing lineaments and volcanic features. Two sets of lineaments are seen here that increase in number from the plains into the fine-scale ridges. The northwest-trending lineaments and shields are confined to the fine-scale fabric. (c) Topographic profile of A-A' in (b).

northern part of Fig. 2 displays some lava flows from Pl$_2$ that were too thin to cover the northwest lineaments. The boundary between the plains units is also marked by a change in slope from 2° in the younger unit to 6°; the slope may then increase to as much as 25° at the plains-tessera border. This is interpreted to mean that the dark plains were emplaced along the margin of the tessera, tilted up, and deformed, followed by the emplacement of the bright plains, which also have been tilted upward and deformed. Deformation features are grabenlike and interpreted to be extensional in origin. The deformation of the plains follows one of the major trends in the tessera interior [4,5].

There is a range of interactions between the northeast- and northwest-trending lineaments; fine-scale ridges and troughs are common within western Alpha while large graben up to 6 km in width occur less frequently. In addition, the tessera along Western Alpha contains numerous domes, pits, and small shield volcanos that both predate (Fig. 1) and postdate the intense tessera deformation. These small shields are very similar to the array of shield volcanos that have been mapped on the Venus plains [6], and we interpret this to mean that these tessera regions are formed from adjacent volcanic plains. In addition, blocks (<100 km in length) of crust that have radar characteristics that make them indistinguishable from undeformed plains are observed in the tessera along the western margin. Each of these characteristics, in addition to the distinct difference in ridge spacing in western Alpha, suggests that western Alpha Regio may consist of plains that are sequentially

deformed, tilted, and uplifted, ultimately being incorporated into the tessera. In addition, it has been proposed that fine-scale ridges like those of Western Alpha are produced by layering thought to exist within the plains [5].

We have considered two models to explain the characteristics of the edge of Western Alpha. The first is mantle downwelling and underthrusting of plains units due to compression at the edge of the tessera block [5,7]. Shortening and isostatic adjustments due to crustal thickening would cause uplift in Alpha and consequently cause deformation and uplift along the margins of Alpha. The second model is one of gravitational relaxation of the Alpha tessera block. Gravitational relaxation of a plateau is expected to produce extensional features within the interior of the crustal block that change to compressional features at the margins of the block [8,5,3]. This is consistent with the presence of relatively young and undeformed intertessera plains in Alpha and the fine-scale compressional features on its western margin. We favor the gravitational relaxation model for these reasons and because it is an ongoing process favored under Venus conditions of high temperatures and low erosion rates [9,10]. This model fails to explain, however, why the deformation seen on the western edge of Alpha does not extend over the entire margin of the tessera block.

In summary, the western border of Alpha Regio has two sets of lineaments that extend into the surrounding plains. This deformation has occurred over a time period marked by at least two sets of plains emplacement. Western Alpha also contains small shield
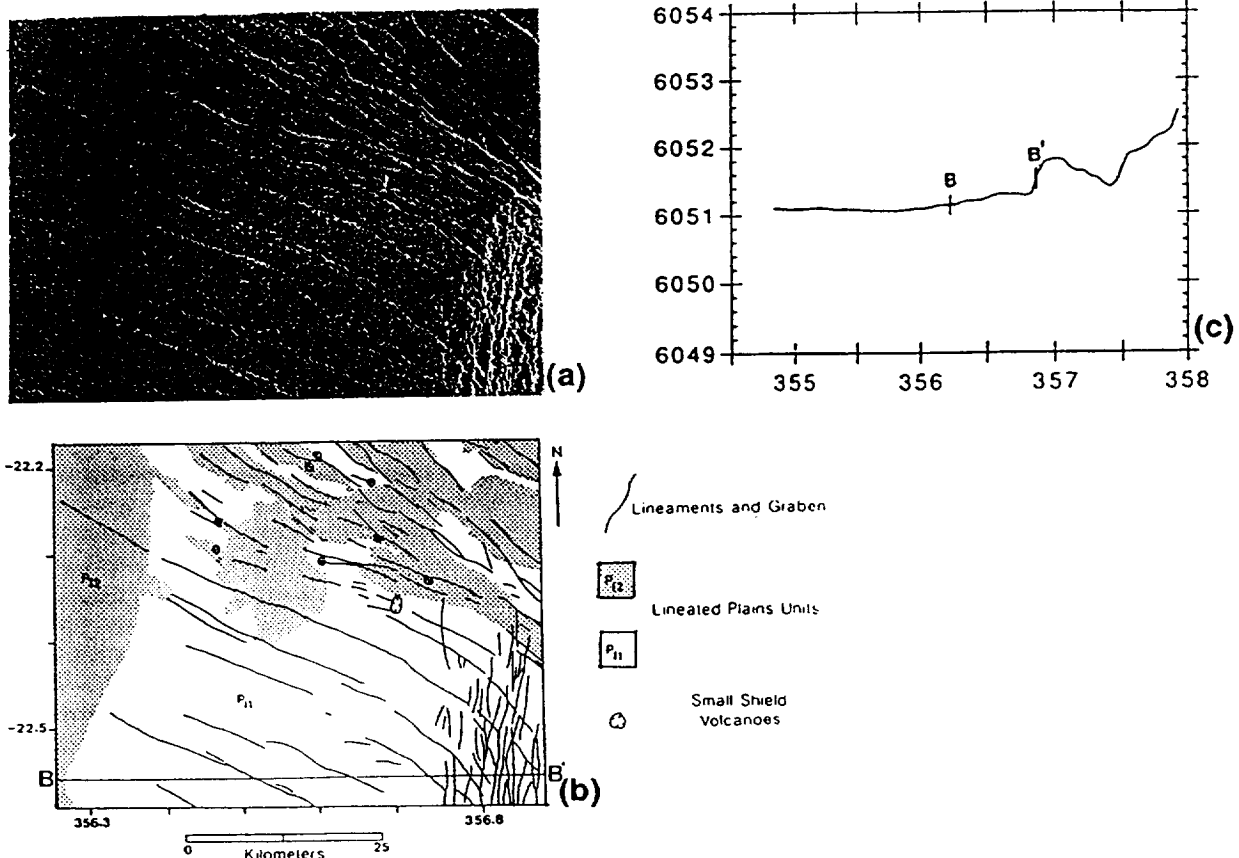
Fig. 2.   (a) SAR image of a portion of western Alpha Regio including two units of plains and fine-scale lineaments. (b) Sketch map of (a) emphasizing the northwest-trending lineaments and graben and volcanos. In general, these lineaments are more abundant and have a closer spacing in the older unit Pl$_1$ than in the younger Pl$_2$. The younger unit has embayed the older, covering most lineaments. Continued deformation has caused fracturing to extend through both units. (c) Topographic profile of B-B' in (b).

volcanos and blocks of undeformed plainslike crust. Each of these features suggests that Alpha is deforming, uplifting, and possibly incorporating plains lavas onto its western edge. Gravitational relaxation of Alpha tessera may be the mechanism producing this deformation and may contribute to the features found at other type II boundaries on Venus. The total length of type II (deformational) boundaries on Venus is less than type I (embayed by plains lavas) boundaries, but type II boundaries occur at some point along many tessera blocks of all sizes [3]. We are continuing our investigation of this and other similar boundaries.

References: [1] Basilevsky A. T. et al. (1986) *Proc. LPSC 16th*, in *JGR*, *91*, D399. [2] Bindschadler D. L. and Head J. W. (1991) *JGR*, *96*, 5889. [3] Ivanov M. A. et al. (1992) *LPSC XXIII*, 581. [4] Senske D. et al. (1991) *Earth Moon Planets*, *55*, 97. [5] Bindschadler D. L. et al. (1992) *JGR*, submitted. [6] Aubele J. et al. (1992) *LPSC XXIII*, 47. [7] Bird P. (1979) *JGR*, *84*, 7561–7571. [8] Bindschadler D. L. and Parmentier E. M. (1990) *JGR*, *95*, 21329. [9] Weertman J. (1979) *PEPI*, *19*, 197. [10] Smrekar S. E. and Solomon S. C. (1992) *JGR*, in press.

N93-14318

VENUSIAN HYDROLOGY: STEADY STATE RECONSIDERED.
David H. Grinspoon, Laboratory for Atmospheric and Space Physics, University of Colorado, Boulder CO 80309, USA.

In 1987 Grinspoon proposed that the data on hydrogen abundance, isotopic composition, and escape rate were consistent with the hypothesis that water on Venus might be in steady state rather than monotonic decline since the dawn of time [1,2,3]. This conclusion was partially based on a derived water lifetime against nonthermal escape of approximately 10^8 yr. De Bergh et al. [4], preferring the earlier Pioneer Venus value of 200 ppm water to the significantly lower value detected by Bezard et al. [5], found H$_2$O lifetimes of >10^9 yr. Donahue and Hodges [6] derived H$_2$O lifetimes of 0.4–5 × 10^9 yr. Both these analyses used estimates of H escape flux between 0.4 × 10^7 and 1 × 10^7 cm^{-2} s^{-1} from Rodriguez et al. [7]. Yet in more recent Monte Carlo modeling Hodges and Tinsley [8] found an escape flux due to charge exchange with hot H$^+$ of 2.8 × 10^7 cm^{-2} s^{-1}. McElroy et al. [9] estimated an escape flux of 8 × 10^6 cm^{-2} s^{-1} from collisions with hot O produced by dissociative recombination of O$_2^+$. Brace et al. [10] estimated an escape flux of 5 × 10^6 cm^{-2} s^{-1} from ion escape from the ionotail of Venus. The combined estimated escape flux from all these processes is approximately 4 × 10^7 cm^{-2} s^{-1}. The most sophisticated analysis to date of near–IR radiation from Venus' nightside reveals a water mixing ratio of approximately 30 ppm [11], suggesting a lifetime against escape for water of less than 10^8 yr. Large uncertainties remain in these quantities, yet the data point toward a steady state. Further evaluation of these uncertainties, and new evolutionary modeling incorporating estimates of the outgassing rate from post-Magellan estimates of the volcanic resurfacing rate, will be presented.

If Comet Halley has a mass of 10^{18} g and is approximately 50% water ice, then impact of such an object provides roughly 10% the current atmospheric water inventory on Venus. The terminal Creta-

ceous impactor on Earth may have been a 10^{19}-g comet [12]. A similar impact on Venus would provide a mass of water roughly equal to the current inventory. The occasional impact of such large comets and more frequent encounters with smaller volatile-rich objects will produce a spectrum of stochastic variations in water abundance [3]. Thus our evolutionary extrapolations that assume that the current H abundance and escape flux are representative of the overall history of the planet must be stated with the humility required by knowledge of our temporally parochial vantage point.

References: [1] Grinspoon D. H. (1987) *Science, 238,* 1702–1704. [2] Grinspoon D. H. (1988) Ph.D. thesis, University of Arizona, Tucson. [3] Grinspoon D. H. and Lewis J. S. (1988) *Icarus,* 74, 21–35. [4] de Bergh C. et al. (1991) *Science, 251,* 547–549. [5] Bezard B. et al. (1990) *Nature, 345,* 508–511. [6] Donahue T. M. and Hodges R. R. (1992) *JGR, 97,* 6083–6091. [7] Rodriguez J. M. et al. (1984) *Planet. Space Sci., 32,* 1235–1255. [8] Hodges R. R. and Tinsley B. (1986) *JGR, 91,* 13649–13658. [9] McElroy M. B. et al. (1982) *Science, 215,* 1614–1615. [10] Brace L. H. et al. (1987) *JGR, 92,* 15–26. [11] Pollack J. B. et al. (1992) *Icarus,* submitted. [12] Lewis J. S. et al. (1982) *GSA Spec. Pap. 190,* 215.

N93-14319

DETERMINING STRESS STATES USING DIKE SWARMS: THE LAUMA DORSA EXAMPLE.

Eric B. Grosfils and James W. Head, Department of Geological Sciences, Brown University, Providence RI 02912, USA.

Introduction: Initial examination of the Magellan coverage of Venus has revealed between 150 and 300 large, radially lineated landforms distributed across the planet's surface [1,2]. Where the lineaments have been examined in detail, the majority fail to exhibit signatures indicative of relief at or above the resolution of the radar; however, when the sense of topographic relief may be ascertained, the lineaments commonly appear as fissures or flat-floored trenches interpreted as graben. Individual lineaments can display graben, fissure, and zero relief behavior along their length, suggesting either that these differences are a function of the resolution of the radar, or that the morphological distinctions are real but somehow genetically linked. In many instances, radial lineaments exhibiting these characteristics are directly associated with surface volcanism, including flanking and terminal flows, superimposed shield domes and pit chains, and central, calderalike topographic lows. These observable characteristics, as well as theoretical studies and comparison with similar terrestrial features, have led to the working hypothesis that many of the radial fracture systems on Venus are the surface manifestation of subsurface dikes propagating laterally from a central magma source [3–7]. If this interpretation is correct, studies of terrestrial dikes suggest that the lineament directions, with localized exceptions and barring subsequent deformation, should be perpendicular to the orientation of the least compressive stress at the time of their formation [8–11]. To test this hypothesis, we briefly examine a radial fracture system (63.7°N, 195°E) located between two deformation belts in Vinmara Planitia, and verify that the lineaments to the east behave in the expected manner. We have also chosen this feature, however, because of its proximity to Lauma Dorsa to the west. On the basis of Venera 15/16 data, both compressional and extensional origins for this deformation belt have been proposed [12,13]. By examining the stratigraphy and applying our interpretation that the fracture system is linked to the presence of subsurface dikes, we present an independent evaluation of the stress

state associated with Lauma Dorsa, and thus contribute to the assessment of its origin.

Test of the Dike Hypothesis: Vinmara Planitia is a section of flat, deformation belt-bounded lowlands a few hundred meters below the mean planetary radius of 6051.84 km [14]. Bounding the plains to the east is a tessera belt trending north to south, roughly 75 km wide and slightly concave west in plan view. Although sections of the belt approach the altitude of the surrounding lowlands, most of the belt is elevated from a few hundred meters to as much as 1500 m above the level of the plains. At a finer scale, the tessera is characterized by long, narrow ridges as well as fissures at the crest indicative of gravitational collapse, all striking parallel to the local trend of the belt. Both the fine-scale and regional morphology are consistent with the general interpretation that ridge belts form in compression rather than extension, in this case implying an east-west compressive field [15–17].

Superimposed on the plains is a fracture system extending radially outward up to 450 km from a centrally located circular depression some 50 km in diameter. The depression is bounded by concentric graben and is interpreted as a caldera, perhaps associated with magma withdrawal from a central storage region. The lineaments exhibit the negative relief associated with dikes, as well as rare examples of shield domes and pit chains superimposed upon individual lineaments. Terminal and flanking flows are not observed; however, closely spaced parallel fractures and en echelon behavior, both characteristic of terrestrial near-surface dike emplacement, are present [18]. These latter features imply a component of vertical propagation in addition to the dominant lateral sense, suggesting dike top depth variations caused by either small-scale topography or changes in driving pressure and temporal supply rate [19].

To the east the fracture system displays lineaments that vary smoothly from radial orientations near the central depression to strikes that are perpendicular to the plains-tessera contact along the edge of the concave west border. While this behavior is exemplified to the northeast, it also occurs to the southeast. If the lineaments are dikes, this suggests they were emplaced in an east-west compressive regime. This conclusion is in agreement with the stress state inferred to have formed the tessera belt, and thus supports the hypothesis that dikes form perpendicular to the direction of least compressive stress.

Application to Lauma Dorsa: To the west of the radial fracture system is Lauma Dorsa, a north-south trending diffuse ridge belt that extends up to 300 km in width. While the topography varies along its length, Lauma Dorsa coincides with a long linear depression ranging from a few hundred meters up to 2000 m in depth. While some contend that the coincidence of the depression and belt argue for formation in an extensive regime [12], others maintain that the observations are better explained by a compressional origin, invoking underthrusting or subduction to explain the depressed topography [13]. Examination of the radial lineaments striking westward from the central caldera may provide an independent means of testing these hypotheses.

To the northwest of the caldera, the radial lineaments appear to curve beneath the ridge belt, striking northwest, and then reappear further north, striking to the northeast. The interpretation of this "buried" set of lineaments is based strongly upon observations of adjacent lineaments that do not curve beneath the edge of the ridge belt. These leave the caldera region radial to the center, parallel to those further west that then vanish at the edge of the ridge belt, then
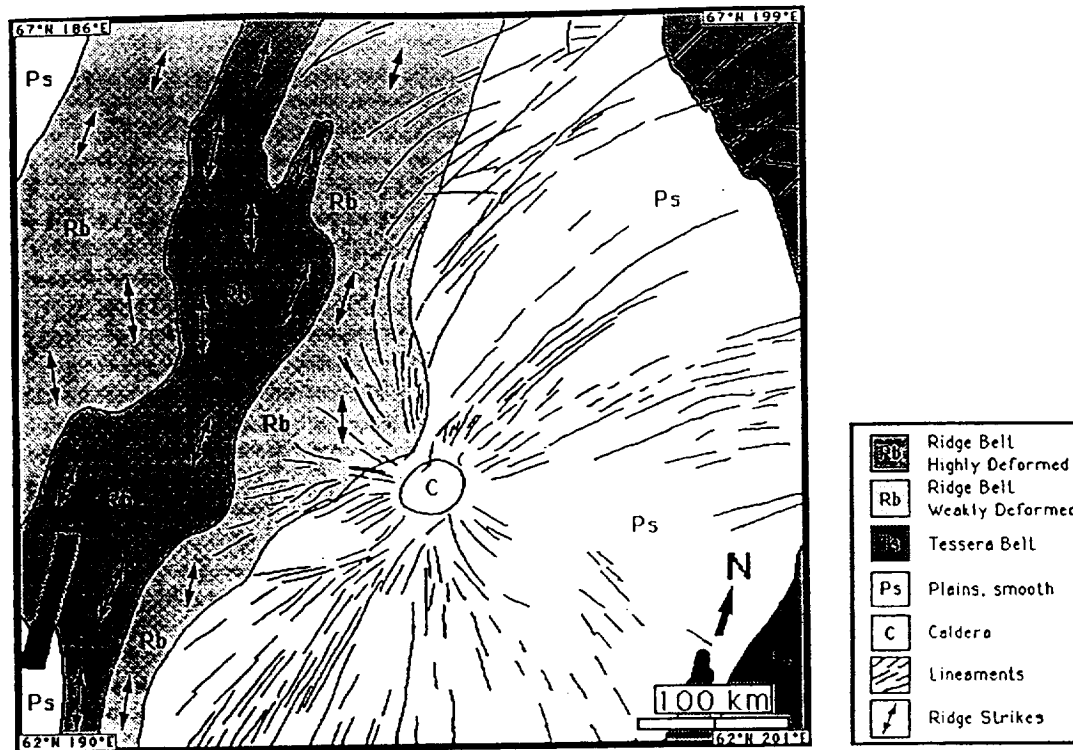
Fig. 1. Arachnoid in Vinmara Planitia. The lineaments shown include graben, fissures, and fractures. Note the right-angle intersection with the adjacent tessera belt, as well as the unusual behavior to the northwest of the caldera. For details, see text.

arc back toward the northeast, assuming the same strike as those lineaments that "reemerge" from beneath Lauma Dorsa. It is not clear from the stratigraphic relations in this region whether the radial lineament set is older and has been disrupted by formation of the ridge belt, or whether the two formed contemporaneously.

Due west of the caldera the stratigraphic relationships are clearer. Radial lineaments both crosscut and are deformed by large antiform structures associated with the ridge belt. This implies that the belt and radial fracture system formed at roughly the same time, and therefore presumably under the same regional stress conditions. If this is so then a number of factors suggest that the region was not undergoing east-west extension during rift formation. First, if one can assume that all the lineaments formed in a geologically brief interval, then the proposed dikes to the east are unlikely to have formed under east-west extension. Second, the curvature to the northwest is inconsistent with extensional rifting, since this regime offers no incentive for the dikes to deviate from a rift-parallel path. Finally, like those to the east, the orientation of the lineaments due west of the caldera is not consistent with east-west extension. As a complication, dikes southwest of the caldera strike predominantly parallel to the ridge belt along a topographic bulge. This type of behavior is consistent with formation during east-west extension, and the lack of relative stratigraphic markers does not allow us to rule out this option. Another possible interpretation, however, is that the dikes propagate along the crest of a flexural bulge produced by compression, with the near-surface stress in the upper half of a bending elastic plate favoring an orientation parallel to the antiform [20].

Conclusion: Many radial lineament patterns are interpreted as the surface manifestation of laterally propagating subsurface dikes. The stress state implied by one of these structures, located in

Vinmara Planitia, is consistent with the surrounding geology, supporting the contention that this fracture system is analogous to a radial terrestrial dike swarm. By using this information, additional insight is gained into the origin of Lauma Dorsa. While examination of the dikes to either northwest, west, or southwest of the central caldera alone can be ambiguous, behavior of the radial system as a whole offers firmer insight into the stress state associated with formation of Lauma Dorsa, suggesting that the belt is associated with regional shortening rather than an extensive regime.

References: [1] Grosfils E. B. and Head J. W. (1992) *LPSC XXIII*, 457–458. [2] Parfitt E. A. and Head J. W. (1992) *LPSC XXIII*, 1029–1030. [3] Grosfils E. B. and Head J. W. (1991) *LPSC XXII*, 499–500. [4] Head J. W. et al. (1991) *Science, 252*, 276–288. [5] Head J. W. and Wilson L. (1992) *JGR, 97*, 3877–3903. [6] McKenzie D. et al. (1992) *JGR*, in press. [7] Parfitt E. A. and Head J. W. (1992) *JGR*, in press. [8] Ode H. (1957) *Bull. GSA, 68*, 567–576. [9] Muller O. H. and Pollard D. D. (1977) *Pageoph, 115*, 69–86. [10] Pollard D. D. (1987) *Geol. Assoc. Can. Spec. Pap., 34*, 5–24. [11] Rubin A. M. and Pollard D. D. (1987) *U.S. Geol. Surv. Prof. Pap., 1350*, 1449–1470. [12] Sukhanov A. L. and Pronin A. A. (1989) *Proc. LPSC 19th*, 335–348. [13] Frank S. L. and Head J. W. (1990) *Earth Moon Planets, 50/51*, 421–470. [14] Ford P. G. and Pettengill G. H. (1992) *JGR*, in press. [15] Basilevsky A. T. et al. (1988) *Proc. LPSC 16th*, in *JGR, 93*, 13221–13235. [16] Solomon S. C. et al. (1991) *Science, 252*, 297–312. [17] Squyres S. W. et al. (1992) *JGR*, in press. [18] Mastin L. G. and Pollard D. D. (1988) *JGR, 93*, 13221–13235. [19] Ryan M. P. (1987) In *Magmatic Processes: Physiochemical Principles* (B. O. Mysen, ed.), 259–287, Geochemical Society, University Park, PA. [20] Turcotte D. L. and Schubert G. (1982) *Geodynamics*, Wiley, New York, 450 pp.

N93-14320

VENUS MESOSPHERIC WINDS AND THE CARBON MONOXIDE BULGE.

Mark A. Gurwell[1], Duane O. Muhleman[1], and Kathryn Pierce Shah[2], [1]California Institute of Technology, Mail Stop 170-25, Pasadena CA 91125, USA, [2]Goddard Institute for Space Studies, New York NY, USA.

One of the most striking features of Venus is the superrotation of the atmosphere with a period of about 4 days, compared to the solid-body rotation period of 243 days. The winds were discovered by B. A. Smith [1] in 1967 from changes of the ultraviolet markings. The mid- and lower-latitudinal zonal winds have been directly measured by radio tracking of the Pioneer entry probes from about 65 km altitude down to the surface and by radio tracking of the Vega balloon, which floated at about 55 km. The measured winds reach a maximum speed of about 100 m/s at 65 km [2] and values above that, until recently, have been basically theoretical. In 1985, Clancy and Muhleman [3] interpreted their microwave spectral line observations of CO in the Venus mesosphere (roughly 70 to 110 km in altitude) as evidence for the continuation of the zonal winds to at least 100 km, the altitude of their experimental weighting functions. They showed, using planet-averaged measurements of the CO absorption line, that the abundance had a maximum (or "bulge") a few hours after local midnight. Pioneer Venus *in situ* mass spectrometer measurements [4] made at about 160 km had found a similar postmidnight bulge in helium but the abundances of the other species (including O, N_2, CO, and CO_2) appeared to be symmetrically distributed around the antisolar point in the thermosphere.

Recently, our group [5] mapped the CO absorption lines on the disk of Venus in 1988 using the synthetic aperture array at the Owens Valley Radio Observatory. Observations were made in the (0–1) rotational transition of CO at 115 GHz, or a wavelength of 2.6 mm. Systematic variations in the doppler shifts of the lines (particularly near the limbs) enable the group to directly map the wind field at 100 ± 10 km, the peak altitude for the experimental weighting functions used. These measurements show that the winds are indeed of order 100 m/s at this altitude. Previously, many had assumed that the vertical wind profile would quickly fall to zero above the cloud tops, due to cyclostrophic breakdown. This work is reviewed in this talk.
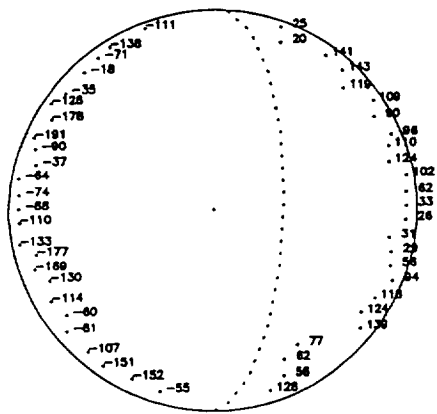
Fig. 1. Wind speeds (in m/s) near the limb of Venus in 1988 at 100 ± 10 km found from doppler shifts in CO line cores, corrected for incidence angle. Positive speeds represent winds approaching sub-Earth longitude and negative speeds winds receding. Dotted line represents the evening terminator.
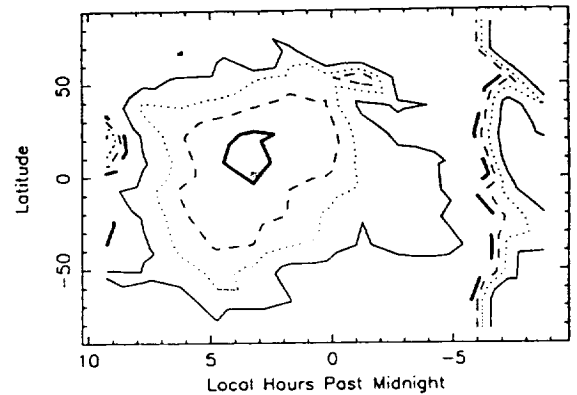
Fig. 2. The mixing ratio of CO at 96.5 km found from inversion of (0–1) rotational spectra. The map is a synthesis of data from 1986 (morning terminator) and 1988 (evening terminator) observations. The thick solid contour stands for a mixing ratio of 10^{-3} and the thick dashed contour stands for 10^{-4}. Intermediate contours for the night (–6 to 8.5 local hours) are 7×10^{-4} (thin dashed), 5×10^{-4} (dotted), and 3×10^{-4} (thin solid). For the afternoon (–6 to –9 local hours) the same contour styles represent 7×10^{-5}, 5×10^{-5}, and 3×10^{-5} respectively.

The combination of the 1988 measurements, made when the evening terminator was visible from Earth, and 1986 measurements of the disk [6], which observed the morning terminator, has allowed us to map the CO abundance over most of the planet in the altitude range from 80 to 105 km. The abundance map is shown in latitude and local time coordinates in Fig. 2 for an altitude cut at 96.5 ± 1.25 km. The CO bulge is clearly visible centered at 3:30 a.m. and near the equator. Carbon monoxide is produced in the photodissociation of the major atmospheric constituent CO_2 and is cycled back in catalytic reactions involving Cl or possibly OH radicals on the dayside of the planet.

Apparently, the CO molecules are created on the dayside, mostly in the region between 65 and 90 km in altitude, and are then "blown" to the nightside. The abundances of species capable of destroying CO falls off rapidly from the dayside to the nightside, allowing CO to pile up at high altitudes without being destroyed. It was suggested in [3] that this process may be controlled by solar to antisolar winds in the thermosphere ($z \geq 110$ km), an idea that has been developed further by Bougher [7] and his colleagues based on the Dickenson-Ridley thermospheric models. Their three-dimensional model was used to investigate the effects of zonal circulation in the thermosphere, and found that light species (H and He) had maxima displaced 3 to 5 hr LT toward the morning, but that heavier species (CO, O, and CO_2) would be mostly unaffected, leading to symmetric distributions around local midnight at 160 km. Their model assumed that zonal wind speeds near 100 km were essentially zero.

We will present new evidence for superrotating winds in the Venus mesosphere, including the first high-resolution maps of the CO distribution at several altitudes. We argue that the displacement from local midnight toward the morning terminator of the nighttime CO bulge is due to mesospheric zonal winds, complementing the CO doppler shift analysis of Shah et al. The sensitivity of our measurements extends to over 100 km, and it seems possible that the winds continue up through at least 160 km, as in the models of Bougher et al. In this case, at some altitude above 110 km but below 155 km the zonal superrotation would somehow cease to affect the CO distribution, and above that CO becomes symmetric around local midnight.

References: [1] Smith B. A. (1967) *Science, 203*, 114–116. [2] Counselman C. C. III et al. (1980) *JGR, 85*, 8026–8030. [3] Clancy R. T. and Muhleman D. O. (1985) *Icarus, 64*, 183–204. [4] Niemann H. B. et al. (1980) *JGR, 85*, 7817–7827. [5] Shah K. et al. (1991) *Icarus, 93*, 96–121. [6] Gurwell M. A. et al., in preparation. [7] Bougher S. W. et al. (1988) *Icarus, 73*, 545–573.

N93-14321

TECTONICS AND VOLCANISM OF EASTERN APHRODITE TERRA: NO SUBDUCTION, NO SPREADING.

Vicki L. Hansen, Myra Keep, Robert R. Herrick, and Roger J. Phillips, Department of Geological Sciences, Southern Methodist University, Dallas TX 75275, USA.

Introduction: Eastern Aphrodite Terra is approximately equal in size to the western North American Cordillera, from Mexico to Alaska. Its size and unique landforms make it an important area for understanding the tectonics of Venus, yet models for its formation are diametrically opposed. This region is part of the Equatorial Highlands, which was proposed as a region of lithospheric thinning, isostatic uplift, and attendant volcanism [1,2]. Head and Crumpler [3] suggested, on the basis of topographic symmetry and proposed cross-strike lineaments interpreted from Pioneer Venus data, that this area represents a zone of crustal divergence, analogous to terrestrial midocean ridges. Using Magellan SAR data, Suppe and Connors [4] proposed that Eastern Aphrodite Terra forms part of a circumglobal rift zone separating two major venusian plates. In contrast, McKenzie et al. [5] interpreted Eastern Aphrodite Terra as a region dominated by crustal shortening and subduction of venusian crust. They argued that structures resembling trenches display the same curvature and topographic asymmetry as terrestrial subduction zones. Sandwell and Schubert [6] modeled the trench and outer rise topography of the rim of Artemis and Latona coronae as a thin elastic plate subjected to a line load with a bending moment beneath the coronae. They calculated elastic thicknesses and bending moments, and used these values together with a yield strength model to estimate lithospheric temperature gradients. They concluded that the amplitudes of the trench and outer rise are too large to be explained by thermal subsidence alone, and they propose a lithospheric subduction model wherein the lithosphere outboard of the corona perimeter subducts as the corona diameter increases [7]. Thus, Eastern Aphrodite Terra has been interpreted as a region analogous to both a terrestrial midocean ridge extensional plate boundary and a terrestrial subduction plate boundary.

Observations: Structural mapping and kinematic interpretation of Magellan SAR imagery of Eastern Aphrodite Terra provide new evidence for the formation of this region. Eastern Aphrodite Terra comprises a band of predominantly circular structures and east-trending fractures that extends from Artemis corona to Atla Regio. The belt is approximately 1500 km wide and greater than 8000 km long. The circular structures vary in diameter from 100 to 2500 km and they fit the description of coronae as described by many workers and summarized by Stofan et al. [8]. The largest circular structure is Artemis corona, although Artemis does not exhibit many of the features discussed here. The curvature of these features generally varies between 180° and 270°, although 360° is preserved locally, particularly in structures of small diameter. The circular structures commonly display both radial and concentric fractures. A single circular structure may have as many as four nested sets of concentric fractures, each separated by a region marked by little or no deformation. Fractures from one structure commonly overlap with those of adjacent structures. The circular structures are the sites of extensive volcanism. Flows emanate from both the center of the structures and

the concentric fractures. Artemis corona is different from adjacent circular features; it is almost three times the size of the next largest feature and it does not show nested concentric fractures, although it has associated volcanism.

Detailed examination of one of these circular features with center at 14°S, 164°E, herein referred to as 14S/164, reveals that the structure is approximately 600 km in diameter, with at least three sets of concentric fractures stepping outward from the center (e.g., 11.5°S, 164°E). Locally, radial fractures <100 km in length form normal to concentric fractures (e.g., 12.5°S, 166.5°E). Lava flows emanate from the center of the circular structures into channels formed by radial fractures. Extensive lava flows also emanate from each set of concentric fractures and flow outward. The central radial flows are radar-dark whereas the youngest flows from the concentric fractures are radar-bright. Radar-dark flows are interpreted as generally less viscous than radar-bright flows because radar-dark regions appear to flood into preexisting fractures and are influenced by local topography, whereas radar-bright flows form lobate structures and define their own boundaries (e.g., 14.5°S, 168°E). The spatial and temporal relations between radar-bright and radar-dark flows may provide evidence for magma differentiation at depth. Examination of the outermost concentric fracture set reveals that radar-dark flows fill a moat outside this concentric fracture set as evidenced by the sharp truncation of earlier cross fractures. Radar-bright flows, ~30 km wide and greater than 100 km long, flow outward from the concentric fracture set. Flows from each of the concentric fracture sets are cross-cut by the next outward concentric fracture set. Therefore, the concentric fracture sets are interpreted to become younger outward, with the youngest fractures farthest from the center of the circular feature.

Radial fractures within the circular features are readily identifiable where flooded by volcanic material from the center of the structure (e.g., 16.5°S, 162.5°E). The radar look direction, as well as structure orientation, must be considered while mapping individual sets of structures and in interpreting the timing relations between structures. For example, north-trending lineaments, oriented perpendicular to the radar look direction, commonly appear dominant, and therefore they may be interpreted as cross-cutting less visible east-trending lineaments (e.g., 17.5°S, 163°E). In this particular circular structure, central radial fractures cut concentric fractures where the radial set is north trending, and lava flows following east-trending radial fractures are not apparently truncated by circular north-trending concentric fractures. We therefore interpret these lava-filled radial fractures as younger than the inner concentric fractures. The presence of lava flows makes these east-trending troughs visible; without the lava fill the east-trending troughs are difficult to see. The temporal relations, radial fractures younger than adjacent concentric fractures, imply that these radial fractures are relatively deep in order to act as lava conduits. It is possible that the central radial fractures and their attendant volcanic flows completely disguise early formed, inner-concentric fracture sets. The presence of volcanic flows in both the center and associated with the outermost concentric fractures indicates that volcanism played an important role in the formation of 14S/164.

East- to east-northeast-trending fractures overprint 14S/164. These fractures belong to a regional fracture set that trends northeast between Latona and Alta Regio, to the east west of Latona, and to the east-northeast west of Dali and Diana Chasmata. The relationship between 14S/164 and Diana and Dali Chasmata is not clear. The two outermost sets of concentric fractures of 14S/164 trend into parallelism with the trough of Diana Chasma, which is itself parallel to the set of regional east-trending fractures. Radar-bright volcanic

flows emanate and flow northward from east-trending fractures parallel to Diana Chasma. Radar-dark flows flooded the region north of Diana Chasma.

The circular structures comprising Eastern Aphrodite Terra are connected by east-northeast-striking fracture sets that dominantly postdate formation of the circular structures, although locally deformation related to the circular structures cross-cuts the regional fractures. The regional fracture set trends parallel to the radar look direction, and therefore the character of the fractures is difficult to distinguish. However, we interpret the regional fractures as troughlike features on the basis of their sharp boundaries and relatively straight and continuous character (i.e., they are not anastomosing). We further interpret these features as regional extensional fractures similar in nature to fractures of the Guor Linea trough region of Eistla Regio [9].

Formation of these structures is consistent with the model for coronae formation outlined by Squyres et al. [10]; however, we are able to document successive outward stepping of the nested concentric fractures with time. Initial circular uplift of the crust, caused by rising and spreading magma, leads to the formation of radial and concentric fractures. With further uplift the crustal welt grows in diameter and new concentric fracture sets are formed. Once the welt reaches a critical diameter, a moat forms around its perimeter, outward from the oldest concentric fracture set. Lava escapes out of the concentric fractures filling the moat. Within 14S/164 flows emanate from the concentric fracture sets with diameters of ~240, 380, and 510 km. Less viscous radar-dark flows may predate the escape of more viscous radar-bright flows, which can be traced back to individual vents. As the structure continues to expand outward the zone of concentric fractures steps outward and the earlier-formed fracture set and moat are uplifted. A new concentric fracture set and moat form. The newly formed concentric fractures deform earlier-formed volcanic flows, and new flows emanate from these new fractures. This process continues until the structure reaches an average diameter of ~600-800 km. The concentric fracture set may not be equally well developed around the entire 360° arc; in fact, structure 14S/164 is developed around an arc of ~270°. We interpret that the circular structures within Eastern Aphrodite Terra formed in a manner similar to that of 14S/164. This model is similar to a model of corona formation by blistering of the lithosphere as a result of the ascent of a magma diapir to the base of the lithosphere [9,10], although the sequence of deformation and volcanism proposed here is different. Magma diapirs rising passively within a region of crustal extension may be responsible for the circular structures that characterize Eastern Aphrodite Terra [e.g., 11].

Subduction and Spreading: Eastern Aphrodite Terra appears to lack the cross-strike discontinuities proposed from Pioneer Venus data. In addition, it lacks crustal or structural symmetry, which might be predicted for a terrestrial-type rift zone. The area is dominated by circular features as opposed to linear features transected by transform faults. The proposed transform fault [5] that joins Diana and Dali Chasmas is comprised of ridges with no apparent strike-slip or noncoaxial shear component preserved across the belt. In addition, the ridge zone appears to curve into parallelism with east-striking fractures in both Diana and Dali Chasmas; further, the orientation of the ridge belt with respect to the proposed extension troughs (Diana and Dali Chasmata) is kinematically infeasible to be a transform structure.

If Diana and Dali Chasmata are subduction zones as proposed [5], the presence of the radar-bright flows is puzzling as the region north of Diana Chasma should be a subducting lower plate. In addition, a subduction scenario requires a structural distinction

between upper and lower plates. However, radial fractures from the center of Latona can be traced through and across its southern boundary (e.g., 21°S, 167.7°E). The continuity of structures across the trough also argues against the interpretation of this trough as a subduction zone [i.e., 5–7]. Furthermore, terrestrial subduction zones are <180°, and generally <120° along their arc, whereas these circular structures are often preserved up to 270°, and locally up to 360°. Subduction along >180° is kinematically difficult; subduction along 270° is even more difficult. In addition, the diameters of the circular features within this region are much smaller than subduction zones on Earth. Artemis, the largest of the circular structures in this region, is equivalent in size to the Sandwich Islands subduction system [5–7], one of the smallest terrestrial subduction zones. Therefore, we believe that Eastern Aphrodite Terra does not represent a zone of major lithospheric spreading, nor does it represent a region of terrestrial-like subduction. Rather, detailed analysis of SAR imagery indicates that Eastern Aphrodite Terra may be the result of rising magma diapirs that blister the surface within a zone of lithospheric tension.

In conclusion, Eastern Aphrodite Terra is dominated by circular structures within which deformation and volcanism are intimately related. These structures are marked by radial and concentric fractures, and volcanic flows that emanate from a central vent, as well as from concentric fracture sets. Cross-cutting relations between flows and concentric fracture sets indicate that outer concentric fractures sets are younger than inner fractures sets. The circular structures are joined by regional northeast- to east-trending fractures that dominantly postdate formation of the circular structures. We propose that the circular structures "grow" outward with time. Although these structures probably represent addition of crust to the lithosphere, they do not represent significant lithospheric spreading or convergence, and the region does not mark the boundary between two distinct tectonic plates. This region is not easily explained by analogy with either terrestrial midocean rifts or subduction zones. It is perhaps best explained by upwelling of magma diapirs that blister the surface, but do not cause significant lithospheric spreading [1]. Further study of the structural and volcanic evolution of this region using Magellan altimetry and SAR data should lead to better understanding of the tectonic evolution of this region.

References: [1] Phillips R. J. and Malin M. C. (1983) *Venus,* 159–214. [2] Phillips R. J. and Malin M. C. (1984) *Annu. Rev. Earth Planet Sci.,* 411–413. [3] Head J. W. and Crumpler L. S. (1987) *Science,* 1380–1385. [4] Suppe J. and Connors C. (1992) *LPSC XXIII,* 1389–1390. [5] McKenzie D. et al. (1992) *JGR,* in press. [6] Sandwell D. T. and Schubert G. (1992) *JGR,* in press. [7] Schubert and Sandwell (1992) *Science,* submitted. [8] Stofan E. R. et al. (1992) *JGR,* in press. [9] Grimm and Phillips (1992) *JGR,* in press. [9] Stofan E. R. and Head J. W. (1990) *Icarus,* 216–243. [10] Squyres S. W. et al. (1992) *JGR,* in press. [11] Tackely and Stevenson (1991) *Eos, 72,* 287.

N93-14322

WESTERN APHRODITE TERRA, TECTONICS, GEOLOGY, AND LINE-OF-SIGHT GRAVITY. John E. Hays and Paul Morgan, Department of Geology, Box 6030, Northern Arizona University, Flagstaff AZ 86011–6030, USA.

Aphrodite Terra is the largest area of high-standing topography on Venus, and isostatic considerations strongly suggest that this high topography is supported at least in part by thickened crust [1]. Previous studies of line-of-sight gravity data from the Pioneer Venus orbiter indicate rapidly changing apparent depths of compen-
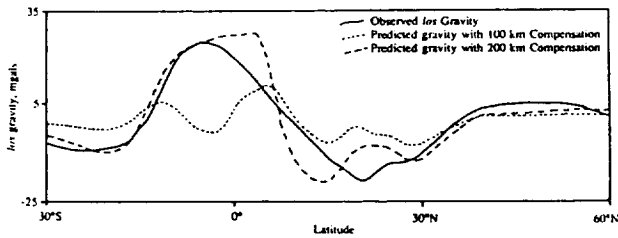
Fig. 1. Observed and predicted line-of-sight (los) gravity as a function of latitude for orbit 440 of the Pioneer Venus orbiter [from 4]. Line extends from approximately 30°S, 77°E to 60°N, 122°E, and the location of the southern portion of the line with respect to the region mapped from Magellan data is shown on Fig. 2. Predicted gravity values were computed using ORBSIM, an orbital simulation program [5], assuming perfect isostatic compensation of topography with compensation masses at 100 and 200 km, as indicated.

sation across Aphrodite Terra as shown in Fig. 1 [2–4]. Magellan imaging data provide the first detailed images of this region, and we are mapping the region along Pioneer Venus orbit 440 to investigate whether the changing apparent depths of compensation correlate with changes in surficial tectonics.

We have commenced our mapping effort at the southern end of Pioneer Venus orbit 440, where the gravity modeling indicates good agreement among the observed los gravity and los gravity predicted with a 200-km apparent depth of compensation, but less agreement with los gravity predicted for a shallower depth of compensation. We have mapped three C1 radar images (C1-MIDRP.15S095;1, C1-MIDRP.15S077;1, and C1-MIDRP.30S081;1) at a scale of approximately 4,000,000:1, and these maps are summarized in Fig. 2. Along the portion of Pioneer Venus orbit 440 covered by these images, surface features include a major corona in relatively smooth lowland plains to the south of Aphrodite Terra at an elevation of about –1 km relative to mean planetary radius (mpr), and the steep rise to the axis of Aphrodite Terra in tessera and tectonized terrain at elevations up to 4 km above mpr. In this region, the terrains and the topography appear to be relatively well correlated, but the large apparent depth of compensation (200 km, Fig. 1) suggests that this correlation may be fortuitous. The gravity data suggest that the primary compensation of western Aphrodite Terra is in the mantle, and may not be directly linked to crustal thickness variations associated with surficial tectonics.

Immediately to the north of the area covered by the map in Fig. 2 there is very poor correlation among the observed and predicted los gravity data for apparent compensation depths of either 100 or
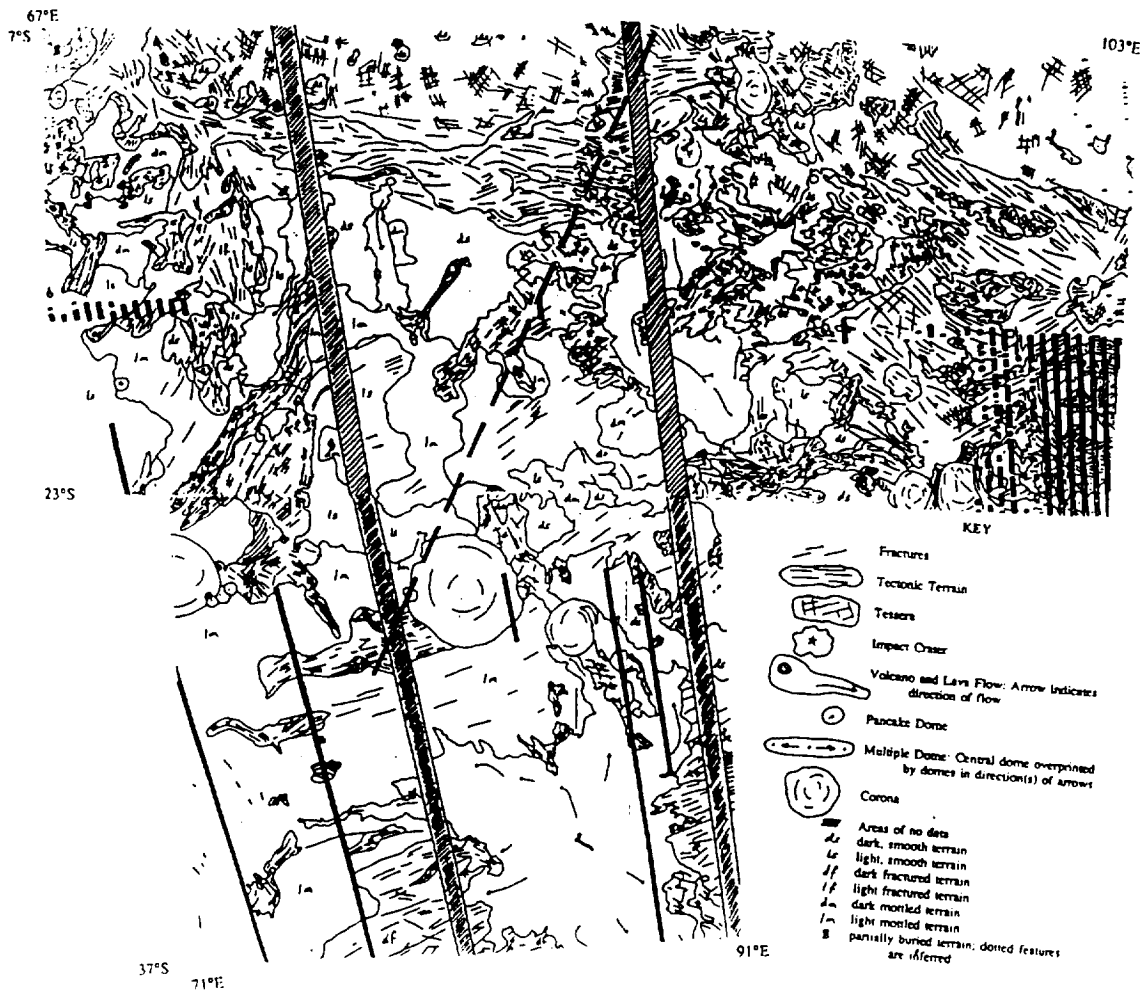
Fig. 2. Sketch map of the geological features of a region of southern, western Aphrodite Terra covered by Magellan images C1-MIDRP.15S095;1, C1-MIDRP.15S077;1, and C1-MIDRP.30S081;1. Mapped area is approximately 3600 km in longitude and 3100 km in latitude. Dashed line shows the approximate location of the southern end of useful los gravity data available from orbit 440 of the Pioneer Venus orbiter.

200 km. The apparent depth of compensation appears to shallow from about 200 km at 7°S to close to 100 km at about 10°N. Preliminary mapping of this region (image C1-MIDRP.00N095;1) indicates complex terrain, dominated by tessera, and represents the northern slope of Aphrodite Terra where elevations drop to around mpr or lower. We interpret this region to be a zone of rapidly changing crustal thickness, resulting in a relatively shallow apparent depth of compensation. Five impact craters have been mapped in this region, perhaps suggesting that this may be a region of relatively old crust.

At approximately 20°N, the observed and predicted los gravity anomalies are roughly anticorrelated, a low in the observed gravity corresponding to highs in the predicted gravity for compensation depths of both 100 and 200 km. Much of this region is below an elevation of −1 km relative to mpr, and the relatively dense subsurface predicted by the isostatic models is clearly in error. Subsurface densities appear to be less dense than expected in this region, suggesting flexural or more likely dynamic control of this low topography. Coronae and fractured volcanic features dominate this region.

From approximately 30°N to 60°N the observed and predicted los gravity anomalies are in reasonable agreement, and there is clearly little resolution of the apparent depths of compensation in this region as there is little difference among the anomalies predicted for 100- and 200-km compensation depths. This region is mostly lowland plains at an elevation of −0.5 ± 0.5 km relative to mpr. Major terrain differences between this region and the region immediately to the south, where observed and predicted gravity are very poorly correlated, are not readily apparent in the Magellan images.

Preliminary mapping of geological features on Magellan images along the path of Pioneer Venus orbit 440 do not indicate a first-order correlation among surface features and changes in the apparent depth of compensation of los gravity data. The apparent depth of compensation appears to be most variable in regions dominated by tessera, but not all areas of tessera have distinct gravity signatures. There is a weak correlation among areas in which impact craters are relatively common and areas in which the observed and predicted gravity anomalies are poorly correlated.

References: [1] Morgan P. and Phillips R. J. (1983) *JGR, 88*, 8305–8317. [2] Morgan P. and Reagan M. T. (1985) *LPSC XVI*, 577–578. [3] Reagan M. T. (1986) *Eos, 67*, 299–300. [4] Reagan M. T. (1987) M.S. thesis, Purdue University, West Lafayette, IN, 108 pp. [5] Phillips R. J. et al. (1978) *JGR, 83*, 5455–5464.

N93-14323

VENUS VOLCANISM: A GLOBAL OVERVIEW FROM MAGELLAN DATA.

J. W. Head[1], L. S. Crumpler[1], J. C. Aubele[1], and the Magellan Team, [1]Department of Geological Sciences, Brown University, Providence RI 02912, USA.

A preliminary analysis of a global survey of Magellan data covering over 90% of the surface and designed to document the characteristics, location, and dimensions of all major volcanic features on Venus has revealed over 1660 landforms and deposits [1]. These include over 550 shield fields (concentrations of small volcanos <20 km in diameter), 274 intermediate volcanos between 20 and 100 km diameter with a variety of morphologies, 156 large volcanos in excess of 100 km diameter, 86 calderalike structures independent of those associated with shield volcanos and typically 60–80 km in diameter, 175 coronae (annulus of concentric ridges or fractures), 259 arachnoids (inner concentric and outer radial network pattern of fractures and ridges), 50 novae (focused radial fractures forming stellate patterns), and 53 lava flood-type flow fields and 50 sinuous lava channels (all of which are in excess of 10^2–10^3 km in length).

The near-global coverage of Magellan data analyzed in this study confirms and extends the results of earlier observations [2] that showed that volcanism is a widespread and significant process on the surface of Venus for the period of time in the presently observed record (less than about the last one billion years [3,4]). Volcanic units comprise in excess of 80% of the surface of the planet, and indeed the remainder of the planet largely consists of tessera, which itself may be deformed lava flows. The minimal influence of erosion on the surface results in the stunning preservation of the wide array of volcanic features and edifices documented in this study. The high-resolution and global coverage of the Magellan image data has provided the opportunity for the global inventory [1]. On the basis of the characteristics of the landforms and deposits, the vast majority of the units appear to be of basaltic composition, consistent with the results of the earlier Venera landers [5]. However, important morphologic variations suggest a wider range of lava compositions on the surface, consistent with a range of petrogenetic environments [6]. For example, the morphology of the steep-sided domes and festoons [7,8] suggests that they may represent more viscous magmas with more evolved compositions. Long sinuous rilles and channels may indicate the location of sites of extrusion of ultramafic or other very fluid magmas [9]. The large lava floods indicate that effusions comparable to terrestrial flood basalts were a relatively common occurrence on Venus. In addition, the array of features that have associated volcanism strongly suggest that volcanism is related to a wide variety of scales of mantle upwelling, from hot-spot-like plumes of about 200 km diameter [10] to much larger several thousand-kilometer-diameter broad rises such as Beta and Atla Regiones [11]. Similarly, the variations in surface morphology and amount of associated volcanism of many of these features strongly suggest that there is a wide range of intrusive and extrusive processes operating, including the largely intrusive aspects of arachnoids, the radial dikelike patterns associated with novae [10,12], and the predominantly extrusive large volcanos. Indeed, there is some evidence that there may be an evolutionary sequence of features beginning with novae, extending through large volcanos, and ending in coronae. Evidence also exists for large calderas, coronae, and other features that indicate that many magma reservoirs may be relatively large on Venus compared to Earth. One of the major outstanding questions in Venus volcanology is the nature of the melting process, the evolution of the melts, and the intrusion to extrusion ratios typical of different environments.

The distribution of volcanic features on Venus (Fig. 1) is not concentrated along linear zones, such as the divergent and convergent plate boundaries concentrations seen on Earth. This, and the distribution of impact craters [3,4], is further evidence for the lack of large-scale crustal spreading in the last hundreds of millions of years. However, the distribution is not random, and there is evidence for a major Tharsis-like concentration in the Beta/Atla/Themis region that covers about 20% of the planet and is probably related to major mantle anomalies [1,13]. There is also a deficiency of many features in the lowlands and this is attributed to a combination of altitude-dependent eruption conditions [14] and partial burial of features in lowland regions. Ongoing detailed analysis of these
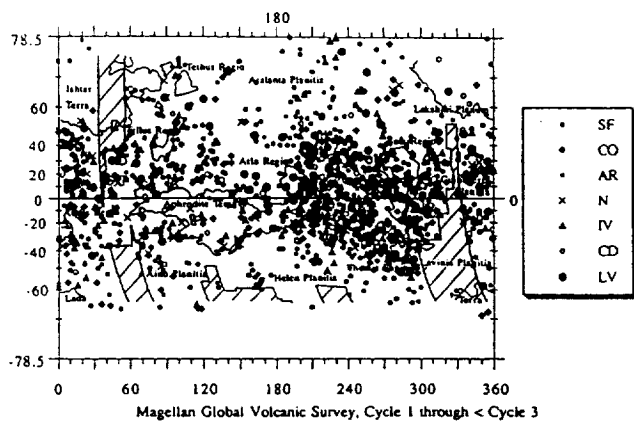
Fig. 1.   Global distribution of volcanic features [1]. (SF = shield fields; CO = coronae; AR = arachnoids; N = novae; IV = intermediate volcanos CD = calderas; LV = large volcanos).

regions covered by repeat imaging is designed to detect volcanic deposits emplaced between cycles, but so far the duration of observations has been small and no changes that could be confidently attributed to volcanic activity have been observed.

On the basis of these analyses, what are the rates, styles, and nature of crustal formation processes on Venus [15]? The global distribution of volcanic features shows that volcanism is widespread across the planet and that in the time period represented by the present surface, volcanism was active at one time or another on virtually every part of the planet. Crustal formation processes clearly are linked to vertical differentiation and vertical crustal growth, in contrast to the lateral crustal spreading and lateral crustal propagation typical of the Earth's seafloor. Although the general factors involved in this process are known (e.g., extrusion, intrusion, and underplating), the details of the relative importance of each of these components and the mechanisms of resurfacing to produce the observed volcanic and impact crater record are not.
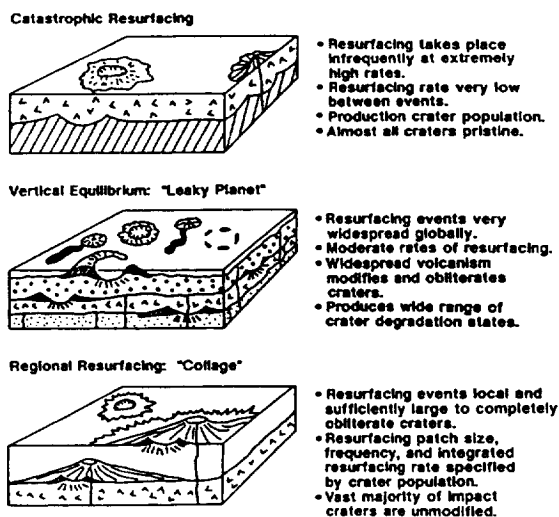
Fig. 2.   Volcanic resurfacing models for Venus. Block diagrams illustrate the three types of crustal resurfacing scenarios consistent with the observed impact crater population.

The observed crater population on Venus can lead to three possible endmember resurfacing models [3], and the volcanic record [1] bears on the assessment of these (Fig. 2). The scale of volcanic features and deposits suggests that each feature covered areas much less than about 125,000 km^2, and that resurfacing may have proceeded by serial emplacement of local to regional features and deposits. Serial volcanism is visualized as a sequence of volcanic events varying in time and space, but ultimately influencing the whole planet over the timescale of hundreds of millions of years. In the serial volcanism or regional resurfacing process, volcanism proceeds in somewhat of a "collage" or "cookie-cutter" mode; volcanic features are produced in different parts of the planet at different times and because of the low crater density and small area covered by crater deposits, volcanic deposits can commonly be emplaced in a "matrix-filling" mode between craters; however, when they are emplaced on a crater, they tend to obliterate it (Fig. 2). Evidence in support of serial volcanism as a process is the large number of features that appear to be related to mantle instabilities on the scale of several hundred kilometers (shield fields, coronae, arachnoids, novae, large volcanos). These data suggest that the majority of near-surface melting is linked to pressure-release melting associated with mantle plumes or hot spots, rather than globally pervasive shallow melting as would be envisioned in the equilibrium resurfacing endmember model. However, the total volume of extrusive volcanism associated with these features is much less than that predicted by the model, but it is also clear that large areas of plains have been emplaced by mechanisms other than the features mapped here, and by processes not completely understood. The serial volcanism or regional resurfacing concept is in contrast to a "leaky planet" model, in which volcanism is much more uniformly distributed with time and is proceeding almost everywhere simultaneously (Fig. 2). In this case the crust is thickening relatively uniformly with time. The paucity of impact craters in intermediate to advanced stages of burial favors the serial volcanism or catastrophic resurfacing model over the "leaky planet" model; however, there is a level of uncertainty about the exact number of craters that actually postdate the surface, as described above. The "catastrophic resurfacing" model end member interprets the crater population to be a production population and calls on a pulse of resurfacing about 500 m.y. ago of sufficient thickness to obliterate the preexisting crater population and to produce a pristine surface on which the production population accumulates [4]. Volcanism subsequent to this time is viewed as minor and volumetrically minimal. The small number of impact craters highly modified by volcanism is viewed as supporting this hypothesis, and the total volume associated with the features observed [1] implies a low rate of volcanism, less than that implied by the serial volcanism model. However, a major unknown is the volume and mode of emplacement of the plains not related to the features mapped in this study. These plains may have formed as part of the catastrophic resurfacing event, or they may represent the sequential emplacement of deposits over the last several hundred million years. The stratigraphy, mode of emplacement, and scale of the plains-forming events is one of the major problems in Venus geology and volcanology at the present time, and detailed regional and global geologic mapping is required to begin to address this problem. Although the catastrophic resurfacing model seems unusual from a uniformitarian point of view, one must nevertheless remember that we may be dealing with differences in the thermal evolution of Venus relative to Earth, or in the consequences of long-term and continuous vertical crustal formation (Fig. 2), and the production of major instabilities in a depleted mantle layer [16]. Refinement of catastrophic resurfacing models

will help to make more specific predictions that can be tested with observations of the style and distribution of volcanism. In addition, Monte Carlo simulations of the interaction of impact cratering and volcanic processes in the production and evolution of the Venus crust [17] will provide data that can then be compared to observations in order to further distinguish between models for the resurfacing history of Venus.

Finally, we have information on only about the last 20% or less of the history of Venus as presently observed in the surface record. Assessment of thermal evolution models for the first 80% of the geological and volcanological history of Venus may provide an important context for the presently observed record.

References: [1] Head J. et al. (1992) *JGR*, in press. [2] Barsukov et al. (1986) *JGR*, *91*, 378. [3] Phillips R. et al. (1992) *JGR*, in press. [4] Schaber G. et al. (1992) *JGR*, in press. [5] Surkov Yu. et al. (1984) *JGR*, *89*, 393; (1987) *JGR*, *92*, 537. [6] Hess P. and Head J. (1990) *Earth Moon Planets*, *50/51*, 57. [7] Pavri B. et al. (1992) *JGR*, in press. [8] Moore H. et al. (1992) *JGR*, in press. [9] Baker V. et al. (1992) *JGR*, in press. [10] Stofan E. et al. (1992) *JGR*, in press; Squyres S. et al. (1992) *JGR*, in press. [11] Senske D. et al. (1992) *JGR*, in press. [12] Parfitt E. and Head J. (1992) *LPSC XXIII*, 1029. [13] Crumpler L. et al. (1992) *LPSC XXIII*, 277. [14] Head J. and Wilson L. (1992) *JGR*, *97*, 3877. [15] Head J. (1990) *Earth Moon Planets*, *50/51*, 25. [16] Parmentier E. and Hess P. (1992) *LPSC XXIII*, 1037. [17] Bullock M. et al. (1992) *LPSC XXIII*, 175

N93-14324

CHEMICAL DIFFERENTIATION ON ONE-PLATE PLANETS: PREDICTIONS AND GEOLOGIC OBSERVATIONS FOR VENUS.

J. W. Head, E. M. Parmentier, and P. C. Hess, Department of Geological Sciences, Brown University, Providence RI 02912, USA.

Recent studies have examined the partial melting of planetary interiors on one-plate planets and the implications for the formation and evolution of basaltic crust and the complementary residual mantle layer [1–3]. In contrast to the Earth, where the crust and residual layer move laterally and are returned to the interior following subduction, one-plate planets such as Venus are characterized by *vertical* accretion of the crust and residual layer. The residual mantle layer is depleted and compositionally buoyant, being less dense than undepleted mantle due to its reduced Fe/Mg and dense Al-bearing minerals; its melting temperature is also increased. As the crust and depleted mantle layer grow vertically during the thermal evolution of the planet, several stages develop [2,3]. As a step in the investigation and testing of these theoretical treatments of crustal development on Venus, we investigate the predictions deriving from two of these stages (a stable thick crust and depleted layer, and a thick unstable depleted layer) and compare these to geologic and geophysical observations, speculating on how these might be interpreted in the context of the vertical crustal accretion models. In each case we conclude with an outline of further tests and observations of these models.

Implications of the Presence of a Stationary Thick Depleted Mantle Layer: In this scenario (Fig. 1), the crust has thickened to several tens of kilometers (less than the depth of the basalt/eclogite transition) and overlies a thick depleted mantle layer.

Volcanism. Rates of surface extrusion should have decreased with time due to evolving thermal gradient and increase in depleted layer thickness and should be low. Present rates of volcanism on Venus are apparently low (<0.5 km³/a), comparable to terrestrial
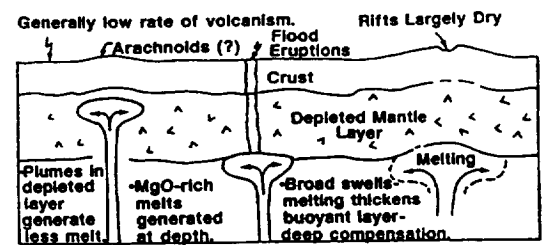
Fig. 1. Stationary thick depleted mantle layer.

intraplate volcanism rates [4]. For plumes, if conditions were comparable on Venus and Earth, the higher lithospheric temperature on Venus caused by the higher surface temperature would result in plumes ascending to shallower depths, and greater pressure-release and lithospheric melting there [5]. In the scenario described here (Fig. 2), plumes ascending from depth would not penetrate to shallow depths and thus should undergo less pressure-release melting and less melting and incorporation of a cooler and depleted mantle layer. Although volcanism is associated with many features interpreted to be plumes on Venus (shield volcanos and many coronae), there is a wide range of other features (arachnoids and numerous coronae) that show minimal signs of volcanism [4,6]. This could be consistent with the presence of a thick depleted layer. Another implication of the presence of the thick depleted layer is that plumes undergoing pressure-release melting at the depth of the base of this layer (Fig. 1) will produce MgO-rich melts that should yield very voluminous, low-viscosity surface flows [7]. This could be consistent with the abundant large-volume and apparently fluid lava flows and sinuous rillelike features observed in the Magellan data [4,8]. Another consequence of the presence of a thick depleted layer is that volcanism should be concentrated in regions above the largest upwellings (Fig. 2). This could be consistent with the observation that much of the volcanic activity (particularly edifices and structures) on Venus is associated with large rises such as Beta, Atla, and Themis, and the adjacent regions [4,9,10].

Tectonics. A stable depleted mantle layer will enhance lithospheric buoyancy and will inhibit the development of crustal spreading and plate tectonics. In addition, rifting may commonly be unaccompanied by volcanism ("dry"), except in extreme cases. This could be consistent with the lack of presently observed crustal spreading on Venus [11] and the general paucity of volcanism associated with rift zones except locally in regions of broad rises [10].

Crustal/upper mantle structure. On Venus, the apparent depth of compensation of many regional-scale features is much greater than on Earth [12]. If density variations in a viscous mantle are the cause of these features, a low-viscosity zone in the upper mantle
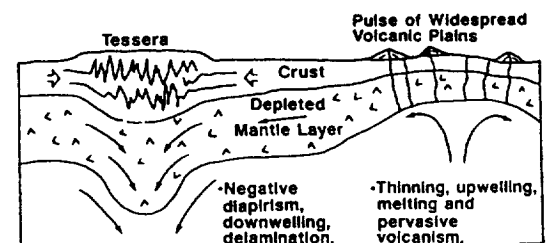
Fig. 2. Instabilities that develop in a depleted layer.

caused by mantle material approaching its melting temperature, as it does on Earth, would be highly improbable on Venus. The colder, thicker depleted mantle layer with a higher melting temperature than normal mantle would inhibit and perhaps preclude partial melting and the development of a low-viscosity zone. Thus, the great apparent depths of compensation could be related to the presence of a thick depleted layer. Regions of deepest compensation on Venus (e.g., Beta Regio) are characterized by broad rises and associated rifting and centers of volcanism and are thought to represent the surface expression of mantle plumes [10]. If these plumes penetrated to the bottom of the depleted layer, melting would locally thicken the buoyant layer, and this greater thickness of low-density mantle may support the broad surface topography. Thus, in this scenario, the apparent depth of compensation may reflect the thickness of the depleted layer.

Implications of Instabilities Developing in a Thick Depleted Mantle Layer: As it thickens and cools, the depleted mantle layer may become unstable (for example, tradeoffs between compositional and thermal buoyancy related to general planetary cooling can result in net negative buoyancy for the depleted layer [2,3]). In these cases, the depleted layer will mix into the convecting interior, the base of the thermal boundary layer and melting rise to shallow depths, large amounts of melting occur, contributing again to the growth of the crust (with voluminous and widespread volcanism) and the complementary depleted mantle layer. Some of the predicted consequences of such a period of instability (Fig. 2) would be negative diapirs, delamination, upwelling, massive pressure-release melting, and a period of widespread volcanic flooding and resurfacing. These events would be short term, and separated in time by long periods of crustal buildup (Fig. 1) to the next instability event.

Volcanism. Such a scenario may be consistent with volcanological implications of many aspects of the crater population. The impact crater population cannot be distinguished from a completely spatially random population [13], and this can be interpreted to mean that it is in production and is superposed on a substrate that was produced over a very short period of time about 500 m.y. ago and that has been only locally modified by volcanism since [14]. In this scenario, the cratered surface of Venus was completely resurfaced by volcanic deposits to a depth of at least 10 km in a very short period of time [14], erasing all previous craters. This thickness (10 km) corresponds to the creation of 0.46×10^{10} km^3 of volcanic deposits, a rate of about 46 km^3/a if the event took place over 100 m.y., and 460 km^3/a if it took place over 10 m.y. The latter value is equivalent to a global layer 1 mm thick per year. This new surface then begins to accumulate a production crater population during which there is a much decreased rate of volcanism. The very small number of craters that have been clearly modified by volcanism is cited as supporting this scenario [14].

Tectonism. In the process of development and evolution of instabilities in the depleted layer, crustal shortening, thickening, and surface deformation is likely to occur (Fig. 2). The scales and styles will be related to the scale of the instabilities and the rheology of the crust and depleted mantle material. We consider the possibility that the tessera regions represent relict sites of downwelling associated with such instabilities. Tesserae show crater densities comparable to the rest of Venus [13,14], are highly deformed [15,16], represent regions of thickened crust [17], make up between 10% and 20% of the planet [16], and often have borders suggesting deformation and underthrusting [15,16]. These borders often extend for many hundreds to thousands of kilometers, indicating that the underthrusting events were large scale [16]. In addition, some areas,

like Western Ishtar Terra, are ringed by distinctive mountain ranges of compressional origin, suggesting large-scale downwelling there [18]. Thus, these regions could be linked to large-scale downwelling events associated with depleted-layer instabilities. Two scenarios for instabilities and surface deformation and volcanism seem plausible. In one, the residual layer becomes negatively buoyant and diapirism is widespread, but the diapirs are not closely coupled with the uppermost mantle and crust, and surface deformation is limited and localized to the region above the negative diapir. In this scenario, fertile mantle material would flow in to replace the lost diapir region and pressure-release melting at depths previously occupied by the depleted layer would cause extensive regional volcanism. Resurfacing would take place focused on these regional centers of diapirism. In another scenario, coupling of the negative instability and the upper mantle and crust would be more complete, and an instability would cause large-scale crustal downwelling and thickening, lateral thinning of the crust and depleted layer in distal regions (Fig. 2), and the possibility of rifting and the initiation of crustal spreading to create new crust in these regions. During this process, the models suggest that crustal recycling is taking place; one challenge is to identify places in the geologic record where this might have taken place (e.g., Ishtar Terra). Crustal spreading could be a major part of the renewal process, with old crust being thickened, deformed, underthrust, and possibly subducted over regions of downwelling, and crustal thinning, large-scale pressure-release melting, and crustal spreading occurring over the complementary regions of the planet. Modest crustal spreading rates (similar to those on the Earth, e.g., ~5 cm/a) for a total ridge length equivalent to a planetary circumference could result in creation of new crust for between one-third and one-half of the planet in 100 m.y. Further analysis of the scale of development of instabilities and the implication of rates and thermal structure for uppermost mantle and crustal coupling are required to develop these scenarios to the point that they can be tested with observations.

Implications of Vertical Crustal Accretion for the Geological History of Venus: A range of parameters has been explored for these models and different conditions can result in variations in the thickness of the crust and the depleted layer [2,3]; however, several themes emerge as characteristic of all models and might be thought of as predicted consequences of vertical crustal accretion on a one-plate planet. These include:

1. *Early stability.* Early period of history where crust and depleted layer are growing and are broadly stable. This period may be marked by the loss of crustal material from the base of the crust and by convective mixing of the base of the depleted mantle layer.

2. *Decrease of surface volcanism as a function of time.* This results from the secular cooling of the interior but is enhanced by the growth of the depleted layer.

3. *Onset of instability.* Midway through the history of Venus, an initial instability develops in the depleted layer, causing major crustal modification and resurfacing.

4. *Cyclical nature of instabilities.* Following the initial instability event, the models predict that the growth and destruction of the depleted layer will take place at 300–500-m.y. intervals. The surface of Venus as presently observed is less than a billion years old [13,14], and there is no evidence of more ancient heavily cratered terrain. The large volume of crust predicted by thermal evolution models suggests that some mechanisms of crustal loss must have operated on Venus in its past history [19]; these models provide a mechanism for the initial buildup as well as subsequent removal and renewal of crustal material.

Further Development and Tests of these Scenarios: No one observation can be shown to uniquely confirm these models and scenarios, but many of the features predicted by the models are consistent with the observed characteristics of Venus geology and geophysics. These models therefore merit further consideration. Some of the things that are required to permit the further analysis and testing of these scenarios include (1) Better definition of the growth, stability, and style of renewal of the crust and depleted layer, and the relation to lithosphere evolution. (2) Analysis of the scale and nature of instability: Is it characterized by catastrophic surface turnover and crustal spreading, or deeper negative diapirs and resurfacing of a relatively stable and intact veneer? (3) Do the heavily deformed tesserae show patterns consistent with the initiation and subsequent deformation during the period of instability? (4) If crustal spreading has taken place as part of the resurfacing process, what geometries and rates are compatible with the cratering record? (5) How fast does resurfacing have to be to be consistent with the crater record? Is this reasonable from turnover and magma generation point of view?

Crustal formation processes have been characterized as primary (resulting from accretional heating), secondary (resulting from partial melting of planetary mantles), and tertiary (resulting from reprocessing of secondary crust [20]. Venus appears to represent a laboratory for the study of vertical accretion of secondary crust, which may have important implications for the earliest history of the Earth.

References: [1] Dupeyrat L. et al. (1992) *LPSC XXIII*, 319. [2] Parmentier E. and Hess P. (1992) *LPSC XXIII*, 1037; Phillips R. and Grimm R. (1980) *LPSC XXI*, 958. [3] Parmentier E. and Hess P., this volume. [4] Head J. et al. (1992) *JGR*, in press. [5] Erickson S. and Arkani-Hamed J. (1992) *GRL, 19*, 885. [6] Stofan E. et al. (1992) *JGR*, in press; Squyres S. et al. (1992) *JGR*, in press. [7] Hess P. and Head J. (1990) *Earth Moon Planets, 50/51*, 57. [8] Baker V. et al. (1992) *JGR*, in press. [9] Crumpler L. et al. (1992) *LPSC XXIII*, 275. [10] Senske D. and Head J. (1992) *LPSC XXIII*, 1269. [11] Solomon S. et al. (1992) *Science, 252*, 297. [12] Phillips R. et al. (1991) *Science, 252*, 651. [13] Phillips R. et al. (1992) *JGR*, in press. [14] Schaber G. et al. (1992) *JGR*, in press. [15] Bindschadler D. and Head J. (1991) *JGR, 96*, 5889. [16] Ivanov M. et al. (1992) *LPSC XXIII*, 581. [17] Smrekar S. and Phillips R. (1991) *EPSL, 107*, 582. [18] Bindschadler D. and Parmentier E. (1990) *JGR, 95*, 21329. [19] Head J. (1990) *Earth Moon Planets, 50/51*, 25. [20] Taylor S. (1989) *Tectonophysics, 161*, 147.

N93-14325

DYNAMICS OF THE VENUS ATMOSPHERE. A.P. Ingersoll, California Institute of Technology, Pasadena CA 91125, USA.

The superrotation of the Venus atmosphere is a major unanswered problem in planetary science [1]. At cloud-top levels (65–70 km altitude) the atmosphere rotates with a five-day period, corresponding to an equatorial wind speed of 90 m/s [2–4]. Angular velocity is roughly constant on spherical shells, and decreases linearly with altitude to zero at the surface. The direction of rotation is the same as that of the solid planet, which is retrograde—opposite to the direction of orbital motion, but the 5-day period is short compared to the 243-day spin period of the solid planet or to the mean solar day, which is 117 Earth-days at the surface.

The problem with the superrotation is that shearing stresses tend to transfer angular momentum downward, and would slow the atmosphere until it is spinning with the solid planet. Some organized circulation pattern is counteracting this tendency, but the pattern has not been identified. A simple Hadley-type circulation cannot do it because such a circulation is zonally symmetric and Hide's theorem [5] states that in an axisymmetric circulation an extremum in angular momentum per unit mass M can exist only at the surface. Venus violates the last condition, having a maximum of retrograde M on the equator at 70–80 km altitude. This leaves waves and eddies to maintain the superrotation, but the length scales and forcing mechanisms for these motions need to be specified.

The wind speed at cloud-top level is proportional to the equator-to-pole temperature difference through a relation known as the thermal wind equation [1]. The magnitude of the temperature difference reflects a balance between radiative forcing, which tends to warm the equator and cool the pole, and poleward heat transport by atmospheric motions—including the same waves and eddies that are maintaining the superrotation. The great mass and large heat-carrying capacity of the lower atmosphere limits the temperature gradient there. The temperature difference at cloud-top level is of order 30 K [1]. If the circulation were more efficient at all altitudes, the temperature difference would be smaller and the superrotation would be weaker. Understanding the superrotation is equivalent to understanding the equator-to-pole temperature distribution, and neither are understood at present.

The mean meridional wind at cloud-top level is poleward in both hemispheres, according to cloud-tracked wind analysis from 1974 to 1990 [2–4]. The zonal wind varied from 80 to 100 m/s during the same period. Both the eddies and the symmetric circulation are tending to remove angular momentum from the equator at cloud-top levels [2,3], thereby adding to the load that other waves and eddies must carry. The most visible global feature is the Y, a dark marking centered on the equator that looks like the letter Y rotated counterclockwise by 90°. Its four-day period is significantly shorter than that of small-scale markings that drift with the flow, so it is probably a Kelvin wave with zonal wavenumber equal to one [6,7]. On Earth, the eastward-propagating Kelvin waves and the westward-propagating Rossby-gravity waves alternate in driving the winds of the equatorial stratosphere to the east and west, respectively, in a cycle known as the quasibiennial oscillation (QBO). The waves are presumably driven by convection in the troposphere, but the exact nature of their excitation is not yet fully understood [5]. The role of these waves on Venus, how they are excited, and why they do not produce larger swings in the equatorial zonal wind are still unanswered questions. Convection occurs in two altitude ranges on Venus: from the surface to about 30 km altitude, and within the clouds from 49 to 55 km altitude [1]. It is possible that small-scale convective motions randomly excite the large-scale Kelvin wave, which carries retrograde momentum upward and maintains the superrotation.

Tides are the other major class of atmospheric motions that could be maintaining the superrotation [8–10]. They are the atmosphere's linear response to daily heating by the Sun. Both the heating and the response are global in scale and are phase-locked to the Sun as the atmosphere rotates beneath it. Tides propagate vertically, away from the altitudes where solar heat is absorbed. On Venus this heating is located near the tops of the clouds. The propagating waves carry energy and momentum away from this layer and could lead to a net retrograde acceleration. Tides are seen in the Venus images [2,3,6] and temperature data [11], and many of the observed features are reproduced in the models. The problems center around the distribution of tidal heating, the dissipation of tidal energy, the relation between tides and convection, which also has a diurnal component, and the role of the deep atmosphere, which is difficult

to model because of its long thermal response time and convective temperature distribution.

More observations are needed to sort out the different possibilities. A network of probes or balloons would help define the types of waves that are present. Measuring the correlations between the different components of velocity with each other and with temperature at different points in space and time is the time-honored way of measuring heat and momentum transports. The same methods that have worked for the Earth's atmosphere should work for Venus.

References: [1] Schubert G. (1983) In *Venus* (D. M. Hunten et al., eds.), 681–765, Univ. Ariz., Tucson. [2] Limaye S. S. et al. (1988) *Icarus, 73*, 193–211. [3] Rossow W. B. et al. (1990) *J. Atmos. Sci., 47*, 2053–2084. [4] Belton M. J. S. et al. (1991) *Science, 253*, 1531–1536. [5] Lindzen R. S. (1990) *Dynamics in Atmospheric Physics*, Cambridge Univ., 310 pp. [6] Del Genio A. D. and Rossou W. B. (1990) *J. Atmos. Sci., 47*, 293–318. [7] Smith M. D. et al. (1992) *Science, 256*, 652–655. [8] Pechmann J. B. and Ingersoll A. P. (1984) *J. Atmos. Sci., 41*, 3290–3313. [9] Fels S. B. et al. (1984) *Nature, 312*, 431–434. [10] Baker N. L. and Leovy C. B. (1987) *Icarus, 69*, 202–220. [11] Elson L. S. (1983) *J. Atmos. Sci., 40*, 1535–1551.

N93-14326

LARGEST IMPACT CRATERS ON VENUS. B. A. Ivanov[1], C. M. Weitz[2], and A. T. Basilevsky[3], [1]Institute for Dynamics of Geospheres, Russian Academy of Sciences, Moscow, Russia, [2]Jet Propulsion Laboratory, California Institute of Technology, Pasadena CA 91109, USA, [3]Vernadsky Institute of Geochemistry and Analytical Chemistry, Russian Academy of Sciences, Moscow, Russia.

Introduction: High-resolution radar images from the Magellan spacecraft have allowed us to perform a detailed study on 25 large impact craters on Venus with diameters from 70 to 280 km. The dimension of these large craters is comparable with the characteristic thickness of the venusian lithosphere and the atmospheric scale height. Some physical parameters for the largest impact craters on Venus (LICV), such as depth, ring/diameter ratio, and range of ballistic ejecta deposits, have been obtained from the SAR images and the altimetry dataset produced by MIT [1].

Crater Depth Results: Impact crater depths previously measured using Venera 15/16 images [2,3,4] are in close agreement with the depths measured from the Magellan altimetry for the craters with diameters larger than the altimeter footprint on the surface.
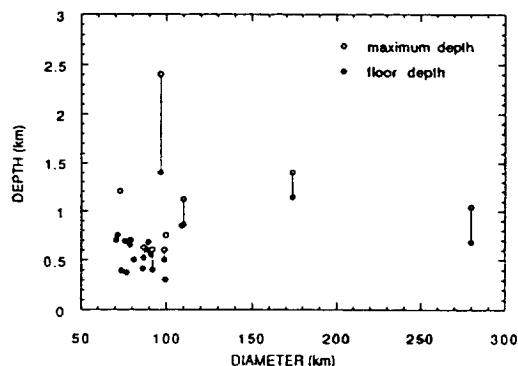
Two craters seem to have anomalous depths: Cleopatra (D = 100 km) and Mead (D = 280 km) (Fig. 1). Cleopatra is approximately twice as deep as other craters with the same diameter. Several hypotheses on the origin of Cleopatra have already been discussed [5,6]. Mead is a double-ring structure with an inner-ring flat floor depth of about 700 m and a maximum depth of 1000 m below the surrounding terrain. This maximum depth is approximately 100 m less than the depth for Klenova (D = 140 km). The maximum depth of Isabella (D = 173 km) is about 1400 m, which is about 400 m deeper than for Mead. A comparison of our data with estimates made by Grimm and Solomon [7] suggests that Mead may be one of the first examples of crater relaxation on Venus due to viscous flow of the crust. Because of the large footprint of the altimeter, viscous relaxation in smaller craters cannot be seen, yet we cannot reject this process. Hopefully, parallax measurements made from different viewing geometries will allow us to make better depth measurements, especially for the smaller craters.

Ring Diameter Ratios: A majority of venusian impact craters with diameters larger than 70 km have a double-ring structure. All craters with D > 90 km are double ring. Melosh [8] separated the cratering data for all terrestrial planets into peak-ring craters (PRC) and multiring basins (MRB). For PRC, he found that the inner-to-outer ring diameter ratio (RDR) is about 0.5 for all planetary bodies, while the morphology of MRB is specific for each planet depending upon the details of the upper crust structure. Many of the LICV have RDR of 0.5 and smaller and may be classified as PRC (Fig. 2). Three craters with diameters from 90 to 280 km have RDR from 0.6 to 0.67. These three craters may be candidates for venusian MRB, but more morphologic and comparative studies need to be done for proper classification. An interesting finding is the coexistence of craters with RDR ≤ 0.5 (four structures) and RDR > 0.5 (three structures) in the diameter range from 90 to 110 km. By comparing the local geologic setting around each crater, it may be possible to determine if the terrain is influencing the RDR for this diameter range.

Distance of Ballistic Ejecta Deposits (BED): The measurement of the outer distance of ballistic ejecta deposits has some uncertainty due to the obliqueness of the impact and ejecta disturbed by radar-bright outflows from some craters. Measurements may be done more accurately in the future when geologic mapping is completed for all the craters under investigation in this study. The data we now have for 25 craters shows that the radial distance of the BED from the crater rim increases for craters with diameters less than 100 km (Fig. 3). For larger craters, the width of the BED seems to stay at approximately 50 km from the crater rim. This observed

Fig. 1.   Depth vs. diameter for LICV.
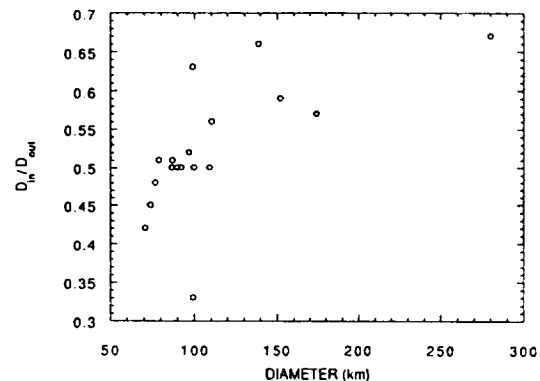
Fig. 2.   Ratio of the inner peak ring to the outer ring plotted vs. diameter.
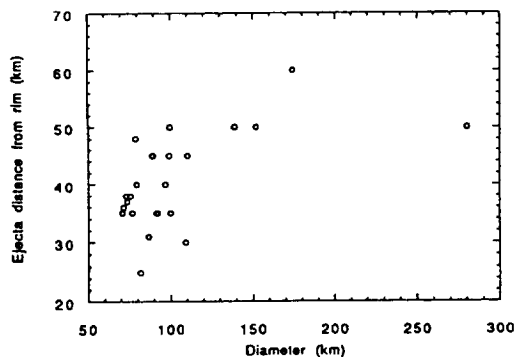
Fig. 3. Ejecta distance from the crater rim vs. diameter.

phenomenon needs additional study to investigate the effect of the atmospheric scale height on ejecta deposition.

The Inner Ring Position: A number of venusian impact craters have asymmetric BED blankets, which may result from the obliqueness of the impact. The general features of this asymmetry have been investigated experimentally for small-scale impacts [9]. At least two venusian craters (Cohran: D = 100 km, RDR = 0.5; Marie Celeste: D = 99 km, RDR = 0.62) have a definite offset of the inner ring in respect to the outer crater ring. If this offset is a consequence of an oblique impact, then we would expect the inner ring to be shifted to the deepest part of the transient cavity, which should be on the uprange side. In fact, Cohran and Marie Celeste have their inner ring offset downrange rather than uprange. Although these two craters suggest that we cannot accurately predict the formation of the multiring structures, we still have a poor understanding of cratering mechanics at this time so we need to investigate this process further. This investigation of the largest craters on Venus is therefore providing new constraints both for cratering mechanics and for the regional geologic study of Venus.

References: [1] Pettengill et al. (1991) *Science, 252*, 260–265. [2] Basilevsky et al. (1987) *JGR, 92*, 12869–12901. [3] Ivanov B. A. (1989) *Solar System Research* (translated from Russian), *Astron. Vestnik, 23*, 39–49. [4] Ivanov B. A. (1992) In *Venus Geology, Geochemistry, Geophysics: Soviet Point of View* (V. L. Barsukov et al., eds.), Univ. Ariz., Tucson. [5] Basilevsky A. T. and Ivanov B. A. (1989) *GRL, 17*, 175–178. [6] Masursky H. et al. (1980) *JGR, 85*, 8232–8260. [7] Grimm R. E. and Solomon S. C. (1988) *GRL, 93*, 11911–11929. [8] Melosh H. J. (1989) *Impact Cratering, A Geologic Process*, Oxford, New York, 245 pp. [9] Gault D. E. and Wedekind J. A. (1978) *LPSC IX*, 3843–3876.

N93-14327

VENUSIAN EXTENDED EJECTA DEPOSITS AS TIME-STRATIGRAPHIC MARKERS. Noam R. Izenberg, McDonnell Center for Space Sciences, Washington University, St. Louis MO 63130, USA.

In contrast to the Moon, Mars, and Mercury, where millions of impact craters cover or influence nearly all surface terrains, on Venus there are only about 850 craters. For the Moon, Mars, and Mercury, relative densities of craters on different geologic surfaces provide clues regarding relative age relationships for surface units, both on regional and local scales. For Venus, the population of craters is well dispersed, and based on extensive statistical analysis of the spatial distribution of impact craters, Magellan investigators [1] find that the hypothesis that craters are randomly distributed

cannot be rejected. Relative age dating using crater statistics alone is therefore not possible for Venus. However, in the absence of actual rock samples, the venusian crater population is the only tool available for determining a general planetary timescale. An average surface age of approximately 500 Ma is indicated by the total abundance of impact craters, using the assumption that all craters produced over that time have been retained and observed by the Magellan spacecraft [2]. One of the first-order questions regarding Venus presently is whether areas of the planet are clearly older or younger than this statistically determined average age.

On the regional scale, the question of relative age can be approached by examining the crater population and its associations with large-scale geologic terrains. Upon construction and examination of a crater distribution plot, craters appear randomly distributed across the planet. A density plot in which the total crater population has been binned in 20° radius circles every 10° of latitude and longitude to maximize the visibility of regional trends in the concentrations of craters has also been constructed. Some areas show regions with one-third to one-fourth the average planetary crater density, while others represent regions with up to twice the planetary mean. If these low- and high-density areas correlate with the regional geology of the planet, then these regions have ages younger and older than the planetary mean respectively.

The work of [3] and [4] has shown that correlations between crater concentrations and geology do exist. For example, the Beta-Atla-Themis region, shown to have the highest density of volcanic structures on the planet [5], has a low density of impact craters. Likewise, south central Aphrodite Terra, including Artemis Chasma (a large coronae feature on the southern edge of Aphrodite), also has a low crater density. These two areas probably represent broad regions younger than the planetary average age.

On the local scale, both the paucity and distribution of impact craters precludes them as relative age indicators. Relative ages must be established using other means, such as through interpretation of stratigraphic relationships between surface units. Extended ejecta deposits, which cover many times the surface area of their parent craters, are units that provide areally extensive time-stratigraphic markers for their respective localities. Superposition relationships between these deposits, volcanic materials, and tectonic zones would establish relative timing for the deposition of the units involved.

Use of impact crater ejecta as time-stratigraphic markers was established during lunar geologic mapping efforts [6,7]. The basic premise is that the deposition of impact ejecta, either by itself or mixed with impact-excavated material, is superimposed on a surface. The deposit becomes an observable, mappable unit produced in a single instant in geologic time. Up to two-thirds of Venus craters exhibit extended ejecta deposits. Most deposits have low specific radar cross sections, appearing dark on Magellan images relative to surrounding units. Some deposits have specific cross sections higher than the local mean, and some have a number of high and low specific cross-section components. The deposits range in characteristics from extensive parabolic features to halolike zones only a few crater diameters across. Parabolic features are interpreted to be due to interactions of ejecta with strong east-to-west zonal winds [8,9,10]. They extend up to 20 crater radii from the impact site. Ejecta halos, 3 to 10 times the parent crater radius in areal extent, are interpreted to be due to a combination of shock-induced crushing of preexisting material and accumulation of ejecta from the relevant impact crater [1,2,11].

The areal extent of a given extended deposit is significantly greater than that of its parent crater. The largest extended ejecta

deposits are associated with craters Greenaway and Stanton and cover about 100 times the area of each crater, 2.6 and 3.4 million km², or 0.6% and 0.8% of the total surface area of Venus respectively. Assuming that extended ejecta is contemporaneous with the parent crater as a given, it follows logically that extended ejecta deposits are local time-stratigraphic markers. Such extended units will not improve temporal resolution (i.e., they will not give a better constraint on absolute time, since they are present around a subset of the already small, spread-out crater population). However, the extended deposits will improve the spatial domain significantly, as the deposits cover up to millions of square kilometers in a single geologic instant, allowing for determination of relative time progressions in many localities.

A reconnaissance survey of 336 craters (about 40% of the total population) was conducted. About half the craters examined were located in and around the Beta-Atla-Themis region, and half were spread over the western hemisphere of the planet. The survey was conducted using primarily C1-MIDR images. The preliminary survey shows (1) Of the 336 craters, 223 were found to have extended ejecta deposits. This proportion is higher than that found in other Venus crater databases by up to a factor of 2 [12]. (2) 53% of all extended ejecta craters were unambiguously superimposed on all volcanic and tectonic units. Figure 1 shows a representative example of this group. Crater Annia Faustina's associated parabolic ejecta deposit is clearly superimposed on volcanic flows coming from Gula Mons to the west (Gula is not shown). Parabola material from Faustina has covered the lava flows, smoothing the surface and reducing its specific backscatter cross section. The stratigraphy implies that the parabola material is the youngest observable unit in the region. (3) 12% of extended ejecta deposits are superimposed by volcanic materials. Figure 2 shows a typical example. Crater Hwangcini has extended ejecta that has been covered by volcanic flows from a dome field to the northwest, implying that the volcanic
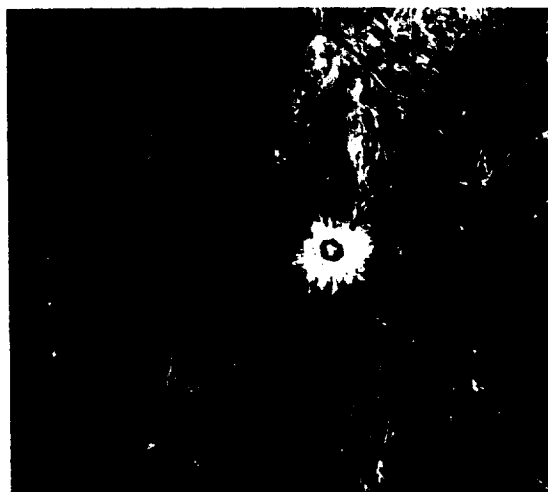
Fig. 2. Crater Hwangcini, 31 km in diameter with a low cross-section halo of about 230 km diameter that has been embayed to the west by flows associated with the dome field there. The crater is located northwest of Thetis Regio.

units were emplaced subsequent to the ejecta deposit and are the youngest units in the locality. (4) It is difficult to determine the stratigraphic relationships of the remaining extended ejecta deposits in SAR at C1-MIDR resolution. Examination of higher resolution images and application of the other Magellan datasets in a systematic manner should resolve most of the ambiguous cases.

Results from the preliminary survey indicate that extended ejecta deposits are effective time-stratigraphic markers for their localities. If stratigraphic relationships between the deposits and surrounding units are studied on a case-by-case basis over the whole planet, they should provide useful constraints on Venus history and development of the surface through time. The continuation of this research will expand the study to include the entire crater population and the Magellan emissivity, altimetry, reflectivity, and rms slope datasets.

References: [1] Phillips R. J. et al. (1992) *JGR*, submitted. [2] Schaber G. G. et al. (1992) *JGR*, submitted. [3] Izenberg N. R. et al. (1992) *LPSC XXIII*, 591–592. [4] Arvidson R. E. et al. (1992) *Eos, 73*, 161–169. (5) Head J. W. et al. (1992) *JGR*, submitted. [6] Shoemaker E. M. (1962) *Physics and Astronomy of the Moon* (Z. Kopal, ed.), 283–359, Academic, New York. [7] Wilhelms D. E. (1987) *U.S. Geol. Surv. Prof. Pap. 1348*. [8] Arvidson R. E. et al. (1991) *Science, 252*, 270–275. [9] Vervack R. J. and Melosh H. J. (1991) *Eos, 72*, 289. [10] Campbell D. B. et al. (1992) *JGR*, submitted. [11] Phillips R. J. et al. (1991) *Science, 252*, 249–252. [12] Herrick R. R. (1992) personal communication.

Fig. 1. Crater Annia Faustina, located east of Gula Mons. The crater is 22 km across, and the parabola is 6630 km long and and 720 km across. Parabola material from Faustina clearly darkens lava flows from Gula Mons where it appears that centimeters to decimeters of covering ejecta material reduces the radar wavelength scale roughness of the surface.

LONG-TERM VARIATIONS IN ABUNDANCE AND DISTRIBUTION OF SULFURIC ACID VAPOR IN THE VENUS ATMOSPHERE INFERRED FROM PIONEER VENUS AND MAGELLAN RADIO OCCULTATION STUDIES.

J. M. Jenkins[1] and P. G. Steffes[2], [1]SETI Institute, NASA Ames Research Center, Moffett Field CA 94035, USA, [2]Georgia Institute of Technology, Atlanta GA 30332, USA.

Radio occultation experiments have been used to study various properties of planetary atmospheres, including pressure and temperature profiles, and the abundance profiles of absorbing constitu-
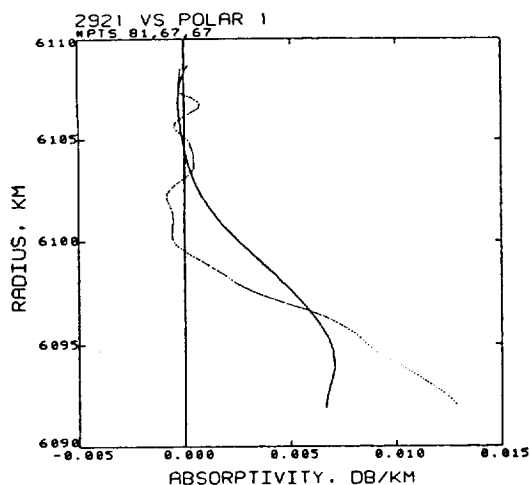
Fig. 1. Absorptivity profiles for near-polar PVORO experiments from 1979 (dotted line) and 1986 (solid line). Since $H_2SO_4(g)$ is the dominant 13-cm absorber in the Venus atmosphere, this plot suggests that the abundance of $H_2SO_4(g)$ decreased form 1979 to 1986 in the high northern latitudes.

ents in those planetary atmospheres. However, the reduction of amplitude data from such experiments to determine abundance profiles requires the application of the inverse Abel transform (IAT) and numerical differentiation of experimental data. These two operations preferentially amplify measurement errors above the true signal underlying the data. A new technique for processing radio occultation data has been developed that greatly reduces the errors in the derived absorptivity and abundance profiles. This technique has been applied to datasets aquired from Pioneer Venus Orbiter radio occultation studies and more recently to experiments conducted with the Magellan spacecraft.

While primarily designed for radar studies of the Venus surface, the high radiated power (EIRP) from the Magellan spacecraft makes it an ideal transmitter for measuring the refractivity and absorptivity of the Venus atmosphere by such experiments. Two transmitter frequencies were used: 2.3 GHz and 8.4 GHz (13 cm and 3.6 cm, respectively), and the measurements were made during spacecraft ingress on three consecutive orbits on October 5, 1991. Since the stability of the spacecraft transmitted frequencies is critical for accurate retrieval of atmospheric properties from the signals recorded on Earth, the spacecraft transmitter was locked to a 2.1-GHz uplink from DSS-43 (Tidbinbilla, Australia), which also received the signals. Because of the high gain of the spacecraft antenna, and the large ray bending in the deep Venus atmosphere, a spacecraft tracking maneuver was designed to keep the spacecraft antenna pointed in the direction of the refracted ray path back to Earth. This tracking maneuver, plus the high EIRP of the Magellan transmitter, yielded 3.6-cm refractivity and absorptivity profiles down to altitudes below 36 km, and 13-cm profiles to altitudes below 34 km (above a radius of 6052 km). These experiments probed much deeper in the atmosphere than previous radio occultation experiments conducted with the Pioneer Venus Orbiter, which reached altitudes of 54 km at 3.6 cm, and 40 km at 13 cm.

The longevity of the Pioneer Venus Orbiter has made it possible to study long-term changes in the abundance and distribution of sulfuric acid vapor, $H_2SO_4(g)$, in the Venus atmosphere between 1979 and 1992. The abundance of $H_2SO_4(g)$ can be inferred from vertical profiles of 13-cm absorptivity profiles retrieved from radio occultation experiments [1]. Data from 1979 and 1986–87 suggest

that the abundance of $H_2SO_4(g)$ at latitudes northward of 70° decreased over this time period (see Fig. 1). This change may be due to a period of active volcanism in the late 1970s followed by a relatively quiescent period, or some other dynamic process in the Venus atmosphere. While the cause is not certain, such changes must be incorporated into dynamic models of the Venus atmosphere.

Potentially, the Magellan spacecraft will extend the results of Pioneer Venus Orbiter and allow the continued monitoring of the abundance and distribution of $H_2SO_4(g)$ in the Venus atmosphere, as well as other interesting atmospheric properties. Without such measurements it will be difficult to address other issues such as the short-term spatial variability of the abundance of $H_2SO_4(g)$ at similar latitudes in Venus atmosphere, and the identities of particles responsible for large-scale variations observed in NIR images [2].

References: [1] Jenkins J. M. and Steffes P. G. (1991) *Icarus*, *90*, 129–138. [2] Ragent B. et al. (1991) *Bull. A.A.S.*, *23*, 1192.

N93-14329

VARIATIONS IN LITHOSPHERIC THICKNESS ON VENUS.

C. L. Johnson and D. T. Sandwell, Scripps Institution of Oceanography, La Jolla CA 92093–0208, USA.

Recent analyses of Magellan data have indicated many regions exhibiting topographic flexure [1,2,3]. On Earth, flexure occurs at oceanic trenches and around seamounts. On Venus, flexure is associated predominantly with coronae [1,3] and the chasmata within Aphrodite Terra [2,3]. Modeling of these flexural signatures allows the elastic and mechanical thickness of the lithosphere to be estimated. In areas where the lithosphere is flexed beyond its elastic limit the saturation moment provides information on the strength of the lithosphere. Modeling of 12 flexural features on Venus has indicated lithospheric thicknesses comparable with terrestrial values. This has important implications for the venusian heat budget.

Model: Flexure of a thin elastic plate due simultaneously to a line load on a continuous plate and a bending moment applied to the end of a broken plate is considered. The mean radius and regional topographic gradient are also included in the model. Features with a large radius of curvature were selected so that a two-dimensional approximation could be used. Comparisons with an axisymmetric model were made for some features to check the validity of the two-dimensional assumption. The best-fit elastic thickness was found for each profile crossing a given flexural feature. In addition, the surface stress and bending moment at the first zero crossing of each profile were also calculated.

Results: Flexural amplitudes and elastic thicknesses obtained for 12 features vary significantly. Three examples of the model fitting procedure are shown in Fig. 1, where the solid line is the data and the dashed line the best-fit model. The lowest elastic thickness was obtained at Nishtigri Corona (8–12 km) where the flexural amplitude is low (0.4 km). Nightingale Corona was typical of several other areas with elastic thicknesses in the range 18–25 km and a flexural amplitude of about 0.8 km. At W. Dali Chasma the lithosphere appears very thick (25–40 km) and the flexural amplitude is large (3 km); a similar result was obtained for other areas in Aphrodite Terra. However, the amplitude of the flexure at Artemis and Latona Coronae and at the chasmata of Aphrodite Terra is extremely large and it is likely that in these areas the lithosphere is flexed beyond its elastic limit. In some regions of extreme curvature it was not possible to model the topography to the base of the flexural moat (e.g., W. Dali Chasma, Fig. 1); this is probably due to extensive faulting. SAR images of several areas exhibiting flexure
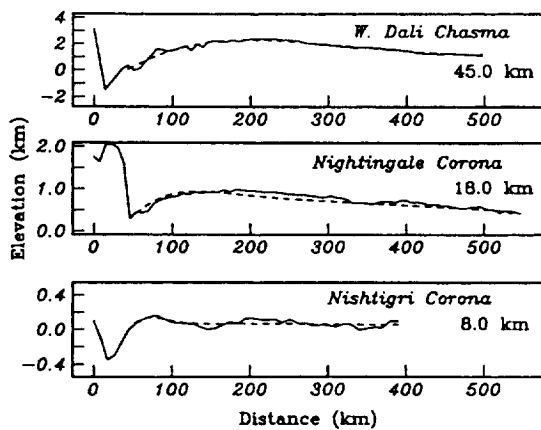
Fig. 1. Profiles (solid lines) and best-fit models (dashed lines) for three flexural features on Venus. The best-fit elastic thickness for each profile is indicated. Note the difference in vertical scales in each case. Elevation is relative to a datum of 6051.0 km.
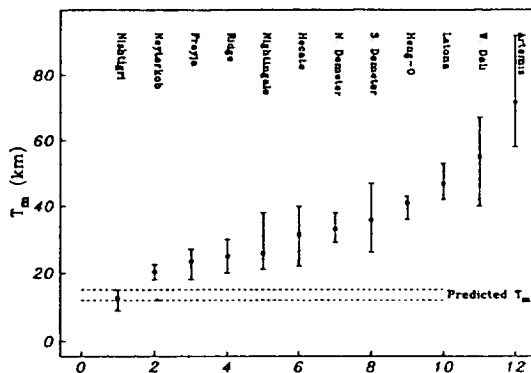
Fig. 2. Mechanical thicknesses obtained for 12 flexural features on Venus. Only Nishtigri Corona gives a lithospheric thickness compatible with that predicted (see text). The very high values obtained for Arcemis Corona and W. Dali Chasma are a result of the lithosphere being flexed beyond its elastic limit at these locations.

reveal circumferential fractures on the flexural outer rise, roughly coincident with the predicted location of high surface stresses.

Elastic thickness and curvature can be used to obtain mechanical thickness if the yield strength envelope for the lithosphere is known [4]. For features that are flexed beyond the elastic limit (i.e., moment saturated) an alternative approach is to calculate the thermal gradient directly from the saturation moment. Results from both these methods will be presented. Figure 2 shows the mechanical thicknesses obtained for Venus, assuming a dry olivine rheology, brittle behavior in the upper lithosphere, and ductile flow in the lower lithosphere [5]. Error bars are calculated from the range of best-fit elastic thickness for a given feature. The horizontal dashed lines are upper and lower bounds on the mechanical thickness expected for Venus, based on heat-flow scaling arguments [6]. It is evident that only one location studied gives a lithospheric thickness compatible with that predicted (15 km). The mechanical thickness at most other features is in the range 20–45 km. This implies mean heat flow values in the range 20–46 mW m^{-2}, much less than the

predicted 74 mW m^{-2}. On Earth lithospheric thickness is related to age. Variation in lithospheric thickness obtained from different coronae on Venus may indicate relative ages and therefore provide a constraint on coronae evolution.

References: [1] Sandwell D. T. and Schubert G. (1992) *JGR*, in press. [2] McKenzie D. P. et al. (1992) *JGR*, in press. [3] Johnson C. L. and Sandwell D. T. (1992) *LPSC XXII*, 619–620. [4] McNutt M. J. (1984) *JGR*, *89*, 11180–11194. [5] Solomon S. and Head J. (1990) *GRL*, *17*, 1393–1396. [6] Phillips R. J. and Malin M. C. (1983) In *Venus* (D. M. Hunten et al., eds.), Univ. of Arizona,

N93-14330

IGNEOUS AND TECTONIC EVOLUTION OF VENUSIAN AND TERRESTRIAL CORONAE. J. S. Kargel and G. Komatsu, Lunar and Planetary Laboratory, University of Arizona, Tucson AZ 85721, USA.

A great variety of tectonic and volcanic features have been documented on Venus. It is widely appreciated that there are close spatial associations among certain types of tectonic structures and some classes of volcanic flows and constructs. Coronae are endowed with a particularly rich variety of volcanism [1,2,3]. It is thought that coupled tectonic and volcanic aspects of coronae are cogenetic manifestations of mantle plumes. An outstanding feature of most venusian coronae is their circular or elliptical shape defined by peripheral zones of fracturing and/or folding. Some coronae are composite, consisting of two or more small coronae within a larger enclosing corona, suggesting complex histories of structured diapirism analogous in some ways to salt dome tectonics [4]. Coronae range widely in size, from smaller than 100 km to over 1000 km in diameter [3].

Volcanic features associated with venusian coronae are further documented in Figs. 1–4. These include lunarlike sinuous rilles, thin lava flows, cinder cone-like constructs, shield volcanos, and pancake domes. Several types of volcanic features are often situated within or near a single corona, in many instances including landforms indicating effusions of both low- and high-viscosity lavas. In some cases stratigraphic evidence brackets emplacement of pancake domes during the period of tectonic development of the corona, thus supporting a close link between the igneous and tectonic histories of coronae. These associations suggest emplacement of huge diapirs and massive magmatic intrusions, thus producing the tectonic deformations defining these structures. Igneous differentiation of the intrusion could yield a range of lava compositions. Head and Wilson [5] suggested a mechanism that would cause development of neutral buoyancy zones in the shallow subsurface of Venus, thereby tending to promote development of massive igneous intrusions.

Large igneous intrusive complexes are common on the modern Earth, especially in magmatic arcs associated with subduction zones. Extensive igneous evolution occurs in magma arc batholiths [6], yielding compositionally diverse magmas. Large terrestrial layered basaltic intrusions, usually not associated with subduction zones, also have been common through Earth history. Some of these, including the famous Skaergaard Intrusion, have undergone considerable igneous differentiation without involving processes directly related to plate tectonics [7].

Although coronae are especially numerous and varied on Venus, Earth also has coronalike structures [8]. Whether terrestrial coronalike analogues truly involved the same tectonic processes responsible for venusian coronae is uncertain, but development of these struc-

Fig. 1. Corona with pancake dome some 20 km in diameter (left center), and field of cinder cones and/or shield volcanos (top center). Scene width 200 km. Radar illumination is from the left.
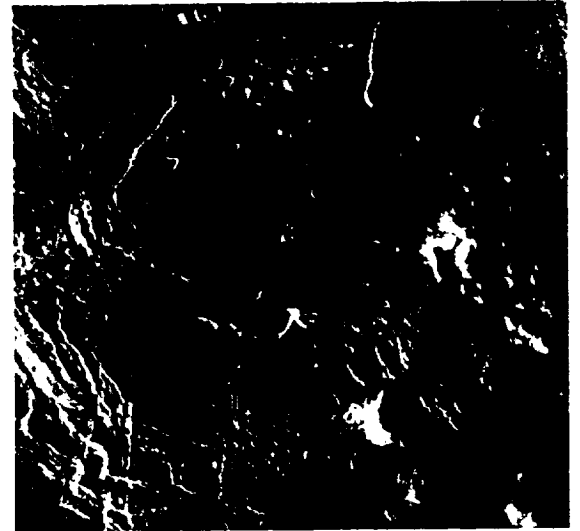
Fig. 3. Small corona containing a pancake dome and associated with other domes and flow fields having high radar contrast. Scene width 460 km. Radar illumination from the left.

Fig. 2. Corona with pancake domes and other steep-sided volcanic constructs (right half) and lunarlike sinuous rilles (upper right). Radar illumination from the left.

Fig. 4. Corona associated with pancake domes ranging from 20 to 60 km in diameter (lower left quadrant) and thin flows having high radar contrast (bottom third of scene). Scene width 570 km. Radar illumination is from the left.

tures was especially common during the Archaean. The Pilbara-Hamersley Craton in Western Australia is among the most compelling terrestrial corona analogues. The principal phase of igneous and tectonic development of this early continental crustal fragment occurred between 2900 and 3500 m.y. ago [9,10] when massive tectonic and igneous activity occurred within a precisely elliptical region (a = 560 km, b = 400 km) bounded by tectonic compressional folds and faults [9]. This tectonic ellipse (Fig. 5) is one of several similar blocks forming most of the Australian shield. These blocks are interpreted as first-order diapiric structures (coronae). The early phase of activity in the Pilbara Craton involved intrusion of 20 or more granitoid batholiths, each typically 30–60 km in diameter.

Each pluton caused complex deformation around its periphery (Fig. 6), producing structures resembling the larger-scale Pilbara ellipse. Sedimentation and extrusive volcanic activity (mainly basaltic) occurred simultaneously with granitoid plutonism, forming inter-pluton volcano-sedimentary piles (the Pilbara Supergroup) up to 30 km thick [10]. These large granitoid batholiths are termed second-order diapirs, which themselves are composed of discrete third-order structures with diameters of order 10 km, many of which also have marginal deformation zones [10,11].

This phase in the evolution of the Pilbara Block was followed by a decline in igneous and tectonic activity. 2700 m.y. ago Pilbara was a rugged landmass, but the principal geologic agents tended to
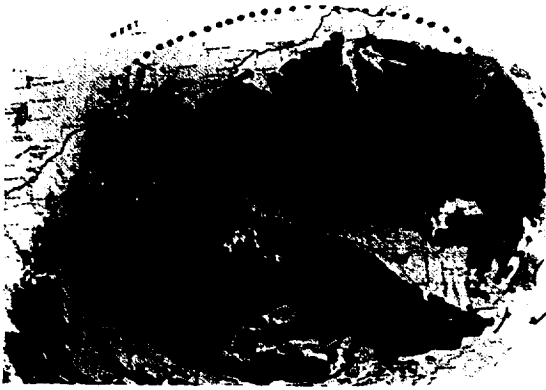
Fig. 5. Portion of geologic map of Pilbara Block and vicinity. Pilbara ellipse has dotted outline. Major granitoid intrusions are in solid outline. Box shows areas of Fig. 6.

Fig. 6. Landsat image portraying three granitoid plutons and intervening volcanic and sedimentary Pilbara Supergroup. The latter originally accumulated in interpluton troughs and were deformed as the plutons intruded. Scene is 150 km left to right.

produce an increasingly graded topography, including mafic volcanism and fluvial and lacustrine processes [9,10]. By 2500 m.y. ago the region had evolved to a tectonically fairly stable marine platform or continental shelf inundated by an epeiric sea, and was dominated by deposition of evaporites (banded iron formation and dolomite) [9,12]. By the end of this phase, the region had acquired essentially its present configuration, although the Pilbara Craton possibly may not have been integrated with the rest of Australia.

References: [1] Head J. W. et al. (1991) *Science*, *252*, 276–287. [2] Solomon S. C. et al. (1991) *Science*, *252*, 297–311. [3] Stofan E. R. et al. (1991) *JGR*, *96*, 20933–20946. [4] Jackson M. P. A. et al. (1990) *GSA Mem.*, *177*, 139 pp. [5] Head J. W. and Wilson L. (1992) *JGR*, *97*, 3877–3904. [6] Pitcher W. S. (1978) *Geol. Soc. Lond.*, *135*, 157–182. [7] Wager L. R. and W. A. Deer (1939) *Medd. om Gronland*, *105*, 4, 1–352. [8] Baker V. R. et al. (1992) in press. [9] Trendall A. F. (1983) In *Iron-Formations: Facts and Problems*, 69–129, Elsevier, Amsterdam. [10] Hickman A. R. (1983) *Geol. Surv. West. Aust. Bull.*, 127. [12] Kargel J. S. and Sonnett C. P. (1992) *EPSL*, submitted.

N93-14331

VENUS: THE CASE FOR A WET ORIGIN AND A RUNAWAY GREENHOUSE.

J. F. Kasting, Department of Geosciences, 211 Deike, Penn State University, University Park PA 16802, USA.

To one interested in atmospheric evolution, the most intriguing aspect of our neighboring planet Venus is its lack of water. Measure-

ments made by Pioneer Venus and by several Venera spacecraft indicate that the present water abundance in Venus' lower atmosphere is of the order of 20 to 200 ppmv [1], or 3×10^{-6} to 3×10^{-5} of the amount of water in Earth's oceans. The exact depletion factor is uncertain, in part because of an unexplained vertical gradient in H_2O concentration in the lowest 10 km of the venusian atmosphere [1], but the general scarcity of water is well established. The interesting question, then, is: Was Venus deficient in water when it formed and, if not, where did its water go?

Planetary formation models developed 20 years ago by Lewis [2] predicted that Venus should have formed dry because of the higher temperatures prevailing at its location in the solar nebula, which would have precluded the condensation of hydrated silicate minerals. The predictions of this "equilibrium condensation" model have since been challenged on two different grounds: (1) Accretionary models now predict extensive gravitational mixing of planetesimals throughout the inner solar system [3] and (2) the condensation of hydrated silicates from the gas phase is now thought to be kinetically infeasible [4]; thus, planetary water must be imported in the form of H_2O ice. Taken together, these new ideas imply that Earth's water was derived from materials that condensed in the asteroid belt or beyond and were subsequently scattered into the inner solar system. If this inference is correct, it is difficult to imagine how Venus could have avoided getting plastered with a substantial amount of water-rich material by this same process. The conclusion that Venus was originally wet is consistent with its large endowment of other volatiles (N_2, CO_2, and rare gases) and with the enhanced D/H ratio in the present atmosphere [5,6]. Maintenance of a steady-state water inventory by cometary impacts [7] cannot explain the present D/H ratio if the water abundance is higher than 20 ppmv because the time constant for reaching isotopic equilibrium is too long [1].

The most likely mechanism by which Venus could have lost its water is by the development of a "runaway" or "moist" greenhouse atmosphere followed by photodissociation of water vapor and escape of hydrogen to space [8–11]. Climate model calculations that neglect cloud albedo feedback [9] predict the existence of two critical transitions in atmospheric behavior at high solar fluxes (Fig. 1): (1) at a solar flux of ~1.1 times the value at Earth's orbit, S_0, the abundance of stratospheric water vapor increases dramatically, permitting rapid escape of hydrogen to space (termed a "moist greenhouse") and (2) at a solar flux of ~1.4 S_0, the oceans vaporize entirely, creating a true "runaway greenhouse." If cloudiness increases at high surface temperatures, as seems likely, and if the dominant effect of clouds is to cool the planet by reflecting incident
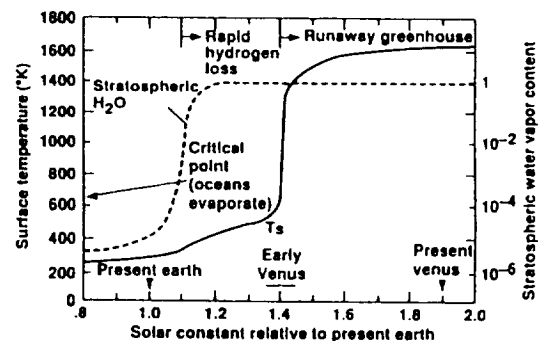
Fig. 1. Diagram illustrating the two key solar fluxes for water loss, as calculated in [9]. The critical point for pure water (above which the oceans evaporate entirely) is at 647 K and 220.6 bar. Figure courtesy of J. Pollack.

solar radiation, the actual solar flux required to create "moist" or "runaway" conditions would be higher than the values quoted above. (Indeed, some authors [12] have argued that cloud feedback would prevent a runaway greenhouse from ever occurring.) Early in solar system history, solar luminosity was about 25% to 30% less than today, putting the flux at Venus' orbit in the range of 1.34 S_0 to 1.43 S_0. Thus, it is possible that Venus had liquid water on its surface for several hundred million years following its formation. Paradoxically, this might have facilitated water loss by sequestering atmospheric CO_2 in carbonate rocks and by providing an effective medium for surface oxidation.

Continued progress in understanding the history of water on Venus requires information on the redox state of the atmosphere and surface. The loss of an ocean of water (or some fraction thereof) should have left substantial amounts of oxygen behind to react with the crust. This oxygen would presumably be detectable if we had core samples of crustal material. Barring this, its presence or absence might be inferred from accurate measurements of lower atmospheric composition. Another spacecraft mission to Venus could help to resolve this issue and, at the same time, shed light on the question of whether clouds will tend to counteract global warming on Earth.

References: [1] Donahue T. M. and Hodges R. R. Jr. (1992) *Icarus,* in press. [2] Lewis J. S. (1972) *Icarus, 16,* 241–252. [3] Wetherill G. W. (1980) *Annu. Rev. Astron. Astrophys., 18,* 77–113. [4] Prinn R. G. and Fegley B. Jr. (1989) In *Origin and Evolution of Planetary and Satellite Atmospheres* (S. K. Atreya et al., eds.), 78–136, Univ. of Arizona, Tucson. [5] Donahue T. M. et al. (1982) *Science, 216,* 630–633. [6] McElroy M. B. et al. (1982) *Science, 215,* 1614–1618. [7] Grinspoon D. H. and Lewis J. S. (1988) *Icarus, 74,* 21–35. [8] Kasting J. F. et al. (1984) *Icarus, 57,* 335–355. [9] Kasting J. F. (1988) *Icarus, 74,* 472–494. [10] Kasting J. F. and Pollack J. B. (1983) *Icarus, 53,* 479–508. [11] Kumar S. et al. (1983) *Icarus, 55,* 369–389. [12] Ramanathan V. and Collins W. (1991) *Nature, 351,* 27–32.

N93-14332

VENUS TECTONIC STYLES AND CRUSTAL DIFFERENTIATION.
W. M. Kaula and A. Lenardic, University of California, Los Angeles CA 90024, USA.

Two of the most important constraints are known from Pioneer Venus data: the lack of a system of spreading rises, indicating distributed deformation rather than plate tectonics; and the high gravity:topography ratio, indicating the absence of an asthenosphere. In addition, the high depth:diameter ratios of craters on Venus [1] indicate that Venus probably has no more crust than Earth. The problems of the character of tectonics and crustal formation and recycling are closely coupled. Venus appears to lack a recycling mechanism as effective as subduction, but may also have a low rate of crustal differentiation because of a mantle convection pattern that is more "distributed," less "concentrated," than Earth's. Distributed convection, coupled with the nonlinear dependence of volcanism on heat flow, would lead to much less magmatism, despite only moderately less heat flow, compared to Earth. The plausible reason for this difference in convective style is the absence of water in the upper mantle of Venus [2].

The most objective measure of the nature of motion that we can hope to infer is the spherical harmonic spectrum of its surface, or near-surface, velocities. A compact expression of this spectrum is a spectral magnitude M and slope n

$$\sigma_1(v) = M\, 1^{-n} \tag{1}$$

where $\sigma_1(v)$ is the rms magnitude of a normalized spherical harmonic coefficient of degree 1. A concentrated flow, characterized by large segments moving together, has a steep slope, thence a high value of n, while a distributed flow, with small segments, has a small value of n. We cannot measure velocities directly on Venus. But in a planet dominated by a strong outer layer, in which the peak stresses are at a rather shallow depth, the magnitudes of gravitational potential V and poloidal velocity v_s are coupled [3]

$$M(\delta V)/M(v_s) = 12\pi G\eta/g \tag{2}$$

where η is the effective viscosity of the lithosphere, the ratio of stress to strain rate over long durations. The value inferred from the magnitudes M for Earth is 4×10^{21} Pa-s, probably most influenced by subduction zones. Support for this model is that the gravity and velocity spectra on Earth have the same slope n to two significant figures, 2.3 [3,4]. On Venus the spectral slope of gravity, $n(\delta V)$, is appreciably lower over degrees that can be determined reliably—about 1.4 [4], strongly suggesting a more regional, less global, velocity field than on Earth.

A basic constraint on the velocity field that is somewhat independent of stresses, and thence rheology, is that, at the mantle depth where convection dominates—more than 150 km—there must be a correlation of vertical velocity v_r (coupled to the poloidal velocity v_s by continuity) and temperature variations ΔT that lead to an integral accounting for most of the total heat delivery Q from greater depths

$$Q = \int \rho C v_r \Delta T dS \tag{3}$$

For a mean heat flow of 60 mW/m² and average temperature variation ΔT of 100°C, equation (3) gives an estimate of 0.6 cm/yr for v_r. In the Earth, plate tectonics lead to such concentrations of v_r and ΔT at shallower depths that it is difficult to draw inferences from observed heat flow relevant to equation (3). However, the constraint exists, and its implication for the velocity spectrum of Venus should be explored.

The altimetry and imagery of Venus also indicate a regionality of Venus tectonics, even though magnitudes of velocities cannot be inferred because of dependence on unknown viscosity. For example, Maxwell Montes is comparable to the Andes in height and steepness (suboceanic). But the material subducted under the Andes clearly comes from the southeast Pacific Rise, over 4000 km away (despite the interruption of the Nazca Rise), while only 500 km from the Maxwell front is a scarp, and beyond that a much more mixed, apparently unrelated, variety of features. Clearly, Maxwell is more local than the Andes. A significant difference of Venus tectonics from Earth is the absence of erosion, which removes more than 1 km/100 m.y. from uplands.

Hypotheses for why Venus does not have crustal formation in a ridge system, but rather a more distributed magmatism correlated with a more regional tectonism, include (1) the lack of plate pull-apart due to inadequate subduction; (2) the lack of plate pull-apart due to drag on the lithosphere from higher viscosity: i.e., no asthenosphere; (3) the lesser concentration of flow from within the mantle, also due to higher viscosity; (4) lower temperatures, due to less initial heating and more effective retention of lithophiles in the crust; (5) higher melting temperatures, due to lack of water content, and (6) lower mobility of magma relative to matrix, due to (a) low

H_2O content, (b) low-density overburden, or (c) lesser horizontal length scale of flow.

Relevant to these hypotheses is that differentiation on Venus requires more than adiabatic upwelling and pressure-release melting. In models of this process on Earth [e.g., 5,6] the availability of mantle material to flow into the region is taken as given; the concern is about the rising of magma within a solid matrix, in particular, the mechanism(s) concentrating the melt in a narrow vertical slab. The viscosity of the melt, and hence its ability to separate, is affected by water content. Differentiation from a plume, without pull-apart, under a layer of higher strength or lower density (as is more likely on Venus), requires a surplus of heat, and thus is likely to lead to a lower rate of magmatism for a given heat flow. Also the inhibition of upward flow by a low-density overlying layer may lead to less differentiation of crust. Application of models of a plume under a lithosphere [7] to Venus features such as Atla and Beta indicate that appreciably higher upper mantle viscosities may cause pressure gradients to account for these great peaks in the geoid.

We have applied finite element modeling to problems of the interaction of mantle convection and crust on Venus [8]. The main emphasis has been on the tectonic evolution of Ishtar Terra, as the consequence of convergent mantle flow. The early stage evolution is primarily mechanical, with crust being piled up on the downstream side. Then the downflow migrates away from the center. In the later stages, after more than 100 m.y., thermal effects develop due to the insulating influence of the thickened crust. An important feature of this modeling is the entrainment of some crustal material in downflows.

An important general theme in both convergent and divergent flows is that of mixing vs. stratification. Models of multicomponent solid-state flow obtain that lower-density crustal material can be entrained and recycled, provided that the ratio of low-density to high-density material is small enough (as in subducted slabs on Earth). The same considerations should apply in upflows; a small percent partial melt may be carried along with its matrix and never escape to the surface. Models that assume melt automatically rising to the crust and no entrainment or other mechanism of recycling lower-density material [e.g., 9] obtain oscillatory behavior, because it takes a long time for heat to build up enough to overcome a Mg-rich low-density residuum. However, these models develop much thicker crust than consistent with estimates from crater depth:diameter ratios [1].

References: [1] Sharpton V. L. and Edmunds M.S. (1991) *Eos*, 72, 289. [2] Kaula W. M. (1992a) *Proc. IUGG Symp. Chem. Evol. Planets*, in press. [3] Kaula W. M. (1980) *JGR*, 85, 7031. [4] Kaula W. M. (1992b) *Proc. IAG Symp. Grav. Field Det. Space Air Meas.*, in press. [5] McKenzie D. P. (1985) *EPSL*, 74, 81. [6] Scott D. R. and Stevenson D. J. (1989) *JGR*, 94, 2973. [7] Sleep N. H. (1990) *JGR*, 95, 6715. [8] Lenardic A. et al. (1991) *GRL*, 18, 2209. [9] Parmentier E. M. and Hess P. C. (1992) *LPSC XXIII*, 1037.

N93-14333

LARGE SHELD VOLCANOS ON VENUS: THE EFFECT OF NEUTRAL BUOYANCY ZONE DEVELOPMENT ON EVOLUTION AND ALTITUDE DISTRIBUTION. S. Keddie and J. Head, Department of Geological Sciences, Brown University, Providence RI 02912, USA.

The Magellan mission to Venus has emphasized the importance of volcanism in shaping the surface of the planet. Volcanic plains make up 80% of the terrain and hundreds of regions of localized eruptions have been identified. Large volcanos, defined as edifices with diameters greater than 100 km, are the sites of some of the most voluminous eruptions. Head et al. [1] have identified 158 of these structures. Their spatial distribution is neither random (see Fig. 1) nor arranged in linear chains as on the Earth; large volcanos on Venus are concentrated in two large, near-equatorial clusters that are also the site of many other forms of volcanic activity [1].

The set of conditions that must be met on Venus that controls the change from widespread, distributed volcanism to focused, shield-building volcanism is not well understood. Future studies of transitional features will help to address this problem. It is likely, however, that the formation and evolution of a neutral buoyancy zone (NBZ) plays an important role in both determining the style of the volcanism and the development of the volcanic feature once it has begun to erupt. Head and Wilson [2] have suggested that the high surface pressure on Venus may inhibit volatile exsolution, which may influence the density distribution of the upper crust and hence control the nature and location of a NBZ. The extreme variations in pressure with elevation may result in significantly different characteristics of such a NBZ at different locations on the planet. In order to test these ideas regarding the importance of NBZ development in the evolution of a large shield and to determine the style of volcanism, three large volcanos that occur at different basal elevations were examined and the distribution of large volcanos as a function of altitude was determined.

The evolution of Sapas Mons, a 600-km-diameter shield volcano, was studied [3]. Six flow units were identified on the basis of radar properties and spatial and temporal relations. The distinctive variation between units was attributed to the evolution of magma in a large chamber at depth. The presence of summit collapse structures and radial fractures, interpreted to be the surface expression of lateral dikes, supports this suggestion. Theory predicts that volcanos located at the altitude of Sapas Mons should have large magma chambers located at zones of neutral buoyancy at relatively shallow depths beneath the substrate [2]. Not only does the evidence from the flow units suggest that such a zone is present, but the size of the summit collapse and the near-surface nature of the radial dikes indicates that the chamber is both large (on the order of 100 km in diameter) and shallow.

In comparison to Sapas Mons, two other volcanos at different elevations were examined. Theory predicts that the volcano at the

Fig. 1. Location of large volcanos as a function of latitude. The dark-shaded columns indicate where volcanos would be located if they were randomly distributed on the surface as a function of the percentage of area at a given latitude. The striped columns show where the volcanos actually occur. Note the paucity of volcanos at higher latitudes and the concentration in the equatorial region of the planet.

highest basal elevation, Maat Mons, should have a well-developed, large, and relatively deeper NBZ and that the volcano at the lowest altitude, an unnamed volcano located southwest of Beta Regio at 10°, 273°, should have either a poorly developed magma chamber or none at all [2]. Preliminary mapping of Maat Mons [3] identified at least six flow units that exhibit greater variations in morphology and radar properties than the flows of Sapas Mons. These units are also spatially and temporally distinct and suggest the eruption of a continuously evolving magma. Although smaller in diameter, the summit caldera is much better defined than the depression at Sapas. The inferred young age of Maat (Klose et al. [4] suggest that it may even be "active") may mean that the chamber has not yet grown to "full size," explaining the relatively smaller caldera. There is no evidence of radial fractures at Maat Mons, suggesting that if lateral dike propagation occurred, it was sufficiently deep that there was no surface expression. In contrast, the unnamed volcano has no summit features, no radial dikes, and only three flow units that exhibit considerable morphologic variations within units [3]. These observations suggest that either the NBZ is very poorly developed or it does not exist and the magma erupts directly at the surface. Thus the character of three large volcanos on Venus supports the suggestion that basal altitude can play a critical role in the development of a NBZ. Examination of other volcanos at a greater range of altitudes will help to further test this hypothesis.

In addition to studying the detailed evolution of three large volcanos, the altitude and height distribution of all volcanos was determined. Although in general there is a broad distribution of large volcanos as a function of altitude, there is somewhat of a paucity of large volcanos at elevations below 6051 km (Fig. 2). Between 6051 and 6053 km the number of volcanos is slightly greater than expected and above this an absence of volcanos is again observed. This absence at the highest elevations is probably due in large part to the predominance of tessera terrain at these elevations. Those volcanos that do occur in this area are associated with regions of uplift and rifting probably caused by mantle upwelling. Head and Wilson [2] suggested that below an elevation of 6051 km it is unlikely that a NBZ would develop, due largely to the high atmospheric pressure, and thus edifice growth would be inhibited. They also found that the first few kilometers above 6051 km would be most favorable for edifice growth as NBZs develop early at rela-
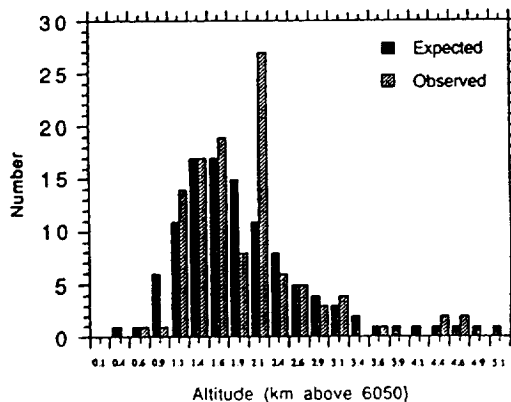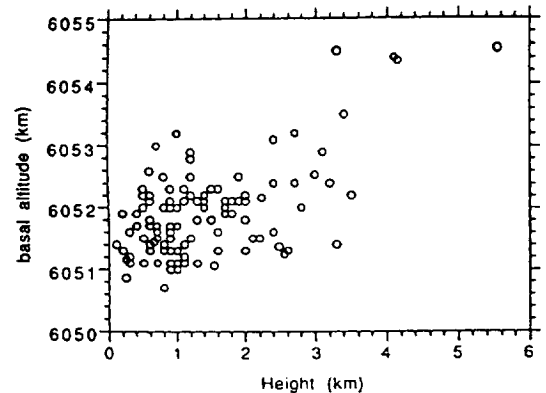
Fig. 3. Graph showing the heights of 110 large volcanos as a function of basal altitude. The majority of volcanos cluster between 6051 and 6053 km and there is a weak positive correlation between height and basal altitude. The majority of volcanos that occur above 6052.8 km and are taller than 2.6 km are located in zones of mantle upwelling and/or rifting.

tively shallow depths beneath the surface. A survey of 110 large volcanos found that this altitude distribution appears to be observed on Venus.

The height of volcanos is also related to basal altitude and the development of zones of neutral buoyancy. There is a weak correlation of volcano height with basal elevation (Fig. 3). Although many factors need to be considered to explain this correlation, in a general sense NBZ development is responsible. As magma chambers become larger, and thus the "life" of the volcano is lengthened, there is an opportunity for a greater number of repeated, relatively small volume eruptions. This type of eruption enhances edifice growth. Head and Wilson [2] suggested that NBZs will grow to relatively larger sizes at greater altitudes. Therefore this correlation of height with altitude is expected.

Although a good deal more work needs to be done to test the idea that basal altitude plays a significant role in the development and evolution of neutral buoyancy zones on Venus, studies of the altitude distribution and heights of many large volcanos, as well as the evolution of individual volcanos, indicates that NBZ development is occurring, that it is varying, apparently as a function of altitude, and that the morphology and history of large edifices is being strongly influenced.

References: [1] Head J. W. et al. (1992) *JGR*, submitted. [2] Head J. W. and Wilson L. (1992) *JGR*, *97*, 3877–3903. [3] Keddie S. T. and Head J. W. (1992) *LPSC XXIII*, 669–670. [4] Klose K. B. et al. (1992) *JGR*, submitted. ·

N93-14334

MANTLE PLUMES ON VENUS REVISITED. Walter S. Kiefer, Code 921, Goddard Space Flight Center, Greenbelt MD 20771, USA.

The Equatorial Highlands of Venus consist of a series of quasicircular regions of high topography, rising up to about 5 km above the mean planetary radius [1]. These highlands are strongly correlated with positive geoid anomalies, with a peak amplitude of 120 m at Atla Regio [2,3]. Shield volcanism is observed at Beta, Eistla, Bell, and Atla Regiones and in the Hathor Mons-Innini Mons-Ushas Mons region of the southern hemisphere [4–10].
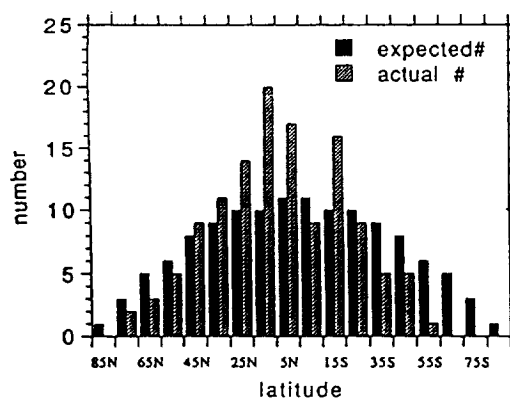

Fig. 2. Location of large volcanos as a function of basal altitude. The dark-shaded columns indicate where volcanos would be located if they were randomly distributed on the surface as a function of the percentage of area at a given altitude. The striped columns show where the volcanos actually occur. See text for a discussion of the implications of this distribution.

Volcanos have also been mapped in Phoebe Regio [11], and flood volcanism is observed in Ovda and Thetis Regiones [10,12]. Extensional tectonism is also observed in many of these regions [5,10,12,14–16].

It is now widely accepted that at least Beta, Atla, Eistla, and Bell Regiones are the surface expressions of hot, rising mantle plumes [e.g., 5,9,10,12,14–16]. Upwelling plumes are consistent with both the volcanism and the extensional tectonism observed in these regions. The geoid anomalies and topography of these four regions show considerable variation. Peak geoid anomalies exceed 90 m at Beta and Atla, but are only 40 m at Eistla and 24 m at Bell [2]. Similarly, the peak topography is greater at Beta and Atla than at Eistla and Bell [1]. Such a range of values is not surprising because terrestrial hotspot swells also have a wide range of geoid anomalies and topographic uplifts [17]. Kiefer and Hager used cylindrical axisymmetric, steady-state convection calculations to show that mantle plumes can quantitatively account for both the amplitude and the shape of the long-wavelength geoid and topography at Beta and Atla [15,18]. In these models, most of the topography of these highlands is due to uplift by the vertical normal stress associated with the rising plume. Additional topography may also be present due to crustal thickening by volcanism and crustal thinning by rifting. Smrekar and Phillips [19] have also considered the geoid and topography of plumes on Venus, but they restricted themselves to considering only the geoid-topography ratio and did not examine either the geoid and topography amplitudes separately or the shapes of anomalies.

Several factors could contribute to the smaller geoid and topography amplitudes at Eistla and Bell Regiones. Comparison of models in axisymmetric and two-dimensional Cartesian geometries shows that elongated upwellings produce smaller geoid anomalies and topographic uplifts [18]. Eistla is an elongated topographic feature [1], suggesting the possibility of an elongated upwelling. Recent modeling of gravity anomalies in this region also indicates a component of elongated upwelling, although there is also evidence for plume-like upwellings with more circular planforms beneath western Eistla (Sif Mons and Gula Mons) and to a lesser extent beneath central Eistla (Sappho Patera) [14]. The elongated nature of the Eistla upwelling could contribute to the relatively small geoid and topography in this area. The geoid and topography of a plume are also increasing functions of the aspect ratio of the upwelling [18]. The plumes inferred to exist beneath western and central Eistla are each about 1000 km across [14], much less than the 2000 to 2500 km dimensions of Beta and Atla. The narrowness of the Eistla plumes could be another factor that contributes to the relatively small geoid and topography in this region. Bell Regio is also smaller than Beta and Atla, which might contribute to its smaller geoid and topography. In the southern hemisphere, the cluster of shield volcanos Hathor Mons, Innini Mons, and Ushas Mons [7] are separated by a maximum distance of about 1500 km. If these features are plume related [15], their moderate amplitude geoid (15 m) and regional topography (1 km) may be due to a relatively narrow underlying plume. Another factor that may contribute to variations in the geoid and topographic uplift associated with different plumes is the temperature contrast between plumes and the adjacent mantle. Both the geoid anomaly and the topographic uplift are linearly proportional to the magnitude of the temperature contrast. On Earth, the temperature contrasts between various plumes and the surrounding mantle are estimated to vary by about a factor of 2 [20]. Time-dependent changes in the thermal structure of a plume, due to the formation of boundary layer instabilities, can

also cause the geoid and topography of a plume to vary by up to about 50% relative to their time-averaged values [21].

Both mantle plumes and cold downwellings have been proposed as possible models for Ovda and Thetis Regiones. Plume models have been proposed by Kiefer and Hager [15,22] and by Herrick and Phillips [16,23]. These models all invoke some form of time-dependent plume behavior, but the details of this behavior were not quantified in these works. Kiefer and Kellogg have begun quantifying the effects of time-dependent convection in spherical axisymmetric geometry on the geoid anomalies and dynamic topography of plumes [21]. An important difference between the plume models for Ovda and Thetis is in the geometry of the plume. In the Herrick and Phillips model [23], a plume is visualized as a discrete blob of hot material that detaches from the lower thermal boundary layer and rises to the surface. This produces an episode of tectonic uplift and extensive magmatism, followed by topographic subsidence and deformation of the thickened crust once the blob collapses at the base of the lithosphere. In the Kiefer and Hager model [15], plumes are assumed to be continuous between the upper and lower thermal boundary layers, although boundary layer instabilities may be superimposed on the basic structure. Continuous plumes are consistent both with the results of numerical modeling [e.g., 15,18] and with the record of nearly continuous volcanism at terrestrial hotspots such as Hawaii [24]. In this model, the ascent of a boundary layer instability up a plume will alter both the geoid anomaly and the topographic uplift of the plume. In models that do not include temperature-dependent viscosity, the increased volume of buoyant material increases both the geoid anomaly and the dynamic topography of the plume [21].

The rising thermal anomaly will heat the upper mantle and should cause a temporary decrease in the regional viscosity. This will alter the expected geoid and topography signatures but has not yet been quantified. At a minimum, the creation of a temporary low-viscosity zone should decrease the apparent compensation depth of these features [25]. This is consistent with the observation that the apparent compensation depths of Ovda and Thetis are shallower than for Beta, Atla, Bell, and Eistla [14,19]. The rising thermal anomaly should also cause an episode of increased volcanic activity; efforts are underway to quantify this effect. An increased volcanism rate should lead to an increased resurfacing rate and a young cratering age, consistent with the observation that Ovda and Thetis have some of the lowest impact crater densities observed on the planet [26]. The increased volcanism rate should also thicken the crust. Thick crust in an area of high heat flow should have a very low vertically integrated strength [27], and should therefore be quite susceptible to tectonic disruption. Sources of stress that could contribute to this disruption include the flow driven by the rising plume (which will vary with time as the plume's thermal structure evolves), viscous flow of the crust down topographic gradients, and other regional stresses that may exist. This may account for the observed high level of tectonic deformation in Ovda, Thetis, and Phoebe [10].

Eventually, the thermal anomaly beneath the highland will dissipate by a combination of lateral advection and conductive cooling and the topography and geoid anomaly of the plume will return to their normal levels. Continuing volcanism at normal rates will gradually cover the surface of the highland, obscuring evidence for earlier episodes of tectonic disruption. This cycle of boundary layer instability formation followed by a period of enhanced volcanism and tectonism may be repeated episodically [21]. The tessera observed on the flanks of Beta and Bell Regiones [6,10,28] may be

remnants of deformation from earlier plume instability cycles that have so far escaped resurfacing since the most recent boundary layer instability events at these plumes. If so, this would essentially invert the sequence proposed by Herrick and Phillips [23], who suggested that Beta Regio represents an early stage of their blob model and that Thetis and Ovda represent later stages.

As an alternative to the mantle plume model, Bindschadler and colleagues [12,29] proposed that Ovda, Thetis, and Phoebe Regiones formed by crustal convergence over downwelling mantle "coldspots." As arguments against a plume model, coldspot advocates [12] point to the absence of evidence for early volcanism, prior to the formation of tessera, in these areas. This could be due to plumes rising beneath preexisting tessera, as suggested for Beta Regio by Senske et al. [28]. Alternatively, tessera formation may be an intrinsic part of the plume instability evolutionary sequence, but the tectonic disruption involved in forming the tessera may be sufficiently severe to destroy any evidence for earlier volcanism. A second argument that has been used against the plume model is the observation that the tessera is embayed by later flood volcanism, which is asserted [12] to be contrary to the plume model. This assertion is based on the detached blob model of a plume [23]. If a vertically continuous plume exists [15,18], then adiabatic decompression provides a continuing source of magma. In this case, volcanism and tectonic deformation can go on simultaneously, leading to possible complex superposition relationships.

Several observations have been asserted to favor the coldspot model, including the existence of steep topographic slopes on the margins of some highlands, margin-parallel compression at high elevations, and extensional deformation superimposed on compressional features [12]. However, a combination of dynamic uplift and crustal thickening by volcanism might be able to produce the observed marginal slopes. Margin-parallel compression might be the result of viscous flow of volcanically thickened crust down the topographic gradient. In such a model, one would expect extension on the topographic highs and compression on the lower flanks of the highland. However, as boundary layer instabilities move laterally through the upper thermal boundary layer, the margin of the highland can migrate laterally outward [21]. Thus, compressional features that originally formed at low elevations can be uplifted to high elevations. As these features are uplifted, they may be overprinted by extensional features. An additional argument that has been asserted to favor the coldspot model is the observation that the apparent compensation depths of Ovda, Thetis, and Phoebe are shallower than for Beta and Atla, and the correlation between gravity anomalies and topography is not as strong [12]. However, as noted above, a decrease in the apparent compensation depth is expected in the plume model because of the effect of the hot thermal anomaly on the mantle's viscosity. The increased volcanism associated with a rising thermal instability should lead to local crustal thickening, which will create topographic highs whose gravity anomalies will be small due to shallow compensation. This should decrease the overall correlation between gravity and topography. Thus, it appears that the time-dependent plume model is at least qualitatively consistent with observations of Ovda, Thetis, and Phoebe. Contrary to some assertions [12], qualitative geological and geophysical arguments cannot rule out the mantle plume model for these regions. Quantitative modeling of both the time-dependent plume model and the coldspot model are needed to assess their relevance to highlands on Venus.

References: [1] USGS (1984) *Map I-1562.* [2] Bills et al. (1987) *JGR, 92,* 10335. [3] Nerem (1992) *Eos, 73,* 83. [4] Campbell et al. (1989) *Science, 246,* 373. [5] Stofan et al. (1989) *GSA Bull.,* 101, 143. [6] Janle et al. (1987) *Earth Moon Planets, 39,* 251. [7] Campbell et al. (1991) *Science, 251,* 181. [8] Head et al. (1991) *Science, 252,* 276. [9] Senske et al. (1992) *JGR,* in press. [10] Solomon et al. (1992) *JGR,* in press. [11] deCharon and Stofan (1992) *LPSC XXIII,* 289. [12] Bindschadler et al. (1992) *JGR,* in press. [13] Schaber (1982) *GRL, 9,* 499. [14] Grimm and Phillips (1992) *JGR,* in press. [15] Kiefer and Hager (1991) *JGR, 96,* 20947. [16] Phillips et al. (1991) *Science, 252,* 651. [17] Monnereau and Cazenave (1990) *JGR, 95,* 15429. [18] Kiefer and Hager (1992) *Geophys. J. Int., 108,* 198. [19] Smrekar and Phillips (1991) *EPSL, 107,* 582. [20] Schilling (1991) *Nature, 352,* 397. [21] Kiefer and Kellogg (1991) *Eos, 72,* 507. [22] Kiefer (1990) Ph.D. thesis, Caltech. [23] Herrick and Phillips (1990) *GRL, 17,* 2129. [24] Shaw et al. (1980) *AJS, 280-A,* 667. [25] Kiefer et al. (1986) *GRL, 13,* 14. [26] Izenberg et al. (1992) *LPSC XXIII,* 591. [27] Zuber (1987) *JGR, 92,* E541. [28] Senske et al. (1991) *GRL, 18,* 1159. [29] Bindschadler and Parmentier (1990) *JGR, 95,* 21329.

N93-14335

PIONEER VENUS POLARIMETRY AND HAZE OPTICAL THICKNESS. W. J. J. Knibbe[1], W. M. F. Wauben[1], L. D. Travis[2], and J. W. Hovenier[1], [1]Department of Physics and Astronomy, Free University, Amsterdam, The Netherlands, [2]Goddard Institute for Space Studies, New York NY, USA.

The Pioneer Venus mission provided us with high-resolution measurements at four wavelengths of the linear polarization of sunlight reflected by the Venus atmosphere. These measurements span the complete phase angle range and cover a period of more than a decade. A first analysis of these data by Kawabata et al. [1] confirmed earlier suggestions of a haze layer above and partially mixed with the cloud layer. They found that the haze exhibits large spatial and temporal variations. The haze optical thickness at a wavelength of 365 nm was about 0.06 at low latitudes, but approximately 0.8 at latitudes from 55° poleward. Differences between morning and evening terminator have also been reported by the same authors.

Using an existing cloud/haze model of Venus, we study the relationship between the haze optical thickness and the degree of linear polarization. Variations over the visible disk and phase angle dependence are investigated. For that purpose, exact multiple scattering computations are compared with Pioneer Venus measurements.

To get an impression of the variations over the visible disk, we have first studied scans of the polarization parallel to the intensity equator. After investigating a small subset of the available data we have the following results. Adopting the haze particle characteristics given by Kawabata et al. [1], we find a thickening of the haze at increasing latitudes. Further, we see a difference in haze optical thickness between the northern and southern hemispheres that is of the same order of magnitude as the longitudinal variation of haze thickness along a scan line. These effects are most pronounced at a wavelength of 935 nm.

We must emphasize the tentative nature of the results, because there is still an enormous amount of data to be analyzed. We intend to combine further polarimetric research of Venus with constraints on the haze parameters imposed by physical and chemical processes in the atmosphere.

Reference: [1] Kawabata K. et al. (1980) *JGR, 85,* 8129–8140.

N93-14336

VENUS INTERNAL MAGNETIC FIELD AND ITS INTERACTION WITH THE INTERPLANETARY MAGNETIC FIELD.
W. C. Knudsen, Knudsen Geophysical Research Inc., Monte Sereno CA 95030, USA.

In a previous study, Knudsen et al. suggested that Venus has a weak internal magnetic dipole field of the order of $7 \times 10 + 20$ G cm^{-3} that is manifested in the form of magnetic flux tubes threading the ionospheric holes in the Venus nightside ionosphere [1]. They pointed out that any internal field of Venus, dipole or multipole, would be weakened in the subsolar region and concentrated in the antisolar region of the planet by the supersonic transterminator convection of the dayside ionosphere into the nightside hemisphere. The inferred magnitude of the dipole field does not violate the upper limit for an internal magnetic field established by the Pioneer Venus magnetometer experiment [2]. The most compelling objection to the model suggested by Knudsen et al. has been the fact that it does not explain the observed interplanetary magnetic field (IMF) control of the polarity of the ionospheric hole flux tubes [3,4]. In this presentation I suggest that a magnetic reconnection process analogous to that occurring at Earth is occurring at Venus between the IMF and a weak internal dipole field. At Venus in the subsolar region, the reconnection occurs within the ionosphere. At Earth it occurs at the magnetopause. Reconnection will occur only when the IMF has an appropriate orientation relative to that of the weak internal field. Thus, reconnection provides a process for the IMF to control the flux tube polarity. The reconnection in the subsolar region takes place in the ionosphere as the barrier magnetic field is transported downward into the lower ionosphere by downward convection of ionospheric plasma and approaches the oppositely directed internal magnetic field that is diffusing upward. The reconnected flux tubes are then transported anti-Sunward by the anti-Sunward convecting ionospheric plasma as well as by the anti-Sunward-flowing solar wind. Reconnection will also occur in the Venus magnetic tail region, somewhat analogously to the reconnection that occurs in the magnetotail of the Earth.

The possibility that reconnection is occurring between the IMF and an internal dipole field may be tested by measuring the orientation of the IMF projected into a plane perpendicular to the solar wind velocity during time intervals for which ionospheric holes are observed. The orientations of the IMF components should fall within a 180° angle.

References: [1] Knudsen W. C. et al. (1982) *GRL*, 765–768. [2] Russell C. T. et al. (1980) *JGR*, 8319–8332. [3] Luhmann J. G. and Russell C. T. (1983) *GRL*, 409–411. [4] Marubashi K. et al. (1985) *JGR*, *90*, 1385–1398.

N93-14337

VENUSIAN SINUOUS RILLES. G. Komatsu and V. R. Baker, Lunar and Planetary Laboratory, University of Arizona, Tucson AZ 85721, USA.

After a preliminary assessment of venusian channels [1], it now seems to be clear that the channels have distinctive classes, which imply a wide range of formation parameters and formation mechanisms [2]. They include outflow channels mainly formed by mechanical erosion from very high discharge flow [3], and canali-type channels requiring either constructional process or mechanical erosion by rather exotic low-viscosity lava such as carbonatite or sulfur [4]. Here we focus on venusian sinuous rilles.

Morphology: Venusian sinuous rilles are generally simple, and originate from a collapsed source. They are shallow and narrow downstream. The venusian sinuous rilles are distinct from canali-type channels, which exhibit almost constant morphologies throughout their entire length, and from outflow channels, which are characterized by wide anastomosing reaches. Venusian sinuous rilles are very similar to many lunar sinuous rilles in their morphologies [1] and even dimensions.

Hypothesized Origins: *Thermal erosion.* The close similarities of venusian sinous rilles to lunar sinuous rilles imply a similar formation by flowing lava. Many mechanisms of lunar sinuous rille formation have been proposed by various workers. Thermal erosion was argued to be a major process for their formation [5]. The lunar sinuous rilles could have been formed initially as constructional
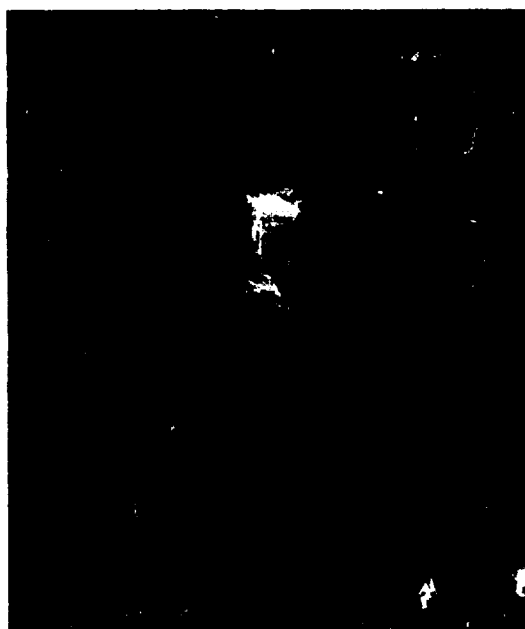
Figs. 1 and 2. Venusian sinuous rilles have morphologies similar to lunar sinuous rilles. The channels have collapsed pits, and shallow and narrow downstream. These morphologies indicate loss of thermal erosion capacity as the lava cools.

Fig. 3. Some venusian sinuous rilles are associated with coronae. Corona volcanism may have provided required conditions for the sinuous rille formation (high discharge, high temperature, low viscosity, etc.).

channels. However, incision was caused by the long flow duration and high temperatures of eruption, along with relatively large discharge rates, possibly assisted by a low viscosity of the channel-forming lava. Channel narrowing and levee formation suggest relatively fast cooling. The venusian channels could have had a similar sequence of formation including rapid cooling.

Lava types. Assuming the substrate is typical tholeiitic lava, the flowing lavas' temperatures have to be higher than the melting temperature of the substrate. The flow should have a low viscosity to cause turbulence and keep a high Raynolds number to sustain efficient thermal erosion. The returned Apollo samples indicate that the lunar lava was enriched in Fe and Ti and had relatively low viscosities and high eruption temperatures [6]. Venera landers reported tholeiitic basalt and alkaline basalt for the composition of plains material. However, none of the landers landed close to venusian sinuous rilles. So the chemical composition of sinuous rille-forming lava remains uncertain. A potential clue comes from geologic associations. The channels are often associated with the coronae [7], which are hypothesized to be related to mantle plume activity. The channel-forming lava may be mantle-derived magmas, e.g., alkaline basalt, picrite, komatiite [2]. They have low viscosities at their melting temperatures, and, since the eruption temperature of these lavas is so high, thermal erosion can be very efficient. Some of the channels' great depths (approximately a few hundred meters deep) may thereby be explained. Because high-temperature lava tends to cool rapidly, the channel narrows, shallows, and terminates over a relatively short distance.

Eruption Conditions: Determining eruption conditions also provides insights to estimate lava composition. Assuming a channel is formed mostly by thermal erosion, the channel's length and longitudinal profile are functions of lava properties. The depth profiles of the channels are measured by radar foreshortening methods and stereo images. Eruption conditions of channel forming lava can be estimated by the methods developed by Hulme [5].

References: [1] Baker V. R. et al. (1992) *JGR*, in press. [2] Komatsu G. and Baker V. R. (1992) *LPSC XXIII*, 715–716. [3] Komatsu G. and Baker V. R. (1992) *LPSC XXIII*, 713–714. [4] Komatsu G. et al. (1992) *GRL*, in press. [5] Hulme G. (1973) *Mod. Geol.*, *4*, 107–117. [6] Murase T. and McBirney A. R. (1970) *Science, 167*, 1491–1493. [7] Komatsu G. et al. (1992) *LPSC XXIII*, 717–718.

N93-14338

RADIATION PRESSURE: A POSSIBLE CAUSE FOR THE SUPERROTATION OF THE VENUSIAN ATMOSPHERE.

J. L. Krause, Hibbing Community College, Hibbing MN 55746, USA.

The superrotation of the venusian atmosphere relative to the planet's surface has long been known. Yet the process by which this vigorous circulation is maintained is poorly understood [1]. The purpose of this report is to show that a mechanism by which the solar radiation interacts with the cloudy atmosphere of Venus could be the principle cause of the superrotation. Radiation pressure is the term used to describe the result of the transfer of momentum from a photon to matter that occurs when a photon interacts with matter by the known processes of absorption, scattering, or reflection.

The simple rotor radiometer (Fig. 1) can be used to demonstrate radiation pressure. It is useful to review this classic demonstration as the proposed mechanism is so closely related to it. It is known that the absorbing surface of the asymmetrical rotor begins to turn toward the radiation when a radiation source is placed before the apparatus. A specific configuration of this system (Fig. 2) aids in the explanation of this rotation. The radiation interacts differently with the different vane surfaces. When a photon strikes the absorbing surface and is absorbed, its momentum is transferred to the vane. When a photon strikes the reflecting surface of the opposite vane, its momentum is transferred to the vane twice in the reflection process.
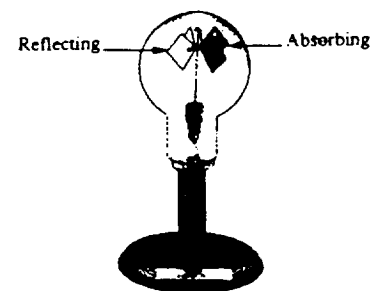
Fig. 1.
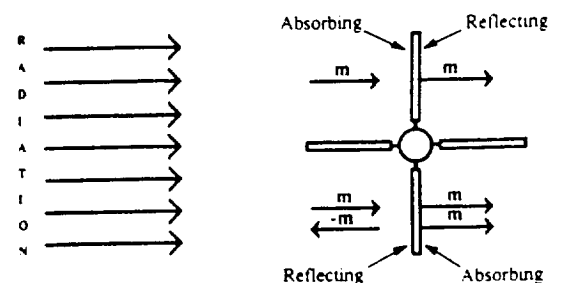
Fig. 2.

To understand the reflection process it is convenient to divide it into two steps. In the first step the photon is stopped (absorbed) by the reflecting surface and the photon's momentum is transferred to the vane. In the second step a photon is immediately emitted from the reflecting surface of the vane. By the principle of equal but opposite reaction a momentum equal to that of the emitted photon must be transferred to the vane during this second step. Therefore, it can be seen that the rotor must rotate so that the absorbing surface turns toward the radiation when opposite vanes are equally illuminated and equal in surface area.

It has been long known that Venus has a high albedo due to the scattering (similar to the reflection process) of solar radiation by the cloud droplets in its atmosphere. The radiation not scattered, but intercepted by the planet and its atmosphere, is mainly absorbed within the cloud layers. Therefore, momentum (equal, more or less, to that of the solar radiation intercepted) is continually transferred to the venusian atmosphere. An atmospheric system is different from the radiometer in that it presents a symmetrical surface (same radiation-matter interaction) toward the solar radiation at its morning and evening limbs (Fig. 3). If the cross-sectional areas at both limbs were equal as illustrated, the momentum transfer at the morning limb would decelerate the atmosphere's rotation while at the evening limb the same transfer would accelerate the rotation an equal amount. The net result of this is that the overall rate of rotation would be unchanged.

Such a symmetrical configuration is not likely since the atmosphere must be warmed as it rotates across the planet's day hemisphere and cooled as it rotates across the planet's night hemisphere. This warming and cooling must result in a formation of an asymmetrical configuration (Fig. 4). It is apparent that the momentum transfer at the evening limb must be greater than that at the morning limb because the atmosphere's greater cross section at the evening limb intercepts a greater amount of solar radiation. It should be noted that very little of the solar radiation is transmitted through the cloud layers, especially at or near the limbs where the atmospheric path length of the radiation is long. This net momentum transfer must be continually added to the angular momentum of the atmospheric system at the same time angular momentum is continually removed from the atmosphere by the frictional drag imposed on the atmosphere by the slowly rotating planet's surface. This completes the description of this mechanism.

There is great pressure to quantify the mechanism just introduced in an effort to evaluate its potential effectiveness. This pressure is resisted for the following reason. What physics professor would demonstrate the existence of radiation pressure and make the success or failure of the demonstration dependent upon the ability to predict the expected rate of rotation of an unknown apparatus? It is enough that the rotor turns in the direction predicted when the radiation source is set before the apparatus.
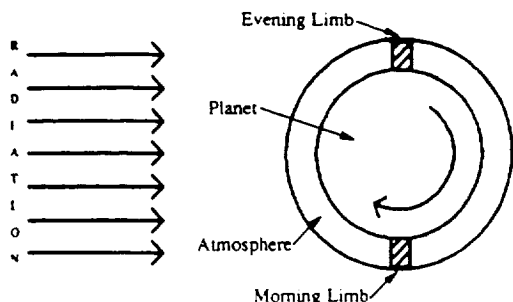
Fig. 3.   Atmosphere not to scale.
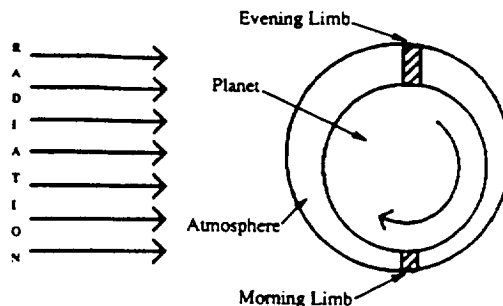
Fig. 4.   Atmosphere not to scale.

It should be enough that the qualitative details of the known superrotation of the venusian atmosphere are entirely consistent with the simple radiation pressure mechanism presented for this mechanism to receive serious consideration. An analysis of the frictional drag expected for the nearly laminar flow found beneath the cloud deck is much beyond my talent, to say nothing about the frictional coupling that exists in the turbulent cloud layer. It is possible that the mechanism might be tested if such frictional effects were reasonably well known.

The mechanism does suggest a possible phenomenon other than superrotation. The acceleration and deceleration that occur at the evening and morning limbs must compress the rotating atmosphere at some morning location and rarefy it at some afternoon location. A more detailed analysis of the expected atmospheric tides due to this mechanism is the subject of a nearly completed separate work.

A simple mechanism involving the phenomenon known as radiation pressure has been proposed to explain the superrotation of the venusian atmosphere. According to basic principles of physics it cannot be denied that the process must be active. It has been shown that support of the proposed mechanism by predictive, quantitative calculations is not presently possible because critical properties of the real system are unknown, or at best, poorly known. The possibility of atmospheric tides that, if observed, would be consistent with the mechanism has been noted. It should also be noted that the solar wind might replace the solar radiation in a similar mechanism. This has not been considered because the physics of the solar wind as it encounters a planet in its path is beyond my abilities.

Reference: [1] Belton M. J. S. et al. (1991) *Science, 253*, 1531–1536. (This article not only reports results from the Galileo venusian encounter, but also is a review of the superrotation phenomenon and is extensively referenced.)

N93-14339

LARGE-VOLUME LAVA FLOW FIELDS ON VENUS: DIMENSIONS AND MORPHOLOGY. M. G. Lancaster[1], J. E. Guest[1], K. M. Roberts[2], and J. W. Head[2], [1]University of London Observatory, University College London, London NW7 2QS, UK, [2]Department of Geological Sciences, Brown University, Providence RI 02912, USA.

Of all the volcanic features identified in Magellan images, by far the most extensive and areally important are lava flow fields. Neglecting the widespread lava plains themselves, practically every C1-MIDR produced so far contains several or many discrete lava flow fields. These range in size from a few hundred square kilometers in area (like those fields associated with small volcanic edifices for example), through all sizes up to several hundred thousand

TABLE 1. Type examples of great flow fields. Areas are the total for each flow field, and the lengths and widths refer to flow units within each field.

Name	Latitude	Longitude	C1–MIDR	Area/km²	Lengths/km	Widths/km	Morphology	Source
Lauma Dorsa	52N–67N	176–200	60n180 60n208	2,529,070	225–540	65–270	Sheet	Ridge belt
Aitra Mons	49N–54N	264–272	60n263 45n265	201,020	270 (aver.)	5–10	Symm. apron	Large volcano
Neago Fluctus	43N–59N	340–355	60n347 45n350	744,470	450–1900	90–450	Transitional	Fissures
Sekmet Mons	42N–50N	239–245	45n244	81,170	150–520	10–40	Asymm. apron	Large volcano
Mist Fossae	37N–43N	242–255	45n244	106,050	140–450	5–20	Subparallel	Rift zone
Kawelu Planitia	40N–52N	253–275	45n265	779,930	630 (max)	120–360	Sheet	Various
Ulfrun/Ganiki	24N–32N	215–223	30n225	197,550	670 (max)	20–45	Subparallel	Rift zone
Rusalka Planitia	10S–8N	170–185	00n180 15s180	773,470	280 (av.) 630 (max)	135 (typical)	Transitional	Various
Ozza Mons (S)	7S–2S	200–212	00n197 00n215	120,690	1460 (max)	35–130	Subparallel	Fissures
NW of Phoebe	1N–6N	266–273	00n266	137,730	260 (av.) 420 (max)	5–15	Apron	Large volcano
Parga Chasma	21S–13S	242–250	15s249	222,600	360 (av.) 632 (max)	≤20	Asymm. apron	Corona
Ammavaru	52S–43S	015–043	45s011 45s032	460,000	460 (fan) 880 (max)	≤30 (fan) ≤80 (ponds)	Fan	Caldera and shield cluster
Kaiwan Fluctus	53S–43S	353–010	45s011 45s350	≥315,000	870 (N) 1250 (max)	5–35	Subparallel	Fissures on rift zone
Mylitta Fluctus	63S–49S 43S	349–359	45s350 60s347	300,000	1000 (max)	5–80	Subparallel	Caldera on rift zone

square kilometers in extent (such as many rift related fields) [1]. Most of these are related to small, intermediate, or large-scale volcanic edifices, coronae, arachnoids, calderas [2,3], fields of small shields [4], and rift zones [5].

An initial survey of 40 well-defined flow fields with areas greater than 50,000 km² (an arbitrary bound) has been undertaken. Following Columbia River Basalt terminology, these have been termed great flow fields [6]. This represents a working set of flow fields, chosen to cover a variety of morphologies, sources, locations, and characteristics. The initial survey is intended to highlight representative flow fields, and does not represent a statistical set. For each flow field, the location, total area, flow lengths, flow widths, estimated flow thicknesses, estimated volumes, topographic slope, altitude, backscatter, emissivity, morphology, and source has been noted. The flow fields range from about 50,000 km² to over 2,500,000 km² in area, with most being several hundred square kilometers in extent. Flow lengths measure between 140 and 2840 km, with the majority of flows being several hundred kilometers long.

A few basic morphological types have been identified. This is not intended as a genetic classification, and the types identified are merely end members of a continuous range in morphology. The main distinction that has been drawn is between sheet flows, which are irregular in outline and show little or no internal structure, and digitate flows [7], which are made up of distinct flow lobes or lava streams. Usually, the digitate flows are related to a centralized source, whereas the sheet flows were erupted from extensive fissures. The sheet flows cannot be divided into individual flow units and may therefore be termed simple flows [8], while the digitate flows, divisible into many flow units, are all compound (although individual flow units may be treated as simple).

Sheet flows are distinguished by their relatively uniform backscatter, lack of internal flow structure such as well-defined lava streams, channels, etc., absence of flow lobes, and irregular boundaries. Of the studied set, they range from 66,210 km² to 2,529,070 km². Sheet widths lie between 60 to 360 km, with maximum lengths between 225 and 680 km. The sheet flow fields are difficult to map in the sense that internal flow boundaries are essentially absent. Source regions for sheet flows are typically the fissures associated with rift zones, but they may also be traced to the annular structures surrounding some coronae. Some of the larger sheet flow fields may conceivably be composed of more than one large flow field.

Digitate flow fields are characterized by many discrete flow lobes or lava streams. They are more common, and show a wider range of morphology than sheet flows. Relative to sheet flow fields they display a wider variation in radar backscatter, often being composed of both radar-bright and -dark flow units within the same field. They have been subdivided into divergent and subparallel morphologies on the basis of the distal widening of the overall flow field and the downstream divergence between flow units. All the divergent flow fields have central sources, whereas half the subparallel fields have been erupted from fissures along sections of
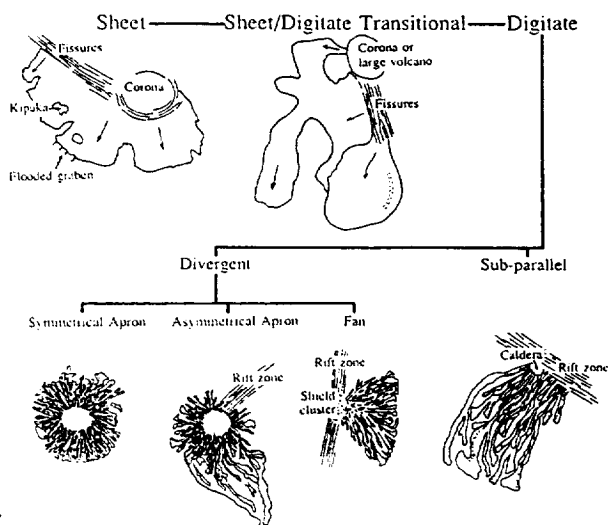
Fig. 1. Morphological types of great flow fields (not to scale).

rift zone. The more centered the source, the greater the degree of divergence of the flow field, although the local topography may also control the direction of flow lobes. The divergent fields contain symmetrical apron and fan end members. However, a large number of aprons are distinctly asymmetric in plan, and may be considered transitional between symmetrical aprons and fans. All the symmetrical aprons surround large volcanos, while the asymmetrical aprons are centered on large volcanos (some of which are on rift zones), coronae, and a cluster of small shields. Of the studied fans, two are related to shield clusters, while a third may be traced to a set of fissures. Fans are the least common of all the surveyed fields. The subparallel fields may be traced to rift zones and fissures, coronae, calderas, and a cluster of small shields.

In all types the widths of individual flow lobes or streams ranges from a few kilometers (usually in the proximal regions) to several tens of kilometers, with distal lobes of asymmetric aprons and subparallel flow fields up to 130 km in width. The symmetrical aprons are typically around 300 km in radius, while the maximum length of the asymmetric aprons are up to 770 km in maxiumum length. The measured subparallel flow fields range between 140 and 1460 km in length, with typical lengths of a few hundred kilometers. Most of the symmetrical and assymetrical aprons have relatively radar-bright proximal regions, while many of the asymmetrical aprons have distal regions of particularly low backscatter. All the divergent types may display channels.

A number of flow fields are transitional between the sheet and digitate types. In these cases, very broad, but sheetlike flow lobes, up to a few hundred kilometers across, may be discriminated. These large lobes tend to have somewhat more variable backscatter than the sheet flows. In several cases these transitional flows appear to consist of large expanses of ponded lava. The transitional flows are all associated with fissures. The plains contain numerous examples of portions of flow fields that cannot be traced to their source. These flows are usually indistinct, and may represent relatively old, degraded flows that have been partly resurfaced by later volcanism. Such indistinct flows occur beyond the distal reaches of some large flow fields such as Mylitta Fluctus [7] and Kaiwan Fluctus [1]. A key question regarding the great flow fields is how they relate to plains development and what their contribution is to volcanic

resurfacing in general [9]. Another key question concerns the effusion rates and emplacement times for these great flows, as has been estimated for Mylitta Fluctus [7]. The set of flow fields has been chosen to address these questions, with initial emphasis (mapping, detailed measurements, etc.) being placed on the type flow fields.

References: [1] Lancaster M. G. et al. (1992) *LPSC XXIII*, 753–754. [2] Crumpler L. S. et al. (1992) *LPSC XXIII*, 277–278. [3] Head J. W. et al. (1992) *LPSC XXIII*, 513–514. [4] Aubele J. C. et al. (1992) *LPSC XXIII*, 47–48. [5] Roberts K. M. et al. (1992) *LPSC XXIII*, 1157–1158. [6] Tolan T. L. et al. (1989) In *Volcanism and Tectonism in the Columbia River Flood-Basalt Province, Boulder, Colorado* (S. P. Reidel and P. R. Hooper, eds.), GSA Spec. Paper 239. [7] Roberts K. M. et al. (1992) *JGR*, special Magellan issue, submitted. [8] Walker G. P. L. (1971) *Bull. Volcanol., XXXV-3*, 579–590. [9] Head J. W. et al. (1992) *LPSC XXIII*, 517–518.

N93-14340

DERIVATION OF SURFACE PROPERTIES FROM MAGELLAN ALTIMETRY DATA.

Amy J. Lovell[1], F. Peter Schloerb[1], and George E. McGill[2], [1]Department of Physics and Astronomy, University of Massachusetts, Amherst MA 01003, USA, [2]Department of Geology and Geography, University of Massachusetts, Amherst MA 01003, USA.

The fit of the Hagfors model [1] to the Magellan altimetry data provides a means to characterize the surface properties of Venus. However, the derived surface properties are only meaningful if the model provides a good representation of the data. The Hagfors model is generally a realistic fit to surface scattering properties of a nadir-directed antenna [2] such as the Magellan altimeter; however, some regions of the surface of Venus are poorly described by the existing model, according to the "goodness of fit" parameter provided on the ARCDR CDRoms. Poorly characterized regions need to be identified and fit to new models in order to derive more accurate surface properties for use in inferring the geological processes that affect the surface in those regions.

We have compared the goodness of fit of the Hagfors model to the distribution of features across the planet, and preliminary results show a correlation between steep topographic slopes and poor fits to the standard model, as has been noticed by others [3,4]. In this paper, we investigate possible relations between many classes of features and the ability of the Hagfors model to fit the observed echo profiles. In the regions that are not well characterized by existing models, we calculate new models that compensate for topographic relief in order to derive improved estimates of surface properties.

Areas investigated to date span from longitude 315 through 45, at all latitudes covered by Magellan. A survey of those areas yields preliminary results that suggest that topographically high regions are well suited to the current implementation of the Hagfors model. Striking examples of such large-scale good fits are Alpha Regio, the northern edges of Lada Terra, and the southern edge of Ishtar Terra. Other features that are typically well fit are the rims of coronae such as Heng-O and the peaks of volcanos such as Gula Mons. Surprisingly, topographically low regions, such as the ubiquitous plains areas, are modeled poorly in comparison. However, this generalization has exceptions: Lakshmi Planum is an elevated region that is not well fit compared to the rest of neighboring Ishtar, while the southern parts of topographically low Guinevere Planitia are characterized quite well by the Hagfors model.

Features that are candidates for improved models are impact craters, coronae, ridges of significant scale, complex ridged ter-

rains, moderate-sized mountains, and sharp terrain boundaries. These features are chosen because the goodness of fit is likely to be most affected either by departures from normal incidence angles or by sharp changes in terrain type within a single footprint. Most large features that are elevated with respect to their surroundings will suffer from steep slope effects, and smaller coronae and impact craters will probably suffer due to rapid changes in their appearance within a single footprint (10–20 km).

Since the surface properties of Venus can be derived only through models, it is crucial that surface scattering models be as accurate as possible. The characterization of terrain and the physical quantities that are estimated from surface properties presume an acceptable level of precision in the data, and are misleading if truly incorrect. Once the problem areas are correctly identified, better estimates of surface properties may be obtained through models tailored to particular fitting difficulties. These surface properties, in turn, will provide a means to estimate physical characteristics of the planet's surface, and address the underlying geological processes.

References: [1] Hagfors T. (1970) *Radio Sci., 5,* 189–227. [2] Ford P. G. and Senske D. A. (1990) *GRL, 17,* 1361–1364. [3] Ford P. G. and Pettengill G. H. (1992) *JGR,* in press. [4] Squyres S. W. et al. (1992) *JGR,* in press.   ◠

N93-14341

THE SOLAR WIND INTERACTION WITH VENUS. J. G. Luhmann, IGPP–UCLA, Los Angeles CA 90024-1567, USA.

The Pioneer Venus Orbiter (PVO) mission has played a key role in establishing the nature of the solar wind interaction with Venus [1]. Although earlier probes had determined that Venus presented an obstacle much smaller than the size of Earth's magnetosphere to the solar wind, they did not carry out *in situ* measurements pertaining to solar wind interaction studies at low enough altitudes to determine why. They also did not provide datasets of sufficient duration to study the variability of the interaction on both short (one day) and long (solar cycle) timescales [2].

The first 600 of the nearly 5000 orbits of PVO magnetometer data have been used to determine a very low upper limit (~10^{-5} of the terrestrial value) on the intrinsic dipolar magnetic moment of Venus [3]. The consequence of that low magnetic moment is that the solar wind interacts directly with the upper atmosphere and ionosphere. Relative to a dipolar field obstacle, the ionospheric obstacle is rather incompressible. A "bow" shock is observed to stand in front of the nearly Venus-sized ionospheric obstacle at a comparatively steady subsolar altitude of ~1.5 R_v (Venus radii). This shock decelerates the supersonic solar wind plasma so that it can flow around the obstacle. It was found to change its average position in the terminator plane from about 2.4 R_v to 2.1 R_v as the solar cycle progressed from the 1978 orbit insertion near solar maximum through the 1986–87 solar minimum, and back again during the latest solar activity increase [4].

Between the bow shock and the ionosphere proper, the slowed solar wind plasma flow diverges near the subsolar point and makes its way across the terminator where it reaccelerates and continues anti-Sunward. The solar wind magnetic field, which is in effect frozen into the flowing plasma, is distorted in this "magnetosheath" region so that it appears to hang up or drape over the dayside ionosphere before it slips around with the flow. These features of the solar wind interaction are also seen when the obstacle is a dipole magnetic field, but there are two important distinctions.

In the wake of the Venus obstacle one finds an "induced" magnetic tail composed of varying interplanetary fields rather than

the constant fields of intrinsic origin [5]. This "magnetotail" is further seen to be populated by heavy (O^+) ions that are evidently escaping from the planet at significant (~10^{-25} s^{-1}) rates [6]. These heavy ions are also observed in the dayside magnetosheath [7]. The interpretation is that ions are produced by both photoionization and solar wind electron impact ionization of the upper neutral atmosphere that extends into the magnetosheath. The flowing solar wind plasma with its imbedded magnetic field "picks up" the ions and carries them tailward. While many escape, some of the picked up ions impact the dayside atmosphere and sputter neutrals [8]. By these means, the solar wind interaction plays a role in the evolution of the Venus atmosphere, although its importance relative to other loss mechanisms is still undetermined. In any event, because the planetary heavy ion contribution to the plasma in the magnetosheath varies with the solar cycle, it may be the cause of the aforementioned shift in the bow shock position. For all the above reasons, researchers sometimes consider that the Venus-solar wind interaction is in many ways cometlike. These features are all a consequence of the weak intrinsic magnetism, and as such should be relevant to Mars [9] where future measurements are likely to further elucidate the scavenging processes.

References: [1] Luhmann J. G. (1986) *Space Sci. Rev., 44,* 241. [2] Russell C. T. and Vaisberg O. (1983) In *Venus* (D. M. Hunten et al., eds.), Univ. of Arizona, Tucson. [3] Phillips J. L. and Russell C.T. (1987) *JGR, 92,* 2253. [4] Zhang T. L. et al. (1990) *JGR, 95,* 14961. [5] Saunders M. A. and Russell C.T. (1986) *JGR, 91,* 5589. [6] Moore K. R. et al. (1990) *JGR, 95,* 12005. [7] Mihalov J. D. and Barnes A. (1981) *GRL, 8,* 1277. [8] Luhmann J. G. and Kozyra J. U. (1991) *JGR, 96,* 5457. [9] *JGR,* special Venus and Mars issue, July, 1991.   ◠   ◠

N93-14342

EXTENSIVE LAVA FLOW FIELDS ON VENUS: PRELIMINARY INVESTIGATION OF SOURCE ELEVATION AND REGIONAL SLOPE VARIATIONS. K. Magee-Roberts[1], J. W. Head[1], J. E. Guest[2], and M. G. Lancaster[2], [1]Department of Geological Sciences, Brown University, Providence RI 02912, USA, [2]University of London Observatory, University College London, London NW7 2QS, UK.

Large-volume lava flow fields have been identified on Venus [1], the most areally extensive (>50,000 km^2) of which are known as "fluctus" and have been subdivided into six morphologic types [2]. Sheetlike flow fields (Type 1) lack the numerous, closely spaced, discrete lava flow lobes that characterize digitate flow fields. Transitional flow fields (Type 2) are similar to sheetlike flow fields but contain one or more broad flow lobes. Digitate flow fields are divided further into divergent (Types 3–5) and subparallel (Type 6) classes on the basis of variations in the amount of downstream flow divergence. Flows that are radially symmetric about a central source (e.g., volcanic shield or corona) are typical of Type 3 flow fields, whereas a similar but slightly asymmetric apron of flows about a central source is characteristic of Type 4 flow fields. A fan-shaped flow field that widens substantially in its distal regions is typical of Type 5 flow fields. Type 6 flow fields (e.g., Mylitta and Kaiwan Fluctus) are not radially symmetric about a central source and do not widen or diverge substantially downstream.

As a result of our previous analysis of the detailed morphology, stratigraphy, and tectonic associations of Mylitta Fluctus [3], we have formulated a number of questions to apply to all large flow fields on Venus. In particular, we would like to address the following: (1) eruption conditions and style of flow emplacement (effusion

rate, eruption duration), (2) the nature of magma storage zones (presence of neutral buoyancy zones, deep or shallow crustal magma chambers), (3) the origin of melt and possible link to mantle plumes, and (4) the importance of large flow fields in plains evolution. To answer these questions we have begun to examine variations in flow field dimension and morphology; the distribution of large flow fields in terms of elevation above the mean planetary radius (MPR ~ 6052 km); links to regional tectonic or volcanic structures (e.g., associations with large shield edifices, coronae, or rift zones); stratigraphic relationships between large flow fields, volcanic plains, shields, and coronae; and various models of flow emplacement in order to estimate eruption parameters.

In this particular study, we have examined the proximal elevations and topographic slopes of 16 of the most distinctive flow fields that represent each of the 6 morphologic types. The locations, dimensions, and source characteristics of these flow fields are tabulated elsewhere [2]. The distribution of this subset of large flow fields with respect to altitude of the proximal portion of the flow field (nearest any identified or presumed source region) is shown in Fig. 1. Of the 16 flow fields in this sample, 9 have source regions at elevations between 6051.5 and 6052.25 km. Three are found at elevations below 6051.5 km and five are located above 6052.25 km (only two are situated above 6053.5 km). This distribution is skewed toward slightly higher elevations than that expected if the distribution were uniform with respect to the percentage of surface area at each elevation interval. This may reflect the fact that the majority of flow fields in this sample are associated with fracture belts, volcanic shields, and coronae located within large rift zones that are locally elevated several kilometers above the MPR.
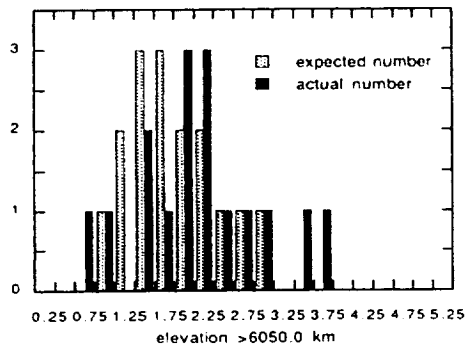
Fig. 1.   Histogram of proximal flow field elevation.
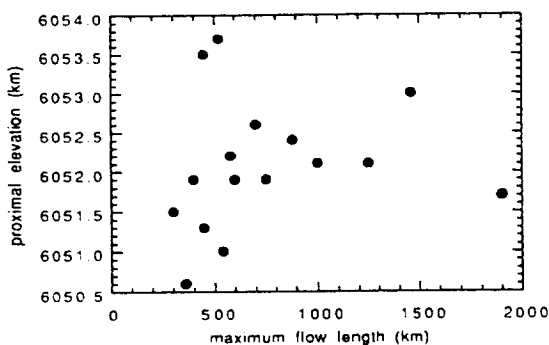
Fig. 2.   Proximal elevation vs. flow length.
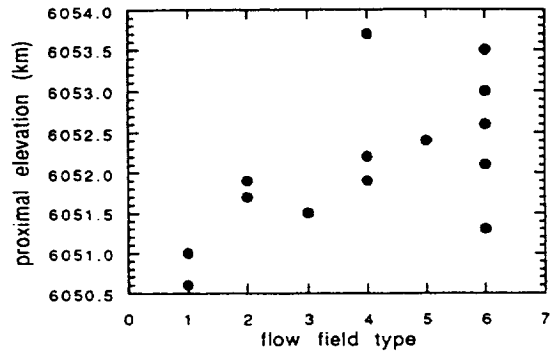
Fig. 3.   Proximal elevation vs. flow field type.
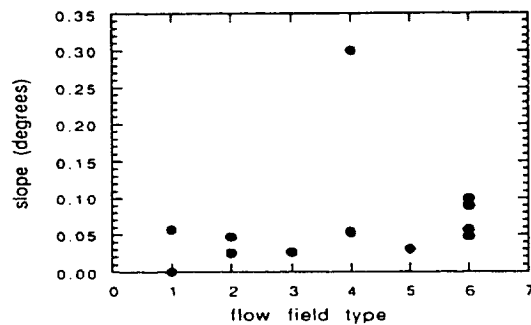
Fig. 4.   Slope vs. flow field type.
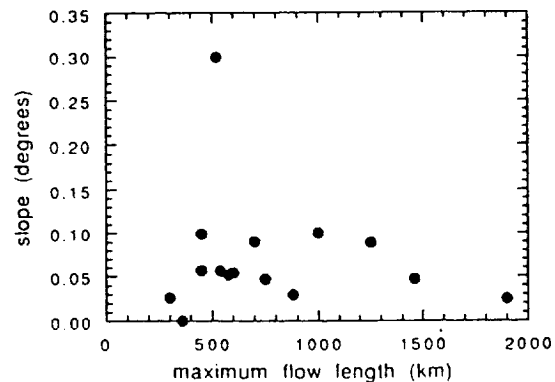
Fig. 5.   Slope vs. flow length.

A recent theoretical analysis of magma reservoirs and neutral buoyancy zones on Venus [4] has indicated that large-volume eruptions should be favored at elevations near and below the MPR due to the potential lack of shallow-level magma chambers in regions of low elevation (a result of increased atmospheric pressure). This prediction is broadly consistent with the fact that the majority of flow fields in this study appear to cluster near the MPR. However, there does not appear to be a strong correlation between flow length (taken as an indicator of flow volume) and proximal elevation (Fig. 2). According to the results of the analysis mentioned above, the largest flow volumes (or lengths, as in this study) are predicted to have occurred at the lowest elevations. The trend in Fig. 2 appears to be the reverse of this, with the longer (and presumably more voluminous) flows erupting at higher elevations. However, proximal elevation appears to exert some control on flow

field morphology (Fig. 3) to the extent that sheetlike flow fields (Types 1, 2) occur at lower elevations than digitate flow fields (Types 3–6). If digitate flow fields represent multiple individual eruptions of lower volume than sheetlike flow fields, then the fact that sheetlike flow fields appear to have been erupted at lower elevations is consistent with the above predictions. These results are only preliminary, however, and do not represent the entire population of large flow fields or take into consideration the possibility of postemplacement elevation of topography.

In addition, preliminary results indicate that topographic slope has little control on flow length or morphology (Figs. 4 and 5). Given the variation in abundance of discrete flow lobes, flow distribution, and downstream divergence among the flow field types, one might have expected a stronger correlation between flow morphology and slope. It is possible that small-scale variations in local slope beyond the resolution of our data may be associated with variations in flow field morphology.

We are currently extending this analysis to the entire population of large-volume flow fields on Venus and are further investigating implications for their origin and emplacement mechanisms.

References: [1] Head J. W. et al. (1992) *JGR*, special Magellan issue, submitted. [2] Lancaster M. G. et al., this volume. [3] Roberts K. M. et al. (1992) *JGR*, special Magellan issue, submitted. [4] Head J. W. and Wilson L. (1992) *JGR*, 97, 3877-3903.

N93-14343

WRINKLE RIDGES ON VENUSIAN PLAINS: INDICATORS OF SHALLOW CRUSTAL STRESS ORIENTATIONS AT LOCAL AND REGIONAL SCALES. George E. McGill, Department of Geology and Geography, University of Massachusetts, Amherst MA 01003, USA.

The plains regions of Venus exhibit a complex array of structural features, including deformation belts of various types, wrinkle ridges, grabens, and enigmatic radar-bright linears [1,2,3]. Probably the most pervasive of these structures are the wrinkle ridges, which appear to be morphologically identical to their counterparts on the Moon and Mars. Almost all workers agree that wrinkle ridges result from horizontal compressive stresses in the crust; they either are explained as flexural fold structures, or alternatively as scarps or folds related to reverse faults [3-8]. Wrinkle ridges generally are narrow, have small amplitudes, and commonly are closely spaced as well, characteristics that imply a shallow crustal origin.

If wrinkle ridges are due to horizontally directed compressive stresses in the shallow crust, as generally has been inferred, then the trends of these features provide a means to map both local and regional orientations of principal stresses in the uppermost part of the venusian crust: maximum compressive stress is normal to the ridges, minimum compressive stress is normal to the topographic surface, and thus the wrinkle ridge trends trace the orientation of the intermediate principal stress. Because there are few plains areas on Venus totally devoid of wrinkle ridges, it should be possible to establish a number of interesting relationships on a near-global scale by mapping the trends of wrinkle ridges wherever they occur. The present study is addressing three questions: (1) Do the trends of wrinkle ridges define domains that are large relative to the sizes of individual plains regions? If so, can these domains be related to large-scale topographic or geologic features? (2) Are regional trends of wrinkle ridges affected by local features such as coronae? If so, is it possible to determine the relative ages of the far-field and local stresses from detailed study of trend inheritance or superposition

relationships? (3) What is the relationship between wrinkle ridges and the larger ridges that make up ridge belts?

Mapping completed as of May 1992 includes parts of Lavinia, Guinevere, Sedna, Tinatin, and Aino Planitiae. Detailed maps of wrinkle ridge trends have been prepared by systematically displaying all of the 56 tiles making up each C1-MIDR on CDROM on a high-resolution monitor connected to a SUN SPARCstation 2. The observed trends are then plotted on the corresponding hard copies of the full MIDRs. The detailed maps are used to generate more generalized plots of wrinkle ridge trends that are digitized and combined for presentation as a global display.

The patterns defined by wrinkle ridge trends vary widely. The simplest cases occur where the ridges all have about the same trend over a very large area, as is the case for much of that portion of Lavinia Planitia imaged on C1-MIDR45s350 [3]. At many localities, however, there are two or even three definable sets of wrinkle ridges with clearly distinct trends. In places, ridges of one set curve into a merging relationship with another set; in other places, one set seems to truncate another; in still other places, sets cross each other, commonly without clear clues concerning relative age. At a few localities, the pattern made by wrinkle ridges can be described as "cellular"; in such places, it is difficult to distinquish any dominant sets defined by trend. Cellular patterns may well indicate localities where the horizontal compressive stresses in the shallow crust are very nearly isotropic. Preliminary results suggest at least partial answers to the three questions posed above.

Trends of wrinkle ridges do define domains that occupy a large fraction of the area of a single C1-MIDR or large fractions of two or more adjacent C1-MIDRs. The boundaries between these domains commonly are regions occupied by complex ridged terrain or elevated young volcanic terrains, but some boundaries do not relate to any obvious geologic or topographic feature. These more enigmatic boundaries are interesting because they may define more subtle regional crustal features. Clearly, wrinkle ridges must be mapped over a substantial fraction of the planet before the large-scale domainal characteristics can be fully understood.

The regional trends of wrinkle ridges that define the large-scale domains clearly are affected by at least some local features, especially coronae. Part of the concentric structure that characterizes coronae consists of closely spaced ridges that are morphologically indistinguishable from wrinkle ridges. The relationships commonly are complex, but in a number of cases it appears as if the regional set of wrinkle ridges both cuts across a corona and is warped into parallelism with the concentric corona structure. A good example occurs where a strong regional set of wrinkle ridges trending slightly north of east interacts with concentric structures related to Heng-O. Some wrinkle ridges parallel to the regional set cross the eastern margin of Heng-O and extend into the center of the structure. Along the northeastern margin of Heng-O the regional wrinkle ridges bend to merge into the corona concentric structure, but also appear to be in part overprinted by these concentric structures. Along the northern and southern margins of Heng-O the regional set of wrinkle ridges appears to be simply enhanced. These relationships suggest that the stresses associated with the formation of Heng-O interacted with far-field stresses; Heng-O formed in part at the same time that the far-field stresses were active, in part later than the far-field stresses. At least some smaller coronae show similar geometric and kinematic relationships with regional wrinkle-ridge sets, but much more work needs to be done before a definitive conclusion can be reached concerning relative ages.

Detailed work in Lavinia Planitia has focused attention on an apparent paradox. Using stratigraphic relationships that are clearer

in the southwestern part of Lavinia Planitia than in most places, it can be shown that many of the ridge belts are older than the areally dominant plains materials on which wrinkle ridges are developed [3]. This relationship indicates that the wrinkle ridges are younger than the ridge belts, and thus suggests that locally similar trends of ridge belts and wrinkle ridges must be explained as due to stress orientations that did not change with time. Nevertheless, there are places in the same general area where it appears as if wrinkle ridges grade along their lengths into ridges of a ridge belt. Taken at face value, this latter relationship suggests that both structures were formed by the same stress field, and presumably at the same time. Because the local relationships send conflicting signals concerning the geometric and kinematic kinship of wrinkle ridges and ridge belts, it is hoped that a more regional perspective might be helpful. At the scale of the entire planitia there is not a consistent relationship between the trends of wrinkle ridges and the trends of ridge belts. This preliminary result suggests that ridge belts and wrinkle ridges are different features. Local similarities in trend and the cases where one seems to grade into the other can be explained by inferring temporal coherence of stress field or by some form of geometric inheritance.

Finally, even though wrinkle ridges appear to be relatively young features, they are evidently older than most or all fresh impact craters. This inference is based mainly on the apparent obliteration of wrinkle ridges by crater ejecta, although this may not be a foolproof criterion (wrinkle ridges might not form in ejecta materials, or might be invisible if present because of no roughness contrast). A single example of a flow emanating from an impact crater being ponded by a wrinkle ridge has been found, and this relationship is considered to be good evidence of relative age.

Wrinkle ridges are important structures on planetary surfaces because they are so common and because they provide useful clues to stresses in the shallow crust. Because so much of Venus is plains, wrinkle ridges are especially useful for inferring crustal evolution on that planet.

References: [1] Solomon S. C. et al. (1991) *Science, 252*, 297–312. [2] Solomon S. C. et al. (1992) *JGR*, in press. [3] Squyres S. W. et al. (1992) *JGR*, in press. [4] Plescia J. B. and Golombek M. P. (1986) *GSA Bull., 97*, 1289–1299. [5] Golombek M. P. et al. (1991) *Proc. LPS, Vol. 21*, 679–693. [6] Watters T. R. (1988) *JGR, 93*, 10236–10254. [7] Maxwell T. A. et al. (1975) *GSA Bull., 86*, 1273–1278. [8] Maxwell T. A. (1982) *Proc. LPSC 13th.* in *JGR 87*. A97–A108.

N93-14344

ESTIMATES OF ELASTIC PLATE THICKNESSES BENEATH LARGE VOLCANOS ON VENUS.

Patrick J. McGovern and Sean C. Solomon, Department of Earth, Atmospheric, and Planetary Sciences, Massachusetts Institute of Technology, Cambridge MA 02139, USA.

Introduction: Magellan radar imaging and topography data are now available for a number of volcanos on Venus greater than 100 km in radius. These data can be examined to reveal evidence of the flexural response of the lithosphere to the volcanic load. On Earth, flexure beneath large hotspot volcanos results in an annular topographic moat that is partially to completely filled in by sedimentation and mass wasting from the volcano's flanks (see [1,2]). On Venus, erosion and sediment deposition are considered to be negligible at the resolution of Magellan images [3]. Thus, it may be possible to observe evidence of flexure by the ponding of recent volcanic flows in the moat. We also might expect to find topo-

graphic signals from unfilled moats surrounding large volcanos on Venus, although these signals may be partially obscured by regional topography. Also, in the absence of sedimentation, tectonic evidence of deformation around large volcanos should be evident except where buried by very young flows.

We have found two examples to date of volcanos with strong evidence for moat formation and infilling by flows. Radar images of Tepev Mons, a volcano about 125 km in radius near the southwestern corner of Bell Regio, reveal a bright flow unit draped around the northern and western flanks of the volcano. An unnamed volcano at 10°N, 275°E (southwest of Beta Regio) exhibits both circumferential flanking flows and lateral spreading of originally radially trending flows. The distal edges of these flows terminate about 240–260 km from the summit. The edges of these flows form an arc of greater than 120° to the north and west of the volcano.

Method: We use analytic solutions in axisymmetric geometry [4] for deflections and stresses resulting from loading of a plate overlying an inviscid fluid. Solutions for a set of disk loads are superimposed to obtain a solution for a conical volcano. The deflection of the lithosphere produces an annular depression or moat, the extent of which can be estimated by measuring the distance from the volcano's edge to the first zero crossing or to the peak of the flexural arch. Magellan altimetry data records (ARCDRs) from data cycle 1 are processed using the GMT mapping and graphics software [5] to produce topographic contour maps of the volcanos. We then take topographic profiles that cut across the annular and ponded flows seen on the radar images. By comparing the locations of these flows to the predicted moat locations from a range of models, we estimate the elastic plate thickness that best fits the observations, together with the uncertainty in that estimate.

Results: Figure 1 shows two cross sections through Tepev Mons. The areas covered by annular flows are marked with arrows. Figure 2 shows deflections calculated analytically for a conical load of height 10 km and radius 150 km for elastic plate thicknesses T_e of 10 km and 20 km. Arrows denote the predicted approximate extent of a moat due to loading in each model. Note that for the analytic solutions, increasing the elastic plate thickness increases both the maximum depth and the radial extent of the predicted moat. The model in Fig. 2a matches the northwestern cross section in Fig. 1a. The area of flows in Fig. 1b is somewhat larger in radial extent and is better matched by the predicted moat in Fig. 2b. Figure 3 shows a cross section through the volcano at 10°N, 275°E. Figure 4 shows calculated deflections for a conical load of height 5 km and radius 250 km, for elastic plate thicknesses of 10 and 20 km. The extent of annular flows is better matched by the smaller thickness.

Discussion: These two volcanos are apparently atypical of large volcanos on Venus in that both topography and flow morphology suggest the existence of a flexural moat. On other large shield volcanos such as Sif Mons and Sapas Mons, topographic evidence of a moat is lacking, and no flows that have convincingly ponded in annular moats can be identified. Large volcanos that form on or near large rift zones (such as Maat Mons, Ozza Mons, and others) also lack topographic evidence of a flexural moat. It should be noted that as altimetry data and stereo imaging from later cycles become available, coverage will improve, gaps will be filled in, and it may be possible to identify topographic signatures of moats that have eluded our search to date.

In contrast to Tepev Mons and the construct at 10°N, 275°E, most large volcanos on Venus are generally characterized by fractures and flow units that have dominantly radial orientations. Given this observation and the assumption that lithospheric flexure has occurred, then the moats must be filled or covered. Mass wasting,
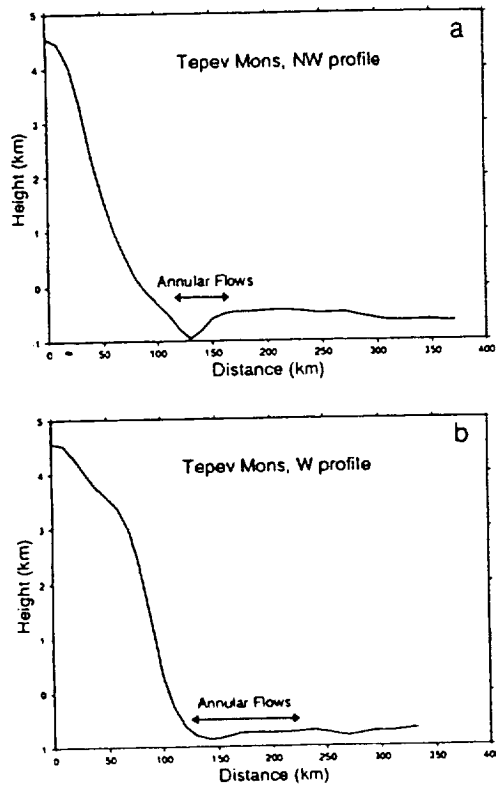
Fig. 1. Topographic cross sections through Tepev Mons: (a) northwestern profile; (b) western profile.
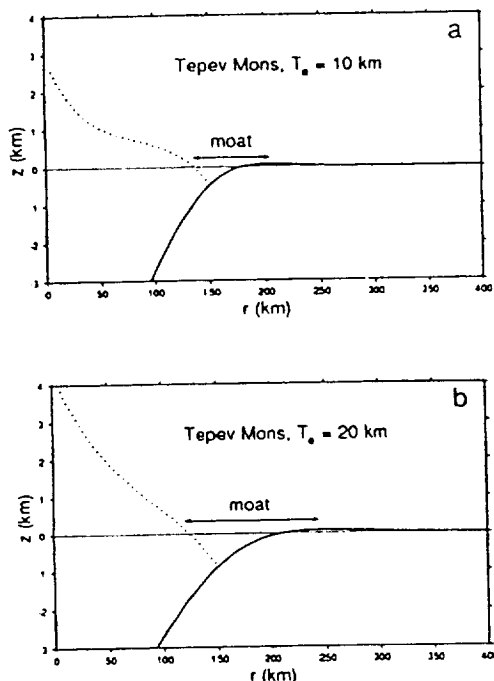
Fig. 2. Analytic solutions for lithospheric deflection by a conical load of height 10 km and radius 150 km. The solid line is the deflection solution, while the dotted line includes the topography from the load. (a) $T_e = 10$ km; (b) $T_e = 20$ km.
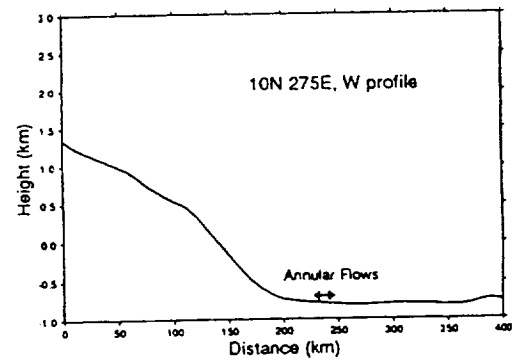
Fig. 3. Topographic cross section through the volcano at 10°N, 275°E, extending westward.
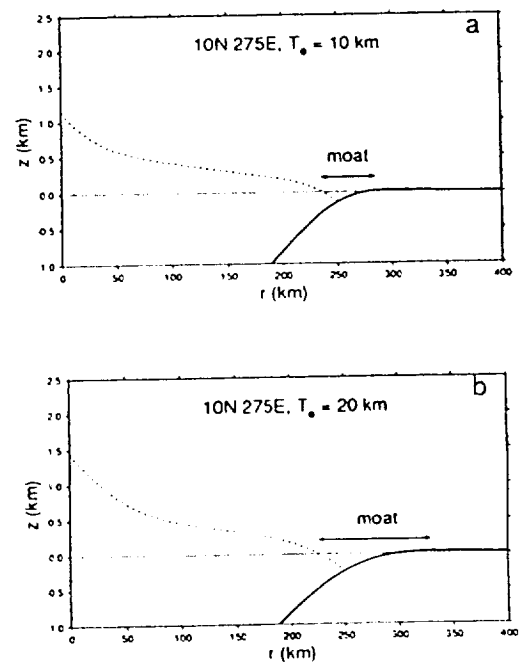
Fig. 4. Analytic solutions for lithospheric deflection by a conical load of height 5 km and radius 250 km. Solid line is deflection solution, dotted line includes the topography from the load. (a) $T_e = 10$ km: (b) $T_e = 20$ km.

through large landslides or slumps such as those discovered off the Hawaiian Islands [2], is one possibility. Moat-filling flows may be covered by later radial flows, a process that may have been repeated many times during volcano growth.

Conclusions: Under the assumption that circumferentially ponded flows surrounding volcanos have at least partially filled a flexural moat, we can compare the position and extent of the moat to predictions from analytic flexure models. For Tepev Mons, models that fit best have plate thicknesses in the range of 10 to 20 km. For the volcano at 10°N, 275°E, the best fit is obtained for a thickness of about 10 km. These values of elastic plate thickness

can be converted to estimates of mechanical plate thickness and thermal gradient [6]. Using parameters appropriate for Venus [7] we obtain thermal gradients values of about 12–25 K/km for Tepev Mons and about 25 K/km for 10°N, 275°E. These gradients are in the range expected if Venus loses most of its internal heat by conduction through a globally continuous, if laterally heterogeneous, lithospheric shell [7].

References: [1] Menard H. W. (1956) *Bull. AAPG, 40*, 2195. [2] Moore R. B. et al. (1989) *JGR, 94*, 17465. [3] Arvidson R. E. et al. (1991) *Science, 252*, 270. [4] Brotchie J. F. (1971) *Mod. Geol., 3*, 15. [5] Wessel P. and Smith W. H. F. (1991) *Eos, 72*, 441. [6] McNutt M. K. (1984) *JGR, 89*, 11180. [7] Solomon S. C. and Head J. W. (1990) *GRL, 17*, 1393.

N93-14345

PANCAKELIKE DOMES ON VENUS. Dan McKenzie[1], Peter G. Ford[2], Fang Liu[2], and Gordon H. Pettengill[2], [1]Institute of Theoretical Geophysics, Bullard Laboratories, Madingley Road, Cambridge CB3 OEZ, UK, [2]Center for Space Research, Massachusetts Institute of Technology, Cambridge MA 02139, USA.

The shape of seven large domes on the plains of Venus, with volumes between 100 and 1000 km^3, is compared with that of an axisymmetric gravity current spreading over a rigid horizontal surface. Both the altimetric profiles and the horizontal projection of the line of intersection of domes on the SAR images agree well with the theoretical similarity solution for a newtonian fluid, but not with the shape calculated for a rigid-plastic rheology, nor with that for a static model with a strong skin. As a viscous current spreads, it generates an isotropic strain rate tensor whose magnitude is independent of radius. Such a flow can account for the randomly oriented cracks that are uniformly distributed on the surface of the domes. The stress induced by the flow in the plains material below is obtained, and is probably large enough to produce the short radial cracks in the surface of the plains beyond the domes. The viscosity of the domes can be estimated from their thermal time constants if spreading is possible only when the fluid is hot, and lies between 10^{14} and 10^{17} Pa s. Laboratory experiments show that such viscosities correspond to temperatures of 610°–690°C in dry rhyolitic magmas. These temperatures agree with laboratory measurements of the solidus temperature of wet rhyolite.

These results show that the development of the domes can be understood using simple fluid dynamical ideas, and that the magmas involved can be produced by wet melting at depths below 10 km, followed by eruption and degassing.

N93-14346

GROUNDBASED NEAR-IR OBSERVATIONS OF THE SURFACE OF VENUS. V. S. Meadows[1], D. Crisp[2], and D. A. Allen[3], [1]University of Sydney, Sydney, Australia, [2]Jet Propulsion Laboratory, Pasadena CA, USA, [3]Anglo-Australian Observatory.

Near-infrared observations of the nightside of Venus have revealed thermal emission from the lower atmosphere in relatively transparent regions of the spectrum centred on 1.0, 1.1, 1.18, 1.27, and 1.31 µm [1,2,3]. The emission in these windows is believed to originate from the very lowest scale heights of the atmosphere and from the surface. Recent groundbased work in the 1.0-µm window [4], and measurements made at 1.18 µm by the Galileo NIMS during its 1990 flyby [3], indicate that the Venus surface topography produces contrasts in the thermal emission. These contrasts are believed to be caused primarily by surface temperature differences

associated with differences in surface elevation. A similar correlation of reduced emissivity with altitude has been seen in 17-cm radio maps [5], although these contrasts are not consistent with topographically related temperature differences alone, and are postulated to be the result of increased reflectivity due to the presence of conducting materials in the highland surfaces. As well as providing information about the surface, observations in the near infrared can be used to obtain estimates of the optical depth of the lower atmosphere at these wavelengths and to constrain the water abundance in the lower atmosphere.

We present images of the nightside of Venus taken in the near-infrared windows at 1.0, 1.1, 1.18, 1.28, 1.31, and 2.3 µm with the new infrared camera/spectrometer IRIS on the Anglo-Australian Telescope. These data were taken in spectral-mapping mode. This technique involves scanning the telescope perpendicular to the slit, while collecting spectra at successive slit positions across the planet. We produce data cubes with one spectral and two spatial dimensions. The spectra have a resolution $\lambda/\Delta\lambda \sim 400$. Images can be extracted over any wavelength regions. Each image has square pixels of 0.8" resolution. Spectral image cubes were obtained on a total of eight days during July, September, and October 1991. The July cubes cover the spectral region 0.820–1.511 µm and the September and October cubes 1.135–1.317 µm. We reduced the scattered light from the sunlit crescent in images extracted from each window by subtracting images taken on either side of the window, where the Venus atmosphere is opaque. Unlike the short wavelength windows, which reveal thermal contrasts that originate primarily from the surface and deep atmosphere, the emission in the 2.3-µm window is produced at much higher altitudes (30–40 km). Emission contrasts seen near 2.3 µm are associated with horizontal variations in the cloud optical depths, and have rotation periods of about six days [2]. These cloud contrasts fade at shorter wavelengths as the cloud deck becomes steadily more transparent, but are still present and must be removed to distinguish the surface emissivity contrasts.

We detect large contrasts in infrared emission (20–40%) across the disc of Venus in the 1.0-, 1.1-, 1.18-, 1.28-, and 1.31-µm images. Contrasts at these wavelengths may be due to a combination of variations in the optical depths of the overlying sulfuric acid clouds and differences in surface emission. Comparison with the 2.3-µm images show that the patterns seen in the 1.28- and 1.31-µm windows are consistent with cloud optical depth variations alone and require no contribution from the surface. However, images at 1.0, 1.1, and 1.18 µm from July 1991 show a dark feature having a contrast that increases with decreasing wavelength (Fig. 1). This behavior is contrary to that expected of cloud absorption. Images taken on three successive days in October show another dark feature that is stationary with respect to the surface. These regions of lower emission correspond closely to the high-altitude surface regions of Beta Regio and Aphrodite Terra.

The images can potentially reveal the near-infrared emissivity of the surface of Venus, thereby complementing Magellan radar reflectivity and groundbased radio emissivity measurements. The contrast ratio between highlands and plains is much smaller than would be expected for blackbody radiation from the surface alone. Unlike at radio wavelengths, where the atmosphere is essentially transparent, at near-infrared wavelengths the atmosphere emits, absorbs, and scatters radiation, and can modify the observed topographically induced contrasts. The additional radiation from the atmosphere reduces the contrast, and further modification would be expected if terrain at different altitudes has different emissivities. A fit to our data therefore requires, and may constrain, a model of the
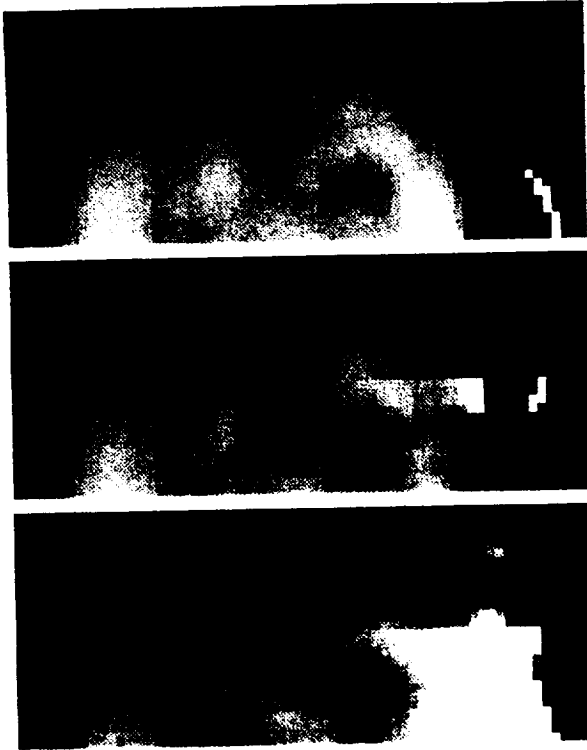
Fig. 1. Data taken on the 27th of July 1991. These are, from the top, images taken in the 1.18-, 1.1-, and 1.0-μm windows. Beta Regio can be seen on the lower right near the crescent. Its apparent contrast with respect to the surrounding plains increases with decreasing wavelength. This feature is not detected in the 1.28- and 1.31-μm windows.

lowest scale height of the atmosphere. More comprehensive surface-atmosphere radiative transfer models are being used to determine whether the observed emission contrasts are consistent with surface elevation-related temperature differences or require surface emissivity variations as well.

References: [1] Allen D. A. (1990) *IAU Circ., 4962*. [2] Crisp D. et al. (1991) *Science, 253*, 1538. [3] Carlson R. W. et al. (1991) *Science, 253*, 1541. [4] Lecacheux J. et al. (1991) *IAU Circ., 5365*. [5] Ford P. G. and Pettengill G. H. (1983) *Science, 220*, 1379.

N93-14347

MAGELLAN STEREO IMAGES AND VENUSIAN GEOLOGY.

H. J. Moore[1], R. S. Saunders[2], J. J. Plaut[2], and T. J. Parker[2], [1]U.S. Geological Survey, Menlo Park CA 94025, USA, [2]California Institute of Technology, Jet Propulsion Laboratory, Pasadena CA 91109, USA.

Areas of Venus imaged by Magellan radar with multiple viewing conditions provide unique data that will contribute to the solution of venusian geologic problems and provide a basis for quantitative comparison of venusian landforms with those on other planetary bodies. Three sets of images with different viewing conditions have been acquired: (1) left-looking with variable incidence angles (cycle 1 profile), (2) right-looking with nearly constant incidence angles (cycle 2 profile), and (3) left-looking with variable incidence angles that are almost always smaller than those in (1) (cycle 3 profiles).

The unique data provided by paired images of the same scene with different incidence angles arises from image displacements caused by the relief of individual landforms at scales comparable to

the ground-range and azimuth resolutions of the images [1]. There are two aspects of the data: (1) Stereopsis achieved by simultaneous viewing of paired left-looking images of the same scene permits three-dimensional perception and interpretation of the morphologies of landforms at resolutions much finer than the altimetry footprints. (2) Measurements of differences of image displacements (parallax) on paired images with known imaging geometries provide quantitative estimates of the relief and shapes of landforms. The potential scientific contributions of the data can be grouped into two interrelated classes: (A) geologic mapping, analysis, and interpretation and (B) topical studies that involve topographic measurements.

A. Stereopsis, without quantitative measurements, enhances geologic mapping, analysis, and interpretation of the rock units of Venus to a degree that cannot be overestimated. In geologic mapping, assemblages of landforms, assessments of backscatter and variations in backscatter, and fine-scale topography are used to define and characterize geologic map units that represent laterally continuous deposits or rock units. Stereopsis adds the important dimension of local relief for characterization of geologic units at a scale that is not possible with Magellan altimetry or products derived from the altimetry. Relative ages of the geologic units are determined using the well-known principles of superposition and intersection. Here, the perception of relief is invaluable because superposition relations among the geological units are more readily and clearly established. The recognition of folds, faults, and fault systems, regardless of their orientations, is facilitated with stereopsis so that sequences of deformation of the geologic units can be determined and structural analyses vastly improved. Shapes of landforms are readily perceived so that they can be properly interpreted. The end result of the mapping, analyses, and interpretations is a geologic history of Venus that includes the sequences of formation and deformation of various geologic units.

B. Measurements of relief at the finest scale possible are necessary for numerous topical studies. Standard altimetry will provide the necessary information on the relief of most large landforms, but it tends to underestimate the relief of small landforms [2] and distorts their shapes. Although special processing of the altimeter echoes improves the estimates of the relief and shapes of some landforms [3], there are uncertainties in the interpretations of the echoes [2]. Examples of topical studies requiring measurements of relief are given below.

Impact Craters: Impact craters are ubiquitous landforms on terrestrial planets and moons. They range in diameter from 1.5 to 280 km on Venus. The shapes and dimensions of venusian craters are important for their interpretation and for comparisons with those on other planets and bodies [4–7]. Two of these dimensions are crater depth and rim height.

Small Volcanic Landforms: Small volcanic edifices and craters are important landforms on most planetary bodies because they indicate certain aspects of the style of volcanism. On Venus, small volcanic landforms include domes, "ticks," cratered cones, rilles, and so forth [8]. Relief of edifices and depths of craters are among the dimensions used to classify volcanic landforms and compare them among the various planetary bodies [9–12].

Tectonic Structures: The crust of Venus exhibits a host of landforms that indicate remarkable variations in style and intensity of deformation [13]. Landforms with relief include scarps of normal faults, ridges of reverse faults, horsts, graben, and nappes. Knowledge of the relief and planform dimensions of these landforms at the fine-scale will help provide estimates of magnitudes of strains involved in the deformations [14,15].

Surface Processes: Surface processes include eolian, mass wasting, and other processes [16]. Examples where measurements of relief will be useful include (1) analyses of erosion-deposition patterns behind obstacles [16], (2) slopes of erosion-deposition environments, (3) slope stability analyses, and (4) estimates of landslide volumes.

Rheological Analyses: There is a host of applications of relief measurements to the analyses of the rheological properties of venusian flow associated with volcanism [8], impact cratering [7], and debris flows [17]. These applications include flow thicknesses and relations between the flows and the adjacent topography. Lava flow thickness as large as 100 to 700 m have already been measured using parallax [18]. According to Magellan altimetry, bright outflows from impact craters flow up slopes, and flow margins may be 100 m or so above the centers of the outflows. If true, these relations have important implications about the kinematics and rheology of the outflows. Relations between the relief and runout may reveal the rheological properties of venusian landslides [17,19].

Backscatter Functions: A better understanding of the relations between backscatter cross sections and incidence angles can be gained by analyses of given classes of landforms and terrains with variable slopes and sufficient relief for stereometric analyses. Multiple viewing conditions are essential in understanding (1) the forms of the scattering laws, (2) the dielectric properties, (3) the contributions of conducting materials to scattering behaviors, (4) the fine-scale roughnesses, and (5) the contributions of quasispecular and diffuse echoes to average backscatter cross sections of tesserae, impact craters, and volcanic edifices, craters, and flows [20]. An understanding of the above will assist in geologic interpretations of tesserae, impact cratering, and volcanism.

Radarclinometry and Shape from Shading: Once the backscatter functions of the various classes of landforms are established, shape from shading can be used to refine the topography of landforms with stereo-relief data [21], and radarclinometry can be used to estimate the relief and shapes of landforms of the same class where there is no stereoscopic coverage and where the landforms are too small for stereo-parallax measurements.

Topographic Analyses: Radargrammetric reduction of stereoscopic models and radarclinometry (shape from shading) [21] may provide information on the topography of venusian surfaces at slope lengths smaller than those achievable with Magellan altimetry and larger than those obtained by analyses of quasispecular echoes from level surfaces with surface tilts smaller than the image resolution [22]. Derived topographic information includes slope probabilities, power spectral densities, and fractal dimensions.

Altimetry: Radargrammetric reduction of stereoscopic models can confirm, refute, or supplement Magellan altimetry where problems with the altimetry exist. The current problem of the steep slopes of Maxwell Montes is an example, but there are others.

References: [1] Leberl F. et al. (1992) *JGR*, special Magellan issue, in press. [2] Leberl F. et al. (1991) *Photog. Engr. Rem. Sens.*, *57*, 1561–1570. [3] McKenzie D. et al. (1992) *JGR*, special Magellan issue, in press. [4] Pike R. J. (1980) *USGS Prof. Paper 1046-C*, 77 pp. [5] Pike R. J. and Davis P. A. (2984) *LPSC XV*, 645–646. [6] Schenk (1991) *JGR*, *96*, 15635–15664. [7] Schaber (1992) *JGR*, special Magellan issue, in press. [8] Head J. W. et al. (1991) *Science*, *252*, 276–288. [9] Pike R. J. (1978) *Proc. LPSC 9th*, 3239–3273. [10] Pike R. J. and Clow G. D. (1981) *USGS Open-file Rept. 81-1038*, 40 pp. [11] Wood C. A. (1979) *Proc. LPSC 10th*, 2815–2840. [12] Blake S. (1990) *IAVCEI Proc. Volcanol.*, *2*, 88–126. [13] Solomon S. et al. (1990) *Science*, *252*, 297–312. [14] Connors C. and Suppe J. (1991) *Eos*, *72*, 285. [15] McGill G.E. (1991) *Eos*,
72, 285. [16] Arvidson R. E. et al. (1991) *Science*, *252*, 270–275. [17] Guest J. E. et al. (1992) *JGR*, special Magellan issue, in press. [18] Moore H. J. et al. (1992) *JGR*, special Magellan issue, in press. [19] Hsu K. J. (1975) *GSA Bull.*, *86*, 129–140. [20] Plaut J. J. (1992) *LPSC XXIII*, 1085–1086. [21] Leberl F. et al. (1991) *Photog. Engr. Rem. Sens.*, *57*, 51–59. [22] Tyler G. L. (1991) *Science*, *252*, 265–270.

N93-14348

FLEXURAL MODELS OF TRENCH/OUTER RISE TOPOGRAPHY OF CORONAE ON VENUS WITH AXISYMMETRIC SPHERICAL SHELL ELASTIC PLATES. W. Moore[1], G. Schubert[1], and D. T. Sandwell[2], [1]University of California, Los Angeles CA, USA, [2]Scripps Institution of Oceanography, University of California–San Diego, La Jolla CA, USA.

Magellan altimetry has revealed that many coronae on Venus have trenches or moats around their peripheries and rises outboard of the trenches [1,2]. This trench/outer rise topographic signature is generally associated with the tectonic annulus of the corona. Sandwell and Schubert [3,4] have interpreted the trench/outer rise topography and the associated tectonic annulus around coronae to be the result of elastic bending of the Venus lithosphere (though the tectonic structures are consequences of inelastic deformation of the lithosphere). They used two-dimensional elastic plate flexure theory to fit topographic profiles across a number of large coronae and inferred elastic lithosphere thicknesses between about 15 and 40 km, similar to inferred values of elastic thickness for the Earth's lithosphere at subduction zones around the Pacific Ocean. Here, we report the results of using axisymmetric elastic flexure theory for the deformation of thin spherical shell plates [5] to interpret the trench/outer rise topography of the large coronae modeled by Sandwell and Schubert [3,4] and of coronae as small as 250 km in diameter. In the case of a corona only a few hundred kilometers in diameter, the model accounts for the small planform radius of the moat and the nonradial orientation of altimetric traces across the corona. By fitting the flexural topography of coronae we determine the elastic thickness and loading necessary to account for the observed flexure. We calculate the associated bending moment and determine whether the corona interior topographic load can provide the required moment. We also calculate surface stresses and compare the stress distribution with the location of annular tectonic features.

The model lithosphere is a spherical elastic shell buoyantly supported by a dense internal fluid. Although the model includes membrane stresses, for a planet the size of Venus the buoyant support provides the dominant reaction to the load. The load is modeled as either an axisymmetric disk (uniform loading) or a ring (peripheral loading). Other load geometries may be achieved by superposition. The wavelength of the flexural feature depends only on the thickness of the plate and not on the details of the loading, allowing a unique determination of the elastic thickness from the best-fitting model. Vertical strains are not included so that the vertical displacement at the top of the lithosphere is the same as that at the bottom where the buoyancy forces are acting. This model includes the effects of a distributed load and a continuous lithosphere that are absent in two-dimensional models and that become important when the radius of the load is reduced to a few flexural wavelengths.

The models are fit to the topography using least squares fitting and the relevant parameters are determined from the best-fitting model. For the corona Latona (diameter = 800 km) we reproduce Sandwell and Schubert's [3] value of approximately 30 km for the

elastic thickness, demonstrating the agreement of the axisymmetric and two-dimensional models in the case of a large corona. For smaller coronae, we find that elastic lithosphere thicknesses between 10 km and 15 km provide the best fits to the flexural topography (Table 1).

TABLE 1.

Corona Name	Location	Diameter (km)	Elastic Thickness (km)
Fatua	17°S, 17°E	310	15
Selu	43°S, 6°E	300	10
Aramaiti	26°S, 82°E	350	10
Boann	27°N, 136°E	300	5
Latona	20°S, 171°E	800	30

The disk loading model can be used to deduce the gravity signature of a corona. We will report calculations of gravity using the disk loads inferred for the larger coronae and compare with recent gravity data, e.g., over Artemis [6].

References: [1] Squyres S. W. et al. (1992) *JGR*, in press. [2] Stofan E. R. et al. (1992) *JGR*, in press. [3] Sandwell D. and Schubert G. (1992a) *JGR*, submitted. [4] Sandwell D. and Schubert G. (1992b) *Science*, submitted. [5] Brotchie I. and Sylvester R. (1969) *JGR*, 74, 5240–5252. [6] Sjogren W. L. (1992) *Eos*, 73, 83.

N93-14349

RADAR-ANOMALOUS, HIGH-ALTITUDE FEATURES ON VENUS. Duane O. Muhleman and Bryan J. Butler, Division of Geological and Planetary Science, California Institute of Technology, Pasadena CA 91125, USA.

Over nearly all of the surface of Venus the reflectivity and emissivity at centimeter wavelengths are about 0.15 and 0.85 respectively. These values are consistent with moderately dense soils and rock populations, but the mean reflectivity is about a factor of 2 greater than that for the Moon and other terrestrial planets (in the case of the Earth, regions free of moisture). Pettingill and Ford [1], using Pioneer Venus reflectivities and emissivities, found a number of anomalous features on Venus that showed much higher reflectivities and much lower emissivities with both values approaching 0.5. These include Maxwell Montes, a number of high regions in Aphrodite Terra and Beta Regio, and several isolated mountain peaks. Most of the features are at altitudes above the the mean radius by 2 to 3 km or more. However, such features have been found in the Magellan data at low altitudes and the anomalies do not exist on all high structures, Maat Mons being the most outstanding example. A number of papers have been written that attempt to explain the phenomena in terms of the geochemistry balance of weathering effects on likely surface minerals; see reference [2] and papers cited therein. The geochemists have shown that the fundamentally basaltic surface would be stable at the temperatures and pressures of the mean radius in the form of magnetite,but would evolve to pyrite (FeS_2) and/or pyrrhotite ($Fe_{0.87}S$) in the presence of sulfur-bearing compounds such as SO_2. Pyrite will be stable at altitudes above 4 or 5 km on Venus. The details of the stability of these rather good electrical conductors depends on the availability of O in excess over that tied up in equilibrium with the parent constituent of the atmosphere, CO_2. This is clearly explained in [2]. However, the abundance of the sulfur compound SO_2 is very

uncertain and arguments are made that it is actually varying with time on a scale of 10 yr.

Although the geochemical arguments are rather compelling, it is vitally important to rationally look at other explanations for the radar and radio emission measurements such as that presented by Tryka and Muhleman [3]. The radar reflectivity values are retrieved from the raw Magellan backscatter measurements by fitting the Hagfors' radar scattering model in which a surface roughness parameter and a normal incidence electrical reflectivity are estimated. The assumptions of the theory behind the model must be considered carefully before the results can be believed. These include that the surface roughness exists only at horizontal scales large compared to the wavelength, the vertical deviations are gaussianly distributed, there is no shadowing, and that the reflection occurs at the interface of two homogeneous dielectric half-spaces. Probably all these conditions are violated at the anomalous features under discussion! The most important of these is the homogeneity of the near surface of Venus, particularly in highlands. Under the assumptions of the theory, all of the radio energy is reflected by the impedance jump at the very boundary. However, in heterogeneous soil some fraction of the illuminating energy is propagated into the soil and then scattered back out by impedance discontinuities such as rocks, voids, and cracks. In light soils, the latter effect can overwhelm the scattering effects of the true surface and greatly enhance the backscatter power, suggesting a much higher value of an effective dielectric constant that would be estimated from Hagfors' model.

The phenomenon of emission is similar but has several important different characteristics. In the case of thermal emission from a smooth, homogeneous dielectric into vacuum, some of the radiation generated in the effective black body passes through the interface to the observer and a fraction is reflected back downward into the material where it is reabsorbed. In the simple case of an isothermal layer (such as the near surface of Venus), radiating from a homogeneous layer, the emissivity is determined by the Fresnel reflection coefficients at the observing angle to the normal. However, if the layer contains multiple scatterers in a light soil, radiation generated even at small depths cannot reach the surface since the tendency is to scatter the energy backward, similar to the strong backscattering reflection from above such a surface. Thus, the emissivity can be greatly depressed and the observed brightness temperature will be low. This phenomenon for Venus was discussed in 1979 [4] as an explanation for the decrease in the average disk temperature of Venus at wavelengths longward of 10–20 cm.

The most outstanding and relevant example of the importance of multiple scattering or volume scattering in radar and microwave emission are the icy satellites of Jupiter [5]. The radar reflectivity of the full disk of Europa at 13-cm wavelength is 0.65 and the emissivity is about 0.42! Certainly, the surface of Europa is almost pure water ice that, if it existed in the form of dense ice, would have a reflectivity of 0.07 and an emissivity of 0.93. If the Europa ice was in the form of a homogeneous layer, under dense frost the reflectivity would be even lower. It is obvious that the reflection and emission phenomena on Europa are independent of the Fresnel surface reflection coefficients and dependent entirely on the physical structure of the near surface, i.e, the existence of lumps, voids, cracks, etc. It is also very important that ice as cold as 130 K is highly transparent at centimeter wavelengths and very little of the energy is ohmically absorbed in the near surface. If that were not the case, the surface would be a good emitter and a rather poor reflector.

The radiative transfer calculations for the emission and reflection from a layer with volume scattering are very complex, with the

results strongly dependent on the details of the individual scattering elements and the electrical parameters of the matrix of material in which the scatterers are "suspended." The most fundamental example for which an analytical solution is known is the case of isotropic scattering in a semi-infinite, plane parallel half space [6]. The assumptions of this theory are important, of course. It assumes that radiation incident on a scatterer is uniformly scattered in all directions. For this to be strictly true, electromagnetic theory requires that the scatterers be ellipsoidal with random orientations and be separated by distances long compared to the wavelength in the medium. Chandrasaker's solution intrinsically assumes that the scatterers are suspended in a transparent medium. The ideas were adopted in [3] with the argument that rocks in light venusian soils may behave this way to first order on average, even though the scatterers are probably far from spherical and may be piled on top of each other. The fact that the matrix supporting the scatterers is not completely transparent is not serious as long as it is sufficiently transparent to allow the radiation to scatter a "few" times before absorption or before the energy is backscattered out of the layer.

If we visualize the scatterers as rocks and fragments we may consider a suite of likely models that would display the microwave observables seen in the PV and Magellan data. Such rocks would exist at all sizes from dust to the rare boulders of many meters. It is reasonable to assume that the particle sizes could be represented by a power law distribution and a good guess at the slope parameter of the distribution would be about −3, consistent with that found from tumbling rocks in a fracturing process. The index is not of great importance. We assume that the soil matrix has a real dielectric constant of 2, consistent with the flat regions on Venus that exhibit the lowest reflectivity. Such soils would have densities under 1 gm/cm^3 and power absorption lengths of order 2–3 m. The rocks would have dielectric constants in the range of 5–8, primarily dependent on the metal content, and corresponding absorption lengths of about 0.6–0.1 m. Silicate rocks have low complex dielectric constants and mafic rocks such as basalts high in Fe have large values. We have applied the theory from [3] to a typical granite and a typical basalt and the resulting 13-cm reflectivities and emissivities at normal incidence are shown in Table 1. An important unknown parameter is the largest size cutoff of the power law size distribution. Obviously, if the "particles" could be as large as kilometers, the results would degenerate to the parameters of the largest sphere and scattering would not be important. The results are presented in the table as a function of the cutoff radius of the size distribution.

TABLE 1.

	Maximum Radius (cm)	Reflectivity	Emissivity
Granite	5	0.617	0.355
	10	0.496	0.486
	30	0.383	0.599
	50	0.341	0.637
	100	0.291	0.679
Basalt	5	0.486	0.509
	10	0.386	0.581
	30	0.304	0.664
	50	0.273	0.690
	100	0.245	0.728

It is clear that this explanation is sufficient for the Venus anomalous features. Furthermore, the parameters approach the average values of the Venus surface when the value of the maximum particle size is increased moderately. There are ambiguities in these calculations, but the ambiguities are intrinsic to the Magellan measurements themselves in rough, heterogeneous areas on Venus where the Hagfors' assumptions are severely bent. New scattering theories involving Monte Carlo techniques will be presented.

References: [1] Pettingill G. H. et al. (1988) *JGR, 93*, 14885. [2] Klose K. et al. (1992) *JGR*, special Magellan issue. [3] Tryja K. and Muhleman D. O. (1992) *JGR*, special Magellan issue. [4] Muhleman D. et al. (1979) *Ap. J., 234*, 1979. [5] Muhleman D. and Berge G. (1991) *Icarus, 93*, 263. [6] Chandrasaker S., *Radiative Transfer*, Dover Publications.

N93-14350

THE GABBRO-ECLOGITE PHASE TRANSITION AND THE ELEVATION OF MOUNTAIN BELTS ON VENUS.

Noriyuki Namiki and Sean C. Solomon, Department of Earth, Atmospheric, and Planetary Sciences, Massachusetts Institute of Technology, Cambridge MA 02139, USA.

Introduction: The linear mountain belts of Ishtar Terra on Venus are notable for their topographic relief and slope and for the intensity of surface deformation [1,2]. The mountains surround the highland plain Lakshmi Planum. Volcanism is rare to absent in Maxwell, Freyja, and Akna Montes, but a number of magmatic features are evident in Danu Montes [2,3], the mountain range least elevated above Lakshmi Planum. Whether western Ishtar Terra is a site of mantle upwelling and consequent hot spot volcanism [4–6] or of mantle downwelling and consequent convergence of lithospheric blocks [7,8] is currently a matter of debate. However, the mountains are generally regarded as products of large-scale compression of the crust and lithosphere [2,9].

Among the four mountain belts surrounding Lakshmi Planum, Maxwell Montes is the highest and stands up to 11 km above the mean planetary radius and 7 km above Lakshmi Planum. The bulk composition and radioactive heat production of the crust on Venus, where measured, are similar to those of terrestrial tholeiitic basalt [10]. Because the thickness of the low-density crust may be limited by the gabbro-garnet granulite-eclogite phase transitions (Fig. 1), the 7–11-km maximum elevation of Maxwell Montes is difficult to understand except in the unlikely situation that the crust contains a large volume of magma [11]. A possible explanation is that the base of the crust is not in phase equilibrium. It has been suggested that under completely dry conditions, the gabbro-eclogite phase transition takes place by solid-state diffusion and may require a geologically significant time to run to completion [12]. Solid-state diffusion is a strongly temperature-dependent process. In this paper we solve the thermal evolution of the mountain belt to attempt to constrain the depth of the gabbro-eclogite transition and thus to assess this hypothesis quantitatively.

Thermal Model: The one-dimensional heat equation is solved numerically by a finite difference approximation. The deformation of the horizontally shortening crustal and mantle portions of the thermal boundary layer is assumed to occur by pure shear, and therefore the vertical velocity is given by the product of the horizontal strain rate $\dot{\gamma}$ and depth z. The thermal diffusivity is assumed to be 1.0×10^{-6} m^2 s^{-1} in both crust and mantle. Crustal heat production is assumed to equal 1.4×10^{-13} K s^{-1}. The initial temperature profile is determined by the assumption of steady-state conditions with zero velocity. Temperature at the surface and the

bottom of the thermal boundary layer are fixed at 750 K and at a value T_{bl} taken as free parameter.

The phase diagram is assumed to be that of tholeiitic basalt [13], and the densities of gabbro and eclogite are taken to be 2900 and 3500 kg m^{-3}. The density of garnet-granulite is assumed to increase linearly from that of gabbro to that of eclogite as pressure increases at a given temperature. The density of the mantle is assumed to be 3400 kg m^{-3}. The micromechanism of the gabbro-eclogite transition is not well understood. In this study we assume that the volume diffusion of cations is the most likely rate-limiting process of the transformation, which involves chemical as well as phase changes. The volume fraction of reacted component, Ψ, is given by

$$\dot{\Psi}\Psi = D/r^2$$

where r is the grain radius and D is the diffusion coefficient [12]. Since the slowest-moving cation limits the reaction rate and Al^{3+} is likely to be this cation, we adopt as a minimum value for D the lower end of the range of estimates of the diffusion rate of Al^{3+} in orthopyroxene [14]

$$D = D_{Al,Opx} = 1.1 \times 10^{-5} \exp(-400\ kJ/RT)$$

where R is the gas constant and T is the absolute temperature. The diffusion rate, however, is experimentally uncertain because Al^{3+} diffusion is extremely sluggish, particularly at low temperature. In order to bound D from above, we use the diffusion rate of Fe in garnet ($D_{Fe,Gt} = 6.4 \times 10^{-8} \exp[-(270\ kJ + 5.7 \times 10^{-5} P)/RT]$), where P is in Pa. For each parcel of shortening lithosphere, Ψ is obtained by integration over time. The density at a given depth is determined from the volume fractions of unreacted and reacted components.

Numerical Results: Temperatures in the thickening crust and mantle are calculated for rates of horizontal convergence of 10^{-15} (Fig. 1a) and 10^{-16} s^{-1} (Fig. 1b). For all models discussed here (Table 1), thicknesses of crust and thermal boundary layer are assumed to be initially 20 and 50 km, respectively, and to increase to 100 and 250 km, respectively. Temperature profiles for the strain rate of 10^{-15} s^{-1} are vertically stretched as the crust and lithospheric mantle are thickened (Fig. 1a). Temperatures do not increase significantly from initial values because heat is mainly transferred by advection and the contribution of crustal heat production is minor. Hence gabbro remains metastable for 50 m.y. or more, and
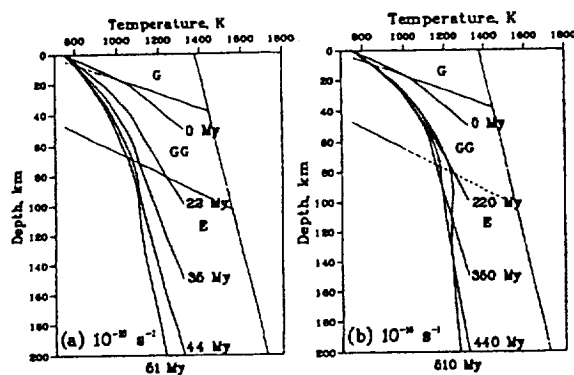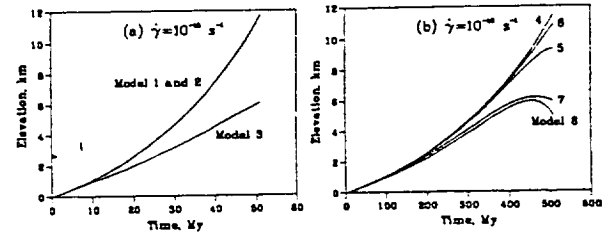
Fig. 2. Temporal variations of elevation for the models in Table 1.

the elevation of shortened lithosphere can increase as much as 12 km above the surrounding plains in that time interval (Fig. 2a). The phase transition proceeds, i.e., elevation is limited, only if grains are small and diffusion is fast (Model 3).

For $\dot{\gamma} = 10^{-16}$ s^{-1}, crustal heat production dominates advective heat transfer after the crust becomes as thick as 60–80 km (Fig. 1b). The resulting increase in temperature hastens the phase transition. The slower strain rate also lengthens the formation time of the mountains relative to the characteristic reaction time, which depends on r, D, and temperature at the base of the crust. For larger grains (r = 10 mm), the elevation reaches 11 km or more if the initial temperature at the base of the crust, T_c, is 1150 K (Model 6 in Fig. 2b). For the same value of T_c the elevation is at most 6 km for grains of 1-mm radius (Model 7). This result constitutes an upper bound on T_c for small grain size. If D = $D_{Fe,Gt}$ is assumed, that upper bound is lowered to 1050 K (Model 8).

Discussion: Because at long wavelengths the topography of western Ishtar Terra is correlated with the gravity field, dynamical support of the broad 4-km elevation of the region is likely [e.g., 15]. Therefore, the 7-km elevation of Maxwell Montes above the adjacent plateau is a more meaningful constraint on maximum relief than the 11-km elevation above mean planetary radius. The results are insensitive to the assumed initial thickness of crust but are sensitive to the density difference between crust and mantle. If densities of 3000 and 3300 kg m^{-3} for crust and mantle are assumed, elevations are 40% lower than the values presented here. Such changes constrain the models of thermal structure and phase transition depth more severely at low strain rate than the density values adopted above.

Two diffusion rates have been assumed in this study so as to represent a wide range of diffusion data. We should note, however, that under wet conditions, i.e., in the presence of either water [16] or melt [17], grain-boundary diffusion becomes much more efficient than volume diffusion. This is potentially noteworthy for understanding the contrast between Maxwell and Danu Montes. Despite the fact that Danu Montes display compressional deformation as extensive as the other mountain belts, the maximum elevation is as little as 0 km above the bounding plateau. Such comparatively modest elevation may be related to the presence of magmatic features within Danu Montes, if elevation is limited by an enhanced diffusion rate because of the melt at grain boundaries. Assessing the cause of higher temperatures beneath Danu Montes requires more detailed thermal models than the simple one-dimensional model considered here.

Conclusions: Taking into account the temperature-dependent reaction rate of the gabbro-eclogite phase transition, horizontal strain rates of 10^{-15} and 10^{-16} result in significant differences in the maximum elevation of mountains, not only because of the difference in the formation time for relief, but also because of the difference in the thermal regime from advection-dominated to

Fig. 1. Thermal evolution of crust and mantle thickened by a uniform horizontal strain rate of (a) 10^{-15} and (b) 10^{-16} s^{-1}. The phase diagram of the gabbro (G)—garnet granulite (GG)—eclogite (E) transition [13] is also shown. The models shown correspond to models (a) 1, 2, and 3, and (b) 4, 5, and 8 in Table 1.

TABLE. 1. Model parameters.

Models	r, mm	$\dot{\gamma}$, s⁻¹	D	T_c, K	T_{bl}, K
1	1	10^{-15}	$D_{Al,Opx}$	1050	1321
2	10	10^{-15}	$D_{Al,Opx}$	1050	1321
3	1	10^{-15}	$D_{Fe,Ot}$	1050	1321
4	1	10^{-16}	$D_{Al,Opx}$	1050	1321
5	10	10^{-16}	$D_{Al,Opx}$	1050	1321
6	10	10^{-16}	$D_{Al,Opx}$	1350	1521
7	1	10^{-16}	$D_{Al,Opx}$	1150	1521
8	10	10^{-16}	$D_{Fe,Ot}$	1050	1321

crustal-heat-production dominated. For $\dot{\gamma} = 10^{-15}$ s⁻¹, the observed maximum elevation of mountain belts can be explained as a consequence of disequilibrium phase boundary depth for a wide range of physical parameters, although a comparatively young age for Maxwell Montes (50 m.y.) is implied. For the lesser horizontal strain rate of 10^{-16} s⁻¹, only limited parameter values for thermal models are allowed.

References: [1] Barsukov V. L. et al. (1986) *Proc. LPSC 16th*, in *JGR, 91*, D378. [2] Solomon S. C. et al. (1991) *Science, 252*, 297. [3] Head J. W. et al. (1991) *Science, 252*, 276. [4] Pronin A. A. (1986) *Geotectonics, 20*, 271. [5] Basilevsky A. T. (1986) *Geotectonics, 20*, 282. [6] Grimm R. E. and Phillips R. J. (1990) *GRL, 17*, 1349. [7] Roberts K. M. and Head J. W. (1990) *GRL, 17*, 1341. [8] Bindschadler D. L. and Parmentier E. M. (1990) *JGR, 95*, 21329. [9] Crumpler L. S. et al. (1986) *Geology, 14*, 1031. [10] Surkov Yu. A. et al. (1987) *Proc. LPSC 17th*, in *JGR, 92*, E537. [11] Vorder Bruegge R. W. and Head J. W. (1991) *Geology, 19*, 885. [12] Ahrens T. J. and Schubert G. (1975) *Rev. Geophys. Space Phys., 13*, 383. [13] Ito K. and Kennedy G. C. (1971) *Geophys. Mon., 14*, 303. [14] Smith D. and Barron B. R. (1991) *Am. Mineral., 76*, 1950. [15] Grimm R. E. and Phillips R. J. (1991) *JGR, 96*, 8305. [16] Joesten R. (1991) In *Diffusion, Atomic Ordering and Mass Transport*, 345, Springer-Verlag. [17] Condit R. H. et al. (1985) *Geophys. Mon., 31*, 97. ▲▼

N93-14351

RESULTS OF A ZONALLY TRUNCATED THREE-DIMENSIONAL MODEL OF THE VENUS MIDDLE ATMOSPHERE.

M. Newman, CIRES, University of Colorado, Boulder CO 80309, USA.

Although the equatorial rotational speed of the solid surface of Venus is only 4 m s⁻¹, the atmospheric rotational speed reaches a maximum of approximately 100 m s⁻¹ near the equatorial cloud top level (65 to 70 km). This phenomenon, known as superrotation, is the central dynamical problem of the Venus atmosphere. We report here the results of numerical simulations aimed at clarifying the mechanism for maintaining the equatorial cloud top rotation.

Maintenance of an equatorial rotational speed maximum above the surface requires waves or eddies that systematically transport angular momentum against its zonal mean gradient. The zonally symmetric Hadley circulation is driven thermally and acts to reduce the rotational speed at the equatorial cloud top level; thus wave or eddy transport must counter this tendency as well as friction. Planetary waves arising from horizontal shear instability of the zonal flow (barotropic instability) could maintain the equatorial rotation by transporting angular momentum horizontally from midlatitudes toward the equator. Alternatively, vertically propagating waves could provide the required momentum source. The

relative motion between the rotating atmosphere and the pattern of solar heating, which has a maximum where solar radiation is absorbed near the cloud tops, drives diurnal and semidiurnal thermal tides that propagate vertically away from the cloud top level. The effect of this wave propagation is to transport momentum toward the cloud top level at low latitudes and accelerate the mean zonal flow there.

We employ a semispectral primitive equation model with a zonal mean flow and zonal wavenumbers 1 and 2 [1]. These waves correspond to the diurnal and semidiurnal tides, but they can also be excited by barotropic or baroclinic instability. Waves of higher wavenumbers and interactions between the waves are neglected. Symmetry about the equator is assumed, so the model applies to one hemisphere and covers the altitude range 30 to 110 km. Horizontal resolution is 1.5° latitude, and vertical resolution is 1.5 km. Solar and thermal infrared heating, based on Venus observations and calculations drive the model flow [2]. Dissipation is accomplished mainly by Rayleigh friction, chosen to produce strong dissipation above 85 km in order to absorb upward propagating waves and limit extreme flow velocities there, yet to give very weak Rayleigh friction below 70 km; results in the cloud layer do not appear to be sensitive to the Rayleigh friction. The model also has weak vertical diffusion, and very weak horizontal diffusion, which has a smoothing effect on the flow only at the two grid points nearest the pole.

Simulations were carried out with uniform background angular velocity equivalent to an equatorial speed of u_0, where u_0 was varied between 50 and 75 m s⁻¹. Flow with this angular velocity was the initial condition for half of the simulations. The initial condition for the other half was obtained by adding to this background rotation a horizontally uniform, cyclostrophic-balanced component with zero additional zonal velocity at 30 and 110 km and a smooth increase to a maximum addition of 50 m s⁻¹ at 65 km on the equator. Model runs were also carried out in which the coefficient of vertical diffusion υ was varied. Cases were run for 350 simulated (Earth) days, by which time a statistically steady state was reached. We present averages for the last 40 days of each run.

In the resulting mean zonal flow, the equilibrated equatorial wind maximum was typically between 90 and 105 m s⁻¹, and a jet developed near 40° latitude. The tides, particularly the semidiurnal tide, acted to balance (upgradient/downgradient) vertical advection by the Hadley cell updraft (below/above) the low-latitude zonal wind maximum. Experiments in which u_0 was varied indicated that the shape of this vertical jet (i.e., the vertical wind shear) is less sensitive to the background rotation than is the value of the speed maximum. This suggests that any theory that describes the role of the thermal tides in maintaining the equatorial rotational wind structure against vertical advection cannot oversimplify the vertical wind structure. Vertical diffusion acted to counter the tidal acceleration at cloud top, producing a slower zonal wind speed. For example, for two runs employing the sheared 60 m s⁻¹ background rotation, reduction of υ from 2.5 to 1.0 m² s⁻¹ produced an increase of more than 10 m s⁻¹ in the equatorial zonal wind maximum. The diurnal tide transported angular momentum horizontally from the region of the midlatitude jet toward lower latitudes, acting to smooth the zonal wind profile between the midlatitude jets and the equator; thus, the jet does not become significantly barotropically unstable.

The tides also acted to weaken the Hadley circulation through both their meridional and upward heat fluxes. At the equator, the vertical convergence of the upward heat flux compensates part of the zonally averaged solar heating in the cloud top region. This effect reduced the mean equatorial cloud-level updraft by half, as compared to zonally symmetric model runs. Thus the tides act to
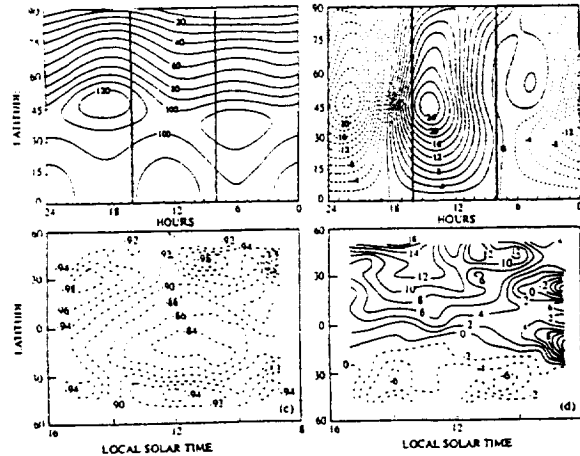
Fig. 1. Comparison of model distributions of cloud top zonal and meridional winds with local time, (a) and (b), with distributions derived from cloud drift measurements, (c) and (d) [3]. The heavy black lines mark the region of UV cloud observations. Model results are averages from the last 40 days of the 350-day simulation with initial sheared angular velocity, for $u_0 = 60$ m s^{-1} and $\upsilon = 2.5$ m^2 s^{-1}.

maintain the mean zonal flow at cloud top level in two ways: directly through tidal fluxes of angular momentum, and indirectly, by reducing the thermal forcing of the Hadley cell.

At the cloud top level, the model zonal wind has a distinct minimum during daytime such that the midlatitude jet is substantially diminished from the zonal mean value. The daytime meridional wind, on the other hand, is strongly poleward and is at a maximum in early afternoon (Fig. 1). This is a robust result that is consistent with both the near absence of midlatitude jets and the strong meridional winds deduced from cloud drifts. Cloud drifts can be measured only during the period from about 0800 to about 1600 hours local time, but they have been used to infer zonally averaged zonal and meridional winds [3]. As shown by the results, this is inappropriate and would lead to spurious estimates.

Also present are nontidal wave components: a wavenumber 2 component with typically a 2.6-day period, and a weaker wavenumber 1 component with the same angular phase speed and 5.2-day period. These are confined mainly to midlatitudes and are due to baroclinic and barotropic instabilities of the zonal mean flow in the lower cloud region. These features may be related to a wavenumber 1 5.2-day spectral feature that has been detected in cloud-level observations. The wavenumber 2 feature became stronger relative to wavenumber 1 as the background rotation was increased between runs, which caused the jet to be centered at slightly lower latitude. This relative wavenumber 2 dominance may also be a consequence of the omission of wave-wave interactions. These waves did not contribute to maintenance of the zonal mean flow near the equator, but in mid to high latitudes they did act to transport momentum from the middle to lower cloud region, and thus possibly contributed to the slight (~5 K) temperature rise in the cloud-top polar region. Although the model did not duplicate the observed cloud top polar warm region, it appears that a higher-latitude jet in the middle cloud region could act to both increase the wavenumber 1 component and duct the waves more toward the pole, inducing warmer temperatures there.

To determine the robustness of these results, further model runs are currently being conducted to more completely explore the parameter space described above. These results also suggest that a Venus GCM will either need sufficient resolution to capture the

tides, or else a parameterization scheme that can adequately capture their effects.

References: [1] Holton J. R. and Wehrbein W. (1980) *Pure Appl. Geophys., 284*; Newman M. (1991) thesis, Univ. of Washington; Newman M. and Leovy C. B. (1992) *Science*, submitted. [2] Crisp D. (1983) thesis, Princeton Univ. [3] Limaye S. S. et al. (1988) *Icarus, 90*, 193; Rossow W. B. et al. (1990) *J. Atmos. Sci.*, 2053.

N93-14352

A MODEL FOR THE FORMATION OF THE EXTENDED PARABOLOIDAL HALOS AROUND SOME IMPACT CRATERS ON VENUS.

W. I. Newman[1], E. M. Jones[2], D. B. Campbell[3], and N. J. S. Stacy[3], [1]Departments of Earth and Space Sciences, Astronomy, and Mathematics, University of California, Los Angeles CA 90024–1567, USA, [2]Earth and Environmental Sciences Division, Los Alamos National Laboratory, Los Alamos NM 87545, USA, [3]National Astronomy and Ionosphere Center and Department of Astronomy, Cornell University, Ithaca NY 14853, USA.

Many parabolic-shaped extended impact crater-related features have been found in Magellan synthetic aperture radar and emissivity data covering much of the surface of Venus. They are oriented east-west with the apex to the east and the impact crater located just west of the apex. A model for the formation of the parabolic features is developed based on the injection of small particles into the upper atmosphere at the time of impact, and their subsequent transport to the west by the east-west zonal winds. Fallout times from 50 km in the Venus atmosphere for particles of this size are about two hours, allowing westerly drifts of several hundred kilometers for zonal winds of 50 to 100 m s^{-1}

N93-14353

VENUS: PRELIMINARY GEOLOGIC MAPPING OF NORTHERN ATLA REGIO.

A. M. Nikishin[1] and G. A. Burba[2], [1]Geological Faculty, Moscow State University, 119899, Moscow, Russia, [2]Vernadsky Institute, Russian Academy of Science, 117975, Moscow, Russia.

A preliminary geologic map of C1 sheet 15N197 was compiled according to Magellan data (Fig. 1). Northern Atla Regio is dominantly a volcanic plain with numerous volcanic features: radar-bright and -dark flows and spots, shield volcanos, volcanic domes and hills with varied morphology, and coronalike constructions. Tesserae are the oldest terrains semiflooded by plain materials. There are many lineated terrains on this territory. They are interpreted as old, partly buried ridge belts. Lineated terrains have intermediate age between young plains and old tesserae. Ozza Mons and Sapas Mons are the high shield volcanos.

The prominent structure of northern Atla Regio is Ganis Chasma rift. The rift dissected the volcanic plain and evolved nearly contemporaneously with Ozza Mons shield volcano. Ganis Chasma rift valley is highly fractured and bounded by fault scarps. There are a few relatively young volcanic features in the rift valley. The rift originated due to 5–10% crustal extension and crustal subsidence according to analysis of fracturing and rift valley geometry. Ganis Chasma is characterized by rift shoulder uplifts. Geological structures of Atla Regio and Beta Regio are very similar as assumed earlier [1,2].

References: [1] Nikishin A. M. (1990) *Earth Moon Planets, 50/51*, 101–125. [2] Senske D. A. and Head J. W. (1989) *LPSC XIX*, 986–987.

GEOLOGIC MAPPING OF NORTHERN ATLA REGIO: Nikishin A. M. and Burba G. A.
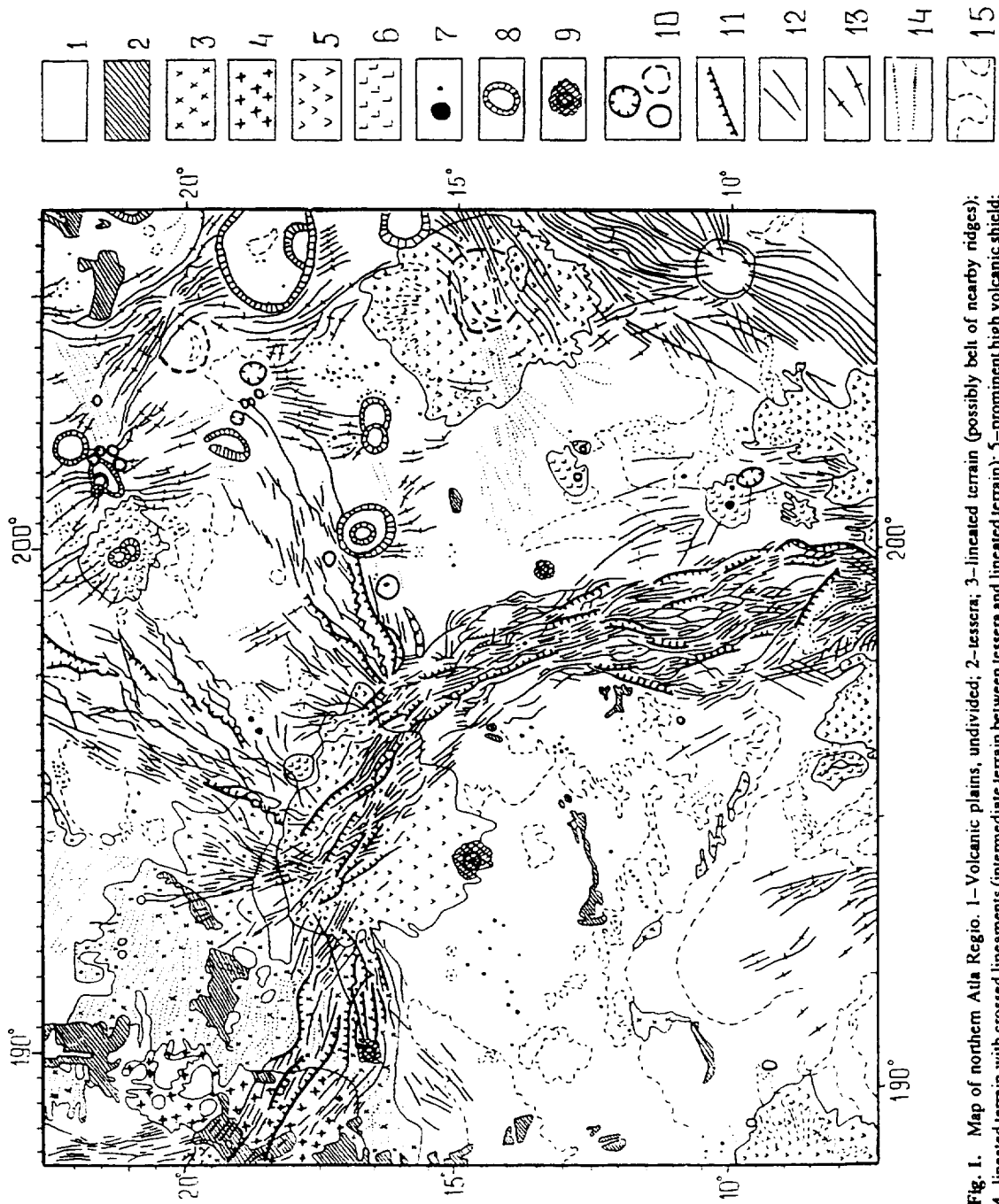
Fig. 1. Map of northern Atla Regio. 1–Volcanic plains, undivided; 2–tessera; 3–lineated terrain (possibly belt of nearby ridges); 4–lineated terrain with crossed lineaments (intermediate terrain between tessera and lineated terrain); 5–prominent high volcanic shield; 6–low volcanic shield; 7–volcanic domes and hills; 8–corona or arachnoid (ringed ridge system); 9–impact crater; 10–calderalike depressions; 11–prominent fault scarp (normal fault); 12–narrow grabens or normal faults; 13–ridges; 14–narrow radar-bright lineaments with unclear relief; 15–boundaries of areas with different radar brightness (possibly boundaries of volcanic flows). Sheet C1-15N197.

GEOLOGIC MAPPING OF SOUTHERN BETA REGIO–NORTHERN PHOEBE REGIO: Nikishin A. M. and Burba G. A.

Fig. 1. Sheet C1-15N283.1– Volcanic plain, undivided; 2–tessera; 3–hilly plain (possibly semiflooded tessera); 4–lineated terrain (possibly belt or nearby ridges); 5–ridged plain (plain with a system of sparse ridges); 6–prominent high volcanic shield; 7–low volcanic shield; 8–volcanic domes and hills; 9–corona or arachnoid (ringed ridge system); 10–impact crater; 11–calderalike depression; 12–prominent fault scarp (normal fault); 13–narrow grabens or normal faults; 14–ridges (compressional structures); 15–structural lineaments within tessera; 16–narrow radar-bright lineaments with unclear relief; 17–boundaries of areas with different radar brightness.

GEOLOGIC MAPPING OF SOUTHERN BETA REGIO–NORTHERN PHOEBE REGIO: Nikishin A. M. and Burba G. A.
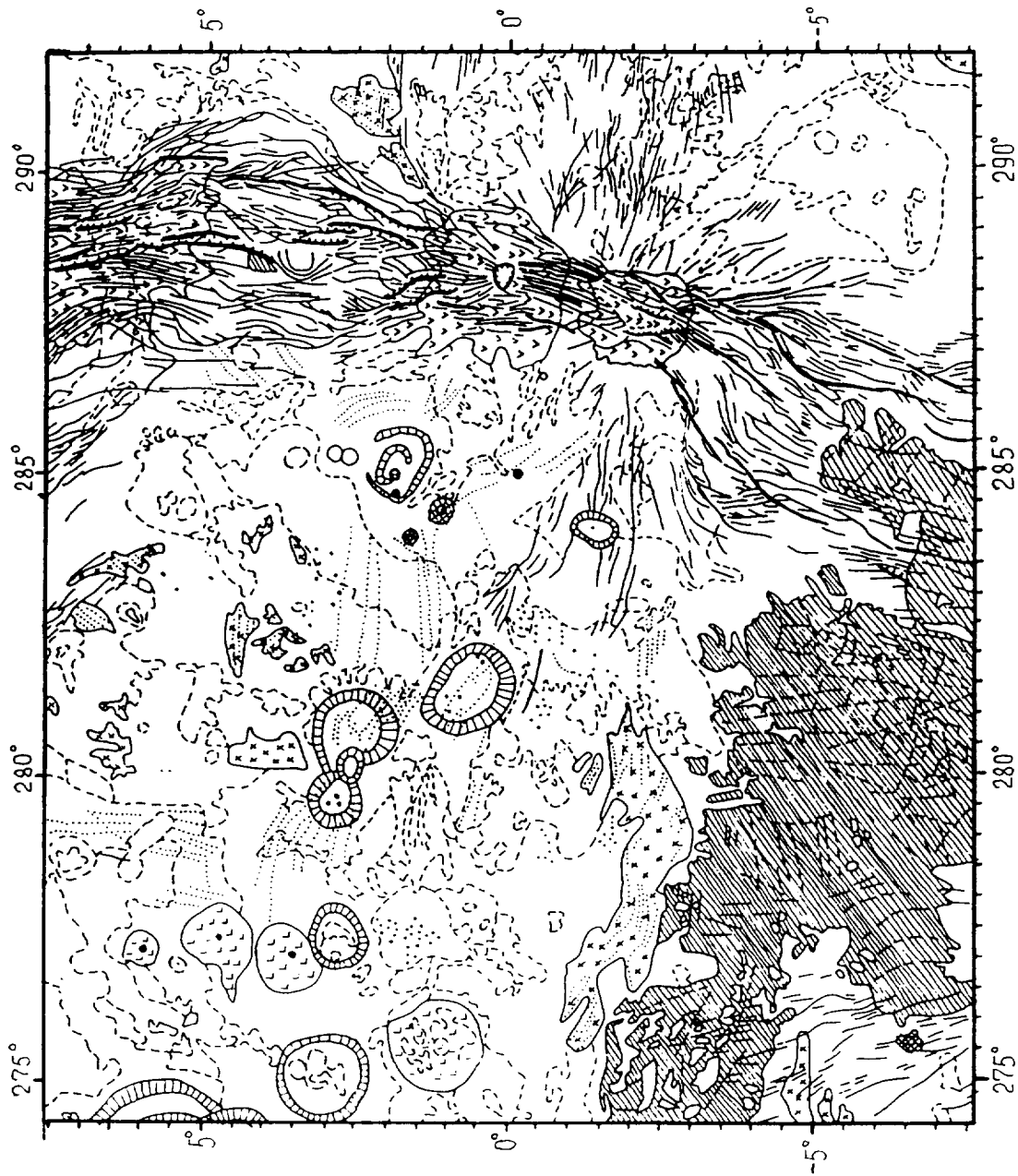
Fig. 2.   Sheet C1-00N283. 1–Volcanic plain, undivided; 2–tessera; 3–hilly plain (possibly semiflooded tessera); 4–lineated terrain (possibly belt or nearby ridges); 5–ridged plain (plain with a system of sparse ridges); 6–prominent high volcanic shield; 7–low volcanic shield; 8–volcanic domes and hills; 9–corona or arachnoid (ringed ridge system); 10–impact crater; 11–calderalike depression; 12–prominent fault scarp (normal fault); 13–narrow grabens or normal faults; 14–ridges (compressional structures); 15–structural lineaments within tessera; 16–narrow radar-bright lineaments with unclear relief; 17–boundaries of areas with different radar brightness.

GEOLOGY OF BETA REGIO RIFT SYSTEM: Nikishin A. M. et al.
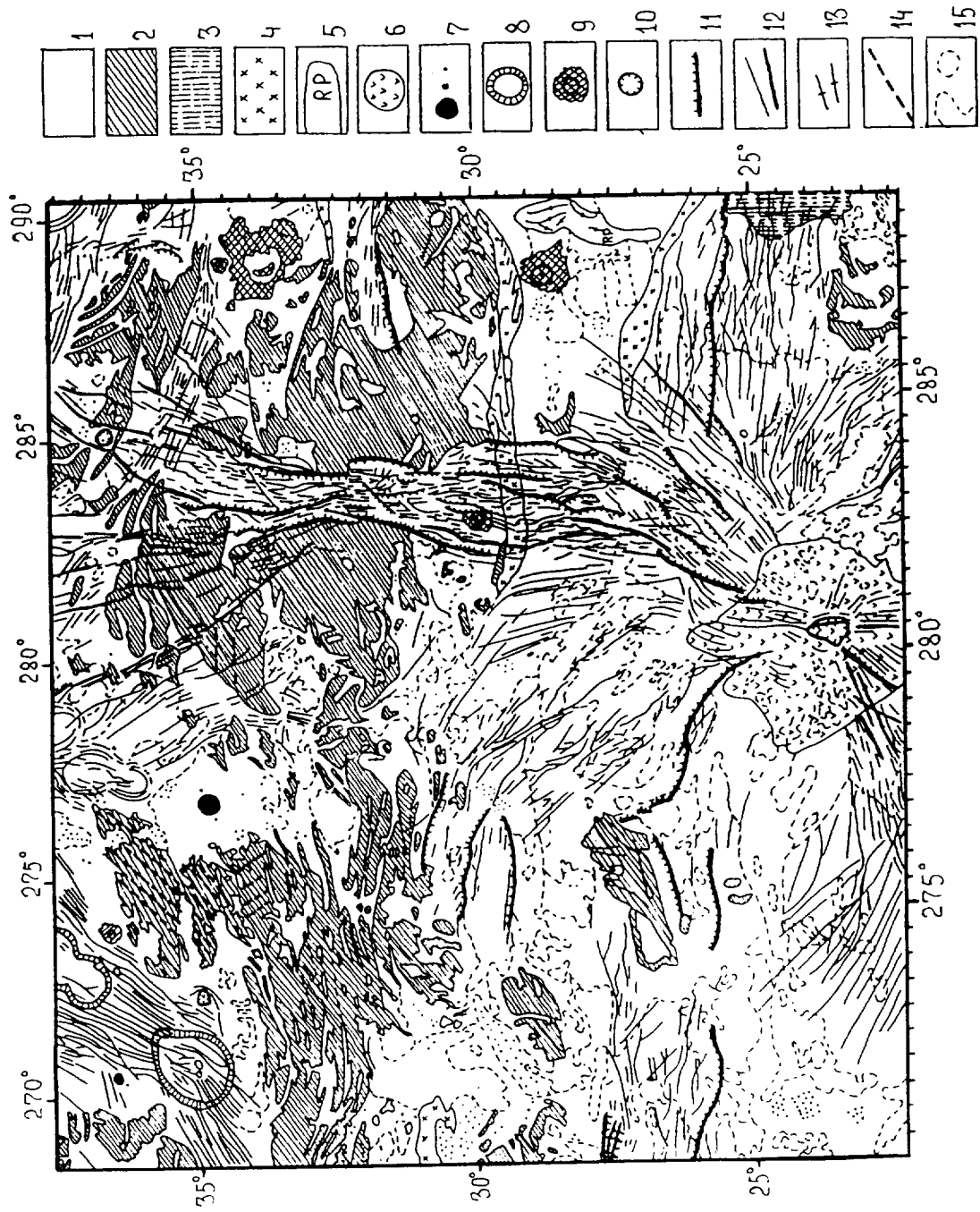
Fig. 1. Geologic map of Northern Beta Regio. 1–Volcanic plain, undivided; 2–tessera; 3–hilly plain (possibly semiflooded tessera); 4–lineated terrain (possibly belt of nearby ridges); 5–ridged plain (plain with a system of sparse ridges); 6–prominent high volcanic shield; 7–volcanic domes and hills; 8–corona or arachnoid (ringed ridge system); 9–impact crater; 10–calderalike depression; 11–prominent fault (normal fault); 12–narrow grabens or normal faults; 13–ridges (compressional structures); 14–structural lineaments within tessera; 15–boundaries of areas with different radar brightness. The map is compiled according to Magellan data.

GEOLOGY OF BETA REGIO RIFT SYSTEM: Nikishin A. M. et al.
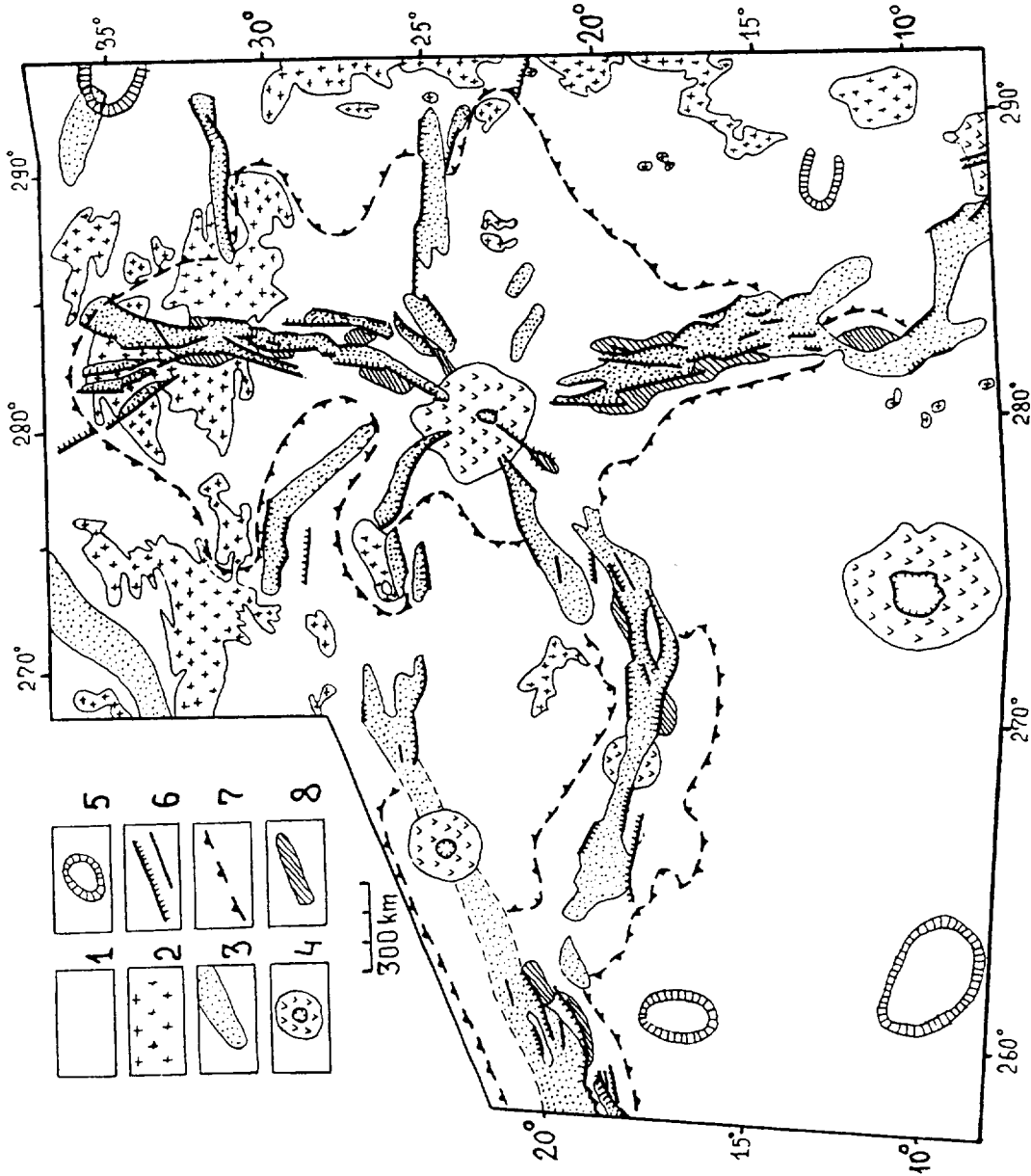
Fig. 2. Tectonic scheme of Beta Regio. 1–Mainly plain, undivided; 2–tessera; 3–rift valley with fractured floor; 4–shield volcano; 5–corona; 6–normal fault; 7–contours of tectonically uplifted region; 8–uplifted shoulder of rift. The scheme is compiled according to Magellan topography and radar images.

N93-14354

VENUS: PRELIMINARY GEOLOGIC MAPPING OF SOUTHERN BETA REGIO-NORTHERN PHOEBE REGIO. A. M. Nikishin[1] and G. A. Burba[2], [1]Geological Faculty, Moscow State University, 119899, Moscow, Russia, [2]Vernadsky Institute, Russian Academy of Science, 117975, Moscow, Russia.

New preliminary geologic maps of C1 sheets 15N283 and 00N283 were compiled according to Magellan data (Figs. 1 and 2). The oldest terrains are tesserae that have fragmentlike shapes. Its margins are partly buried by younger plain materials. Volcanic plains are the dominant types of terrains. There are many different volcanic features on plains: radar-bright and -dark flows and spots, shield volcanos, volcanic domes and hills with varied morphology, and coronalike constructions.

Devana Chasma rift crosses the surface between Beta Regio and Phoebe Regio. The rift's normal faults dissect volcanic plains and shield volcanos. The rift valleys are relatively young structures. According to structural analysis of the rift valleys we conclude the rift originated due to 5–10% crustal extension and crustal subsidence. Devana Chasma rift is characterized by shoulder uplifts.

N93-14355

VENUS: GEOLOGY OF BETA REGIO RIFT SYSTEM. A. M. Nikishin[1], V. K. Borozdin[2], G. A. Burba[2], and N. N. Bobina[2], [1]Geological Faculty, Moscow State University, 119899, Moscow, Russia, [2]Vernadsky Institute, Russian Academy of Science, 117975, Moscow, Russia.

Beta Regio is characterized by the existence of rift structures [1,2,3]. We compiled new geologic maps of Beta Regio according to Magellan data (Figs. 1 and 2). There are many large uplifted tesserae on Beta upland. These tesserae are partly buried by younger volcanic cover. We can conclude, using these observations, that Beta upland formed mainly due to lithospheric tectonic uplifting and was only partly constructed by volcanism.

Theia Mons is the center of the Beta rift system. Many rift belts are distributed radially to Theia Mons. Typical widths of rifts are 40–160 km. Rift valleys are structurally represented by crustal grabens or half-grabens. There are symmetrical and asymmetrical rifts. Many rifts have shoulder uplifts up to 0.5–1 km high and 40–60 km wide.

Preliminary analysis for rift valley structural cross sections lead to the conclusion that rifts originated due to 5–10% crustal extension. Many rifts traverse Beta upland and spread to the surrounding lowlands. We can assume because of these data that Beta rift system has an "active-passive" origin. It formed due to regional tectonic lithospheric extension. Rifting was accelerated by upper-mantle hot spot origination under the center of passive extension (under the Beta Regio).

References: [1] Campbell D. B. et al. (1984) *Science, 226,* 167–170. [2] Senske D. A. and Head J. W. (1989) *LPSC XIX,* 986–987. [3] Stofan E. R. et al. (1989) *GSA Bull., 101,* 143–156.

N93-14356

THE ORIGINS OF RADIAL FRACTURE SYSTEMS AND ASSOCIATED LARGE LAVA FLOWS ON VENUS. Elisabeth A. Parfitt[1], Lionel Wilson[1,2], and James W. Head[1], [1]Department of Geological Sciences, Brown University, Providence RI 02912, USA, [2]Environmental Science Division, Lancaster University, Lancaster LA1 4YQ, UK.

Magellan images have revealed the existence of systems of radial fractures on Venus that are very similar in form to terrestrial

dike swarms such as the Mackenzie swarm in Northern Canada. The association of many of the fracture systems with lava flows, calderas, and volcanic edifices further support the idea of a dike emplacement origin [1]. A global survey of the Magellan images has allowed the location of 300 such fracture systems [1]. The fracture systems vary widely in form but can be broadly divided into two types or classes (Figs. 1 and 2).

Classes of Fracture Systems: Figure 1 shows a fracture system in which fractures radiate away from the outer edge of a caldera 70 km in diameter and feed short, indistinct flows that have built an edifice 700 m high. The form of this feature is very reminiscent of the style of dike emplacement and eruption seen in places like Hawaii and Iceland where emplacement of dikes occurs laterally from magma chambers situated at shallow levels [2–5]. The existence of a caldera in the feature in Fig. 1 is suggestive of localized storage of magma at relatively shallow levels, though the greater diameter of the caldera compared with terrestrial examples may imply deeper storage than is seen in Hawaii or Iceland (where magma storage is centered at a depth of ~3 km below the surface). Thus this first type of radial fracture system has properties consistent with lateral dike emplacement from a magma chamber situated at depths of probably a few kilometers below the surface. By contrast, the feature shown in Fig. 2 has no caldera, but instead is largely contained within a much greater diameter (~200 km) concentric trough. In addition, the radial fractures show a more complex

0   25   50 km   Figure 1
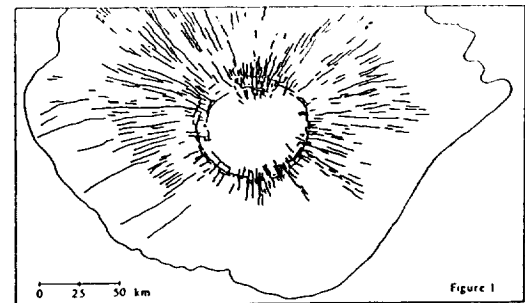
Fig. 1. Map of a radial fracture system located at 38°S 23°.

0   50   100 km   Figure 2
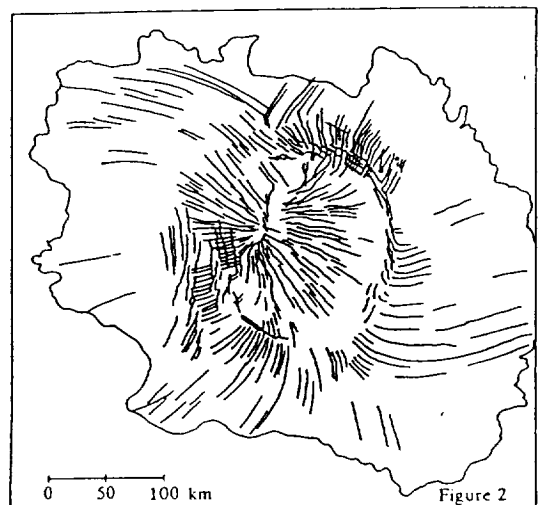
Fig. 2. Map of a radial fracture system located at 15°S 215°.

relationship at the center of the swarm radiating from a central point with some apparently crossing the central region, rather than radiating from it. This pattern seems more consistent with vertical dike emplacement from a deeper source associated with the concentric fracturing and deformation. However, the radial fractures still have a basic radiating form that, like that in the example in Fig. 1, is very suggestive of lateral propapagation. Thus the second type of fracture system (Fig. 2) probably results from growth of dikes from deep levels, possibly from the head of a mantle plume. At depth, propagation would be primarily vertical due to the buoyancy of the magma, but as the dikes propagated to shallower depths, propagation seems to have developed a lateral component, probably due to the reduced density contrast between the magma and crust. Recently it has been shown that dikes within the Mackenzie swarm in Canada show evidence of vertical magma flow close to the center of the swarm and of lateral flow at greater distances from the center [6]. This is consistent with the pattern of dike emplacement discussed above.

Dike Emplacement Modeling: A series of models was developed to simulate the emplacement of dikes on Venus [7]. Observations of fracture lengths and widths were then used to constrain the emplacement conditions [7]. The model results show that the great length and relatively large width of the fractures can only be explained if the dikes that produce them were emplaced in high driving pressure (pressure buffered) conditions. Such conditions imply high rates of melt production, which, particularly in the case of type 2 swarms, is consistent with the melt being derived directly from a plume head.

Associated Volcanism: Approximately 50% of the radial fracture systems found on Venus are associated with lava flows. These flows typically have lengths of tens to hundreds of kilometers and widths of a few kilometers. The thicknesses of the flows are not known, but their lack of expression in the altimetry data suggests that they are <100 m thick and they may well be considerably thinner than this. The lobate or digitate form of such flows suggests that they are cooling-limited, while the fact that the flows from one radial fracture swarm tend to be fairly similar suggests that the flows are emplaced under eruption conditions that vary little through the history of a swarm. Eruption rates for such flows can be estimated using the flow length, width, and thickness. Pinkerton and Wilson [8] developed a relationship between the geometry of a cooling-limited flow and the eruption rate at the vent. If the flow has a length L, a width W, and a thickness D, then the volume eruption rate V is given by

$$V = \frac{300\, L\, W\, \kappa}{D}$$

where κ is the thermal diffusivity, which for basalt has a value of $\sim 10^{-6}$ m^2/s. If we take typical dimensions for a flow from a radial fracture system—L = 75 km, W = 10 km, and D = 10 m (the latter is probably a minimum estimate)—an estimate of the typical eruption rate can be calculated and is found to be $\sim$0.08 km^3/hr, implying an emplacement time of $\sim$3 days. This eruption rate is $\sim$2.5 times higher than the maximum eruption rate calculated for the Laki fissure eruption in Iceland [9] and 1/50 of the estimated eruption rates for the most rapidly emplaced Columbia River flows [10].

Eruption Rates Implied by Dike Modeling: We have recently modeled the vertical emplacement of a dike from the top of a mantle plume and calculated the eruptions rates such a dike would produce on reaching the surface. This modeling shows that eruption rates of $\sim$0.1 km^3/hr can readily be generated by such a dike, consistent with the above results. However,the sensitivity of the

model to dike width and therefore driving pressure means that eruption rates from dikes emplaced from the base of the crust or the head of a mantle plume could be orders of magnitude higher than this. Clearly, therefore, the model needs to be refined in order to better constrain eruption conditions. However, it is worth noting here that the initial results do show that even for moderate dike widths (<10 m), eruption rates could be at least on the order of those estimated for terrestrial flood basalts. As our modeling of the lengths and widths of fractures ([7] and above) imply dikes of up to 75 m in width, effusion rates could be considerably higher than this. There is no obvious physical limit on how high eruption rates can be, and indeed, given the widths implied for these dikes (and these widths compare remarkably well with those found for terrestrial dike swarms; see, e.g., [6]), it is difficult to avoid having very high eruption rates. Thus dikes propagating to the surface from the head of a mantle plume could give rise to flows emplaced at very high rates which would therefore be expected to form broad sheetlike flows, i.e., flows like those forming the plains areas on Venus [11].

References: [1] Parfitt E. A. and Head J. W. (1992) *LPSC XXIII*, 1029–1030. [2] Klein F. W. et al. (1987) In *USGS Prof. Paper 1350*. [3] Rubin A. M. and Pollard D. D. (1987) In *USGS Prof. Paper 1350*. [4] Sigurdsson H. (1987) *Geol. Assoc. Can. Spec. Paper 34*, 55–64. [5] Gudmundsson A. (1987) *J. Volcanol. Geotherm. Res.*, *34*, 65–78. [6] Ernst R. E. and Baragar W. R. A. (1992) *Nature, 356*, 511–513. [7] Parfitt E. A. and Head J. W. (1992) *LPSC XXIII*, 1027–1028. [8] Pinkerton H. and Wilson L. (1988) *LPSC XIX*, 937–938. [9] Thordarson Th. (1990) M.S. thesis, Univ. of Texas. [10] Swanson, D. A. et al. (1975) *AJS, 275*, 877–905. [11] Head J. W. et al. (1992) *JGR*. in press. _

N93-14357

APPLICATION OF LEFT- AND RIGHT-LOOKING SAR STEREO TO DEPTH MEASUREMENTS OF THE AMMAVARU OUTFLOW CHANNEL, LADA TERRA, VENUS.

T. J. Parker, California Institute of Technology, Jet Propulsion Laboratory, Pasadena CA 91109, USA.

Venusian channels are too narrow to be resolved by Magellan's radar altimeter, so they are not visible in the standard topographic data products. Stereo image data, in addition to their benefit to geologic mapping of Venus structures as a whole [1], are indispensible in measuring the topography across the channels. These measurements can then be used in conjunction with the regional topographic maps based on the altimeter data to produce cross-sectional areas for the channels and estimate the fluid discharge through them.

As an example of the application of the stereo image data to venusian channels, a number of test depth and profile measurements were made of the large outflow channel system in Lada Terra [2,3], centered at 50°S latitude, 21°E longitude (F-MIDR 50S021). These measurements were made by viewing the cycle 1 and 2 digital FMIDRs in stereo on a display monitor, so as to minimize the errors in measuring parallax displacement as much as possible. The MIDRs are produced at a scale of 75 m/pixel. This corresponds to a vertical scale of about 17 m/"pixel," when calculating the height of a feature from its parallax displacement. An error in placement determination of 1 pixel was assumed to characterize the vertical accuracy as ±17 m.

When this technique was applied to the outflow channel, it was noted that the walls of the collapsed terrain source and "trough reach" of the channel are laid over in both the cycle 1 and 2 images (incidence angles around 23°–25° for both right- and left-looking data). This is evident when examining the distance between features

N93-14358

CHEMICAL DIFFERENTIATION OF A CONVECTING PLANETARY INTERIOR: CONSEQUENCES FOR A ONE-PLATE PLANET SUCH AS VENUS. E. M. Parmentier and P. C. Hess, Department of Geological Sciences, Brown University, Providence RI 02912, USA.

Partial melting of the interior of a planet to generate its crust must inevitably leave behind compositionally buoyant residual mantle. This basalt-depleted mantle is chemically less dense than undepleted mantle due to its reduced Fe/Mg and dense Al-bearing minerals such as garnet. The chemical density difference is substantial: for 20% melt extraction the density decrease is as large as that due to a 500°C temperature increase. The melting temperature of this depleted residual mantle is also increased. Deep mantle circulation driven by cold strong sinking lithosphere associated with plate tectonics may mix the depleted mantle back into the mantle. In the absence of plate tectonics, less mixing will allow a buoyant depleted layer to collect at the top of the mantle [1,2].

Chemically depleted mantle forming a buoyant, refractory layer at the top of the mantle can have important implications for the evolution of the interior and surface. On Venus, the large apparent depths of compensation for surface topographic features [3] might be explained if surface topography were supported by variations in the thickness of a 100–200-km thick chemically buoyant mantle layer or by partial melting in the mantle at the base of such a layer. Long volcanic flows seen on the surface [4] may be explained by deep melting that generates low-viscosity MgO-rich magmas. The presence of a shallow refractory mantle layer may also explain the lack of volcanism associated with rifting [5]. As the depleted layer thickens and cools, it becomes denser than the convecting interior and the portion of it that is hot enough to flow can mix with the convecting mantle. Time dependence of the thickness of a depleted layer may create episodic resurfacing events as needed to explain the observed distribution of impact craters on the venusian surface [6].

We consider a planetary structure like that shown in Fig. 1 consisting of a crust, depleted mantle layer, and a thermally and chemically well-mixed convecting mantle. The thermal evolution

Fig. 1.

Fig. 2.

on the plateau and the cliff walls in the two images (Fig. 1). The layover "shifts" the features closer to the apparent edge of the wall relative to the oppositely illuminated image. Figure 1 also shows one "single-point" depth measurement, illustrating the large parallax displacement between the left- and right-looking data in areas of moderate relief. At the bottom of each scene is a sample profile trace across the trough and part of the channel connecting the collapsed source with the trough. Figure 2 is a plot of this data using the cycle 1 image sample values for placement on the x axis. Vertical height values are relative values, and are a function of the parallax displacement of features relative to the projection of the two FMIDRs.

References: [1] Moore H. J. et al., this volume. [2] Parker T. J. et al. (1991) *LPSC XXII*, 1035–1036. [3] Baker V. R. et al. (1992) *JGR*, in press.

Fig. 1. Planetary structure considered in models of thermal/chemical internal evolution. These models examine the role of a chemically buoyant basalt-depleted mantle layer and crustal recycling on planetary evolution.

of the convecting spherical planetary interior is calculated using energy conservation: the time rate of change of thermal energy in the interior is equated to the difference in the rate of radioactive heat production and the rate of heat transfer across the thermal boundary layer (cf. [7]). Heat transfer across the thermal boundary layer is parameterized using a standard Nusselt number-Rayleigh number relationship $Nu=(Ra/Ra_{crit})^{1/3}$. The radioactive heat production decreases with time corresponding to decay times for the U, Th, and K. The planetary interior cools by the advection of hot mantle at temperature $T_{interior}$ into the thermal boundary layer where it cools conductively. The crust and depleted mantle layers do not convect in our model so that a linear conductive equilibrium temperature distribution is assumed as shown in Fig. 1.

The rate of melt production is calculated as the product of the volume flux of mantle into the thermal boundary layer and the degree of melting that this mantle undergoes. The volume flux of mantle into the thermal boundary layer is simply the heat flux divided by amount of heat lost in cooling mantle to the average temperature in the thermal boundary layer. The degree of melting is calculated as the temperature difference above the solidus, approximately $(T_{interior}-T_m)/2$ where T_m is the melting temperature (see Fig. 1), divided by the latent heat of melting. A maximum degree of melting, 25% in the results described below, is prescribed corresponding to the maximum amount of basaltic melt that the mantle can initially generate. As the crust thickens, the pressure at the base of the crust becomes high enough and the temperature remains low enough for basalt to transform to dense eclogite. We assume that basalt does not transform to eclogite below a prescribed kinetic blocking temperature T_{ge}, which we vary over the range 700°–900°C. Basalt that transforms to eclogite is assumed to sink into the convecting mantle and to mix instantaneously with it, both thermally and chemically. Heat-producing elements fractionated into the crust are thus returned to the mantle. It is not yet clear based on surface images alone whether or how crust is recycled on Venus, but the large amount of crust predicted by our models suggests that recycling must occur.

The stability of the depleted mantle layer depends on its density relative to that of the convecting interior. We take $\Delta\rho/\rho_o = \alpha(T_{interior}-T_{depleted}) - \beta X$ where $T_{depleted}$ is the average temperature in the part of the depleted layer that can flow (T > T_{flow}), X is the average degree of melting, and the coeffient β accounts for the chemical density variations described above. We take T_{flow} = 1100°C. The stability conditions for the depleted layer are then simply that if $\Delta\rho > 0$, the depleted mantle instantaneously mixes with the convecting mantle, while if $\Delta\rho < 0$, the layer is stable and does not mix at all with the convecting mantle. The latter condition, in particular, is oversimplified because it does not account for the possibility that viscous stresses in the convecting mantle can entrain buoyant material if its $\Delta\rho$ is not sufficiently large [8].

With a prescribed initial temperature and heat generation rate, the time evolution of this model is calculated numerically. One result of such a calculation, in Fig. 2, shows temperatures, crust and depleted layer thicknesses, and degree of melting as functions of time. The interior temperature decreases only slightly in this particular case because the rate of heat production is nearly sufficient to balance secular cooling. The crust initially thickens but quickly reaches a thickness of about 60 km at which crustal recycling begins. The depleted mantle layer at first thickens because the layer is below the temperature T_{flow}. However, as the crust thickens, the temperature of the depleted layer becomes greater than T_{flow}. In addition, the temperature difference between the interior and the depleted layer is large enough that the depleted layer is
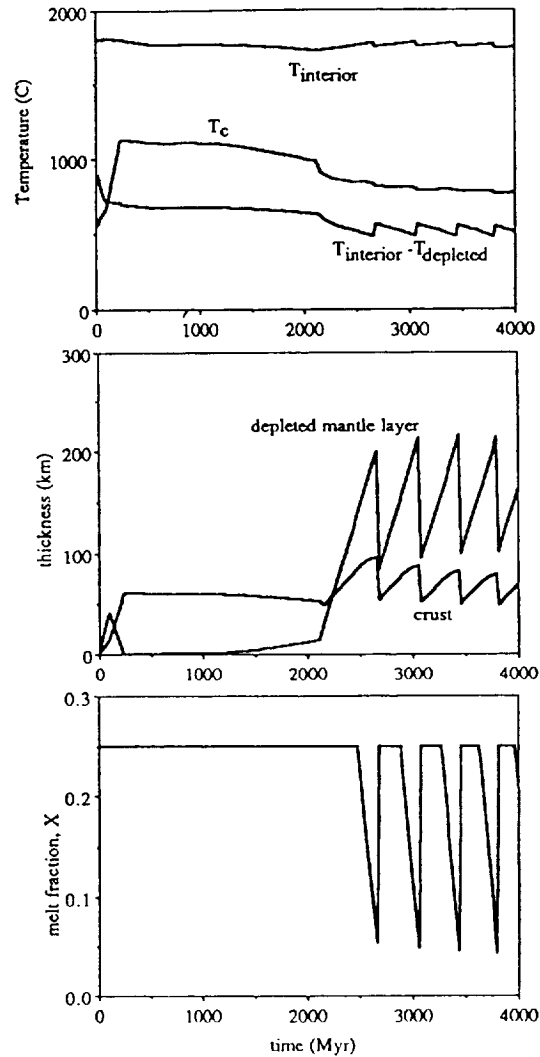
Fig. 2. Planetary evolution including the effects of crustal recycling and the dynamics of a chemically buoyant basalt-depleted mantle layer. Temperatures (top), thicknesses of crust and depleted mantle layers (middle), and melt fraction (bottom) illustrate the evolution that is discussed in the text. In this example the initial interior temperature is 1800°C, the rate of heat production is 0.5 of a steady-state Earth, T_{flow} = 1100°C, and T_{ge} = 900°C.

denser than the interior. Thus for a period of the evolution a depleted layer does not accumulate. However, as the interior cools, a growing thickness of depleted material is cooler than T_{flow}. As $T_{interior}-T_{depleted}$ decreases, negative thermal buoyancy becomes less than the positive compositional buoyancy. The depleted layer then thickens rapidly (at slightly more than 2000 m.y. in Fig. 2). As the depleted layer thickens, the thermal boundary layer and region of melting move deeper into the interior. As the melting temperature at the base of the thermal boundary layer increases, due to this increase in the depth of melting, the amount of melting decreases as shown in Fig. 2. The average compositional buoyancy of the depleted layer thus decreases, until the thermal buoyancy results in a net negative buoyancy. The layer then mixes into the convecting interior, the thermal boundary layer and region of melting rise to lower pressure, larger amounts of melting resume, and the depleted layer thickens once more. This process repeats itself at very regular intervals of about 400–450 m.y. This time interval is remarkably similar to the inferred resurfacing age of Venus.

We have explored behavior of this model for a range of the parameters. The time-averaged thickness of the depleted layer is controlled in part by T_{flow}: decreasing T_{flow} to 1000°C reduces this thickness by about 50%. Decreasing T_{ge} to 700°C reduces the time-average thickness of the crust by about 20 km. However, the cyclical variation in depleted layer thickness, along with the accompanying fluctuation in crustal thickness, is a robust feature of the models. Varying the initial temperature by ±200°C and radioactive heating, expressed as a fraction of that required to explain all the Earth's present–day heatflow by radioactivity, by a factor of 2 influences the onset time of this behavior, but the period of the variation remains on the order of 300–500 m.y. for the complete range of conditions considered.

The parameterized convection model assumes that instabilities are globally synchronous. If the instability described by this model is global in scale, it may take the form of episodic plate spreading and subduction. But studies of impact crater densities on Venus [6] and the distribution of volcanic features [4] suggest that resurfacing may occur in patches rather than globally. Localized volcanic resurfacing on Venus may be a consequence of local instability of the lithosphere or alternatively may mean that large, exceptionally hot plumes penetrate even thick, buoyant lithosphere. The Archean greenstone belts on Earth, which are flooded by high MgO volcanics, require similar mechanisms of formation. Komatiites, for example, require potential temperatures of at least 1800°C [9,10] and mean depths of melt segregation of 160–330 km [11], yet average mantle temperatures in the Archean are thought to be only 100°–150°C higher than present [12]. These contradictions are best explained by a model in which komatiites form only in plumes, whereas more typical terrestrial basalts form at spreading centers. The chemical differentiation of Venus described in this study almost demands that komatiite-to-picrite volcanics form the dominant portion of the venusian crust.

References: [1] Dupeyrat L. et al. (1992) *LPSC XXIII*, 319. [2] Parmentier E. M. and Hess P. C. (1992) *LPSC XXIII*, 1037. [3] Smrekar S. E. and Phillips R. J. (1991) *EPSL, 107*, 582. [4] Head J. W. et al. (1992) *LPSC XXIII*, 517. [5] Solomon S. C. et al. (1992) *LPSC XXIII*, 1333. [6] Phillips R. J. et al. (1992) *LPSC XXIII*, 1065. [7] Turcotte D. L. et al. (1979) *Proc. LPSC 10th*, 2375. [8] Olson P. and Kincaid C. (1991) *JGR, 96*, 4347. [9] Hess P.C. (1990) *LPSC XXI*, 501. [10] Miller G. H. et al. (1991) *JGR, 96*, 11849. [11] Herzberg C. (1992) *JGR, 97*, 4521. [12] Turcotte D.L. (1980) *EPSL, 48*, 53.

N93-14359

VENUS STEEP-SIDED DOMES: RELATIONSHIPS BETWEEN GEOLOGICAL ASSOCIATIONS AND POSSIBLE PETROGENETIC MODELS.

B. Pavri and J. W. Head III, Department of Geological Sciences, Brown University, Providence RI 02912, USA.

Introduction: Venus domes are characterized by steep sides, a circular shape, and a relatively flat summit area. In addition, they are orders of magnitude larger in volume and have a lower height/diameter ratio than terrestrial silicic lava domes [1]. The morphology of the domes is consistent with formation by lava with a high apparent viscosity [2]. Twenty percent of the domes are located in or near tessera (highly deformed highlands), while most others (62%) are located in and near coronae (circular deformational features thought to represent local mantle upwelling). These geologic associations provide evidence for mechanisms of petrogen-

esis and several of these models are found to be plausible: remelting of basaltic or evolved crust, differentiation of basaltic melts, and volatile enhancement and eruption of basaltic foams.

Development of Models: Hess and Head have shown that the full range of magma compositions existing on the Earth is plausible under various environmental conditions on Venus [11]. Most of the Venera and Vega lander compositional data are consistent with tholeiitic basalt [3–6]; however, evidence for evolved magmas was provided by Venera 8 data consistent with a quartz monzonite composition [7]. Pieters et al. have examined the color of the Venus surface from Venera lander images and interpret the surface there to be oxidized [8].

Preliminary modeling of dome growth has provided some interpretations of lava rheology. Viscosity values obtained from these models range from 10^{14}–10^{17} Pa·s [9], and the yield strength has been calculated to be between 10^4 and 10^6 Pa [1], consistent with terrestrial silicic rocks. The apparent high viscosity of the dome lavas suggests that the domes have a silicic composition or must augment their viscosity with increased visicularity or crystal content.

Petrogenetic Models: Sixty-two percent of the Venus domes are associated with coronae, circular features that have been proposed as sites of mantle upwelling, and 20% of the domes are located near tessera, relatively high areas of complex deformed terrain. We have investigated several models that are consistent with these geologic associations. The first case involves the differentiation of basalt in a magma reservoir in the crust, perhaps produced by partial melting within a mantle plume. The second case is melting at the base of thickened basaltic crust, and the final case is volatile exsolution and enhancement within a basaltic magma reservoir. The association of domes with tessera might be explained by crustal remelting, while the association with coronae may be consistent with chemical differentiation of a magma reservoir or the exsolution and concentration of volatiles in the reservoir before eruption.

Chemical Differentiation: High-silica magmas can be produced under reducing or oxidizing conditions, and regardless of whether the crust is wet or dry. If water is present, crystal fractionation of a basaltic magma will produce intermediate to silicic magmas. Differentiation of dry oxidized basalt in a magma reservoir can also produce silica-rich magma, as well as a suite of intermediate composition magmas [10]. The production of immiscible silica-rich melts and ferrobasalts occurs under reducing conditions, but no intermediate magma is produced [10].

Crustal Remelting: The melting of dry tholeiite basalt at pressures of 15–25 kbar or above will result in SiO_2-rich magmas for <20% partial melting [11]. Depths of 53–88 km are necessary so that melting occurs in the eclogite facies where garnet is present as a low-silica phase in the residue. For higher degrees of melting, andesites or basaltic andesites will form. The presence of water would allow the formation of high silica melts at shallower depths since amphibole could replace garnet as a low silica residue. An excess of water would also reduce the viscosity of a high silica melt, making it easier to transport. The volume of crustal melting required to produce one dome would be reduced considerably if tessera represents evolved crust, as proposed by Nikolayeva [7].

Volatile Exsolution/Basalt Foam: Volatile enhancement represents an alternative mechanism for increasing magma viscosity. In this model, magma viscosity is increased by two mechanisms. First, as more vesicles form in the magma, the bubbles have difficulty moving past one another and second, the liquid has difficulty moving along the thin interbubble walls as the vesicles

become close-packed. The maximum vesicle content that a lava can sustain without disruption is 75% vesicles; this represents the maximum viscosity increase achievable with this mechanism.

Model Comparisons: One difficulty with the chemical differentiation model involves trying to concentrate large volumes of silicic melt so that the eruption can occur as a single, steady effusion of lava before the magma freezes or is trapped in the crystal mush. It is uncertain whether the low melt fractions will be able to move through the crust to collect in a reservoir. Work by Wickham indicates a threshold of >30% melt for the efficient escape of silica-rich magmas from a crystal mush [12]. If this mechanism is active in forming dome lavas, then this is probably an indication that the dome lavas are of an intermediate composition.

The crustal remelting model has its difficulties, as well. First, the strong correlation of gravity with topography at the scale investigated by Pioneer Venus [13] argues against deep isostatic compensation for many features on the planet. If this is true for tessera blocks, then eclogite would not be expected at the depths necessary for the formation of high silica melts. It is possible that subduction could transport basaltic or eclogite crust to the depths necessary for garnet to be present in the residue [14,15], but it is difficult to invoke this mechanism to explain the global dome distribution. However, if amphibolite is present as the low-silica melt residue, deep crustal melting is not necessary to generate high-silica melts. An additional problem with this model is its inability to explain the presence of domes on the periphery of the tessera, but not in the tessera itself. It seems most likely that the domes would be emplaced directly above the melting region, not hundreds of kilometers laterally displaced from it. It is necessary to develop a mechanism that will transport high-viscosity, silicic magma to the plains surrounding tessera, while simultaneously discouraging the eruption of this same magma in the tessera. An alternative explanation might be that domes are formed in the tessera, but that subsequent tectonic strain has destroyed them, and the domes on the plains survive because they are emplaced in a less tectonically active environment.

The volatile enhancement mechanism will need to be examined more closely to resolve some of the difficulties inherent in the model. First, the exsolution of volatiles should increase pressure in the chamber and prevent further exsolution unless the excess pressure is released. At present, it is difficult to envision a mechanism that allows the concentration of the volatiles into a "foam layer" at the top of the chamber without allowing the volatiles to escape before eruption. Perhaps an uneven chamber roof could trap pockets of volatile-rich foam that are not drawn off by earlier eruptions that release pressure from the chamber. An additional problem is the altitude distribution of the domes. Modeling by Head and Wilson indicates that the necessary shallow magma chambers in which this volatile exsolution could occur are not likely to form at altitudes at or below the mean planetary radius [16].

We have also examined the case of partial melts from the mantle. If the mantle of Venus is similar to Earth's (of a peridotitic composition), it is impossible to generate a silica-rich melt from the direct partial melting of the mantle without some secondary differentiation process occurring. If a buoyant, depleted mantle layer forms under the crust, it will be even more refractory than pristine mantle and will tend to trap rising plumes. This will encourage melting of plumes at the base of the depleted layer, resulting in the production of MgO-rich low-viscosity melts [17].

Conclusions: We have shown that there are at least three plausible models for the petrogenesis of high effective viscosity magmas on Venus, and we have suggested geologic environments in which these different mechanisms might be active. Chemical differentiation and crustal remelting are common mechanisms for generating silicic, high-viscosity magmas on the Earth, and are consistent with dome associations with coronae and tessera respectively. In both cases, further research will be necessary to understand how the magma is able to escape the crystal mush and migrate to the surface. The crustal remelting model has the additional difficulty of the lack of domes in tessera, above the supposed melting region. The volatile exsolution model will require future research in order to determine if a layer enhanced in volatiles can form at the top of a magma reservoir, and if the shallow reservoirs necessary for volatile exsolution can form at the low altitudes at which the domes are found. Further research will focus on refining the models, examining their implications for crustal evolution, and developing tests to determine which are active in different environments on Venus.

References: [1] Pavri B. et al. (1992) *JGR*, special Magellan issue, in press. [2] Head J. et al. (1991) *Science, 252,* 276–288. [3] Surkov Yu. A. et al. (1977) *Space Research, 17,* 659. [4] Surkov Yu. A. et al. (1983) *Proc. LPSC 13th,* in *JGR, 88,* A481–A494. [5] Surkov Yu. A. et al. (1984) *Proc. LPSC 14th,* in *JGR, 89,* B393–B402. [6] Surkov Yu. A. et al. (1987) *Proc. LPSC 17th,* in *JGR, 92,* E537–E540. [7] Nikolayeva O. V. (1990) *Earth Moon Planets, 50/51,* 329–341. [8] Pieters C. M. et al. (1986) *Science, 234,* 1379–1383. [9] McKenzie D. et al. (1992) *JGR,* special Magellan issue. [10] Hess P. C. (1989) *The Origins of Igneous Rocks,* Harvard Univ., Cambridge. [11] Hess P. C. and Head J. W. (1990) *Earth Moon Planets, 50/51,* 57–80. [12] Wickham S. M. (1987) *J. Geol. Soc., London, 144,* 281–297. [13] Anada M. P. et al. (1980) *JGR, 85,* 8308–8318. [14] Head J. W. (1990) *Earth Moon Planets, 50/51,* 25–56. [15] Burt J. D. and Head J. W. (1992) *GRL,* submitted. [16] Head J. W. and Wilson L. (1992) *JGR, 97,* 3877–3903. [17] Parmentier E. M. and Hess P. C. (1992) *LPSC XXIII,* 1037–1038.

N93-14360

DIELECTRIC SURFACE PROPERTIES OF VENUS. G. H. Pettengill, R. J. Wilt, and P. G. Ford, Center for Space Research, Massachusetts Institute of Technology, Cambridge MA 02139, USA.

It has been known for over a decade [1] that certain high-altitude regions on Venus exhibit bizarre radar-scattering and radiothermal-emission behavior. For example, observed values for normal-incidence power reflection coefficients in these areas can exceed 0.5; enhanced backscatter in some mountainous areas in the Magellan SAR images creates a bright surface with the appearance of snow; and reduced thermal emission in the anomalous areas makes the surface there appear hundreds of degrees cooler than the corresponding physical surface temperatures. The inferred radio emmissivity in several of these regions falls to 0.3 for horizontal linear polarization at viewing angles in the range 20°–40°.

Several explanations have been offered for these linked phenomena:

1. Single-surface reflection from a sharp discontinuity separating two media that have extremely disparate values of electromagnetic propagation. The mismatch may occur in either or both the real (associated with propagation velocity) or imaginary (associated with absorption) components of the relevant indices of refraction, and the discontinuity must take place over a distance appreciably shorter than a wavelength. An example of such an interaction on Earth would occur at the surface of a body of water. At radio wavelengths, water has an index of refraction of 9 (dielectric permittivity of about 80), and an associated loss factor that varies

strongly with the amount of dissolved salts, but is generally significant. Its single-surface radar reflectivity at normal incidence is about 0.65, and the corresponding emissivity (viewed at the same angle) is therefore 0.35. Both these values are similar to the extremes found on Venus, but in the absence of liquid water, the process on Venus requires a different explanation. Two of the present authors (Pettengill and Ford [1]) have suggested that scattering from a single surface possessing a very high effective dielectric permittivity could explain many of the unusual characteristics displayed by the Venus surface.

2. Volume scattering that results from successive interactions with one or more interfaces interior to the planetary surface. If the near-surface material has a moderately low index of refraction (to ensure that a substantial fraction of the radiation incident from outside is not reflected, but rather penetrates into the surface), and a very low internal propagation loss, successive internal reflections can eventually redirect much of the energy back through the surface toward the viewer. The necessary conditions for this process to be effective are a low internal propagation loss coupled with efficient internal reflection. At sufficiently low temperatures, fractured water ice displays both the necessary low loss and near-total internal reflection. Scattering of this type has been seen from the three icy Galilean satellites of Jupiter, Saturn's rings, and the polar caps of Mars (and probably Mercury). The possibility that this mechanism might also be acting on Venus (but not, of course, involving ice) has recently been put forward [2].

How can one distinguish between these processes? Scattering from a single interface is usually modeled as a combination of quasispecular reflection, involving coherent processes [3] that may be described by the usual Fresnel equations, and a diffusely scattering component arising from rough surface structure of the order of a wavelength in size [4]. The combination of undulating surface and small-scale roughness allows this model to be adjusted to fit almost any observed variation in backscatter with the angle of incidence. What it cannot do is produce strong depolarization in the scattered power, since only the component of small-scale roughness can contribute to depolarization and that is a relatively inefficient process, typically yielding only about 30% of the total diffuse scattering as depolarized energy.

Volume scattering, on the other hand, does not favor backscattering near normal incidence, as quasispecular scattering generally does, but tends to backscatter efficiently without much variation over a wide range of angles of incidence [5, 6]. Moreover, volume scattering is a very efficient depolarizer, often returning a virtually unpolarized echo to the observer, it can even produce an inverted circular polarization ratio, i.e., favoring an echo having the same circular sense as the incident wave [6].

From the above considerations, it would seem that the two processes are distinguished most easily by their quite different effects on the polarization states of the scattered or thermally emitted radiation. Such observations have been attempted using ground-based radars, but have so far yielded only limited results. Unfortunately, the Magellan radar and radiometer instrument emits and receives only the same single linear polarization.

Radar scattering by the first process above, should yield only a modest amount of backscattered energy in the depolarized (often called the "unexpected") mode. For linear transmitted polarization, the depolarized mode is the orthogonally polarized linear state; for circular transmitted energy, it is the same sense, since coherent reflection reverses the circular sense while preserving the linear position angle. Preliminary analysis from observations made using the Arecibo 12.6-cm radar system [7] suggest that depolarization is

virtually complete for circularly polarized radar echoes received from Maxwell Montes. Thus this evidence favors the internal volume scattering hypothesis. On the other hand, comparison of vertically and horizontally polarized emission data from low-emissivity areas in Beta Regio, which were obtained during a special test carried out by the Magellan spacecraft, show a substantially larger linearly polarized emission component in the vertical than in the horizontal, a result that can only result from the first process. Surprisingly, then, it seems that we may need to invoke a third process not yet conceived to explain the high backscatter and low emissivity observed in selected high-altitude regions on Venus

References: [1] Pettengill G. H. et al. (1982) *Science, 217,* 640–642; Ford P. G. and Pettengill G. H. (1983) *Science, 220,* 1379–1381. [2] Tryka K. A. and Muhleman D. O. (1992) *JGR*, in press. [3] Hagfors T. (1970) *Radio Sci., 5,* 189–227. [4] Pettengill G. H. and Thompson T. W. (1968) *Icarus, 8,* 457–471. [5] Ostro S. and Shoemaker E. (1990) *Icarus, 85,* 335–345. [6] Hapke B. (1990) *Icarus, 88,* 407–417. [7] Campbell D. B. (1992) personal communication.

N93-14361

TECTONIC CONNECTIONS TO INTERIOR PROCESSES ON VENUS.

R. J. Phillips, McDonnell Center for the Space Sciences and Department of Earth and Planetary Sciences, Washington University, St. Louis MO 63130, USA.

Introduction: The ultimate goal of geophysical/geological exploration of Venus is to relate the present tectonic (and volcanic) state of the lithosphere to interior processes, particularly mantle convection, operating both now and in the past. The Magellan mission has provided a spectacular view of the surface, and upcoming gravity measurements, particularly if the Magellan orbit is circularized, will provide significant constraints on the state of the interior. This abstract focuses on several controversial issues regarding venusian tectonics and its relationship to geodynamic mechanisms in the planet's interior.

Highlands: A major debate within the Venus science community concerns the origin of certain highland features on Venus [1,2,3]. While there is general agreement that the origins of highland regions on Venus must be linked directly to mantle convection, there is a strong dichotomy of opinions on the relative roles of mantle upwelling (hotspots) and downwelling (coldspots) [4]. In particular, do such areas as Ovda and Thetis Regiones and Lakshmi Planum, characterized as "crustal plateaus" [1], sit over upwellings or downwellings? One of the main objections to the hotspot model is that in its evolutionary cycle it must be capable of developing significant strain—as observed in crustal plateaus—and this has not been demonstrated. The chief criticism [3] of the coldspot model is that significant secondary crustal flow is required to turn a region over a convective downwelling into positive topographic relief of the magnitude observed. This issue has become more severe recently: It is now understood that experimental viscous flow laws heretofore used for the venusian crust are, because of the presence of hydrous phases, probably significantly weaker than the real planet [5]. Thus characteristic times to develop positive topography over downwellings may be unreasonable geologically—in excess of a few billion years. The coldspot model has been attractive because it was able to provide both high-standing topography and significant compressional strain, although convection must be particularly vigorous to explain Ishtar Terra. If secondary crustal flow is not an important process on Venus, then it is reasonable to investigate other models to understand their plausibility ·in meeting these

constraints. In the coldspot model, high-standing topography could also be created by convective shear tractions on the base of the lithosphere, leading to imbrication—the stacking of lithospheric thrust sheets. This process requires that new lithospheric surface area be created somewhere on Venus (e.g., lithospheric spreading); so far, this has not been observed. Addition of mass is usually required for compressional strain, and the hotspot model is actually attractive because new mass is provided vertically from the mantle by partial melting, and it is not necessary to obtain it horizontally from the lithosphere. Major strain associated with crustal plateaus might arise from crustal thickness instabilities [6,7] and from detachment [8] arising from eclogite formation in plateau roots.

Coronae: Coronae are large circular surface structures, which are observed in Magellan images to range up to 2600 km in diameter [9]; they are associated with both volcanism and tectonism. While it is generally agreed that coronae form in response to buoyantly rising material [9,10], there is no convergence of opinion on the nature of the diaper. Three endmember models are (1) thermal plumes from the mantle (which may then undergo pressure release partial melting), (2) compositional plumes that arise perhaps from melting induced by broader-scale thermal plumes, and (3) instabilities arising in regions that are partially molten or at the solidus [11,12]. In the last mechanism, the instability is triggered by an upward velocity perturbation, and on Venus such perturbations could arise from extensional strain events in the lithosphere associated with both upwelling and downwelling mantle flow. The coincidence of coronae with extensional features [9] provides evidence for this process.

Trenches and Subduction: On the basis of Venera 15–16 data, it has been proposed [13] that lithospheric convergence and underthrusting has occurred on the northern boundary of Ishtar Terra. The steep front and trench on the western side of Maxwell Montes also supports this idea. More recently, it has been suggested that trenches associated with the boundaries of certain large coronae mark the sites of "rollback" or retrograde subduction [14; see also 15]. In this hypothesis, the lithosphere associated with a corona extends outward and material is replaced by upward mantle flow (in analogy to terrestrial back-arc spreading). The expanding corona "consumes" lithosphere on its boundary (i.e., the surrounding lithosphere is subducted beneath the corona). The hypothesis for retrograde subduction is based on topographic and flexural analogy to terrestrial subduction trenches [14,15,16]. While evidence for outward migration of coronae is seen in the radar images, continuity of structures across proposed plate boundaries (i.e., trenches) argues against the subduction hypothesis [17].

Lithospheric subduction on Venus would require an active driving mechanism. No indication of spreading ridges is observed in the Magellan data, so "ridge push" can probably be discounted. Direct convective coupling from the underlying mantle may provide sufficient force, however [1]. The proposed retrograde subduction requires the lithosphere to be negatively buoyant. This may only be possible if garnet granulite or eclogite can form in the lower crust. The notion that the temperature gradient on Venus may be as low as 10°/km (or less) in places [16] has implications for a relatively thick crust [18,19,20] and for the existence of such high-density phases encountered at depth in the lower crust before solidus temperatures are reached. However, the proposal that coronae mark the sites of mantle upwelling argues against such a low temperature gradient.

References: [1] Phillips R. J. et al. (1991) *Science, 252,* 288. [2] Bindschadler D. L. et al. (1992) *JGR,* special Magellan issue, in press. [3] Grimm R. E. et al. (1992) *LPSC XXIII,* 453–454.

[4] Solomon S. C. et al. (1992) *JGR,* special Magellan issue, in press. [5] Kohlstedt D. L. (1992) In *Workshop on Mountain Belts on Venus and Earth,* 24, LPI, Houston. [6] Busse F. H. (1978) *Geophys. J. R. Astr. Soc., 52,* 1–12. [7] Lenardic A. et al. (1991) *GRL, 18,* 2209–2212. [8] Turcotte D. L. (1989) *JGR, 94,* 2779–2785. [9] Stofan E. R. et al. (1992) *JGR,* special Magellan issue, in press. [10] Stofan E. R. and Head J. W. (1990) *Icarus, 83,* 216–243. [11] Tackley P. J. and Stevenson D. J. (1991) *Proceedings of NATO Advanced Study Institute,* in press. [12] Tackley P. J. and Stevenson D. J. (1991) *Eos, 72,* 287. [13] Head J. W. (1990) *Geology, 18,* 99–102. [14] Sandwell D. T. and Schubert G. (1992) *Science,* submitted. [15] McKenzie D. et al. (1992) *JGR,* special Magellan issue, in press. [16] Sandwell D. T. and Schubert G. (1992) *JGR,* special Magellan issue, in press. [17] Hansen V. L. et al., this volume. [18] Zuber M. T. (1987) *Proc. LPSC 17th,* in *JGR, 92,* E541–E551. [19] Grimm R. E. and Solomon S. C. (1988) *JGR, 93,* 11911–11929. [20] Zuber M. T. and Parmentier E. M. (1990) *Icarus, 85,* 290–308.

N93-14362

"PROBLEM" FOOTPRINTS IN MAGELLAN ALTIMETRY DATA. Jeffrey J. Plaut, Jet Propulsion Laboratory, MS 230–225, 4800 Oak Grove Drive, Pasadena CA 91109, USA.

Introduction: The intensity, time-delay, and frequency content of radar echoes from the Magellan altimetry system are reduced to several parameters that are of great use in addressing many geological issues of the surface of Venus. These parameters include planetary radius, power reflection coefficient (reflectivity, both uncorrected and corrected for diffuse scattering), rms slope, and scattering functions (the behavior of backscatter as a function of incidence angle) [1,2]. Because the surface of Venus often reflects radio energy in unpredictable ways, models of radar scattering and their associated algorithms occasionally fail to accurately solve for the above surface parameters. This paper presents methods for identifying possible "problem" altimetry data footprints, and techniques for resolving some key ambiguities.

Data Acquisition and Reduction: For each footprint, Magellan's nadir-pointing altimeter transmits 1.1-µs bursts containing 17 pulses coded with a "chip" duration of 0.442 µs. These constraints, combined with the delay response and the highly elliptical orbit, yield an effective along-track resolution of 8 to 20 km, and a cross-track resolution of 13 to 31 km [1]. The finest resolution is obtained near the periapsis latitude of 10°N, and the coarsest resolution is obtained at high latitudes. Processing in the frequency domain ensures that the along-track footprint dimension accurately reflects the sources of echo power. In the cross-track dimension, however, strong reflections from outside the footprint can contribute to the echo, leading to ambiguities in reduction to surface parameters [P. Ford, personal communication].

The primary standard data product generated from altimetry data is the Altimetry and Radiometry Composite Data Record (ARCDR) [3]. For each Magellan orbit, a separate file is produced for altimetry and radiometry data. For each footprint within the altimetry files, echo profiles, in range-sharpened and range-unsharpened formats, are included, along with the derived parameters such as radius, rms slope, and reflectivity, and best-fitting model echo "templates" from which the surface parameters are estimated. The radius estimate is from the template fit to the range-sharpened profile, while the rms slope and reflectivity estimates are from the template fit to the range-unsharpened profile. Examination of the echo profiles, and comparison to the templates selected to match the

profiles, provide useful information for resolving issues associated with "problem" footprints.

Case Studies: *Sapas Mons.* At a regional level, Magellan altimetry and SAR image data provide a consistent picture of Sapas Mons: a 400-km-diameter shield volcano that rises approximately 1.5 km above the surrounding elevated plain in western Atla Regio, to a maximum elevation of 6055.7 km radius. In the summit region, however, an apparent discrepency is encountered between the morphology of structures seen in the SAR images and the radius measurements derived from the altimetry data. In particular, altimetry orbit 1467 passes directly across two scalloped dome structures at the volcano summit. While the SAR data clearly suggest these are positive in relief, eight altimetry footprints in orbit 1467 (11–13 and 16–20) have ARCDR radius values far below the typical summit region values of ~6055 km. Footprints 11–13, for example, have radius values more than 2 km below the preceding and following footprints (10 and 14, respectively). The combination of large fluctuations in radius values and apparent discrepencies between SAR and altimetry morphology provides an obvious "flag" that the derived altimetry data may contain spurious values.

Examination of the range-sharpened profiles and best-fit templates for the questionable footprints helps illuminate the possible source of the discrepencies. Figure 1 shows the profile and template used to determine the radius for footprint 20 of orbit 1467. The template echo, shown in a dashed line, is associated with a peak in the echo that appears to follow by 43 bins the leading edge of the measured echo. This delay of 43 0.21-μs bins corresponds to a round-trip travel time of 9.03 μs, giving an elevation difference of 1.35 km. Correcting the radius value of footprint 20 by this amount results in a value of 6055.2 km, consistent with surrounding footprints. Why should this echo contain two strong peaks, one of which produces a spuriously low radius value? Footprint 20 lies along the southwest flank of the southern summit dome feature. This suggests that echoes from the top of the dome may have "leaked" into the footprint, giving a spurious value for the area actually under consideration. For a given spacecraft altitude and time delay of a suspect echo peak, a family of combinations of feature height and feature offset from nadir can be calculated to understand the source of a secondary peak. Figure 2 shows a plot of such a family of geometries that could explain the secondary peak in footprint 20.
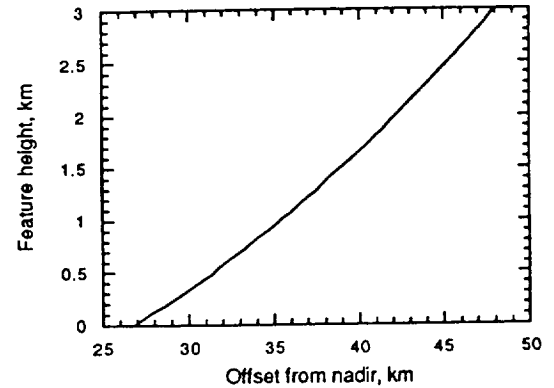
SAR data indicate that the dome sits within 25–30 km of the nadir, consistent with a dome height <0.5 km. The possibility that late echoes from outside the footprint can lead to spuriously low radius values increases toward periapsis, as the radius of curvature of the transmitted wavefront becomes much smaller than that of the planet. This phenomenon may be responsible for the occasional topographic "holes" seen in low- to mid-latitude areas of rapidly varying relief.

Kuan Tao-sheng impact crater parabola. In the high southern latitudes southwest of Imdr Regio, several impact-related "parabola" features display highly anomalous scattering behavior [4]. Among these anomalous properties are unusually high values of rms slope and reflectivity in the ARCDR dataset. The two parameters are highly correlated along a narrow hairpin-shaped parabolic feature approximately 800 × 2000 km in size. Many of these surfaces show anomalously high cycle 1 SAR backscatter values when compared with cycle 2. Southeast of Kuan Tao-sheng Crater (45 km diameter), numerous altimetry footprints have "unphysical" ARCDR reflectivity values >1.0. The same footprints have ARCDR rms slope values in the range 8°–12°, unusually high for plains surfaces that appear relatively smooth in the SAR images, and relatively flat in radius (topography) data. The anomalous footprints frequently are surrounded by footprints with reasonable values, leading to sharp discontinuities. This combination of characteristics (unusually high rms slope and reflectivity values, apparent discrepencies with SAR and radius data, and sharp discontinuities), should again provide a "flag" that the altimetry data reduction procedure may have yielded spurious values. Examination of the range-unsharpened echo profiles and their associated templates indicates that while the leading edge of the echoes appears to have been accurately tracked, yielding accurate radius values, the wide dispersion of echo power with time may have led to spurious rms slope and reflectivity solutions. Apparently the statistics of height and slope distributions assumed in the Hagfors quasispecular scattering model do not adequately describe the surface geometry within these footprints. The possible east-west asymmetry associated with these parabolic crater features [4] may account for the unusually wide dispersion of the echo. The analysis of scattering functions provided in the Surface Characteristics Vector Data Record (SCVDR) [2], in which fits to non-Hagfors scattering behavior are reported, will be of use in further
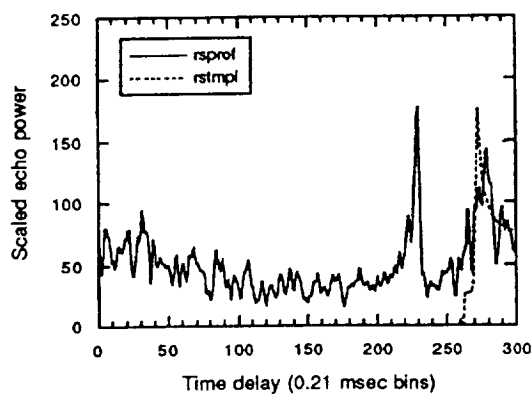

Fig. 1. Echo power vs. time delay, range-sharpened (rsprof), for orbit 1467, footprint 20 (Sapas Mons summit area). Also plotted is the best-fitting template from which the radius value was determined.

investigations of areas that display these unusual scattering characteristics.

References: [1] Pettengill G. H. et al. (1991) *Science, 252,* 260–265. [2] Tyler G. L. et al. (1992) *JGR,* special Magellan issue, in press. [3] Ford P. G. (1992) *ARCDR Software Interface Specification* (CD-ROM USA_NASA_JPL_MG_2001). [4] Plaut J. J. et al., this volume.

N93-14363

ANOMALOUS SCATTERING BEHAVIOR OF SELECTED IMPACT "PARABOLA" FEATURES: MAGELLAN CYCLE-TO-CYCLE COMPARISONS.

J. J. Plaut[1], R. S. Saunders[1], E. R. Stofan[1], R. L. Kirk[2], G. G. Schaber[2], L. A. Soderblom[2], P. G. Ford[3], G. H. Pettengill[3], D. B. Campbell[4], N. J. S. Stacy[4], R. E. Arvidson[5], and R. Greeley[6], [1]Jet Propulsion Laboratory, MS 230–225, 4800 Oak Grove Drive, Pasadena CA 91109, USA, [2]U. S. Geological Survey, Flagstaff AZ 86001, USA, [3]Center for Space Research, Massachusetts Institute of Technology, Cambridge MA 02139, USA, [4]National Astronomy and Ionospheric Center, Cornell University, Ithaca NY 14853, USA, [5]Department of Earth and Planetary Sciences, Washington University, St. Louis MO 63130, USA, [6]Department of Geology, Arizona State University, Tempe AZ 85287, USA.

Introduction: Magellan observations indicate that many venusian impact craters have associated surfaces, typically lower in backscatter and emissivity than the surroundings, that extend up to hundreds of kilometers to the west of craters, in parabolic planforms [1,2]. During Magellan's second mapping cycle, a number of these parabolic features were imaged for a second time, under a different viewing geometry. In some cases, the SAR backscatter appearance of portions of the parabolic features was quite different in the two datasets. In this paper, we present a description and preliminary interpretations of the anomalous appearance of these features as observed during Magellan's first and second mapping cycles.

Observations: Two types of structures within the parabolas show significant differences in appearance. These are "bright patches" and "streaks." Bright patches are irregular, diffuse-appearing areas of high backscatter (relative to surroundings). Values are typically 0 to 5 dB above the expected (Venus average) sigma zero, while surroundings are typically below the expected value. Differences in sigma zero between cycles can be as high as 9 dB, with comparable incidence angles but opposite look azimuths (cycle 1 east-looking, cycle 2 west-looking). Bright patches usually occur along the "arms" of the parabola features, but some are also seen in the central portions. Their distribution appears to be partly controlled by local small-scale (1–20 km) topography, such as wrinkle ridges. Discontinuous patches are often seen between (rather than straddling) wrinkle ridges, and some patches appear to terminate along ridges. Bright patch areas that are seen only in cycle 1 data occur at the craters Kuan Tao-sheng (–61.1, 181.7, 45 km), Eudocia (–59.1, 201.9, 29 km), and Boulanger (–26.5, 99.3, 57 km); patches seen only in cycle 2 data occur at the craters Stowe (–43.3, 233.2, 78 km), Kuan Tao-sheng, Austen (–25.0, 168.3, 47 km), Adaiah (–47.3, 253.3, 19 km), and Aksentyeva (–42.0, 271.9, 40 km).

"Streaks" are alternating high and low backscatter bands 1–20 km wide, up to 500 km long. The bright bands have still relatively low sigma zero values (within 2 dB of the expected), while the dark bands are almost always lower than the expected value. Streaks are often associated with, or are part of, bright patches. Trends of the streaks are consistently east-west, within about 10°. Like the bright

patches, streaks are commonly truncated along wrinkle ridges. Streaks are more common near the axes of the parabolas (i.e., due west of the crater), although some also are seen on the parabola arms. At Kuan Tao-sheng and Eudocia, streaks seen in cycle 1 SAR data are rarely seen in cycle 2. At Stowe, many streak sets are visible only in cycle 2 data, some are visible only in cycle 1 data, while others are visible in both datasets.

Several areas that show anomalous scattering behavior in cycle 1 and cycle 2 SAR data also have unusual properties in the cycle 1 radiometry and altimetry-derived datasets. In particular, the Eudocia/Kuan Tao-sheng area, which shows an extensive (over 1500 × 2000 km) emissivity parabola, also displays extremely unusual behavior in the altimeter-derived reflectivity and rms slope parameters. The two parameters are highly correlated (high values in both) along a narrow hairpin-shaped parabolic feature approximately 800 × 2000 km in size. Many of the surfaces that show anomalously high cycle 1 SAR backscatter values (compared with cycle 2) occur on this hairpin-shaped feature. The magnitude of the rms slope (8°–10°) and reflectivity values (typically > 0.8; some >1.0) on otherwise smooth-appearing, moderately low emissivity plains, suggests that the altimeter echoes are not well-modeled by the Hagfors template matching procedure of [3]. Specifically, examination of the echo profiles shows that the anomalous areas have a wide dispersion in echo power with time. This accounts for the high rms slope solutions. The unphysical (>1.0) reflectivity values may result from a mismatch between the theoretical Hagfors quasispecular scattering formulation and the actual distribution of surface facets within the altimeter footprint.

To summarize the key observations: (1) The differences are only seen in association with impact crater parabola features. (2) The differences are seen in images taken with comparable incidence angles from opposite sides (at Kuan Tao-sheng/Eudocia, angles are within 5°, at Stowe within 3°). (3) The patterns of bright patched streaks are clearly associated with each other and with surface morphology (e.g., wrinkle ridges). (4) The most dramatic differences are confined to a single broad region of the planet: mid to high southern latitudes between Artemis and Phoebe. (5) The differences have both "senses," i.e., bright patches and streaks may be seen uniquely in either cycle 1 or cycle 2 data. (6) The Kuan Tao-sheng/Eudocia area shows anomalously high reflectivity and rms slope values in altimetry-derived data.

Interpretations: The first issue that must be addressed is this: Are the apparent differences in SAR backscatter between cycle 1 and cycle 2 data a result of a modification of the surface (or subsurface) during the eight-month interval between data acquisitions, or are they a result of an azimuthally biased surface (or subsurface) structure in which backscatter is strongly enhanced in either the east- or west-looking configuration?

The best test of the surface change hypothesis involves duplicating the geometry of the cycle 1 acquisition. This experiment, in the Stowe Crater region, should have been conducted by the time of this colloquium, and relevant results will be presented. cycle 1 and cycle 2 emissivity measurements, which were acquired at emission angles equivalent to the SAR incidence angles, show differences at the 2% level at Stowe and Kuan Tao-sheng, but the differences do not correlate well with the SAR differences. However, the bright patches and streaks do not have strong emissivity signatures in either cycle, so changes at the surface may not be detectable in emissivity. At present, altimetry-derived data from cycle 2 have not been reduced for these areas. The similar nadir-looking geometry of the cycle 1 and 2 altimetry measurements eliminates the look-

direction bias, and comparison of the reflectivity and rms slope parameters will also be presented at the colloquium.

The association of anomalous scattering behavior and impact parabola features suggests that impact-derived materials are involved. These probably have unique properties among Venus surface materials with respect to their size distribution (a large component of fines?) and possibly with respect to composition or mineralogy. The presence of streaks suggests that wind processes are involved. Under a surface change scenario, the variations in SAR backscatter are suggested to result from redistribution of a layer of loose material, possibly by wind, during the interval between data acquisitions. However, the scale of the observed differences requires large volumes of material to be redistributed over a short period of time. Furthermore, the common occurrence of impact parabola features on the planet indicates that the age of the population of parabolas is probably on the order of tens to hundreds of Ma. It seems unlikely, if these surfaces were vulnerable to such rapid change, that they would retain their distinctive signatures over such a time span.

The viewing geometry hypothesis requires surfaces that contain geometrical elements that favor or diminish backscatter strength, depending on the side from which the surface is observed. The very nearly identical incidence angles (though east- and west-looking), require that the surfaces have a strong asymmetrical component in the east-west direction. The dominant asymmetry in the parabolic features is in the east-west direction (parabolas "open" to the west), so it may be inferred that structures at a smaller scale have an east-west component of asymmetry. Aeolian bedforms (ripples, dunes) are the prime candidates for such structures in the parabola areas. Terrestrial transverse dunes typically have stoss slopes of $5°-10°$, and slip face slopes of $30°-35°$. The absence of the "speckly" returns commonly observed in SAR images of dunes implies that the bedforms responsible for the extensive bright patches contain faces at scales of tens of centimeters to no more than a few tens of meters. The visibility of aeolian bedforms in SAR imagery is known to be highly sensitive to look azimuth, relative to the dominant strike direction of slopes [4]. In the high southern latitudes discussed here, the look azimuth between cycles differed by ~160°, which may

further affect the visibility of features. Several difficulties remain with the bedform hypothesis. The large enhancement in backscatter on steep faces should have a corresponding smaller enhancement on the shallow faces. This effect is not observed. The reversal in "sense" of the anomalies is also somewhat inconsistent with bedforms developed within a wind regime dominated by one persistent direction of flow, necessary for such widespread, consistent slope distributions.

References: [1] Arvidson R. E. et al. (1991) *Science, 252*, 270–275. [2] Campbell D. B. et al. (1992) *JGR*, special Magellan issue, in press. [3] Pettengill G. H. et al. (1991) *Science, 252*, 260–265. [4] Blom R. G. (1988) *Int. J. Rem. Sens., 9*, 945–965.

N93-14364

CYTHEREAN CRUSTAL BENDING AT SALME DORSA.

J. Raitala and K. Kauhanen, Department of Astronomy, University of Oulu, Finland.

The horseshoe-like, narrow (100 km wide and 600 km long) Salme Dorsa consists of arcuate ridges and grooves opening southeast on the planitia to the south of Ishtar Terra. Magellan radar data was studied in order to find tectonic style and lithospheric thickness of the area. The Salme ridge belt indicates folding and thrust faulting of surface layers due to compression against the tessera foreland zone. The western edge of Salme Dorsa is scarplike. Most ridges follow the main course of the arc and the overall ridge orientation is north-south while ridges subparallel the arcuate edge. The ridge trend at the northeastern end is northeast-southwest, while the southern part of the horseshoe has more northwestern ridges. The ridge belt has elements of normal compression against the zone. It has widened due to the new ridge formation. As this process repeats itself, the crust also becomes thicker making the topographically high ridge belt act as a load.

The scarp along the western edge of Salme Dorsa indicates that the movement has been to the west or northwest. West of Salme Dorsa the crust has bent due to the load and/or thrust of Salme Dorsa, resulting in a trough outside the scarp. The compressional ridge belt has acted either as a nappe overthrust or as a mere surface load due
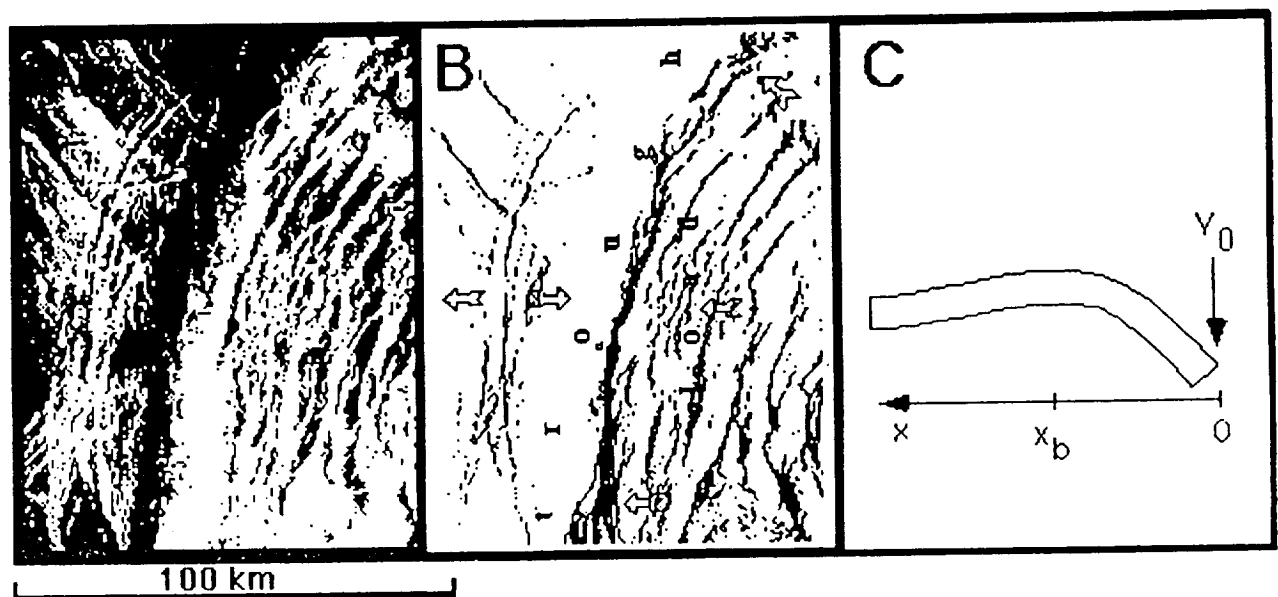
Fig. 1. Radar image of the crustal bending at central Salme Dorsa (a). The load and compression/tension stress system is displayed (b) and modeled with vertical exaggeration (c). The trough depression is next to a surface load and/or compressional massif. Grabens are located on the anticlinal bulge.

to crustal thickening under stress from the east or southeast. Salme Dorsa cuts through the ridges of older Sigrun Fossae. Salme Dorsa has quite a recent border scarp and is obviously relatively young. Interlocking nearby ridge belts indicate repeated compressions.

The trough and bulge west of Salme Dorsa is caused by crustal bending due to the ridge belt load or nappe thrust to the west. Tensional grabens along the crest of the bulge indicate crustal extension. The grabens parallel the ridge belt and trough as gentle arcs that open in the direction of Salme Dorsa on the bulge crest. Elastic deformation of the layered crust and adjoining fracturing of the uppermost brittle surface might be reasonable assumptions. The set of narrow grabens on top of the bulge are due to excess tensile stress in the uppermost brittle layer of the lithosphere. The lack of corresponding troughs, bending, or grabens on the eastern side of the ridge belt may indicate that both the load and the thrust from the east have to be taken into account. The volcanic area inside the Salme Dorsa horseshoe have also weakened the crust on that side.

The elastic layer is confined by the temperature above which the upper mantle has negligible strength [1]. The elastic part of the lithosphere is defined by isotherms 450°C and 650°C and this elastic lithosphere is considerably thinner than the low-attenuation seismic lithosphere. The temperature gradients of 15°C/km [2] and 20°C/km [3] and the surface temperature of 470°C suggest that the lower boundary of the elastic lithosphere is about 12 km or 9 km deep, respectively.

The thickness of the elastic layer is estimated using a flexural approach and a two-dimensional model of a semi-infinite broken elastic lithosphere under a linear load [4] with the only acting force, V_0, applied vertically to its end, where the bending moment is zero. The only measurable quantity, x_b, is the distance between the force and the bulge. The equation for the deflection of a plate includes loading of the lithosphere by vertical forces, hydrostatic restoring force, and the position of the bulge. Assuming a basaltic composition for the crust, $r_c = 3000$ kgm^{-3}, $E = 0.6 \times 10^{11}$ Pa and $\upsilon = 0.25$ and using $r_m = 3300$ kgm^{-3}, $g = 8.6$ ms^{-2} and $x_b = 50$ km we find $h \approx 2.9$ km for the elastic thickness of the lithosphere.

Variations in the magnitudes of the vertical or horizontal loads or the bending moment will alter the displacement but will not alter the position of the top of the bulge. Changes in the model, application of a horizontal force or a bending moment, will have more dramatic effects on the distance of the bulge and the lithospheric thickness. If a bending moment is assumed, the thickness of the lithosphere increases due to the increasing effect on plate curvature. The free edge boundary of our model is justified by volcanic activity that has weakened the lithosphere. Both a three-dimensional model and a continuous elastic plate model will reduce the elastic thickness. Allowing a bending moment to act upon the plate end, the elastic thickness of the lithosphere increases by a factor of 2.

The elastically thick lithosphere can support high compressional stresses or fail by faulting rather than buckling. Compressional stress critical to deformation can be estimated [4] to be approximately 0.4 GPa, taking the previous values. The wavelength of the buckling at the critical stress is about 94 km, and is reduced as the stress increases. This value corresponds well to the distance between Salme Dorsa and the bulge, and thus horizontal forces cannot be totally neglected. Recent research has revealed that buckling of the lithosphere can occur at stress levels much less than the elastic strength of the lithosphere [5]. Horizontal forces may have contributed to the buckling but it is difficult to find out which one of the forces has been active for a thickness of the elastic lithosphere of about 3 km. If both forces are allowed [6], the thickness of this layer of the lithosphere is slightly increased to 3.1 km.

Summary: The Salme ridge belt can be interpreted as being the leading edge of a venusian crustal unit that moved against the highland foreland unit. It is indicative of a compressional zone, with a thrust front facing west. The Salme Dorsa ridge belt with adjoining structures is an evident indication of lateral stresses and adjoining crustal movements on Venus. It supports the idea of southeast compression against and over the foreland planitia, which has bent under the load and/or lateral stress, resulting in trough and bulge formation in front of the ridge belt. The origin of the driving force for the movements remains masked. Laima Tessera is located in the direction from which the thrust is thought to apply [7] but there are no appropriate candidates for a rift zone although a thrust from the southeast would be in good agreement with structures of Laima Tessera. The temperature gradient [2] suggests that the lithosphere is approximately 12 km thick, while its elastic layer is approximately 3 km thick based either on the load-induced flexure model or on the compressional buckling model.

References: [1] Kirby S. H. (1983) *Rev. Geophys. Space Phys., 21*, 1528–1538. [2] Smrekar S. E. and Solomon S. C. (1992) *Workshop on Mountain Belts on Venus and Earth*, 35–37. [3] Solomon S. C. and Head J. W. (1989) *LPSC XX*, 1032–1033. [4] Turcotte D. L. and Schubert G. (1982) *Geodynamics: Applications of Continuum Physics to Geological Problems*, Wiley, New York, 450 pp. [5] Stephenson R. A. and Cloetingh S. A. P. L. (1991) *Tectonophysics, 188*, 27–37. [6] McAdoo D. A. and Sandwell D. T. (1985) *JGR, 90*, 8563–8569. [7] Raitala J. and Tormanen T. (1990) *Earth Moon Planets, 49*, 57–83.

N93-14365

COMPUTER SIMULATIONS OF COMET- AND ASTEROIDLIKE BODIES PASSING THROUGH THE VENUSIAN ATMOSPHERE—PRELIMINARY RESULTS ON ATMOSPHERIC AND GROUND SHOCK EFFECTS. D. Roddy[1], D. Hatfield[2], P. Hassig[2], M. Rosenblatt[2], L. Soderblom[1], and E. De Jong[3], [1]U.S. Geological Survey, Flagstaff AZ, USA, [2]California Research & Technology, Chatsworth CA, USA, [3]Jet Propulsion Laboratory, Pasadena CA, USA.

We have completed computer simulations that model shock effects in the venusian atmosphere caused during the passage of two cometlike bodies 100 m and 1000 m in diameter and an asteroidlike body 10 km in diameter. Our objective is to examine hypervelocity-generated shock effects in the venusian atmosphere for bodies of different types and sizes in order to understand (1) their deceleration and depth of penetration through the atmosphere and (2) the onset of possible ground-surface shock effects such as splotches, craters, and ejecta formations. The three bodies were chosen to include both a range of general conditions applicable to Venus as well as three specific cases of current interest.

These calculations use a new multiphase computer code (DICE–MAZ) designed by California Research & Technology for shock-dynamics simulations in complex environments. The code has been tested and calibrated in large-scale explosion, cratering, and ejecta research. It treats a wide range of different multiphase conditions, including material types (vapor, melt, solid), particle-size distributions, and shock-induced dynamic changes in velocities, pressures, temperatures (internal energies), densities, and other related parameters, all of which were recorded in our calculations. DICE–MAZ is especially useful in our Venus study because of the advance capability in multiphase adaptive zoning and because of the color coding associated with displaying the complex variations in

DICE-MAZ M201 (2-D VENUS, 100 M, Link-2) R07 M201PL1
CYCLE= 2724, TIME= 10.00 S
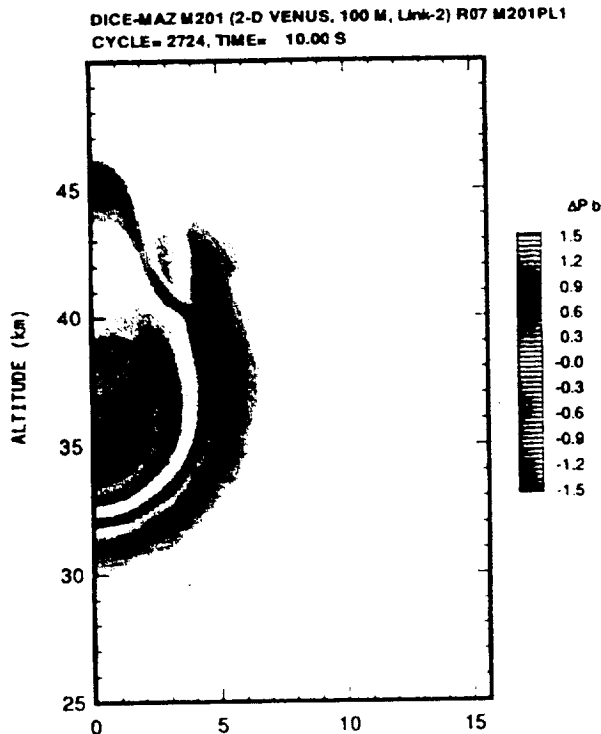
Fig. 1. Numerical simulation of bow shock-wave pressure field (ΔPb) surrounding the highly dispersed 100-m-diameter body now composed of vapor, melt (?), and original fragments at about 32-km altitude. The highest pressure in the bow shock wave is about 1.5 bar and is too weak to effect the venusian surface.

dynamic changes in parameters for the shocked bodies and surrounding atmosphere.

This preliminary study modeled the venusian atmosphere following [1], but without winds. An initial velocity of 20 km/s with a vertical trajectory was assumed for all cases. The 100-m and 1000-m bodies had a mean density of 1.0 g/cm³ (cometlike) and the 10-km body had a mean density of 2.5 g/cm³ (asteroidlike). For the 100-m and 1000-m cometlike bodies, the basic calculations were started at an altitude of 80 km; the complete numerical simulations were started at 45 km altitude, where deceleration of the 100-m body became significant. At altitude, on the order of 45 km, shock pressures in excess of 5 kbar were calculated at the leading edge of these bodies. We believe that these large differential body pressures could catastrophically break up low-strength, low-density bodies in the size range chosen. Therefore, we elected to model these two cases as fragmented for the remainder of their descent below 45 km into Venus' atmosphere. Fragmentation distributions of equal total mass per decade size bins ranging between 0.01 and 1000 cm were used. Consequently, the simulations represent only one plausible set of a wide range of possible body strengths, fragmentation histories, and entry conditions that remain to be explored. The 10-km body was assumed to not fragment under our initial conditions and was modeled as a rigid, nondeformable sphere; this choice was made mainly to permit direct comparisons with a similar set of calculations of asteroid impacts on the Earth in which the atmosphere is not dense enough to induce fragmentation for a body this size [2]. A fragmenting body 10 km in size should be calculated for direct comparisons with the other two bodies modeled here for Venus, but this was beyond the scope of our preliminary study. Oblique

trajectories are also important and the three-dimensional capability of the DICE-MAZ code should be used in later studies.

The 100-m-diameter fragmented body decelerated rapidly between 45 km and about 32 km altitude and the majority of its fragments were converted to vapor due to shock heating. The vapor and fragments experienced extensive outward separation due to flow along the bow shock wave generated in the atmosphere. The body took about 10 s to travel from 45 km down to about 32 km altitude with continuous deceleration and dispersion as vapor, melt (depending on materials present), and original fragments. These materials expanded to about 5 km across in a low-density band immediately behind the downward moving bow-shock wave. At about 32 km altitude, the dispersed vapor (~75%) was expanding in all directions and the remaining original fragments (~25%), including any melt, were in free fall to the surface. At about 32 km altitude, the pressure in the bow shock wave had decayed to about 1 bar and would produce no effect on the venusian surface.

The 1000-m-diameter fragmented body traveled downward in an increasingly dispersed configuration from 45 km altitude to the venusian surface in about 4.5 s, decelerating less rapidly than the 100-m body. As in the case of the 100-m body, the 1000-m body decelerated and dispersed as vapor, melt (depending on materials present), and original fragments. These materials spread into in a narrow band behind the bow-shock wave as the entire system penetrated downward in the atmosphere and expanded finally to over 10 km across near the ground. In this case, the 1000-m body had sufficient size and energetics to create a strong bow shock that reached the venusian surface with pressures of about 2.0 kbar at ground zero and decayed to 100 bar at 15 km ground range. The bow shock was followed immediately by a band of low-density, dispersed vapor (~25%) and original fragments (~75%), including melt (?), moving down and radially outward with peak horizontal velocities of about 0.5 km/s in the atmosphere at ranges of 10 km from ground zero (about 10 s). Of course, no impact-cratering effects occurred because the density and velocity of vapor and

DICE-MAZ M204: 2-D VENUS, D = 1000 m
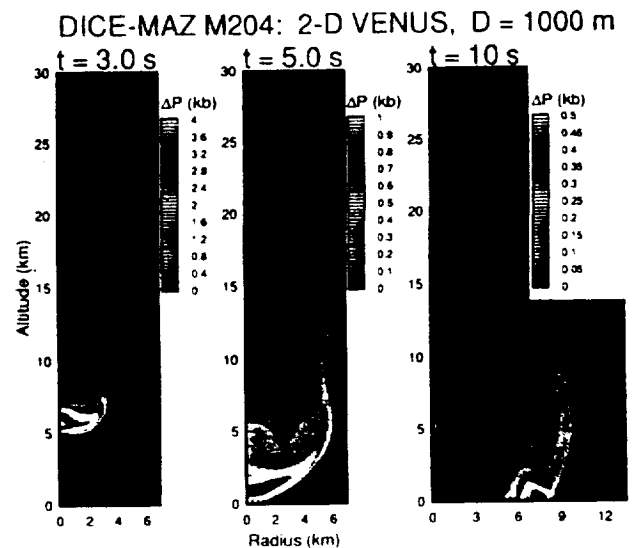
Fig. 2. Numerical simulations of bow shock wave pressure fields (ΔPkb) surrounding the dispersed 1000-m-diameter body that consists of vapor, melt (?), and original fragments. At 4.5 s, the leading edge of the bow shock has reached the venusian surface with a peak pressure of about 2.0 kbar at ground zero and decays to 100 bar at 15 km range; at 10 s, peak horizontal velocities in the atmosphere are about 0.5 km/s at 10 km range.

fragments were too low to induce a ground-shock condition sufficient for cratering. However, we do suggest that this body developed bow-shock peak overpressures and shock-initiated winds in the atmosphere near the ground sufficient to cause incipient disturbances on the venusian surface, depending on rheologic states of the target materials.

The 10 km-diameter body traveled from 45 km altitude down to the surface in 2 s with less than 2% deceleration and would have caused major atmospheric, impact-cratering, and ejecta effects. We estimate that the final crater would have been 150 to 200 km across but only a few kilometers deep, which we infer would be due in part to the high temperature, low strength, rapid relaxation rate of the target rock. This large body generated an enormous bow-shock wave with pressures in excess of 600 kbar that reached the ground surface and swept outward at over 10 km/s. It also evacuated a region over 40 km in diameter along the trajectory of the body in the atmosphere. This hot (~20,000–200,000 K), low-density region continued to expand and remained open for over several minutes after impact with substantial amounts of high-angle ejecta traveling through it to high altitudes. The effects of the 10-km body in Venus' environment are still under analysis, but several of the major aspects appear similar to the asteroid-impact results calculated for the Earth. The energetics of such large events tend to initially overwhelm both atmospheres.

In summary, our numerical simulations indicate that for weak, cometlike objects impacting into Venus' atmosphere at 20 km/s, a 100-m-diameter body completely disintegrates at high altitude and produces no ground surface effects. A 1000-m-diameter body also disintegrates but produces a strong bow-shock wave immediately followed by a dispersed band of vapor, melt (?), and fragments that reach the ground to produce strong shock pressures and radial winds in the near-ground atmosphere. We suggest that these conditions could induce incipient surface disruption and produce subtle surface features, depending on the rheologic states of the target materials. We suspect that the dark and light splotches that are several tens of kilometers in diameter seen in the Magellan SAR images [3–8], and believed to be impact induced, could have been generated by cometlike bodies a few kilometers in diameter. The bodies could be somewhat smaller if the splotches were produced by stronger asteroidlike bodies that fragmented lower in the atmosphere; these cases remain to be explored.

References: [1] Seiff A. (1983) In *Venus*, 1045–1048, Univ. of Arizona, Tucson. [2] Roddy D. J. et al. (1987) *Int. J. Impact Engng.*, 525–541. [3] Arvidson R. E. et al. (1991) *Science*, 270–275. [4] Phillips R. J. et al. (1991) *Science*, 288–297. [5] Zahnle K. J. (1991) *Eos*, 44, 289. [6] Zahnle K. J. (1992) *LPSC XXIII*, 1565. [7] Soderblom L. A. et al. (1992) *LPSC XXIII*, 1329–1330. [8] Schaber G. G. et al., in press.

N93-14366

THE EFFECTS OF VENUS' THERMAL STRUCTURE ON BUOYANT MAGMA ASCENT.
S. E. H. Sakimoto and M. T. Zuber, Department of Earth and Planetary Sciences, The Johns Hopkins University, Baltimore MD 21228, USA.

The recent Magellan images have revealed a broad spatial distribution of surface volcanism on Venus [1]. Previous work in modeling the ascent of magma on both Venus and Earth [2–5] has indicated that the planetary thermal structure significantly influences the magmatic cooling rates and thus the amount of magma that can be transported to the surface before solidification. In order to understand which aspects of the thermal structure have the greatest

influence on the cooling of ascending magma, we have constructed magma cooling curves for both plutonic and crack buoyant ascent mechanisms, and evaluated the curves for variations in the planetary mantle temperature, thermal gradient curvature with depth, surface temperature gradient, and surface temperature. The planetary thermal structure is modeled as

$$\frac{T}{T_0} = 1 - \tau\left(1 - \frac{Z}{Z_0}\right)^n \tag{1}$$

where T is the temperature, T_0 is the source depth temperature, $\tau = 1 - (T_s/T_0)$ where T_s is the planetary surface temperature, Z is the depth, Z_0 is the source depth, and n is a constant that controls thermal gradient curvature with depth. Equation (1) is used both for mathematical convenience and flexibility, as well as its fit to the thermal gradients predicted by the cooling half-space models [6]. We assume a constant velocity buoyant ascent, body-averaged magma temperatures and properties, an initially crystal-free magma, and the same liquidus and solidus for both Venus and Earth.

The cooling model for the plutonic ascent has been described in detail in earlier publications [2–5], and is a low Reynolds number, high Peclet number problem of heat transfer through a thin thermal boundary layer around a sphere. The resulting plutonic cooling curves, which are dominated by the convective cooling terms and strongly influenced by the planetary thermal structure, are then expressed mathematically by

$$\frac{T}{T_0} = \frac{J}{J+\gamma}\left(1 - e^{-(J+\gamma)t}\right) + e^{-(J+\gamma)t} + \left(\frac{J}{J+\gamma}\right)\left(\frac{\tau}{[(J+\gamma)t_0]^n}\right)$$

$$\left[e^{-(J+\gamma)t}(-1)^n n! - \sum_{p=0}^{n}\frac{(-1)^p \, n! \, [(J+\gamma)t]^{n-p}}{(n-p)!}\right] \tag{2}$$
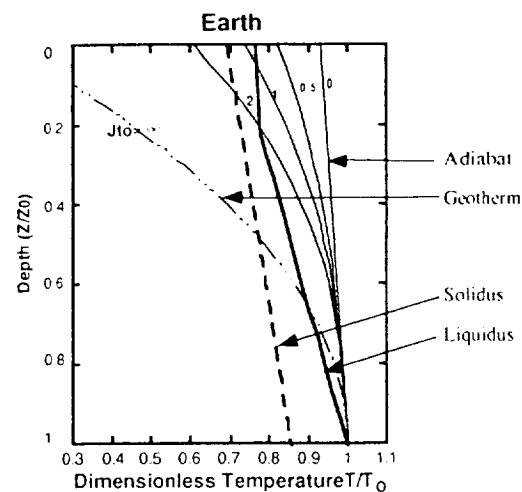
Fig. 1. Example of a typical cooling curve plot for pluton ascent. The curves are plotted for a given thermal structure and/or planet, and are contoured with their associated dimensionless ascent (Jt_0) values. In order for the magma to reach the surface unsolidified, the cooling curve must not cross the solidus. This plot is for a dry olivine tholeiite. The liquidus and solidus are obtained from [11]. Thermal structure parameters: n = 2; dT/dZ = 1.0 (dT/dZ of Earth); Z_0 = 1.0 (Z_0 of Earth).

where J = 3NuK/a², γ = αgV/C$_p$, t is time, t$_0$ is total ascent time, Nu = 0.8Pe$^{1/2}$, Pe = Va/K, Pe is the Peclet number, V is the velocity of magmatic ascent, a is the body radius, K(=1 × 10^{-6} m²s^{-1}) is the thermal diffusivity, α(=6 × 10^{-5} deg^{-1}) is the coefficient of thermal expansion, g is the gravitational acceleration, and C$_p$(=1.25 × 10^{-4} ergs Kg^{-1}°K^{-1}) is specific heat capacity. T is the mean magma temperature, T$_0$ is the magma temperature in the source region, and n is a constant that defines the shape of the planetary thermal gradient (equation (1)). Equation (2) reduces to the expression for the thermal gradient (equation (1)) for an infinitely slow ascent (dimensionless ascent time Jt$_0$ = ∞), and to the adiabatic curve T/T$_0$ = e$^{-\gamma t}$ for an infinitely fast ascent (Jt$_0$ = 0). A typical plot of the resulting cooling curves for terrestrial conditions, contoured in Jt$_0$ values, is illustrated in Fig. 1. In order for the magma to reach the surface unsolidified, the cooling curve must not cross the solidus before it reaches the surface. The allowable Jt$_0$ values obtained from the cooling curve plots for Venus and Earth can be directly compared to obtain relative minimum magma ascent velocities, source depths, and body sizes. The results are shown in Fig. 2.

The cooling model for the buoyant crack ascent has previously been described briefly in [2]. It is the problem of a magma at an initial temperature T$_0$ placed in contact with the wall rock of temperature T$_m$. This problem was initially solved by [7], and their solution for the average temperature T as a function of time is

$$\frac{T - T_m}{T_0 - T_m} = \frac{8}{\pi^2} \sum_{m=1}^{\infty} \frac{\exp\left\{-(2m-1)^2 \pi^2 Kt/4a^2\right\}}{(2m-1)^2} \quad (3)$$

where the notation is the same as in equation (2), and the right side is constant for any single dimensionless ascent time (Kt/a²). This result is for a constant wall rock temperature, but can be adapted to a variable wall rock (thermal gradient) temperature by approximating an incremental magma ascent in a simple numerical scheme where the initial magma temperature T$_0$ at any location m is, instead of the source depth temperature, the final magma temperature at the previous location m–1 [2]. If heat is conducted ahead of the magma body, the boundary temperature of the magma and wall rock will not be constant (T$_{contact}$ = T$_m$) at any given location, but will be the average of the two initial temperatures of the magma and wall rock

at any location for the majority of the cooling time [8]. For this case, the contact temperature at the mth position is the average of the final temperature of the magma at the m–1 position (T$_{m-1}$) and the initial wall rock temperature at the mth position (T$_{m0}$). The preliminary results from this model indicate that the effect of the planetary thermal structure is of the same order of the effect seen in the pluton model.

In general, for both ascent mechanism models presented here, the influence of the planetary thermal structure parameters for Venus in the probable order of decreasing importance is surface temperature, surface temperature gradient, thermal gradient curvature with depth, and planetary mantle temperature. The higher surface temperature of Venus, for otherwise similar planetary thermal structures, allows considerably smaller minimum possible crack sizes and/or magma body sizes, and slower ascent velocities than would be possible on Earth for a reasonable range of Venus source depths and surface thermal gradients. This surface temperature effect is greater for more primitive magma compositions, and may be greater for magmas of higher crystallinity. A higher venusian surface thermal gradient has the same effect of the higher surface temperature on magma transport, but to a much lesser degree. Similarly, for higher values of thermal gradient curvature with depth (higher n in equation (1)), the minimum possible ascent velocity and body/crack size also decreases slightly. If the mantle temperature for Venus is elevated by a hundred degrees or so over that of Earth [9], it should result in a modest increase of melt production and magma transport to the surface compared to Earth. The effect of the range of Venus surface temperatures with elevation (390°–470°C or 660°–740°K [10]) is under investigation, and is also anticipated to have a significant effect on magma transport, possibly greater than that of the higher mantle temperature.

References: [1] Head J. W. et al. (1991) *Science, 252*, 276–288. [2] Marsh B. D. (1978) *Phil. Trans. R. Soc. Lond., A288*, 611–625. [3] Marsh B. D. and Kantha L. H. (1978) *EPSL, 39*, 435–443. [4] Sakimoto S. E. H. et al. (1992) *LPSC XXIII*, 1203–1204. [5] Marsh B. D. (1982) *Am J. Sci., 282*, 808–855. [6] Sclater J. G. et al. (1980) *Rev. Geophys., 18*, 269–312. [7] Williamson E. D. and Adams L. H. (1919) *Phys. Rev., 14*, 99–114. [8] Jaeger J. C. (1964) *Rev. Geophys., 2*, 443–466. [9] Sotin C. et al. (1989) *EPSL, 95*, 321. [10] Seiff A. (1983) In *Venus*, 215–279, Univ. of Arizona, Tucson. [11] Lambert I. B. and Wyllie P. J. (1972) *J. Geol., 80*, 693–708.

N93-14367

EVIDENCE FOR RETROGRADE LITHOSPHERIC SUBDUCTION ON VENUS. David T. Sandwell[1] and Gerald Schubert[2], [1]Scripps Institution of Oceanography, La Jolla CA 92093, USA, [2]Department of Earth and Space Sciences, University of California, Los Angeles CA 90024, USA.

Though there is no plate tectonics per se on Venus [1], recent Magellan radar images [2] and topographic profiles [3] of the planet suggest the occurrence of the plate tectonic processes of lithospheric subduction [4] and back-arc spreading [5]. The perimeters of several large coronae (e.g., Latona, Artemis, and Eithinoha) resemble Earth subduction zones in both their planform and topographic profile. McKenzie et al. [4] have compared the planform of arcuate structures in Eastern Aphrodite with subduction zones of the East Indies. The venusian structures have radii of curvature that are similar to those of terrestrial subduction zones. Moreover, the topography of the venusian ridge/trench structures is highly asymmetric with a ridge on the concave side and a trough on the convex side; Earth subduction zones generally display this same asymmetry.

Fig. 2. Plot of the results for basaltic pluton ascent on Venus. The results are nondimensionalized by the corresponding terrestrial values, and the source depth values are the direct result of the assumed planetary thermal structure (equation (1)). For example, for a Venus thermal gradient the same as the terrestrial thermal gradient and n = 2, the corresponding minimum source depth is about 60% of the terrestrial value the minimum ascent velocity is about 30% of Earth's and the minimum body size is about 70% of Earth's. Thermal structure parameters: n = 2; dT/dZ = 1.0 (dT/dZ of Earth); Z$_0$ = 1.0 (Z$_0$ of Earth).

Trench/Outer Rise Topography: Latona Corona (eastern Aphrodite, Venus) provides a striking resemblance to the South Sandwich Trench (South Atlantic, Earth) as shown in Fig. 1. The Sandwich subduction zone is a deep arcuate trench having a radius of curvature of about 330 km. A topographic profile across the Sandwich trench (A–A') displays the characteristic trench/outer rise signature that is caused by downward flexure of the lithosphere prior to subduction [6]. We have modeled this lithospheric flexure to determine the elastic plate thickness, the curvature of the plate and the bending moment that is needed to support the topography of the outer rise; the best-fit model has a 40-km-thick plate. Like most other trenches on the Earth, the extreme curvature of topography on the outer trench wall is sufficient to permanently deform the lithosphere prior to subduction [7]. This inelastic behavior is marked by trench-parallel normal faults extending from the trench axis to the outer rise.

Latona Corona displays essentially the same topographic and flexural characteristics seen at the Sandwich arc (Figs. 2 and 3). The deep arcuate trench along the southern margin of Latona has the

Fig. 1. (Top image) Bathymetry of South Sandwich Trench (Earth) as a tall volcanic ridge, a deep ocean trench, and the characteristic trench/outer rise signature associated with lithospheric flexure prior to subduction (A–A'). (Bottom image) Topography of Latona Corona (East Aphrodite, Venus) at the same horizontal and vertical scale as the Sandwich Trench (top). The southern arc displays a prominent ridge-trench-outer rise signature (B–B'). The southernmost ridge is not massive enough to maintain the bending moment of the trench/outer rise flexure. Additional bending moment can be supplied by a subducted slab or by the second interior ridge.

same radius of curvature as the Sandwich trench (340 km) and inboard of the trench axis lie two tall arcuate ridges. A topographic profile across the Latona trench (Fig. 3) displays the characteristic trench/outer rise signature associated with lithospheric flexure although its overall amplitude is somewhat less than at the Sandwich trench. As in the case of the Sandwich trench, we applied the flexure model to the trench/outer rise topography at Latona and estimated an elastic plate thickness of 30 km, which is similar to the elastic thickness at the Sandwich trench. Like trenches on the Earth, the outer trench wall of the Latona trench has a high curvature, suggesting that the plate is flexed beyond its elastic limit, perhaps in preparation for subduction. SAR images display prominent circumferential fractures on the outer trench wall in agreement with the plate flexure model [5].

Since venusian trenches display the major characteristics of Earth trenches and since the Earth's lithosphere is known to be subducting, it is possible that the venusian lithosphere is also subducting. We have tested this hypothesis by determining whether the overriding coronal ridge is massive enough to supply the measured bending moments; if the ridge cannot supply the required moment then one must invoke a negatively buoyant subducted slab to make up the deficit. At Artemis, about two-thirds of the coronal ridge is needed to balance the trench/outer rise bending moment; all of this topography lies within 100 km of the trench axis. At Latona, however, the outermost coronal ridge (southernmost ridge in Fig. 2) is insufficient to balance the trench/outer rise moment; the second interior ridge must be included but in this case most of this topographic moment lies more than 150 km from the trench axis (i.e. more than one-half of the flexural wavelength). We performed the same calculation at the Sandwich Trench and found that only about one-half of the volcanic arc is needed to balance the trench/outer rise moment. However, on the Earth, the downward force exerted by the topography of the volcanic arc is largely balanced by the upward buoyancy of its thick crustal roots and the topographic moment does not support the trench/outer rise moment. The same isostatic compensation might occur on Venus. Thus, while the Venus moment balance calculation does not demonstrate the need for a negatively buoyant subducted slab, it cannot disprove the subduction hypothesis either.

Retrograde Subduction Around Coronae: These observations and calculations can be explained by a model of lithospheric foundering, trench rollback, and back-arc extension that was developed to explain the geometries and kinematics of many subduction zones on Earth including the Sandwich Trench. The corona is essentially a hole in the lithosphere whose edges sag downward beneath its outer rim. Sinking and rollback (or retrograde migration) of the exterior lithosphere is accompanied by inflow of mantle material beneath the corona and extension of the corona interior (back-arc spreading). The interior extension occurs in a more distributed and disorganized way than the ridgelike spreading in terrestrial back-arc basins. The downward bending of the exterior lithosphere beneath the rim of the corona produces the trench or moat around the corona; the outer rise is an elastic flexural response to the downwarping.

The occurrence of retrograde subduction on Venus is consistent with our understanding from fluid dynamics [8] that convection in a largely internally heated mantle should be dominated by downwelling instabilities from the cold upper thermal boundary layer (lithosphere). Thus, we propose that the same physical process that drives plate tectonics on Earth is also important in the tectonics of Venus even though the lithosphere subduction forces on Venus do

not apparently result in a completely analogous platelike tectonic configuration.

On Earth, the mantle is mainly cooled by the cold subducting lithosphere [8]. Lithospheric subduction on Venus should play a similar role in cooling the mantle. We can evaluate the potential importance of subduction on Venus to planetary heat transfer by estimating the total length of subduction zones on Venus [9] and comparing it with the total length of terrestrial subduction zones (37,000 km [10]). Retrograde subduction on Venus may be occurring not only at the marginal trenches of the large coronae Artemis, Latona, and Eithinoha, but also at arcuate trenches such as Dali and Diana chasmata in Eastern Aphrodite Terra [4] and elsewhere on the planet (e.g., Hecate Chasma, Hestia Rupes, Nightingale Corona, and Parga Chasma). The total length of these arcuate trenches is about 15,000 km [11]. The estimate would be greater if features such as Quetzalpetlatl Corona and the margins of plateau highlands such as Western Ishtar Terra and Thetis Regiones [12] were included. Of course, we do not know if any of these features are presently active. Assuming that they are all active and have terrestrial convergence rates, this trench-length estimate indicates that mantle cooling by lithospheric subduction is a potentially important process on Venus.

References: [1] Solomon S. C. et al. (1991) *Science, 252*, 297; Solomon S. C. et al. (1992) *JGR*, in press. [2] Saunders R. S. et al. (1992) *JGR*, in press. [3] Ford P. G. and Pettengill G. H. (1992) *JGR*, in press. [4] McKenzie D. P. et al. (1992) *JGR*, in press. [5] Sandwell D. T. and Schubert G. (1992) *JGR*, in press; Sandwell D. T. and Schubert G. (1992) *Science*, submitted. [6] Caldwell J. G. and Turcotte D. L. (1979) *JGR, 84*, 7572. [7] Turcotte D. L. et al. (1978) *Tectonophysics, 47*, 193; McNutt M. K. and Menard H. W. (1982) *Geophys. J. R. Astron. Soc., 71*, 363. [8] Schubert G. (1992) *Annu. Rev. Fluid Mech., 24*, 359. [9] Stevenson D. J., personal communication. [10] Reymer A. and Schubert G. (1984) *Tectonics, 3*, 63. [11] The following features were identified in a gridded Venus topography map [5] as possible subduction zones based on their ridge-trench-outer rise topography and arcuate planform: Artemis Corona, Latona Corona, Eithinoha Corona, Nightingale Corona, Dali Chasma, Diana Chasma, Hecate Chasma, Parga Chasma, Hestia Rupes, and a number of unnamed arcuate features. There are many other more subtle trenchlike expressions that would almost double the estimated trench length of 15,000 km. [12] Bindschadler D. L. et al. (1992) *JGR*, in press. •

N93-14368

OVERVIEW OF VENUS GEOLOGY: PRELIMINARY DESCRIPTION OF TERRAIN UNITS FOR VENUS GLOBAL GEOLOGIC MAPPING. R. Stephen Saunders, Ellen R. Stofan, Jeffrey J. Plaut, and Gregory A. Michaels, Jet Propulsion Laboratory, California Institute of Technology, Pasadena CA 91109, USA.

Venus terrain units can be categorized on the basis of morphology, reflectivity, backscatter, roughness, and emissivity. Morphology can be inferred from Magellan left-looking nominal incidence angle image mosaics, right-looking coverage, and more limited left-looking stereo. The typical resolution is about 300 m down to about 120 m near periapsis in the cycle one nominal coverage. The scale of geologic mapping governs definition of mappable terrain units. Initial global mapping is being compiled at a scale of 1:50 million. At this scale, the smallest individual features that can be mapped is about 125 km. The categories of terrain types are plains, complex ridge terrain, features with morphology suggesting volcanic or

volcano-tectonic origin, features interpreted to be tectonic in origin, crater units, and surficial units such as splotches and streaks. The following are brief descriptions of terrain units that are being mapped globally at the 1:50 million scale.

Plains:
Smooth plains—Planar surfaces with low radar backscatter and smooth texture.
Smooth plains with wrinkle ridges—Plains with widely spaced (10 km or more) linear to sinuous ridges.
Mottled plains—Plains with many apparently overlapping lobate outline subunits creating a light and dark mottled appearance.
Gridded plains and lineated plains—One or more crossing sets of parallel radar bright lineaments cross the plains.

Complex ridge terrain (CRT):
CRT1—Single trend of generally parallel but irregular ridges and troughs of various wavelengths from a few kilometers to tens of kilometers; individual ridges may exceed 50 km in length.
CRT2—CRT1 disrupted by sets of crosscutting lineaments; Morphology varies from long, sinuous ridge sets to blocky.
CRT3—Two prominent sets of ridges and troughs that are approximately orthogonal; relatively short ridges (25 km) and longer disrupting linear zones (50 km).
CRT4—Chaotic arrangement of ridges and troughs intersecting at a variety of angles and scales; may have lensate or hummocky appearance.

Morphology suggesting volcanic and volcano-tectonic origin:
Corona—Annular arrangement of ridges and troughs; interior varies.
Arachnoid—Circular to quasicircular features with radial systems of lineaments.
Shield—Low h/w often with radial flow-like patterns; diameter 50 to several hundred kilometers.
Dome—Small shield structure with steep sides and broad convex or concave summit; generally simple circular in plan.
Dome field—Cluster of approximately one hundred or more 3- to 10-km dome forms.
Scalloped dome—Dome with radial ridges separating scoop or theater-shaped grooves. Many have surrounding landslide debris.
Flow field—Complex of individual lobate flow-like features typically with parallel alignments and common source.
Channel—Sinuous trough or sinuous linear contrasting pattern on plains.

Features interpreted to be tectonic in origin:
Linear troughs and bright lineaments resembling graben or fractures—Generally steep-sided straight troughs and bright lineaments interpreted to be graben faults and fractures.
Lineament zone—Bands of linear features and broad troughs and basins.
Ridges—Positive linear features similar to lunar wrinkle ridges.
Ridge belts—Bands of ridges having a generally common trend.
Crater units—Various crater related features including ejecta, flow material and pababolic halos.
Splotch—Dark and bright quasicircular features.
Windstreak—Bright and dark streaks generally terminating at one end at a topographic feature such as a dome or ridge.

N93-14369

IMPACT CRATERS ON VENUS: AN OVERVIEW FROM MAGELLAN OBSERVATIONS. G. G. Schaber[1], R. G. Strom[2], H. J. Moore[3], L. A. Soderblom[1], R. L. Kirk[1], D. J. Chadwick[1], D. D. Dawson[2], L. R. Gaddis[1], J. M. Boyce[4], and J. Russell[1], [1]U. S. Geological Survey, Flagstaff AZ, USA, [2]University of Arizona, Tucson AZ, USA, [3]U. S. Geological Survey, Menlo Park CA, USA, [4]NASA Headquarters Code SLC, Washington DC, USA.

Magellan has revealed an ensemble of impact craters on Venus that is unique in many important ways. We have compiled a database describing 842 craters on 89% of the planet's surface mapped through orbit 2578 (Fig. 1) (the craters range in diameter from 1.5 to 280 km). We have studied the distribution, size-frequency, morphology, and geology of these craters both in aggregate and, for some craters, in more detail [1,2]. We find that (1) the spatial distribution of craters is highly uniform; (2) the size-density distribution of craters with diameters ≥35 km is consistent with a "production" population having a surprisingly young age of about 0.5 Ga (based on the estimated population of Venus-crossing asteroids); (3) the spectrum of crater modification differs greatly from that on other planets: 62% of all craters are pristine, only 4% volcanically embayed, and the remainder affected by tectonism, but none are severely and progressively depleted based on size-density distribution extrapolated from larger craters; (4) large craters have a progression of morphologies generally similar to those on other planets, but small craters are typically irregular or multiple rather than bowl shaped; (5) diffuse radar-bright or -dark features surround some craters, and about 370 similar diffuse "splotches" with no central crater are observed whose size-density distribution is similar to that of small craters; (6) other features unique to Venus include radar-bright or -dark parabolic arcs opening westward [3] and extensive outflows originating in crater ejecta.

The first three observations are entirely unexpected. We interpret them as indicating that the planet's cratering record was erased by a global volcanic resurfacing event or events, the latest about 0.5 Ga, after which volcanic activity declined (but did not cease entirely) and a new crater population began accumulating. Several members of the Magellan team have proposed variations of an equilibrium resurfacing model, which requires equilibrium between the rates of volcanism and impact cratering to account for the uniform and spatially random global crater distribution [4–7]. However, the geologic evidence and new Monte Carlo computer simulations of resurfacing using the observed crater distribution totally rule out equilibrium with less-than-global volcanic resurfac-

ing events. Convective thermal-evolution models support our interpretation of a global volcanic resurfacing of the planet about 0.5 Ga [8–11].

The dense atmosphere of Venus has strongly affected the production of craters. Large impactors have been relatively unaffected, intermediate-sized ones have been fragmented and have produced overlapping or multiple craters, a narrow size range (few hundreds of meters in diameter) has produced shock-induced "splotches" but no craters, and the smallest bodies have had no observable effect on the surface. The number of craters eliminated by the "atmospheric filter" is enormous—about 98% of the craters between 2 and 35 km in diameter that Magellan could have observed on a hypothetical airless Venus. Unique crater-related surface features such as parabolas and outflow deposits demonstrate the roles of Venus' high atmospheric density and temperature in modifying the crater-formation process, through interactions as yet poorly understood.

Impact craters have been tentatively classified as six morphologic types largely related to size: those having multiple rings, double rings, central peaks, structureless floors, and those that are irregular or multiple. In part, the sequence of morphologies of venusian craters with increasing diameters is similar to that of craters on other planetary bodies.

Six multiring craters and 41 double-ring craters have been observed on Venus. The onset diameter to ring craters from central-peak craters is about 40 km, compared with 140, 85, 45, and <25 km on the Moon, Mercury, Mars, and Earth [12], respectively. For most of the terrestrial planets—now including Venus—the onset diameter from central-peak craters to double-ring craters shows a general inverse relationship with gravity [13–15], although effective viscosity and other target properties may also be important [15]. For Mars, the onset diameter is about half as large as would be expected on the basis of gravity considerations alone, indicating the importance of possible target characteristics unique to Mars [16].

Adjacent ring-interval ratios on Venus generally fall in the same three groupings as those reported for double- and multiring basins (1.4–1.5 and 2.0) and protobasins (3.3) on the Moon, Mercury, and Mars [17–20]. Mean ring ratios for double- and multiring craters on Venus were found to change as a function of rim diameter (Fig. 2). Similar but respectively less well defined, inverse relationships between ring ratio and basin diameter have also been observed on Mercury, Mars, and the Moon [20]. For venusian double-ring craters ≤60 km in diameter, the ring-spacing mean ratio is 2.8 ± 1.0, a value approaching that of protobasins on the other terrestrial planets. On Venus, however, no well-defined protobasins with both central peaks and incipient inner rings have been observed. For double-ring craters ≥60 km in diameter, the mean ring ratio is 2.05 ± 0.33, the most typical spacing for double- and multiringed basins on the other terrestrial planets. The six multiring craters observed on Venus have a mean ring-spacing ratio for adjacent rings of 1.52 ± 0.2. The transition diameters from simple to complex craters, central-peak to double-ring craters, and double- to multiring craters on Venus are better defined than on any of the other terrestrial planets. Thus they should be extremely useful in further understanding the processes of formation of these structures on all solid bodies in the solar system.

The three largest impact structures on Venus (Mead, Meitner, and Isabella) have a ring outside what is inferred to have been the transient cavity. These rings are suspected to be fault scarps forming the outer boundary of downdropped and inward-rotated "megaterraces" created at some late stage, possibly after deposition of the ejecta.
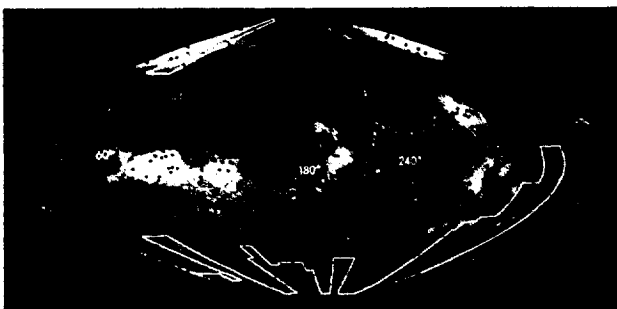
Fig. 1. Map in sinusoidal equal-area projection showing 840 impact craters on 89% of Venus. Basemap is continuous-tone Magellan altimetry (white-highest, black-lowest). Areas of planet not covered through orbit 2578 shown inside white lines.
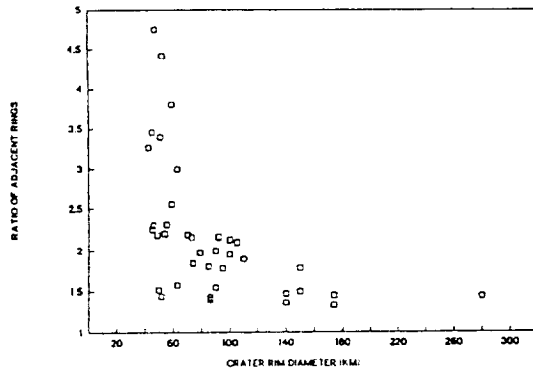
Fig. 2.

The depth/diameter ratios for fresh, large craters on Venus may be more akin to those on the Moon, Mercury, and Mars than to those on Earth. The reasons for this are presently unclear.

Lobate features partly surrounding a crater with a strong backscatter emanate from 43% of the impact sites on Venus. The flow-like features (outflows) extend tens or hundreds of kilometers from their crater rims and have a morphology consistent with a low-viscosity material. There is strong evidence that the outflows are composed primarily of impact melt, although the mechanism of their emplacement is not clearly understood. High temperatures and pressures of target rocks on Venus allow more melt to be produced than on the cooler terrestrial planets, because lower shock pressures are required for melting [21]. In addition, Venus' high atmospheric temperature may allow the melt to remain molten longer by about an order of magnitude than on the cooler planets [22]. The percentage of impact craters with outflows increases with increasing crater diameter. However, three of the largest craters, Mead, Kelenova, and Meitner, have no recognized outflows. Outflow occurrence is also correlative with impact incidence angle and the degree of asymmetry in the ejecta. Of craters with asymmetric ejecta, those with outflows are more numerous than those without above about 15 km in diameter. Forty-eight percent of asymmetric-ejecta craters have outflows, compared with only 34% of those with symmetric ejecta.

"Splotches" or "shadows" (features with low-backscatter centers surrounded by higher backscatter) are common on the surface of Venus. They range in diameter from 10 to 70 km with a mean of about 20 km. A variety of arguments suggest that if the splotches were produced by stony asteroidal objects traveling about 10 km/s, the bolides would have been several hundred meters in diameter with energies of order 10^{18-19}j (10^{25-26} ergs or roughly 100 megatons). A small fraction of the bolides that would have produced 2–10-km craters on an airless Venus (but were filtered in the atmosphere) are thought to have produced the observed splotches. Bolides <100 m in diameter are not thought to affect the surface.

Heavily fractured craters and lava-embayed craters are found to have higher than average densities along the major fracture belts and rifted uplands connecting Aphrodite Terra and Atla, Beta, Themis, and Phoebe Regiones [23], thus providing physical evidence for recent (or ongoing) low-level volcanic and tectonic activity in these regions.

References: [1] Schaber G. G. et al. (1992) *LPSC XXIII*, 1213–1214. [2] Schaber G. G. et al., *JGR*, special Magellan issue, in press. [3] Campbell D. B. et al., *JGR*, special Magellan issue, in

press. [4] Phillips R. J. et al. (1992) *LPSC XXIII*, 1065–1066. [5] Phillips R. J. et al., *JGR*, special Magellan issue, in press. [6] Head J. W. et al. (1992) *LPSC XXIII*, 517–518. [7] Head J. W. et al., *JGR*, special Magellan issue, in press. [8] Arkani-Hamed J. and Toksoz N. (1984) *PEPI, 34*, 232–250. [9] Strom R. G. et al. (1992) *LPSC XXIII*, 1379–1380. [10] Arkani-Hamed J. et al., this volume. [11] Arkani-Hamed J. et al., *GRL*, in press. [12] Pike R. J. (1983) *JGR, 88*, 2500–2504. [13] Hartmann W. K. (1982) *Icarus, 17*, 707–713. [14] Pike R. J. (1988) *Mercury* (F. Vilas et al., eds.), 165–273, Univ. of Arizona, Tucson. [15] Melosh H. J. (1989) *Impact Cratering–A Geologic Process*, Oxford, New York, 245 pp. [16] Wood C. A. (1980) *LPSC XI*, 1271–1273. [17] Hartmann W. K. and Kuiper G. P. (1962) *Lunar Planet. Lab., 1*, 51–56, Univ. of Arizona, Tucson. [18] Hartmann W. K. and Wood C. A. (1971) *Moon, 3*, 3–78. [19] Wood C. A. and Head J. W. (1976) *Proc. LSC 7th*, 3629–3651. [20] Pike R. J. and Spudis P. D. (1987) *Earth Moon Planets, 39*, 129–194. [21] Vickery A. M. and Melosh H. J. (1992) *LPSC XXIII*, 1443–1444. [22] Ivanov B. A. et al., *JGR*, special Magellan issue, in press. [23] Schaber G. G. (1982) *GRL, 9*, 499–502.

N93-14370

ATMOSPHERIC EFFECTS ON CRATER GROWTH ON VENUS. Peter H. Schultz, Brown University, Department of Geological Sciences, Box 1846, Providence RI 02912, USA.

Laboratory experiments allow examining the consequences of complex processes operating over a wide range of scales (both temporal and spatial) and frequently reveal effects that are obvious only in hindsight. Even though all processes may not scale directly, isolation of the controlling variables allows assessing first-order effects through analytical approximations. This approach can be illustrated by the systematic sequence of ballistic ejection [1], the response of an atmosphere to a strong energy source [2], the scaling of ejecta thickness [3], and the role of secondary cratering [4]. Here it is proposed that the effects of atmospheric pressure and density on crater growth (hence, scaling) observed in laboratory experiments [5,6] has particular relevance for craters on Venus.

Crater Growth: Both static (ambient) and dynamic (viscous drag) pressure reduce cratering efficiency (displaced mass/impactor mass) for craters produced in particulate target [5]. Target strength (i.e., internal angle of friction, ϕ) is shown to have minimal effect; in fact, similar reduction in cratering efficiency occurs for craters formed in compacted pumice ($\phi \sim 85°$), loose sand ($\phi \sim 33°$), and low-density microspheres ($\phi < 20°$). Rather, it is found that particle size plays the most important role: The smaller the constituent particle sizes, the greater the reduction in cratering efficiency. This result can be interpreted as the effect of aerodynamic drag acting on both individual particles and the ensemble of these particles comprising the ejecta curtain. By using a helium atmosphere (hence low density at high pressure), the role of static pressure can be separated from the role of dynamic pressure as clearly illustrated by the contrasting evolution of the ejecta curtain [7].

The principal effect of internal angle of friction is in the preservation of the transient crater. Craters in fine sand and microspheres with low internal cohesion collapse, whereas craters in compacted pumice retain their shape. Nevertheless, crater growth and the evolution of the ejecta curtain during growth are essentially the same for the same value of the ratio of drag to gravitational forces. The role of the atmosphere is to choke off crater growth. Since craters first grow downward and then outward [8,9], arresting

crater growth changes the profile of the transient crater. As shown in Fig. 1, increasing atmospheric pressure reduces crater diameter in compacted pumice while maintaining a nearly constant depth. Quarter-space experiments using sand and microspheres clearly reveal the same growth, but the evidence is erased by rim/wall collapse and consequent floor uplift.

Aerodynamic drag affects crater growth at two scales. At broad scales, the ejecta curtain is an extension of the material flow field in the target. The advancing curtain impinges on the atmosphere; or, in the frame of reference of the curtain, the atmosphere impinges on the curtain [7,10]. The force exerted on the curtain in a unit area changes with time because the velocity of the curtain (and its constituent ejecta), as well as the mass behind this unit area, changes with time. At small scales, the redirected air flow created in front of

SCALED ATMOSPHERIC PRESSURE (δ_0, r_0)
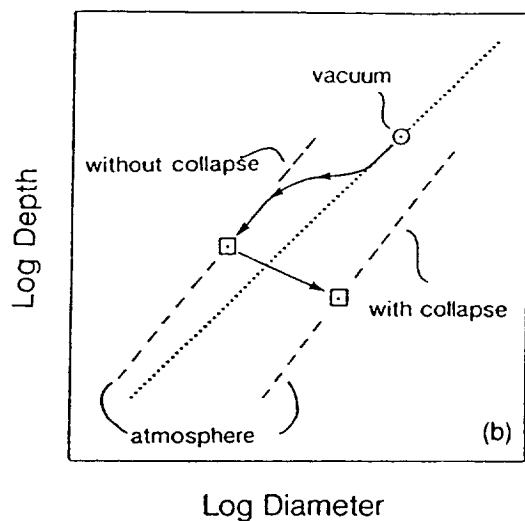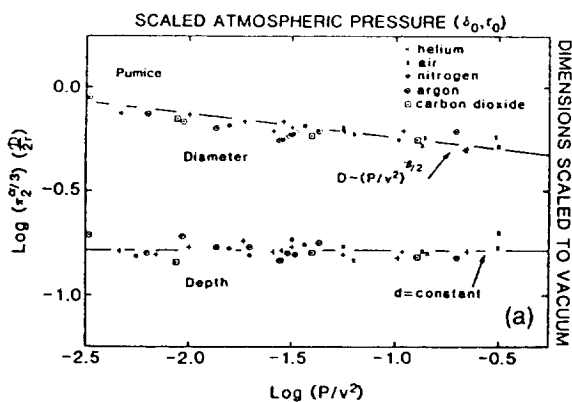
Fig. 1. (a) Effect of atmospheric pressure P on crater diameter and depth scaled to impactor diameter 2r for impacts into compacted pumice. Atmospheric pressure is expressed as a dimensionless ratio involving target density times specific energy of impactor. For a given value of π_2 (the gravity scaling parameter), impact velocity is constant; hence, this plot principally shows the effect of atmospheric pressure. As atmospheric pressure increases, crater growth is stopped prematurely. The identical process is observed for impacts into sand and microspheres with very low strengths, but the craters are unstable and collapse. (b) Schematic represenation of atmospheric effects on crater depth and diameter for craters without rim/wall collapse (compacted pumice) and with collapse (sand). Dotted line represents constant ratio of diameter to depth for vacuum conditions. If the atmosphere affects crater growth (hence scaling) on Venus, it may be revealed in the observed relation between diameter and depth.

the inclined curtain induces aerodynamic drag on individual ejecta. These two effects of drag are expressed by steepening angles of the ejecta curtain before the crater has finished forming and nonballistic ejecta emplacement after formation [7].

Application to Venus: The laboratory results cannot be directly applied to Venus without assessing both the role of the disturbed atmosphere surrounding the impact and the velocity of crater growth. First, the time required for atmospheric density to recover from a strong shock is long compared to the time for crater growth [11]. The evolution of the impact-coupled shock is commonly assumed to resemble a stationary point source [e.g., 12], but laboratory experiments and surface features on Venus indicate that the early-time shock develops from a moving hypervelocity source; consequently, the effects on the atmosphere are displaced downrange, largely decoupled from later-stage crater excavation [13] since most impacts are oblique (i.e., impact angles less than 60°). Interference between the downrange-centered fireball and late-stage ejecta emplacement is clearly recorded around craters on Venus [13]. Second, supersonic advance of the ejecta curtain (and its ejecta) occurs for only a small fraction of crater growth at laboratory scales, yet creates a distinctive turbulent kink in the plume due to shear drag [14]. At the scale of craters on Venus, the advancing ejecta curtain represents a significant fraction of crater growth, but scaling of ejection velocities reveal that even for a 60-km-diameter crater, about 80% of the ejected mass occurs at subsonic velocities [14].

Because passage of the shock wave and shock comminution in the target precedes development of the cratering flow field, it is assumed that the late-stage ejection process is basically the same whether in a vacuum or under the dense atmosphere of Venus. With this assumption, gravity should ultimately limit growth when the ejection velocity falls below a critical value, φ_g, necessary for escaping the cavity. If only static pressure limits growth, then the effects will resemble a strength term [5]. But dynamic pressure acting on the ejecta curtain can also limit growth, since the flow field (including its extension forming the base of the ejecta curtain) is essentially incompressible and hydrostatic. Hence, scaling will be controlled by drag force, d, which replaces gravity g [5]. If drag forces reduce the outward advance of the ejecta curtain (tied to crater growth) to a value below φ_g, then completion of the transient cavity occurs at an earlier stage of growth just as observed in laboratory experiments. In such experiments, the ratio of d/g was found to be the controlling parameter because the ejecta curtain is relatively thin. An alternative approach considers the advancing curtain analogous to a vertical plate [5,7,10]. Deceleration of such a plate of thickness w and unit area A_c from a velocity v_0 to v is simply expressed as

$$\ln v/v_0 = -1/2 \, C_D \, \rho A_c L/M_c \qquad (1a)$$

$$= -1/2 \, C_D \, (\rho/\delta_c) \, (L/w) \qquad (1b)$$

where C_D is the drag coefficient (=2 for a flat plate), ρ is atmospheric density, L is the distance over which the force acts, and M_c is the mass of curtain. Because the curtain width per unit area will map on the surface as ejecta thickness per unit area, w can be given by ejecta thickness t_c at a given scaled range from the crater had it formed in a vacuum. For purposes of illustration, values typical for laboratory impact craters (L ~ 15 cm, t_c ~ 0.05 cm, $\rho = 1.3 \times 10^{-3}$, and $\delta_c = 1.5$) result in a velocity of reduction of 0.77. Since gravity-limited growth varies as $R_v^{1/2}$ [15], this is equivalent to a crater only 0.60 as large, comparable to observations [5]. For a 40-km-diameter Venus,

the same equation predicts arresting crater growth when it had advanced to only about 68% of its size in a vacuum (with the added assumption that the length scale, L, over which the forces act begin after the crater has grown to 50% of its final size). It is important to recognize that equation (1) predicts that atmospheric deceleration on the curtain increases with increasing crater size because $L \sim R_v$ and $t_e \sim R_v^{1/2}$; consequently, $\ln (v/v_0) \sim R_v^{1/2}$.

Tests: Several observations are consistent with the inferences drawn from the laboratory experiments and the simple analogy. First, nonballistic ejecta emplacement near the rim reflects deceleration and collapse of the ejecta curtain. Craters 70 km in diameter on Venus exhibit this transition within 0.25 crater radii of the rim. Second, as atmospheric effects become extreme, the combined roles of rim/wall collapse and decreased ejecta run-out should result in increasing collapse of the uplifted rim and inner ejecta facies with increasing size. Third, diameter-to-depth relations for complex craters on Venus should parallel simple craters on other planets (Fig. 1).

References: [1] Gault D. E. et al. (1968) In *Shock and Metamorphism of Natural Materials* (B. M. French et al., eds.), 87–100, Mono, Baltimore. [2] Schultz P. H. and Gault D. E. (1990) In *GSA Spec. Pap. 247* (V. Sharpton and P. Ward, eds.), 239–261. [3] McGetchin T. R. et al. (1973) *EPSL, 20,* 226–236. [4] Oberbeck V. R. et al. (1975) *Moon, 12,* 19–54. [5] Schultz P. H. (1992) *JGR, 97,* 975–1006. [6] Schultz P. H. (1990) *LPSC XXI,* 1097–1098. [7] Schultz P. H. (1992) *JGR,* in press. [8] Orphal D. et al. (1980) *Proc. LPSC 11th,* 2309–2323.

N93-14371

EFFECT OF IMPACT ANGLE ON CENTRAL-PEAK/PEAK-RING FORMATION AND CRATER COLLAPSE ON VENUS.
Peter H. Schultz, Brown University, Department of Geological Sciences, Providence, RI 02912, USA.

Although asymmetry in ejecta patterns and crater shape-in-plan are commonly cited as diagnostic features of impact angle [1,2], the early-time transfer of energy from impactor to target also creates distinctive asymmetries in crater profile with the greatest depth uprange [1]. In order to simulate gravity-controlled crater growth, laboratory experiments use loose particulate targets as analogs for low-strength material properties following passage of the shock. As a result, impact crater diameter D in laboratory experiments generally is many times greater than the impactor diameter 2r (factor of 40), and early-time asymmetries in energy transfer from oblique impacts are consumed by subsequent symmetrical crater growth, except at the lowest angles (<2.5°). Such asymmetry is evident for oblique (<60° from horizontal) impacts into aluminum where D/2r is only 2 to 4. Because cratering efficiency decreases with increasing crater size [3,4] and decreasing impact angle [1], large-scale planetary craters (40–80 km) should have transient excavation diameters only 6–10 times larger than the impactor [5]. At basin scales, D/2r is predicted to be only 3–5, i.e., approaching values for impacts into aluminum in laboratory experiments. As a result, evidence for early-time asymmetry in impactor energy transfer should become evident on planetary surfaces, yet craters generally retain a circular outline for all but the lowest impact angles.

Evidence for energy-transfer effects in fact occurs on the Moon and Mercury but depends on scale. For simple craters (Messier, Toricelli), crater depth is greatest uprange with a steep uprange and shallow downrange wall slope. For complex craters (Buys-Ballot, Tycho, King), the central peak is offset uprange (corresponding to the greatest depth) but the wall exhibits greater failure uprange

(corresponding to higher slope). Moreover, the central peak in King Crater is breached downrange. For two-ringed basins (Bach on Mercury), the interior ring is breached downrange with evidence for greater rim/wall failure uprange, observations also consistent with the oblong Crisium Basin on the Moon [6]. The cratering record on Venus allows extending such observations where D/2r should be further reduced because of the greater gravity and perhaps effects of the atmosphere [7].

Craters on Venus: Figure 1 illustrates a 42 km-diameter crater with central peak offset uprange, a steep (narrow) uprange inner wall slope, and a broad but gently sloping downrange wall. Since the radar look direction is nearly transverse to impact direction, the observed asymmetry reflects the impact process and not imaging perspective. Figure 2a illustrates a similar uprange offset of a central peak ring and a similar contrast in the uprange/downrange wall. Figure 2b, however, reveals a reversal in this pattern for a larger crater: a downrange offset of the inner ring. It is proposed that this reversal reflects more extensive rim/wall failure as crater depth and uprange slope exceeds a critical value. This proposal is consistent with the concentric scarps within the crater, transform faults crossing the peak ring, and step faulting beyond the rim. The examples in Figs. 1 and 2 are typical for Venus. Exceptions occur only where topography also plays a role or where the impactor was clearly multiple.

If the central massifs (peaks and peak rings) reflect the region of maximum depth, then the size of this disruption may reflect the size of the impactor [7,8]. As a test, crater diameter referenced to peak-ring diameter should increase with decreasing impact angle (judged from the missing sector uprange and the overall degree of ejecta asymmetry) as cratering efficiency decreases. If peak-ring diameter reflects a response to impactor kinetic energy or potential energy (depth), then this ratio should decrease with decreasing impact angle. As shown in Fig. 3, peaking diameter comprises a greater fraction of crater diameter as impact angle decreases; consequently, it is suggested that peak rings indeed may provide markers of impactor size. This marker most likely reflects a limiting (but common) value of peak stress created during penetration [8].

Fig. 1. Crater (42 km in diameter) with central peak offset uprange and exhibiting contrast between steep, narrow and shallow, broad downrange wall. Arrows indicate crater rim. C1-15 S009. Radar look direction from the left; arrow indicates impact direction.

Fig. 2. (a) Crater (50 km diameter) exhibiting a partial central peak ring offset uprange (from lower right) C1-60N 263. Radar look direction is from upper left. (b) Larger crater (103 km diameter) exhibiting central peak ring offset downrange from present rim, opposite to occurrence in (a) and Fig. 1. Reversal in position is related to enhanced rim/wall collapse uprange that widens and circularizes the crater around the deepest portion of the transient crater cavity, which occurs uprange. Further crater widening follows pre-existing structural grain. C1-30N 135.

Fig. 3. Effect of impact angle (from horizontal) on the transverse diameter of the central peak ring d_{cp} referenced to crater diameter. As impact angle decreases (based on degree of ejecta symmetry), size of central peak ring becomes larger relative to crater diameter. Such a trend is expected if central peak ring reflects the size of impactor and cratering efficiency decreases impact angle.

The enhanced uprange rim/wall collapse illustrated in Fig. 2b (and numerous other large oblique impacts on Venus) provides insight for why most craters exhibit a circular outline even though early-time energy transfer comprises a larger fraction of crater growth. Failure of the uprange rim/wall in response to the oversteepened wall and greater floor depth circularizes crater outlines. The rectilinear and conjugate scarp on the pattern uprange rim, however, indicates failure along preimpact stresses. Hence, a corollary is that peak shock levels and particle motion may be reduced uprange during oblique impacts due to the downrange motion of the impactor, analogous to time dilation.

References: [1] Gault D. E. and Wedekind J. A. (1978) *Proc. LPSC 9th*, 3843–3875. [2] Moore H. J. (1979) *U.S. Geol. Surv. Prof. Pap. 812–13*, 47 pp. [3] Gault D. E. and Wedekind J. A. (1977) In *Impact and Explosion Cratering* (D. Roddy et al., eds.), 1231–1244, Pergamon, New York. [4] Holsapple K. A. and Schmidt R. M. (1987) *JGR, 92*, 6350–6376. [5] Schultz P. H. and Gault D. E. (1991) *Meteoritics, 26*. [6] Wichman R. W. and Schultz P. H. (1992) *LPSC XXIII*, 1521–1522. [7] Schultz P. H. (1988) In *Mercury* (F. Vilas et al., eds.), 274–335, Univ. of Arizona, Tucson. [8] Schultz P. H. (1992) *JGR*, in press.

N93-14372

IMPACT-GENERATED WINDS ON VENUS: CAUSES AND EFFECTS.   Peter H. Schultz, Brown University, Department of Geological Sciences, Box 1846, Providence RI 02912, USA.

The pressure of the dense atmosphere of Venus significantly changes the appearance of ejecta deposits relative to craters on the Moon and Mercury. Conversely, specific styles and sequences of ejecta emplacement can be inferred to represent different intensities of atmospheric response winds acting over different timescales. Three characteristic timescales can be inferred from the geologic record: surface scouring and impactor-controlled (angle and direction) initiation of the long fluidized run-out flows; nonballistic emplacement of inner, radar-bright ejecta facies and radar-dark outer facies; and very late reworking of surface materials. These three timescales roughly correspond to processes observed in laboratory experiments that can be scaled to conditions on Venus (with appropriate assumptions): coupling between the atmosphere and earlytime vapor/melt (target and impactor) that produces an intense shock that subsequently evolves into blast/response winds; less energetic dynamic response of the atmosphere to the outward-moving ballistic ejecta curtain that generates nonthermal turbulent eddies; and late recovery of the atmosphere to impact-generated thermal and pressure gradients expressed as low-energy but long-lived winds. These different timescales and processes can be viewed as the atmosphere equivalent of shock melting, material motion, and far-field seismic response in the target.

Early Processes (Direct Effects of Blast and Fireball):   Under vacuum conditions, the fate of the impactor is generally lost; even on the Earth, most impact melt sheets exhibit little trace of the impactor. The dense atmosphere of Venus, however, prevents escape of the impactor through rapid deceleration of ricochet debris and containment of the vapor cloud [1,2]. Figure 1a illustrates the time required for the atmospheric blast front to decelerate to the speed of sound as a function of crater size, where k is the fraction the initial impactor energy (KE_i) coupled to the atmosphere (E_A). On Venus, the shock front dissipates before the crater finishes forming. If the blast is created by deceleration and containment of early high-speed ejecta (downrange jetting and ricochet/vapor), then it will precede ejecta emplacement and should exhibit a source area offset

Fig. 1. (a) Recovery time for atmospheric blast to reduce to the speed of sound on Venus scaled to crater formation time. The value of k represents the fraction of initial impactor kinetic energy (KE_i) coupled to the atmosphere (E_A). On Venus the blast effects should precede crater formation. (b) Recovery time for atmospheric pressure behind the shock front to return to ambient conditions on Venus scaled to crater formation time. Although atmospheric pressure has recovered, high temperatures (the fireball) result in low densitites. Thermal gradients and motion of fireball induce strong recovery winds that rework ejecta at late times.
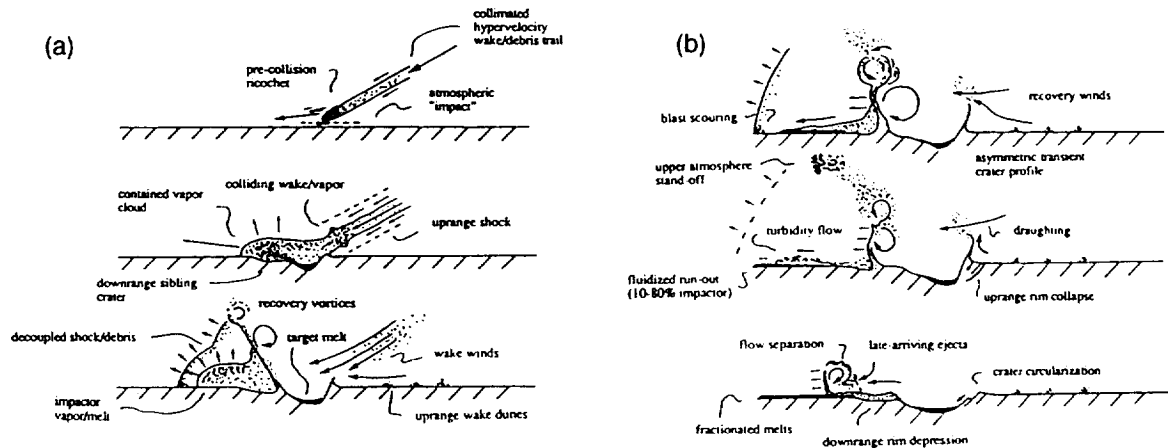
Fig. 2. (a) Scenario for sequence and style of ejecta emplacement at early times based on inferences drawn from laboratory impact phenomena scaled to Venus and surface features revealed by Magellan. At early times, kinetic energy and momentum in the vapor cloud evolves into a downrange-moving fireball that creates strong winds downrange. (b) Scenario for late processes. Winds and turbulence created by the outward-moving ejecta curtain entrain coarse fractions to produce an avalanchelike flow of coarse inner ejecta deposits. Such deposits persist as radar-bright ejecta deposits because of the roughness and low ambient surface winds. Finer fractions entrained in sustained turbulence result in turbidity flows with potentially much greater run-out distances. Deposits from these flows will be more suceptible to subsequent erosion.

downrange from the crater [2,3]. The downrange offset of the center of origin of the shock is observed in laboratory impact experiments. Features consistent with this interpretation can also be found around venusian craters and include [2] topographic barriers shadowing surface disruption from the blast; radar-dark/-bright striations converging on the downrange rim rather than the crater; and diffuse haloes at the base of small hills again focusing on a downrange rim "source" (shock-dislodged debris drawn back into the rarefied, rising fireball). Mo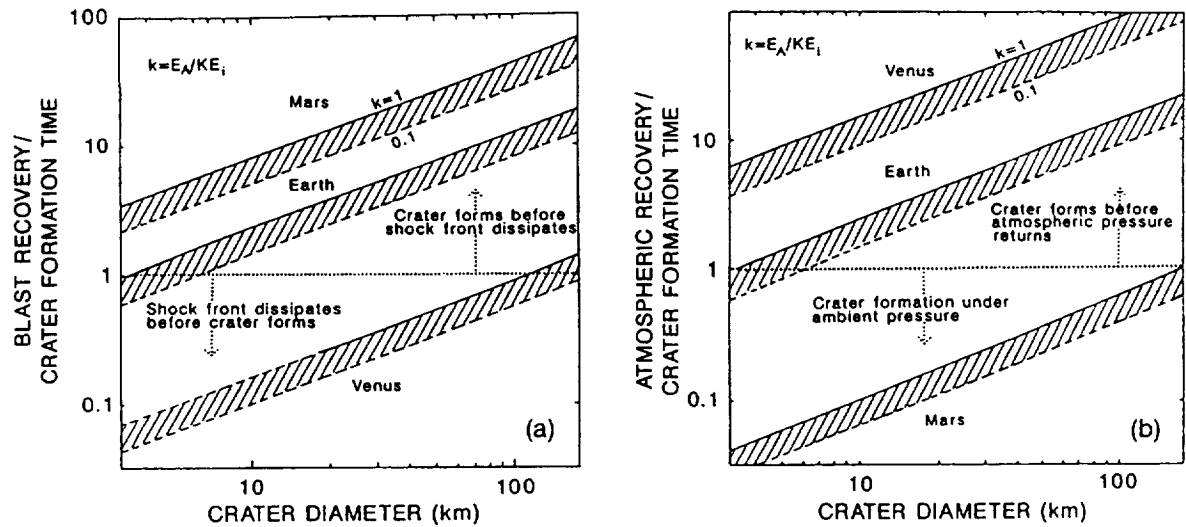reover, radar-dark parabola patterns commonly center on a point downrange and not the crater [2]. In contrast, the time for recovery of the atmosphere to ambient pressure (or density and temperature) is much longer than the time for crater formation

(Fig. 1b). If all craters were formed by vertical impacts, this would mean that the craters form within a fireball or behind the wake characterized by low density (high temperature, low pressure) as postulated in [4]. But most craters are formed by oblique impacts (i.e., 75% formed at angles of 60° or less). Consequently, the early fireball moves away from crater excavation initially at hypervelocities. At low impact angles (<30°), the energy coupled to the atmosphere resembles a rolling fireball containing vapor and dispersed melt moving downrange until decelerated. Because the vapor/melt is higher in density than conditions in the fireball, it collapses within the fireball to form long run-out density flows controlled by local topography, well in advance of ejecta emplace-

ment as observed on Venus [5,6]. Such a process accounts for the long run-out flows consistently originating downrange in oblique impacts (i.e., opposite the missing ejecta sector) even if uphill from the crater rim. Atmospheric turbulence and recovery winds decoupled from the gradient-controlled basal run-out flow continues downrange and produces wind streaks in the lee of topographic highs. Turbulence accompanying the basal density flows may also produce wind streak patterns. Uprange the atmosphere is drawn in behind the fireball (and enhanced by the impinging impactor wake), resulting in strong winds that will last at least as long as the time for crater formation (i.e., minutes). Such winds can entrain and saltate surface materials as observed in laboratory experiments [2,3] and inferred from large transverse dunes uprange on Venus [2].

Atmospheric Effects on Ballistic Ejecta: Even on Venus, target debris will be ballistically ejected and form a conical ejecta curtain until its outward advance is decelerated by the atmosphere. The well-defined, radial ejecta delineating the uprange missing ejecta sector of craters formed by oblique impacts demonstrate ballistic control of ejection. As the inclined ejecta curtain advances outward, however, it creates turbulent vortices, which have been observed in the laboratory experiments [2] and modeled theoretically [7]. The ejecta curtain gradually becomes more vertical in response to atmospheric resistance. The atmospheric density is sufficient to decelerate meter-sized ejecta to terminal velocities [8] that will be entrained in and driven by response winds induced by the outward-moving curtain. While larger ejecta are deposited, smaller size fractions become entrained in an outward ejecta flow. Based on diversion of such flows by low-relief barriers near the rims of craters, the transition from ballistic to nonballistic emplacement occurs within about 0.5 crater radii of the rim. This observation underscores the fact that dynamic atmospheric pressure significantly restricts outward advance of the ejecta curtain. The scaled run-out distance (distance from the crater rim scaled to crater diameter, D) of the ejecta flow should decrease on Venus as $D^{-0.5}$, unless consumed by crater rim collapse. Because of the high atmospheric density, collapse of near-rim ejecta into a flow crudely resembles an avalanche comprised of coarse debris and blocks. But high winds and turbulence created by the outward-moving curtain separate during terminal emplacement of the inner flow, thereby winnowing the finer fractions and creating an overrunning turbidity flow that continues outward.

Turbidity flows containing finer fractions can extend to much larger distances until turbulence supporting entrained debris no longer can support the load. Because turbulent wind velocities greatly exceed ambient surface winds, such vortices are also capable of mobilizing surface materials. It is suggested that the radar-dark lobes extending beyond the inner radar-bright ejecta [2,6] reflect this process. In addition, many craters are surrounded by a very diffuse boundary that masks low-relief ridges and fractures; this boundary may indicate the limits of a third stage of flow separation and deposition. The observed radar-dark signature requires such ejecta to be less than a few centimeters. In contrast with the coarse, radar-bright inner facies, the outer radar-dark facies will be more susceptible to later erosion by ambient or other impact-generated winds because the size fractions were sorted by a similar process. This is consistent with observed removal or reworking of craters believed to be old, based on superposed tectonic features.

Late Recovery Winds (Secondary Effects of Atmospheric Turbulence): On planets without atmospheres, the effects of early, high-speed ejecta and impactor are typically lost. On Venus, however, the dense atmosphere not only contains this energy fraction, but the long recovery time of the atmosphere (Fig. 1b)

results in late-stage reworking, if not self-destruction, of ejecta facies emplaced earlier. Surface expression should include bedforms (e.g., meter-scale dunes and decicentimeter-scale ripples) reflecting eddies created in the boundary layer at the surface. Because radar imaging indicates small-scale surface roughness (as well as resolved surface features), regions affected by such long-lived low-energy processes can extend to enormous distances. Such areas are not directly related to ejecta emplacement but reflect the atmospheric equivalent to distant seismic waves in the target. Late-stage atmospheric processes also include interactions with upper-level winds. Deflection of the winds around the advancing/expanding fireball creates a parabolic-shaped interface aloft. This is preserved in the fall-out of finer debris for impacts directed into the winds aloft (from the west) but self-destructs if the impact is directed with the wind. Exception to this rule occurs for larger crater (>60 km) sufficient to interrupt the flow pattern not only by the fireball but also by the ejecta curtain.

References: [1] Schultz P. H. and Gault D. E. (1990) In *GSA Spec. Pap. 247* (V. L. Sharpton and P. D. Ward, eds.), 239–261. [2] Schultz P. H. (1992) *JGR*, in press. [3] Schultz P. H. (1992) *JGR*, in press. [4] Ivanov B. A. et al. (1986) *Proc. LPSC 16th*, in *JGR*, 91, D413–D430. [5] Schultz P. H. (1991) *Eos*, 73, 288. [6] Phillips R. J. et al. (1991) *Science*, 252, 288–296. [7] Barnouin O. and Schultz P. H. (1992) *LPSC XXIII*, 65–66. [8] Schultz P. H. and Gault D. E. (1979) *JGR*, 84, 7669–7687. [9] Schultz P. H. et al. (1981) In *Multi-Ring Basins, Proc. LPS 12A* (P. H. Schultz et al., eds.), 181–195, Pergamon, New York. [10] Barnouin O. and Schultz P. H. (1992) *LPSC XXIII*, 65–66. [11] Schultz P. H., this volume. [12] Jones E. M. and Sanford M. T. II (1982) In *GSA Spec. Pap. 190* (L. Silver and P. Schultz, eds.), 175–186. [13] Schultz P. H. (1992) *JGR*, in press. [14] Schultz P. H. and Gault D. E. (1982) In *GSA Spec. Pap. 190* (L. Silver and P. Schultz, eds.), 153–174. [15] Post R. L. (1974) *AFWL–TR–74–51*.

N93-14373

MAGELLAN PROJECT PROGRESS REPORT. J. F. Scott, D. G. Griffith, J. M. Gunn, R. G. Piereson, J. M. Stewart, A. M. Tavormina, and T. W. Thompson, Jet Propulsion Laboratory, California Institute of Technology, Pasadena CA 91109, USA.

The Magellan spacecraft was placed into orbit around Venus on August 10, 1990 and started radar data acquisition on September 15, 1990. Since then, Magellan has completed mapping over 2.75 rotations of the planet (as of mid-July 1992). Synthetic aperture radar (SAR), altimetry, and radiometry observations have covered 84% of the surface during the first mission cycle from mid-September 1990 through mid-May 1991.

Operations in the second mission cycle from mid-May 1991 through mid-January 1992 emphasized filling the larger gaps (the south polar region and a superior conjunction) from that first cycle. An Orbit Trim Maneuver (OTM) was performed at the beginning of cycle 2 in order to interleave altimeter footprints at periapsis. This yielded better altimetric sampling of the equatorial regions of Venus. Some 94% of the planet was mapped at the end of mission cycle 2.

Observations in the third mission cycle from mid-January to mid-September 1992 emphasized reimaging of areas covered in cycle 1 and cycle 2 such that digital stereo and digital terrain data products can be produced. A transponder anomaly in January 1992 (just before mission cycle 3 started) forced the project to use a radar data downlink of 115 Kbs instead of 268 Kbs. Although data acquisition is curtailed, some 30–40% of the planet will be mapped
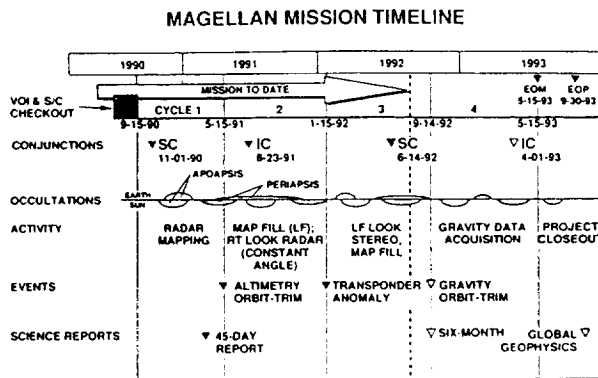
MAGELLAN MISSION TIMELINE

Fig. 1.

in cycle 3. Some 98% of the planet will be mapped at the end of mission cycle 3.

Planned observations in the fourth mission cycle from mid-September 1992 through mid-May 1993 will emphasize high-resolution gravity observations of the equatorial regions of Venus. A second Orbit Trim Maneuver (OTM) at the beginning of this mission cycle will lower periapsis to below 200 km to improve the gravity resolution. Magellan, with its large antenna and X-band radio system, will also improve upon the venusian gravity maps obtained from the Pioneer-Venus spacecraft. These new gravity observations when coupled with superb radar images will provide valuable insights to the interior processes occurring on Venus.

Scientific reports for the project include the "45 Day Report," which was published as a single issue of *Science* in March 1991. A "6-Month Report" will also be published as a special issue of the *Journal of Geophysical Research (JGR) Planets* in the summer of 1992. A "Geophysics Report" on the 360° of gravity observation in cycle 4 will be one or more scientific articles submitted for publication in the summer or fall of 1993.

Magellan data products, the SAR images, altimetry data and radiometry data, are available as analog photographs and digital compact disks (CD-ROMs) at the National Space Science Data Center (NSSDC) at the NASA Goddard Space Flight Center (GSFC) in Greenbelt, Maryland. As of May 1, 1992, over 500 radar mosaics, as well as the altimetry and radiometry data for the first mission cycle, are available. In addition, some 250 photographs have been released and are available to the public. The altimetry and radiometry data for cycle 1 produced by the Massachusetts Institute of Technology (MIT), as well as the cartographic products produced by the U.S. Geological Survey (USGS), are being released to the science community.

N93-14374

ATLA REGIO, VENUS: GEOLOGY AND ORIGIN OF A MAJOR EQUATORIAL VOLCANIC RISE. D. A. Senske and J. W. Head, Department of Geological Sciences, Box 1846, Brown University, Providence RI 02912, USA.

Introduction: Regional volcanic rises form a major part of the highlands in the equatorial region of Venus. These broad domical uplands, 1000 to 3000 km across, contain centers of volcanism forming large edifices, and are associated with extension and rifting. Two classes of rises are observed: (1) those that are dominated by tectonism, acting as major centers for converging rifts such as Beta Regio and Atla Regio, and are termed tectonic junctions [1]; and (2) those forming uplands characterized primarily by large-

scale volcanism forming edifices, Western Eistla Regio and Bell Regio, where zones of extension and rifting are less developed. Within this second class of features the edifices are typically found at the end of a single rift, or are associated with a linear belt of deformation [1,2]. In this paper, we examine the geologic characteristics of the tectonic junction at Atla Regio, concentrating on documenting the styles of volcanism and assessing mechanisms for the formation of regional topography.

Topographic and Geologic Characteristics of Atla Regio: Atla Regio is a 1000-km × 1000-km highland centered near 4°N, 200° and is a broad rise reaching an elevation of 3.0 km (all elevations are referenced to a planetary radius of 6051.0 km) (Fig. 1). The relationship between chasmata (rifts) and volcanic features forms a pattern similar to that observed at Beta Regio, distinguishing Atla as a major tectonic junction [3,4,5]. In addition, Pioneer Venus gravity data show this highland to have a substantial gravity anomaly, centered at Ozza Mons, along with a corresponding large apparent depth of isostatic compensation (>200 km) [6,7]. Interpretations from these data suggest that like Beta Regio, Atla Regio is most likely a site of mantle upwelling.

Magellan altimetry data provide the first detailed coverage of the topography of Atla Regio (Fig. 1). The regional rise has gentle slopes (0.1° to 0.2°), reaching its highest point at Ozza Mons, a 7.5-km-high peak. In plan view the central part of the highland is triangular shaped with its apex pointing to the north where it intersects the north-south-trending rift valley Ganis Chasma. The legs of the triangle correspond to Dali Chasma (southwest/northeast orientation) and Parga Chasma (southeast/northwest orientation). The more distal parts of all three rifts curve, are aligned along a more east-west orientation, and form a "pinwheel" pattern centered on Ozza Mons. At a point just to the south of where Dali Chasma intersects Ozza Mons a second volcano, Maat Mons, is located on the western edge of the rift and rises to an elevation of 9.2 km. To the northwest of central Atla is a second gentle topographic rise (elevation of 2.0 km) on which is located Sapas Mons, a 4.0-km-high volcano that has a substantial gravity anomaly (+25 mgal at a spacecraft altitude of 200 km) (8). The presence of broad domical topography, the large gravity anomaly, and the presence of large-scale volcanism suggests that Sapas is the site of second thermal anomaly.

Regional Geology of Atla Regio: In order to understand the relationships between regional tectonism and volcanism, we examine the geology of the central part of the Atla, concentrating on Ozza Mons and Maat Mons. Geologic mapping of this area (Fig. 2) shows it to contain five general units, the most abundant of which are radar-dark plains. Plains to the northwest of Ozza Mons contain pervasive sinuous ridges (spacing of 10 to 25 km) with a general orientation of N 30°E, parallel to the trend of Ganis Chasma, and are interpreted to be compressional in origin [5]. These structures may have formed by the relaxation of topography or may represent surface deformation linked to large-scale flow in the mantle [5]. To the north of Ozza Mons the plains are disrupted by faulting and fracturing forming a 150- to 250-km-wide rift, Ganis Chasma. Features mapped as edifices correspond to the volcanos Sapas Mons, Maat Mons, and Ozza Montes. An additional volcanic center with a corresponding large gravity anomaly (+35 mgal) is located on the southwest edge of Ganis Chasma (15°N, 195°). This region is located along a chain of gravity highs stretching the length of Ganis Chasma. Lava flows from the volcanic center lie on the edge of the rift, being deposited to the southwest, apparently down the rift flanks and do not appear to contribute to any rift infilling. A number of isolated regions of
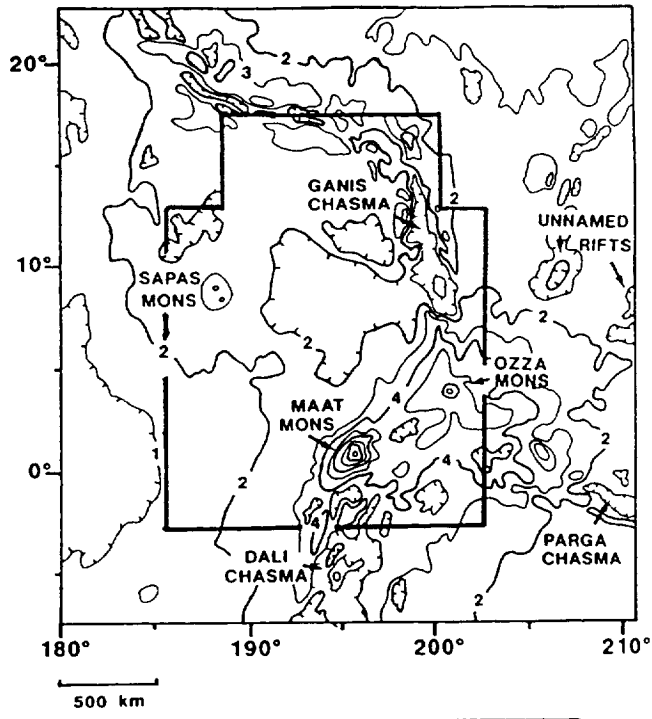
Fig. 1.   Magellan topography of Atla Regio contoured at 1.0-km intervals and referenced to a planetary radius of 6051.0 km. The rifts Dali Chasma, Ganis Chasma, Parga Chasma, and two unnamed rifts trending to the northeast are topographically distinct depressions reaching depths of up to 3.0 km. The two highest features, Maat Mons and Ozza Mons, reach elevations of 9.2 km and 7.5 km respectively. The area outlined by the solid line corresponds to the region shown in Fig. 2.
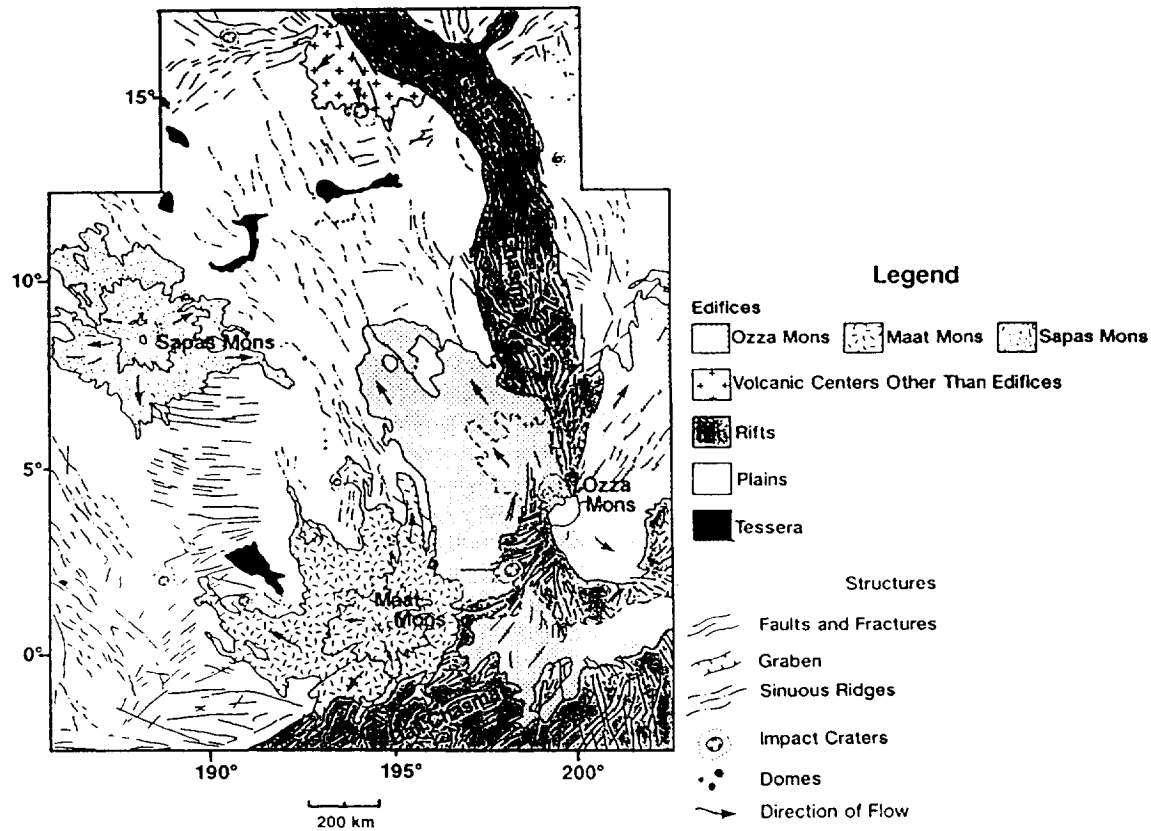
Fig. 2.   Sketch map of the central part of Atla Regio. Ozza Mons is located at the point where Ganis Chasma, Dali Chasma, and Parga Chasma converge, while Maat Mons is located astride the western flank of Dali Chasma.

highly deformed terrain are mapped as tesserae. Unlike Beta Regio, tesserae does not appear to be a major unit Atla [9].

Ozza Mons forms the central part of Atla and is located at the point where Ganis, Dali, and Parga Chasma intersect. The relationship between Ganis Chasma and Ozza Mons is examined along with the general stratigraphic relationships between assemblages of volcanic units. The rift valley, Ganis Chasma, is unique in that it is relatively devoid of infilling from volcanism and sedimentary material. The exception to this trend is evident where it merges with the volcano. At the point where the rift intersects Ozza it narrows from a width of 225 km to 125 km and deformation is confined to a trough on the flank of the volcano. The primary area of disruption is a zone of scarps associated with normal faulting that is offset from the main trend of the rift, changing orientation from a strike that is just west of north to one that is just east of north. Additional scarps with a relatively uniform spacing of 5 km are arrayed with a northeast/southwest orientation on the eastern flank of the edifice and are associated with an unnamed rift aligned to the northeast. The Ganis rift terminates at the summit of Ozza, a radar-dark oval plateau (100 km × 60 km) that rises to an elevation of 1.5 km above its surroundings and contains numerous pits and collapse structures (diameters of 0.5 to 7.0 km). To the north of the summit, just below the plateau, lies a dome field (domes 10 km in diameter) covering an area 80 km × 100 km. Deposits along the eastern edge of the dome field are superposed on faults and fractures from Ganis Chasma, indicating that at this location volcanism postdates faulting and contributes to partial infilling of the rift. Further to the north, where the rift narrows, other lava flows both superpose and are cross cut by faults, indicating that rifting and the deposition of volcanics occurred concurrently.

Four major classes of volcanic deposits are identified on Ozza Mons; the first two are made up of the radar-dark material on the summit and the adjacent dome field. The others correspond to flow units mapped on the distal parts of the volcano, bright flows and mottled bright flows. Bright flows have a relatively uniform texture, with no apparent source regions for the deposits observed. In many places the unit is cut by faults and fractures, deformation associated with rifting. In comparison, it is possible to identify numerous apparent source regions for mottled bright flows. These originate mainly from vents on the outer flanks of the volcano. Like the bright flow unit it is possible to identify places where the mottled bright flows are cross cut by faulting. The boundaries between the units typically form an embayment relationship, with some of the mottled bright flows being channeled down graben, suggesting that they are stratigraphically the younger of the two units. In general the dome field and the mottled bright flows appear to be most recent units.

Maat Mons: Located 600 km southwest of Ozza Mons and lying on the northwest edge of Dali Chasma is Maat Mons. In plan view, this volcano is elliptically shaped (195 km × 120 km) with its major axis oriented in a northeast/southwest direction. Its summit region differs from that of Ozza Mons in that it contains a 25-km-diameter caldera with additional smaller nested pits and collapse structures (diameters between 1.0 and 5.0 km), indicating multiple episodes of magma emplacement and withdrawal. Unlike Ozza Mons, this volcano is not disrupted by faulting, but instead, along its southeast flank, appears to be filling the rift.

Volcanic deposits mapped on Maat range from bright to mottled dark. The most abundant flows have a bright homogeneous texture, are found on the more distal flanks of the volcano, and are interpreted to be associated with the large-scale effusion of lava. Mottled bright flows have a range of textures on the scale of tens of kilometers and are found mainly in the area where the rift is being

filled in. The central part of Maat contains deposits with mottled dark textures that are arrayed in a pattern radial to the summit. In several locations the dark material has a diffuse boundary, suggesting the presence of a mantling deposit. One example corresponds to a cluster of domes (diameters ranging from 5 to 10 km) located in a 2.0 km deep depression 250 km to the north of the summit (3.2°N, 194.9°) and mapped as a dome field. The terrain associated with this area appears etched and is covered by a dark diffuse deposit, suggesting the possible presence of an air fall deposit associated with pyroclastic activity. In general the boundaries between the different flow units are gradational, making stratigraphic relationships difficult to determine.

Summary and Conclusions: Atla Regio is a complex region of converging rifts and volcanism. The largest (areally extensive) volcanic center corresponds to Ozza Mons and has characteristics similar to Theia Mons in Beta Regio [5]. Stratigraphic relationships at Ozza suggest that both the deposition of volcanics and rifting have occurred concurrently. Maat Mons is broadly similar to volcanos identified in Western Eistla Regio (Sif Mons) and contains a well-defined summit caldera. On the basis of regional stratigraphic relationships and the analysis of geophysical data, Atla is interpreted to be a site in which a mantle plume, centered near Ozza Mons, has uplifted plains causing faulting and rifting and volcanic construction at Ozza Mons and Maat Mons.

In addition to Ozza Mons, Sapas Mons, Ganis Chasma, and the area mapped as a volcanic center (separate from the large volcanos), all have substantial positive gravity anomalies. Sapas is interpreted to be a second site of upwelling adjacent to Atla. On the basis of its large gravity anomaly and a corresponding large apparent depth of compensation (>200 km) [7] the zone of extension and rifting at Ganis is interpreted to be linked to mantle dynamics. This array of surface features separate from those at central Atla (Ozza and Maat) may be associated with multiple upwellings, or possibly a single large plume that has produced smaller instabilities [10].

References: [1] Senske D. A. (1990) *Earth Moon Planets, 50/51,* 305–327. [2] Senske D. A. et al. (1991a) *Earth Moon Planets, 55,* 163–214. [3] Campbell D. B. et al. (1984) *Science, 226,* 167–170. [4] Stofan E. R. et al. (1989) *GSA Bull., 101,* 143–156. [5] Senske D. A. et al. (1992) *JGR, 97.* [6] Sjogren W. L. et al. (1983) *JGR, 88,* 1119–1128. [7] Smrekar S. E. and Phillips R. J. (1991) *EPSL, 107,* 582–597. [8] Sjogren et al. (1983) *JGR, 88,* 1119–1128. [9] Senske D. A. et al. (1991b) *GRL, 18,* 1159–1162. [10] Griffiths R. W. and Campbell I. H. (1991) *JGR, 96,* 18295–18310.

N93-14375

THE GEOLOGIC MAPPING OF VENUS USING C-1 FORMAT: SHEETS 75N254, 60N263. I. V. Shalimov, Lomonosov Moscow University, Moscow, Russia

The results of geologic mapping of Venus, produced on the base of Magellan images, are presented. We submit two C-1 format geologic maps with the appropriate legend.

The mapping territory has been taken from Venera 15 and 16 missions and geologic maps have been composed by Sukhanov et al. [2] and Kotelnicov et al. [1]. Magellan images allow us to divide some types of the plains units to determine the lava flow direction and to map with better accuracy.

C-1 sheets 75N254 and 60N263 are shown in Figs. 1 and 2. The correlation of the mapped units is shown in Fig. 3. We regret the difficult perception without the color legend.

References: [1] Kotelnicov V.A. et al. (1989) *Atlas of Venus,* GUGK, Moscow (in Russian). [2] Sukhanov A.L. et al. (1989) *Atlas*
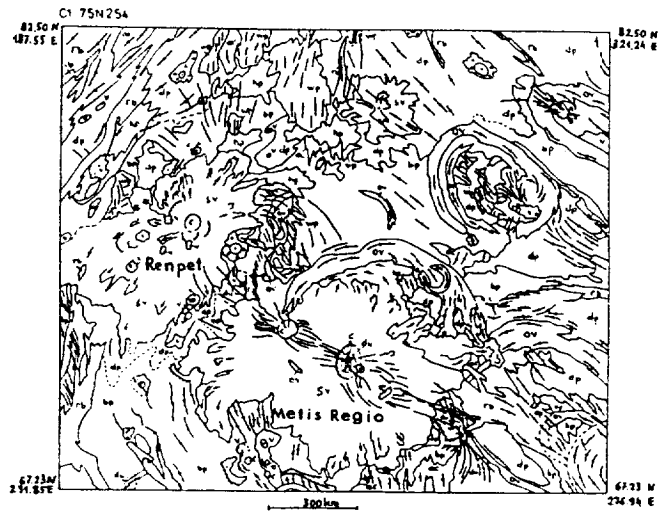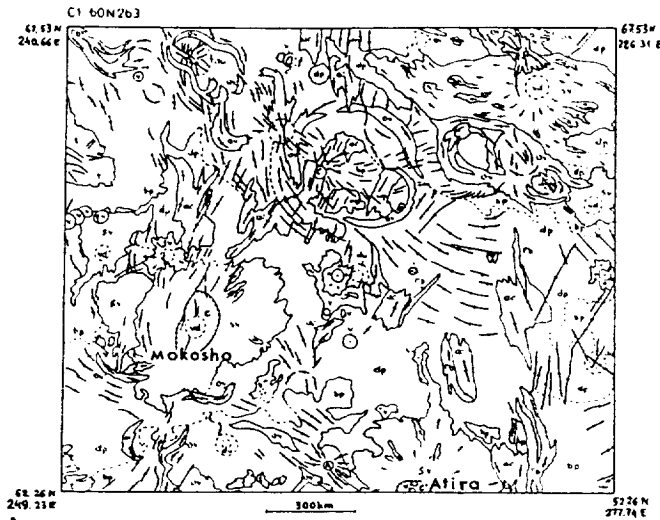
Figs. 1 and 2. 1–Large volcanic shield and gentle slopes covered with overlapping lava flows; 2–central domelike part of some volcanic shields with many small volcanic hills and absence of expressed lava flows; 3–bright, smooth lava plain; possesses numerous lava channels or lava flow fronts; 4–dark lava plain; smooth, or with sharp lava channels; 5–hilly lava plain with clusters of small volcanic hills; 6–wrinkled plain with a net of grabens; 7–area of ridge concentration (one or more interesting systems); 8–ridge belt; 9–undivided tessera; 10–corona; 11–large domelike uplift (beta); 12–volcano and lava flow; 13–caldera; 14–arachnoid; 15–dome (central dark, and outer bright areas are outlined); 16–impact crater and ejecta; 17–ridge; 18–graben and/or fault; 19–scarp; 20–lava flow direction; 21–lava flow boundary and direction.
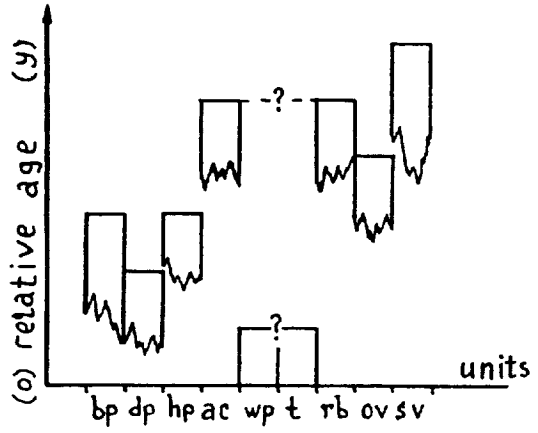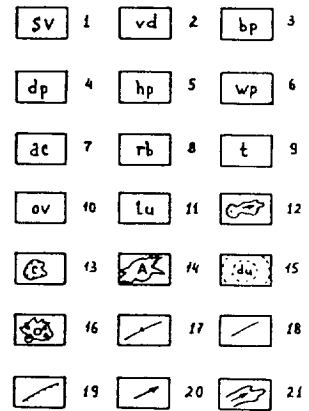
Fig. 3. Correlation of the mapped units shown in Figs. 1 and 2.

of Venus, 1:15,000,000 topographic series, northern hemisphere, V. 15M 90/G. I–2059. U.S. Geol. Surv.

N93-14376

GEOID, TOPOGRAPHY, AND CONVECTION-DRIVEN CRUSTAL DEFORMATION ON VENUS.

Mark Simons, Bradford H. Hager, and Sean C. Solomon, Department of Earth, Atmospheric, and Planetary Sciences, Massachusetts Institute of Technology, Cambridge MA 02139, USA.

Introduction: High-resolution Magellan images and altimetry of Venus reveal a wide range of styles and scales of surface deformation [1] that cannot readily be explained within the classical terrestrial plate tectonic paradigm. The high correlation of long-wavelength topography and gravity and the large apparent depths of compensation suggest that Venus lacks an upper-mantle low-viscosity zone [2–5]. A key difference between Earth and Venus may be the degree of coupling between the convecting mantle and the overlying lithosphere. Mantle flow should then have recognizable signatures in the relationships between surface topography, crustal deformation, and the observed gravity field [6,7].

Model: We explore the effects of this coupling by means of a finite element modeling technique. The crust and mantle in these models are treated as viscous fluids. We solve both the equations of motion and the heat equation at every time step using a modified version of the two-dimensional Cartesian finite-element program ConMan [8]. A passive marker chain tracks the crust-mantle interface and permits variation in the crustal buoyancy as well as specific crustal and mantle rheologies. These rheologies depend on composition, temperature, and stress. In addition to the flow field, the stress field in the lithosphere, the surface topography, and the resulting geoid are readily calculated. The models presented here use an irregular finite-element mesh that is 50 elements high and 160 elements wide. Our maximum resolution is in the 40-km-thick top layer, where each element is 2 km high and 5 km wide. In all, the mesh is 800 km in the horizontal dimension and 400 km in the vertical dimension. We impose free-slip boundary conditions on the top and side walls, with no flow through these walls. Flow at the bottom boundary is constrained to be vertical with no horizontal flow permitted. This last boundary condition gives a virtual 800 km × 800 km box. The surface topography is calculated from the vertical stresses on the top wall of the box. Top and bottom

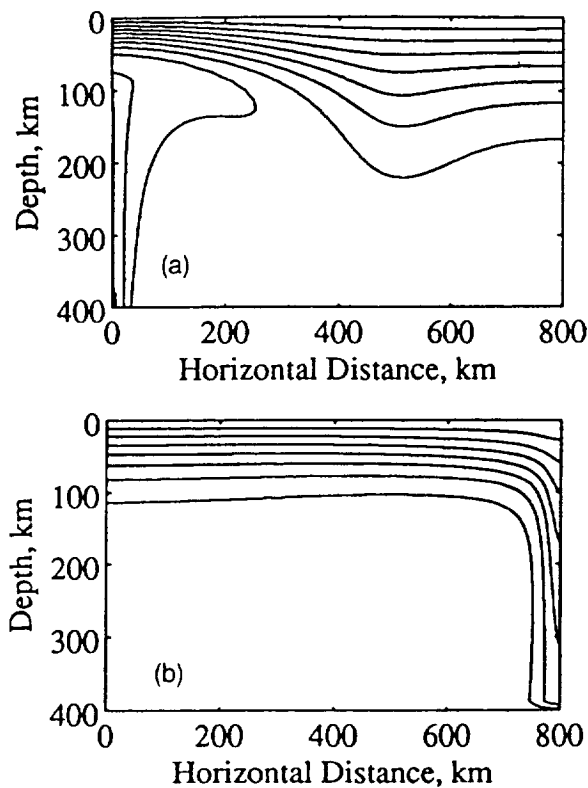**Fig. 1.** Temperature contours at 130 m.y. for the (a) upwelling and (b) downwelling models. Contour interval is 100°C; the top of the box is at 500°C.

temperatures are fixed at 500°C and 1250°C respectively. Initially, we impose a linear temperature gradient across the lithosphere and set the rest of the mantle to be isothermal. We investigate two classes of models. Flow in the first class is initiated with a sinusoidal temperature perturbation throughout the box. This results in mantle flow that is dominated by concentrated downwelling (Fig. 1b). In the second class of models, flow is driven by a hot patch at the side of the box, thereby driving flow by concentrated upwelling (Fig. 1a).

Results: In all our models, convection produces horizontal compressional stresses in lithosphere above downwelling mantle and extensional stresses in lithosphere above upwelling mantle. As the convective vigor increases so does the magnitude of the stress. In models with constant-viscosity mantle overlain by a constant-viscosity crust, stress in the crust reaches values in excess of 100 MPa in less than 100 m.y. We find that the rate of increase in compressive stress decreases with increasing crustal viscosity. This is because the stronger the crust, the more the development of the convective instability in the mantle driving the deformation is impeded. We also find that the magnitude of the peak compressive stress achieved above the downwelling increases with higher viscosities and/or with thinner initial crustal layers; the stronger the crustal lid, the more tractions from mantle convection are supported in the crust. Since force balance on the crust requires that shear traction integrated along the base be balanced by normal tractions integrated through its thickness, the thinner the crust, the larger the horizontal stresses.

Both analytical models [9,10] and our numerical models of convection-induced crustal flow indicate that the amplitude and sign of the topography are highly time and rheology dependent. In general, possible responses of the crust to mantle flow can be

divided into three categories. The first involves little if any crustal flow, and topography results mainly from the transmission of normal tractions induced by density contrasts within the mantle. The second possible regime involves substantial crustal flow, with geologically rapid thickening over convective downwelling and thinning over convective upwelling. In this regime the effects of crustal thickness variations dominate the topography. A third possible regime lies between the first two, with "in phase" deformation on short timescales and crustal flow on longer timescales. A strong mantle lithosphere tends to shield the crust from convective shear tractions, and topography results mainly from the transmission of convective normal tractions. A relatively weak lower crust facilitates crustal deformation, and the isostatic effects of crustal thickness variations dominate the topography.

Consideration of geoid to topography ratios (GTRs) can restrict which regime of crustal response is appropriate for Venus. The distribution of estimated GTRs for several highland regions on Venus is bimodal with two clusters around 10 and 25 m/km [5]. The positive correlation of long-wavelength gravity and topography implies that there are no major regions that have negative GTRs. To keep the GTRs positive, the geoid must follow the surface topography in sign at all times. Although the regime of negligible crustal flow can correctly predict both the sign and magnitude of the GTRs, it does not allow for the crustal deformation (i.e., flow) inferred from observations of tectonic features on Venus.

In contrast to the regime of negligible flow, that of time-dependent crustal flow generates topography that changes sign. Over a mantle downwelling, the topography is negative in the early stages of deformation and positive in the later stages of deformation; the converse holds over a mantle upwelling. During the transitional period the topography goes through zero, the geoid does not go through zero, and the GTR is unbounded; this singularity is not observed on Venus. An example of the evolution of the GTR for a model in the time-dependent regime is shown in Fig. 2. Note that before 90 m.y. both topography and geoid are negative, but at 90 m.y. crustal thickening effects begin to dominate and the topography switches sign, causing the GTRs to first become unbounded and then negative.

In the absence of a mechanism by which the sign of the geoid anomaly mimics that of the topography over a given upwelling or downwelling, only the regime of rapid crustal flow is plausible. In the case of mantle downwelling this would also require that the
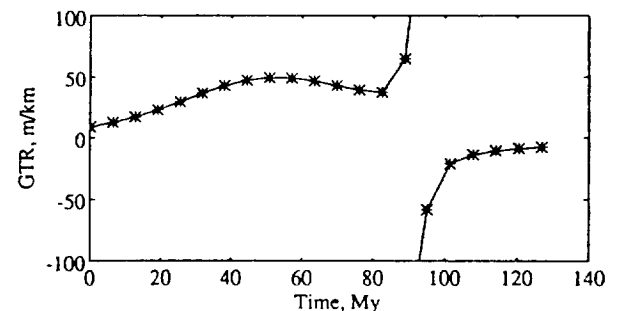
Fig. 2. Evolution of GTR with time. At each time step, the GTR shown is the slope of the best fit line to the collection of geoid and topography values upward continued to 250 km above the surface nodes in the model. The result is for a downwelling model, with a crust of constant viscosity 50 times that of the mantle. In this model the sign of the topography is time-dependent, but that of the geoid is not. The singularity at about 90 m.y. corresponds to the time when topography crosses the zero datum. Note that the GTRs for this model are neither always positive nor always bounded.

lower mantle be more viscous than the upper mantle in order to produce the required positive geoid anomalies. This has already been shown to be true for the Earth, where the observed geoid highs over regions of mantle upwelling and regions of mantle down-welling are best explained by the presence of a strong lower mantle [11,12]. The large positive GTRs and the presence of large shield volcanos in certain highland regions on Venus, such as Beta Regio and Eistla Regio, are best explained as areas of mantle upwelling [5,13,14]. The regime of rapid crustal flow predicts crustal thinning over the upwelling. However, the extensive partial melt and ensuing volcanism expected over such regions of mantle may outweigh the effects of crustal thinning on the surface topography and thus also yield postive GTRs [15].

References: [1] Solomon S. C. et al. (1991) *Science, 252,* 297. [2] Kiefer W. S. et al. (1986) *GRL, 13,* 14. [3] Bills B. G. et al. (1987) *JGR, 92,* 10. [4] Phillips R. J. et al. (1991) *Science, 252,* 651. [5] Smrekar S. E. and Phillips R. J. (1991) *EPSL, 107,* 587. [6] Phillips R. J. (1986) *GRL, 13,* 1141. [7] Phillips R. J. (1990) *JGR, 95,* 1301. [8] King S. D. et al. (1990) *PEPI, 59,* 195. [9] Bindschadler D. L. and Parmentier E. M. (1990) *JGR, 95,* 21. [10] Schmeling H. and Marquart G. (1990) *GRL, 17,* 2417. [11] Richards M. A. and Hager B. H. (1984) *JGR, 89,* 5987. [12] Hager B. H. (1984) *JGR, 89,* 6003. [13] Grimm R. E. and Phillips R. J. (1991) *JGR, 96,* 8305. [14] Grimm R. E. and Phillips R. J. (1991) *JGR,* in press. [15] Phillips R. J. et al. (1991) *Science, 252,* 651.

N93-14377

VENUS GRAVITY: SUMMARY AND COMING EVENTS.
W. L. Sjogren, Jet Propulsion Laboratory, 4800 Oak Grove Drive, Pasadena CA 91109, USA.

The first significant dataset to provide local measures of venusian gravity field variations was that acquired from the Pioneer Venus Orbiter (PVO) during the 1979–1981 period. These observations were S-band Doppler radio signals from the orbiting spacecraft received at Earth-based tracking stations. Early reductions of these data were performed using two quite different techniques. Estimates of the classical spherical harmonics were made to various degrees and orders up to 10 [1,2,3]. At that time, solutions of much higher degree and order were very difficult due to computer limitations. These reductions, because of low degree and order, revealed only the most prominent features with poor spatial resolution and very reduced peak amplitudes.

Another reduction technique was the line-of-sight acceleration mapping that had been used successfully for the Moon and Mars. This approach provided much more detail and revealed the high correlation of gravity with topography [4,5,6]. However, this technique does not produce a global field as do the spherical harmonics. It provided a mapping of features from approximately 50°N to 25°S latitude for 360° of longitude. Other shortcomings were that the accelerations were at spacecraft altitude rather than at the surface and were not vertical accelerations; however, the reductions were quick and cheaply accomplished. Other efforts to analyze these data included local area reductions, where surface masses were estimated [7,8,9].

The computer revolution over the past 10 years has allowed new reductions with spherical harmonics. New fields up to degree and order fifty (2600 parameters) have been made [10,11,12]. These fields now provide the best representation for any serious geophysicist doing quantitative modeling. There is now vertical gravity at the surface from a global model that carries all the requirements of dynamical consistency. There is one sizeable concern in that the

resolution over the entire planet is not uniform. This is due to the Pioneer orbit, which had a high eccentricity, causing the high latitude regions of Venus to be poorly resolved.

The Magellan (MGN) spacecraft, which went into orbit about Venus in August 1990, has returned Doppler data for gravity field reduction. However, because the high gain antenna was pointed at Venus for SAR mapping, no gravity data were acquired until the antenna was pointed back to Earth. This occurred at spacecraft altitudes higher than 2500 km, greatly reducing local gravity sensitivity. MGN has an eccentricity much smaller than PVO, so there is new information in the polar regions. Present reductions include two MGN circulations (486 days), which reduce uncertainties and produce somewhat better resolution.

During March, April, and May 1992 new low-altitude data have been acquired from both PVO and MGN. PVO periapsis latitude has changed 27°, from 16°N to 11°S. These data will provide better definition in the southern hemisphere, particularly over Artemis. The MGN mission now acquires periapsis gravity data for one orbit out of eight (i.e., foregoes SAR mapping for one orbit/day). Since MGN has an X-band radio signal, the data quality is a factor of 10 better than PVO. Only a small block of MGN data was acquired before its periapsis went into occultation May 16. Solar conjunction and periapsis occultation has also occurred for PVO.

In September of 1992 MGN periapsis will exit occultation and its periapsis altitude will be lowered to approximately 170 km. Periapsis will be visible from Earth for a complete 360° longitude coverage period (243 days). This should be an excellent dataset, having low X-band data noise that in turn can be combined with the PVO dataset.

In December 1992 PVO will exit periapsis occultation and low-altitude data (~150 km) in the southern hemisphere will be acquired for about one month before PVO is lost due to the lack of fuel to maneuver to safe altitudes.

In May 1993 there remains the possibility of aerobraking MGN into a circular orbit, thus allowing global uniform resolution gravity data to be acquired. One hopes that NASA has enough foresight to keep Magellan alive so this is a reality. It is anticipated that if this is done, harmonic solutions to degree and order 60–70 (5000 parameters) will be produced. One could then compare similar features globally, resolve coronae and test many interior structure models.

References: [1] Ananda M. P. et al. (1980) *JGR, 85,* 8303–8318. [2] Williams B. G. et al. (1982) *Icarus, 56,* 578–589. [3] Mottinger N. A. et al. (1985) *Proc. LPSC 15th,* in *JGR, 90,* C739–C756. [4] Phillips R. J. et al. (1979) *Science, 205,* 93–96. [5] Sjogren W. L. et al. (1980) *JGR, 85,* 8295–8302. [6] Sjogren W. L. et al. (1983) *JGR, 88,* 1119–1128. [7] Esposito P. B. et al. (1982) *Icarus, 51,* 448–459. [8] Reasenberg R. D. et al. (1981) *JGR, 86,* 7173–7199. [9] Sjogren W. L. et al. (1984) *GRL, 11,* 489–491. [10] Nerem R. S. (1991) *Eos, 72,* 174–175. [11] McNamee J. B. et al. (1992) *JGR,* in press. [12] Konopliv A. R. (1992) private communication of results to be published (AGU presentation in Montreal, Canada).

N93-14378

DIFFERENT TYPES OF SMALL VOLCANOS ON VENUS.
E. N. Slyuta[1], I. V. Shalimov[2], and A. M. Nikishin[2], [1]Vernadsky Institute, Russian Academy of Science, 117975 Moscow, Russia, [2]Moscow University, Moscow, Russia.

One of the studies of volcanic activity on Venus is the comparison of that with the analogous volcanic activity on Earth. The preliminary report of such a comparison and description of a small
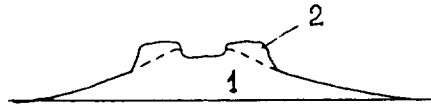
Fig. 1. Sketchy cross-section of flat-top volcanos: 1–shield edifice; 2–cinder flat-top superstructure.
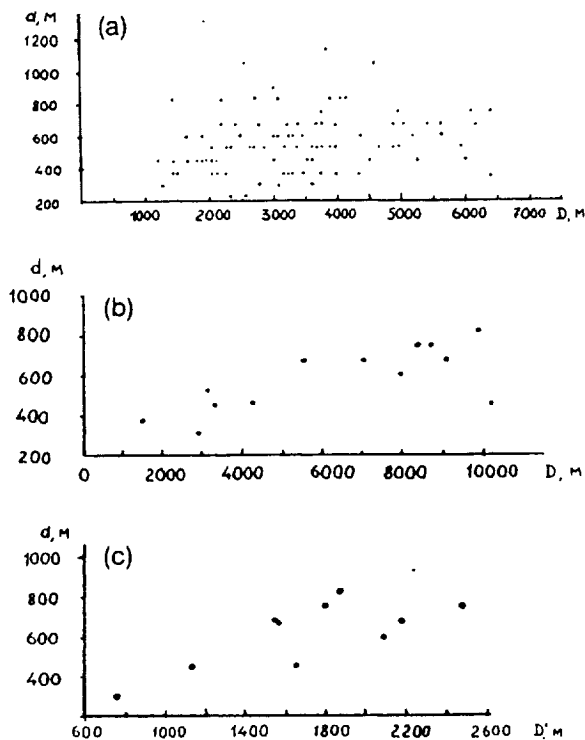

Fig. 2. Distribution of pit diameters relative to edifice diameters: (a) usual small shields; (b) flat-top volcanos (pit diameter relative to shield diameter); (c) flat-top volcanos (pit diameter relative to flat-top part diameter).

Fig. 3. Comparison of crater/edifice diameter ratio histograms for small venusian volcanos (bottom) and possible terrestrial analogs.

cluster of small venusian volcanos is represented in detail in this paper.

The cluster in question of small volcanos on Venus within Sedna Planitia (43°N, 334°E) is localized and compact. The total number of small volcanos recognized within the cluster is about 160 edifices; most of them have a small top pit. Some types of volcanic edifices within the cluster are recognized. The major type of volcanic edifices is small shield volcanos of Iceland type [1]. Small shield average basal diameter is 3750 m. Volcanos with a flat top outlined by a steep flank (Fig. 1) are also observed. There are 15 flat-top edifices (~ 9, 4% of the total number) in the cluster. The basal diameter of those varies from 1500 m to 10,200 m and average basal diameter is 6450 m, i.e., they are sufficiently larger on the average than usual shield edifices. Another difference from regular small shield volcanos is the dependence observed between the crater diameter and the edifice diameter (Figs. 2a,b). The right dependence between crater diameter and flat-top edifice diameter is also observed (Fig. 2c). The crater diameter to edifice basal diameter ratio

is similar to that for shield edifices and terrestrial small shields (Fig. 3) [2]. The crater diameter to flat-top part basal diameter is similar to that for terrestrial cinder cones (Fig. 3). If the slope angle of the flat-top flank corresponds to the angle of natural slip (of rest) of volcanic cinder material on Earth (it is about 30° [3]) the flat-top height can be defined, which varies from 130 to 260 m for different size edifices.

Thus, at least there are two different morphological types of small volcanos within the cluster. The difference may be caused by both eruption conditions including volatile content and different magma compound. It is suggested that venusian flat-top volcanos may have formed in two stages. The first is the formation of usual shield edifice due to effusive eruption and the second is the formation of the flat cinder superstructure on the shield top (Fig. 1) due to subsequently more explosive eruption.

It should be emphasized that venusian small shields are also similar to terrestrial analogs in size [1]. The minimal basal diameter of a venusian small shield obtained by more than 600 measure-

ments of volcanos with accuracy down to pixel is within the 800–900-m range. The smallest terrestrial shield edifice formed by one eruption also has a basal diameter of about 800–900 m [3].

The different types of volcanos can often be observed within the similar volcanic cluster on Earth. There are a variety of volcanic structures in similar clusters of volcanos in Saudi Arabia. The volcanic cluster and volcanos have been described in detail by Camp and Roobol [4]. The scoria cones are 0.5 to 1.3 km in diameter and rise as much as 100 m above the surrounding surface. They are typically steep and have open craters with a diameter of 100–400 m. Scoria cones are the largest group of Arabian volcanos with numbers up to 75% [4]. The shield volcanos are 5–10 km in diameter and rise as much as 1150 m above the surrounding surface. The crater/cone ratio is smaller, which is typical for shield volcanos. This group reaches 12% of the total number of volcanos [4].

References:　[1] Sinilo V. P. and Slyuta E. N. (1989) *LPSC XX*, 1016–1017. [2] Frey H. and Jarosewich M. (1982) *JGR, 87*, 9867–9879. [3] Macdonald G. A. (1972) *Volcanoes*, Prentice–Hall, New Jersey. [4] Camp V. E. et al. (1991) *GSA Bull., 103*, 363–391.

N93-14379

CONSTRAINTS ON CRUSTAL RHEOLOGY AND AGE OF DEFORMATION FROM MODELS OF GRAVITATIONAL SPREADING IN ISHTAR TERRA, VENUS.

Suzanne E. Smrekar and Sean C. Solomon, Department of Earth, Atmospheric, and Planetary Sciences, Massachusetts Institute of Technology, Cambridge MA 02139, USA.

Introduction: Gravitational spreading is expected to lead to rapid relaxation of high relief due to the high surface temperature and associated weak crust on Venus [1,2]. In this study, we use new Magellan radar and altimetry data to determine the extent of gravitational relaxation in Ishtar Terra, which contains the highest relief on Venus as well as areas of extremely high topographic slope. Within Ishtar Terra the only mountain belts found on Venus, Akna, Danu, Freyja, and Maxwell Montes, nearly encircle the smooth, high (3–4 km) plateau of Lakshmi Planum. Finite-element models of this process give expected timescales for relaxation of relief and failure at the surface. From these modeling results we attempt to constrain the strength of the crust and timescales of deformation in Ishtar Terra. Below we discuss observational evidence for gravitational spreading in Ishtar Terra, results from the finite-element modeling, independent age constraints, and implications for the rheology and timing of deformation.

Observations: Magellan data have revealed abundant evidence for localized extension throughout Ishtar Terra [3,4]. Many of the observed extensional features are oriented perpendicular to the downslope direction, implying that they formed as a result of gravitational spreading. In some of the mountainous areas, extensional faults occur parallel to the apparent direction of shortening. By analogy with the Himalayas on Earth [5], we interpret such extension to indicate gravitational spreading during convergence. Areas of possible gravitational spreading are observed in each of the four mountain belts and along both the southern and northeastern margins of Lakshmi Planum. Horizontal strain in these regions is estimated to be 1–20%; this value may be an underestimate if blocks are rotated along the normal faults. The observational evidence for gravitational spreading in Ishtar Terra is discussed more fully in [4].

Models: We use the finite-element algorithm TECTON [6] to model the evolution of gravitational spreading in a vertical section of the crust near the margin of a plateau or the edge of a broad mountain belt. Each model includes an elevated plateau 50 km in width, a sloped margin, and a lowlands region 80 km in width. The code employs a depth-dependent, viscoelastic rheology with non-linear stress dependence and exponential temperature dependence. We adopt a Young's modulus of 6×10^{10} Pa, a Poisson's ratio of 0.25, and a diabase flow law [7]. Although a diabase composition is most similar to the composition determined at Soviet lander sites [8], the flow law determined for diabase may underestimate the strength because of partial melting of samples during the experiment [7,9]. For this reason, we also employ a websterite flow law [10] as an approximate upper bound on crustal strength. The surface temperature is 740 K and increases linearly with depth. Each row of elements in the grid has the same viscosity, which is equivalent to assuming that the temperature is constant along both the bottom and top of the grid. This results in a somewhat higher thermal gradient in the plains than in the plateau. The boundary conditions are zero vertical and horizontal velocity on the bottom of the grid, a free surface top boundary, and zero horizontal velocity and free vertical slip at the sides. The bottom boundary condition approximates an upper mantle layer that is much stronger than the lower crust. Details of the models are given in [4]. Brittle failure is evaluated using a Mohr-Coulomb criterion. The timing of predicted brittle failure and relaxation of relief are found for ranges of plateau height (1–5 km), plateau margin slope (1°–30°), crustal thickness (10–30 km), and thermal gradient (5–25 K/km). Slopes of 1°–30° and plateau or mountain belt heights of 1–6 km are observed in Ishtar Terra. Crustal thickness on Venus is predicted to be 10–30 km [11,12]; the average thermal gradient is expected to be 10–25 K/km [13,14].

The rate of deformation is largely controlled by the effective viscosity, and thus the temperature and stress, at the base of the crust. The greatest deformation occurs at the base of the crust, where the viscosity is lowest. Temperature at the base of the crust increases with crustal thickness (for a fixed thermal gradient), and deviatoric stress near the base of the crust increases with both crustal thickness and plateau elevation. The nonlinear change in predicted failure and relaxation time (see below) is due both to the exponential dependence on temperature and to the power law dependence on deviatoric stress of the effective viscosity.

Failure is predicted to occur when the stresses exceed the Mohr-Coulomb criterion. The earliest failure is located on the plateau. In most cases, failure on the slope follows shortly after failure on the plateau; thrust faulting in the plains is predicted typically only for a crustal thickness of 30 km. Figure 1 shows the time from the start of spreading until the first failure on the plateau as a function of plateau height and crustal thickness, for a margin slope of 3° and a thermal gradient of 15 K/km. Models with both websterite and diabase flow laws are plotted. No times are shown for models that do not fail within 1 Ga. Cases with a diabase rheology, a large plateau height, and a large crustal thickness fail almost immediately. A plateau height of 1 km and a crustal thicknesses of 10 km can take up to tens of millions of years to fail. With a websterite flow law, no failure occurs unless the crust is a least 20 km thick and the plateau elevation is 1–3 km. Changing the thermal gradient by 10 K/km has a large effect on failure times, with a higher thermal gradient decreasing the failure time by a factor of 10^2–10^4, and a lower thermal gradient increasing times by a similar factor. When failure is first predicted, the horizontal surface strain is approximately 0.05%. This strain is unlikely to be recognized as normal faulting in Magellan radar images; a strain of 1%, which accumulates once significant relaxation of the topography begins, is probably a more reasonable value to compare with observations. As faulting is not explicitly modeled, there is some uncertainty in the interpretation of
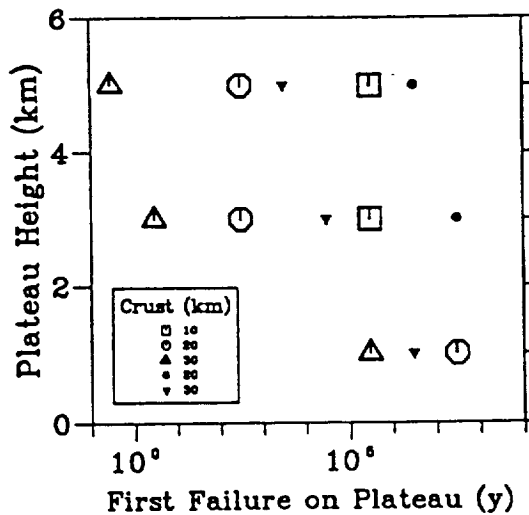
Fig. 1. The time at which failure (by normal faulting) first occurs on the plateau as a function of plateau elevation for three values of plains crustal thickness. The initial slope of the scarp in each model is 3°, and the plains thermal gradient is 15 K/km. Open symbols represent models with a diabase flow law [7]; filled symbols are for a websterite flow law [10]. Times are determined to the nearest order of magnitude.

strain after the initial failure. The total strain may be underestimated. As elevations in Ishtar Terra are among the highest on Venus, we assume that relief has not relaxed by more than 25% of its original value. The time at which the average elevation in the plateau has relaxed by at least 25% is shown as a function of plateau height and crustal thickness, for thermal gradients of 15 and 25 K/km, in Fig. 2. For a given thermal gradient and crustal thickness, predicted relaxation times for plateau heights of 1, 3, and 5 km vary by a factor of 10 at most. A 10-km change in crustal thickness leads to a factor of 10–100 change in relaxation time. Larger differences in relaxation time are predicted for models with the same plateau height and crustal thickness but with thermal gradients that differ by
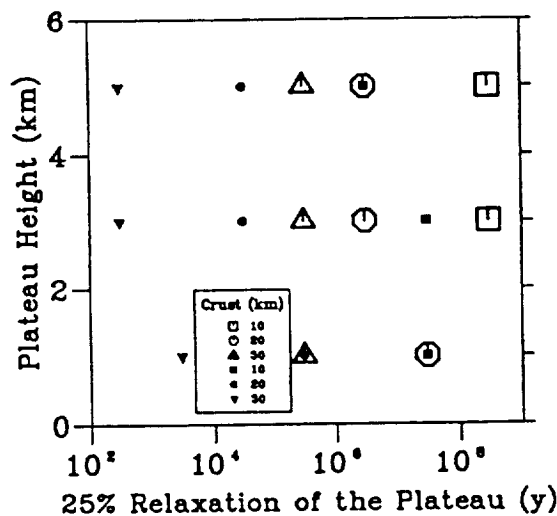

Fig. 2. The time at which the height of the plateau has relaxed by at least 25% as a function of plateau height for three values of plains crustal thickness. The initial slope of the bounding scarp is 3° and the flow law is that for diabase [7]. The open symbols are for a plains thermal gradient of 15 K/km; filled symbols are for a thermal gradient of 25 K/km. Times are determined to the nearest order of magnitude.

10 K/km, as is consistent with the larger changes in basal temperature. For a thermal gradient of 25 K/km and a plateau height of 1–5 km, all the models are predicted to relax by at least 25% within 100 m.y. for a 10-km-thick crust, 0.1 m.y. for a 20-km-thick crust, and 1000 yr for a 30-km-thick crust. A thermal gradient of 15 K/km gives relaxation times of up to 1 G.y., 100 m.y., and 0.1 m.y. for crustal thicknesses of 10, 20, and 30 km, respectively.

Discussion: The range of parameters can be narrowed somewhat by considering the geology and morphology of Ishtar Terra. In areas of possible gravitational spreading, the local topographic slope ranges from 2°–15°. For the purposes of discussion, we will assume a slope of at least 3°. Typical local relief is 2–3 km, although relief is as large as 5–6 km in Maxwell Montes. Thus models with plateau elevations of only 1 km can be eliminated as not relevant, especially given that the elevation may have relaxed somewhat from its original value. The very steep topographic slopes in many parts of Ishtar Terra suggest that the crust has been tectonically thickened and thus the topography is likely to be at least partially isostatically compensated. As mountains in Ishtar Terra rise 4–10 km above the surrounding lowlands, the crustal thickness is probably greater than 10 km. Further, the abundance of volcanism in Ishtar Terra, as well as the overlap of volcanism and extension in many areas [4], implies that the thermal gradient is unlikely to anomalously low. Values of 15 K/km or more are probably applicable. Using these limits on the ranges of parameters appropriate for Ishtar Terra and assuming a diabase flow law constrains relaxation of the topography by 25% to occur within 10 m.y. This result implies that either the crust is anomalous in some way—thinner, colder, or stronger than expected—or that mountain-building processes have maintained the relief in Ishtar Terra until geologically recent times. Independent information on the age of tectonism in Ishtar Terra is necessary to discriminate between these two hypotheses.

Information on the age of Ishtar Terra is inconsistent. The only available measure of absolute age, the average crater retention age for Venus of 500 m.y., implies that much of the surface is quite old [15]. Local geological information must be used to determine whether a region is likely to be older or younger than the average age [15]. In Ishtar Terra, the abundance of volcanism, especially in Lakshmi Planum, suggests that the surface may be less than the average age [16]. In many areas, both the shortening in the mountain belts and episodes of extension postdate local volcanism in Lakshmi Planum [3,4,16]. At least one impact crater in Ishtar Terra appears to be modified by extension due to gravitational relaxation [4]. However, Cleopatra, a 100-km-diameter crater, lies near the crest of Maxwell Montes and appears undeformed [17]. In addition to surface processes, gravity data suggest that dynamic processes in the mantle are actively supporting the long wavelength topography [18]. These dynamic processes may produce stresses capable of inducing the observed short-wavelength, high-amplitude variations in topography.

Both the gravity data and the majority of the geologic indicators favor the hypothesis that the region is likely to be younger than the average crater retention age of Venus, 500 m.y. On the basis of this information and the assumptions discussed above regarding the appropriate parameter range for Ishtar Terra, we interpret the results of our modeling to indicate that tectonic processes have maintained the topographic relief and high slopes of the region until as recently as 10 m.y. and may still be active.

References: [1] Weertman J. (1979) *PEPI, 19*, 197–297. [2] Smrekar S. E. and Phillips R. J. (1988) *GRL, 15*, 693–696. [3] Solomon S. C. et al. (1991) *Science, 252*, 297–312. [4] Smrekar S. E. and Solomon S. C. (1992) *JGR*, in press. [5] Armijo R. et al.

(1986) *JGR, 91*, 13803–13872. [6] Melosh H. J. and Rafesky A. (1980) *Geophys. J. R. Astron. Soc., 60*, 333–354. [7] Caristan Y. (1982) *JGR, 87*, 6781–6790. [8] Surkov Yu. A. et al. (1987) *Proc. LPSC 17th*, in *JGR, 92*, E537–E540. [9] Evans B. et al. (1990) *Geophys. Mono., 56*, 20 AGU. [10] Lallement H. G. Ave. (1978) *Tectonophysics, 48*, 1–27. [11] Grimm R. E. and Solomon S. C. (1988) *JGR, 93*, 11911–11929. [12] Zuber M. T. and Parmentier E. M. (1990) *Icarus, 85*, 290–308. [13] Kaula W. M. and Phillips J. R. (1981) *GRL, 8*, 1187–1190. [14] Solomon S. C. and Head J. W. (1982) *JGR, 87*, 9236–9246. [15] Phillips R. J. et al. (1992) *JGR*, in press. [16] Roberts K. M. and Head J. W. (1990) *Earth Moon Planets, 50/51*, 193–250. [17] Kaula W. et al. (1992) *JGR*, in press. [18] Grimm R. E. and Phillips R. J. (1991) *JGR, 96*, 8205–8324.

N93-14380

MULTIRESOLUTION PATTERN RECOGNITION OF SMALL VOLCANOS IN MAGELLAN DATA.

P. Smyth[1], C. H. Anderson[1], J. C. Aubele[2], and L. S. Crumpler[2], [1]Jet Propulsion Laboratory 238-420, California Institute of Technology, 4800 Oak Grove Drive, Pasadena CA 91109, USA, [2]Department of Geological Sciences, Brown University, Providence RI 02912, USA.

Introduction: The Magellan data is a treasure-trove for scientific analysis of venusian geology, providing far more detail than was previously available from Pioneer Venus, Venera 15/16, or ground-based radar observations [1]. However, at this point, planetary scientists are being overwhelmed by the sheer quantities of data collected—data analysis technology has not kept pace with our ability to collect and store it. In particular, "small-shield" volcanos (less than 20 km in diameter) are the most abundant visible geologic feature on the planet [2].

It is estimated, based on extrapolating from previous studies and knowledge of the underlying geologic processes, that there should be on the order of 10^5 to 10^6 of these volcanos visible in the Magellan data [3,4]. Identifying and studying these volcanos is fundamental to a proper understanding of the geologic evolution of Venus. However, locating and parameterizing them in a manual manner is very time-consuming. Hence, we have undertaken the development of techniques to partially automate this task. The goal is not the unrealistic one of total automation, but rather the development of a useful tool to aid the project scientists. The primary constraints for this particular problem are (1) the method must be reasonably robust and (2) the method must be reasonably fast. Unlike most geological features, the small volcanos of Venus can be ascribed to a basic process that produces features with a short list of readily defined characteristics differing significantly from other surface features on Venus [2]. For pattern recognition purposes the relevant criteria include (1) a circular planimetric outline, (2) known diameter frequency distribution from preliminary studies, (3) a limited number of basic morphological shapes, and (4) the common occurrence of a single, circular summit pit at the center of the edifice.

Pattern Recognition of Natural Objects: There has been little prior work on detecting naturally occurring objects in remotely sensed SAR images. Methods such as direct edge detection and Hough transform approaches deal poorly with the variability and speckle noise present in typical SAR imagery [5,6,7]. One approach toward detecting small volcanos is to use a template-matching method whereby a template of the object of interest is compared with the original target image by scanning the template over the entire scene. For an $N \times N$ square image and a $k \times k$ size template this operation takes the order of N^2k^2 operations. If scale-invariance

is sought then typically the procedure is repeated using a range of template sizes. Wiles and Forshaw [8] have obtained promising results using this method despite the fact that the Magellan data contains significant speckle noise and ambiguity in terms of the appearance of volcanos in the imagery.

We have pursued an alternative approach motivated by the desire to develop real-time search methods that could be used as an interactive software tool by a planetary scientist. The key concept behind our approach is to carry out the detailed pattern matching at the lowest image resolution possible and to focus attention only on relevant parts of the image. Although our work is focused on developing useful image analysis tools rather than biologically plausible visual models, it is interesting to note that this general approach is consistent with high-level models of primate visual systems [9].

Multiresolution Pattern Recognition: The multiresolution paradigm emphasizes the decomposition of an image into a sequence of spatial band-pass components [10]. In this manner, image analysis can occur across various spatial frequencies while still retaining local spatial structure. The basic process is a series of recursive low-pass Gaussian decompositions of the original image, which in turn produces a bandpass Laplacian pyramid (the difference of Gaussians). From a pattern recognition standpoint the key feature of the method is the ability to analyze the image only at the coarsest scale necessary. For pattern matching the computational savings are significant, order of 4^k by working at the kth level of decomposition [11]. Furthermore, provided sufficient detail is retained for discrimination; by reducing the effective resolution of the image the input dimensionality to the detector also decreases by a factor of 4^k. The lower dimensionality makes it much easier to train an accurate detector. Focus of attention is implemented by simply "binning" the pixel values of the Laplacian components and then thresholding. Figure 1 contains an example of this process (note that a significant number of linear features are automatically omitted by focusing attention at the appropriate scale).

Volcano Discrimination: The focus of attention mechanism typically produces about 100 regions of interest (ROIs) per Laplacian image, roughly half of which contain volcanos and the other half primarily ridge or graben segments. Each ROI is labeled and a standard pattern recognition method (a neural network feed-forward classifier using backpropagation) is trained on samples of 5×5 windows of pixel values surrounding the detected bright spots. In our experiments with Magellan data the multiresolution filtering and focusing typically reduces the number of pixels that must be examined to order of 0.5% of those in the original image with a resultant speed-up in computation at the pattern-matching level. Using separate test and training images, roughly 70% mean ROI classification accuracy was attained (up from 50% by simply guessing).

The concept of having "ground truth" classification labels is actually incorrect since there are a significant proportion of ROIs whose labelings are not certain. Hence, by using subjectively estimated probability vectors of class labels (rather than deterministic class-label vectors of 0s and 1s) the mean ROI classification rate improved to about 82%. This probabilistic training method is consistent in terms of modeling posterior probabilities and, furthermore, will produce better posterior estimates than using "hard-decision" class labels given a finite amount of training data [12]. The mean missed detection and false alarm rates were about equal (roughly 20%)—almost all the incorrect decisions were made on windows where local context was not sufficient for accurate discrimination.
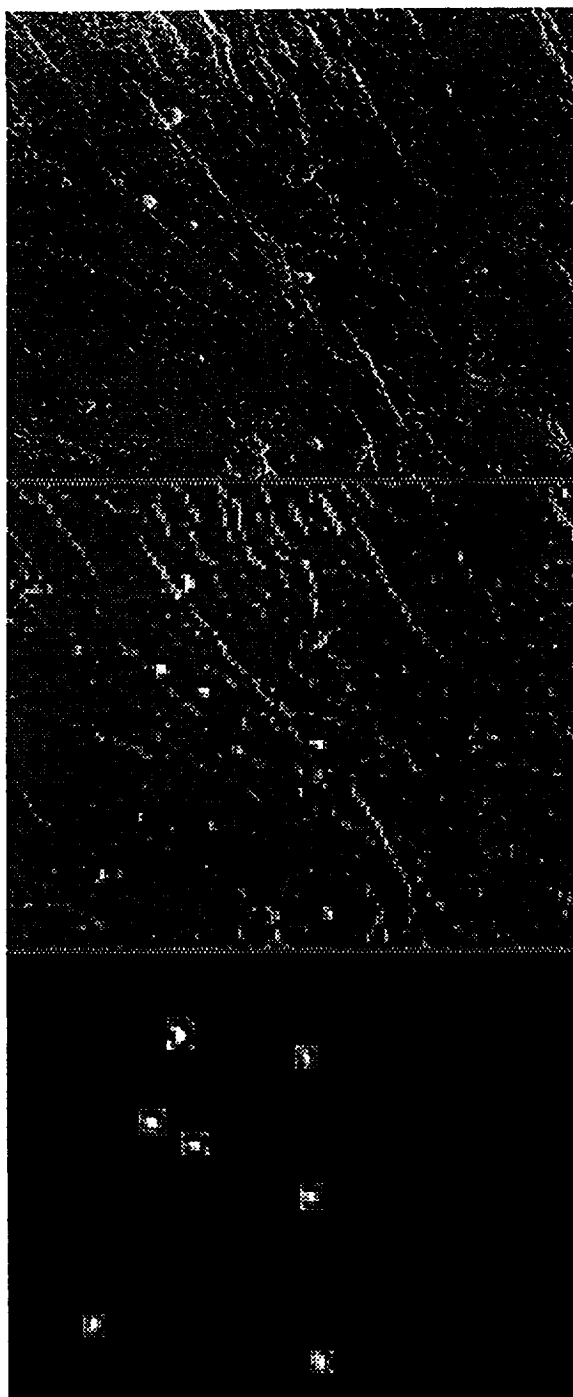
Fig. 1. Original Magellan SAR data (top), bandpass filtered version of same (center), and detected regions of interest (at 1/4 resolution) (bottom).

Ongoing Work: We anticipate that a much higher classification accuracy can be achieved by incorporating prior knowledge about the imaging and geologic processes, i.e., noise properties, surface radar reflectivity, expected volcano diameters, and so forth. By treating the output activations of the network as estimates of posterior class probabilities, both data-driven evidence and prior knowledge can be integrated directly in terms of a coherent probability model such as a Bayesian network, which incorporates appropriate conditional independence assumptions. Note that if the posterior probabilities at a given level are not confident enough (not close to 0 or 1), the Laplacian hierarchy can be descended for a higher-resolution analysis. Another significant issue is the incorporation of global context models (spatial correlation of geologic features) with local evidence. In the context of currently available image analysis algorithms and tools, these issues somewhat push the state-of-the-art.

Conclusions: In terms of pattern recognition, even though 100% accuracy will not be achievable due to the inherent ambiguity in the image data, the general method has significant practical benefit as a basic tool for aiding rapid scientific exploration of the large Magellan database. A short-term scientific benefit will be to answer the basic question regarding the approximate number and distribution of these volcanos on the surface of Venus. Long-term scientific benefits would include subsequent spatial cluster analysis of the volcano locations and the association of the volcanos with local structural patterns. It is reasonable to suggest that the application of pattern recognition techniques will enable basic scientific research that otherwise would not be possible by manual methods.

References: [1] *Science*, special issue on Magellan data, April 12, 1991. [2] Guest J. E. et al. (1992) *JGR*, in press. [3] Aubele J. C. and Slyuta E. N. (1990) *Earth Moon Planets, 50/51*, 493–532. [4] Head J. W. et al. (1992) *JGR*, in press. [5] Skingley J. and Rye A. J. (1987) *Pattern Recognition Letters, 6*, 61–67. [6] Cross A. M. (1988) *Int. J. Remote Sensing, 9*, 1519–1528. [7] Quegan S. et al. (1988) *Phil. Trans. R. Soc. Lond., A324*, 409–421. [8] Wiles C. R. and Forshaw M. R. B. (1992) *LPSC XXIII*, 1527–1528. [9] Van Essen D. C. and Anderson C. H. (1992) *Science*. [10] Burt P. J. and Adelson E. H. (1983) *IEEE Trans. Comm., 31*, 532–540. [11] Burt P. J. (1988) *Proceedings of the DARPA Image Understanding Workshop*, 139–152. [12] Miller J. W. et al. (1992) *IEEE Trans. Info. Theory*, submitted.

N93-14381

MELTING AND DIFFERENTIATION IN VENUS WITH A "COLD" START: A MECHANISM OF THE THIN CRUST FORMATION. Viatcheslav S. Solomatov and David J. Stevenson, Division of Geological and Planetary Sciences, 170–25, California Institute of Technology, Pasadena CA 91125, USA.

Recent works [1–3] argue that the venusian crust is thin: less than 10–30 km. However, any convective model of Venus unavoidably predicts melting and a fast growth of the basaltic crust up to its maximum thickness about 70 km limited by the gabbro-eclogite phase transition [4]. The crust is highly buoyant due to both its composition and temperature and it is problematic to find a mechanism providing its effective recycling and thinning in the absence of plate tectonics. There are different ways to solve this contradiction [5,6]. This study suggests that a thin crust can be produced during the entire evolution of Venus if Venus avoided giant impacts [7].

The absence of giant impacts means that Venus' interiors were more cold and more water-rich than the Earth's after the accretion and core formation. The initial temperature distribution after the core formation is not necessarily convectively unstable: The viscosity is extremely sensitive to the temperature and uncertainties in the initial thermal state easily cover the transition from conductive to convective regimes. Convection and conduction-convection transition are parameterized for the temperature-, pressure- and stress-

dependent viscosity with the help of a recently developed approach [8] and the thermal evolution of Venus with melting and differentiation is calculated.

The model predicts that only a small amount of melt is extracted in the first period of evolution; however, this would result in a strong depletion in radioactive elements and devolatilization of a part of the upper mantle. Independently of the thickness of this differentiated layer, only about a 300-km layer contributes to the crust formation (a depth below which the melt is supposed to be denser than the surrounding rocks). A small buoyancy of this depleted layer is sufficient to stabilize this layer with respect to the undifferentiated mantle. This prevents supply of the undifferentiated material to the melting region. Convection occurs eventually in both layers. The lower, undifferentiated layer is heated from within. The upper, differentiated layer is mainly heated from below. The temperature increases and reaches the anhydrous solidus only after several billion years depending on the rheological model. The young basaltic crust observed on Venus is produced by melting of the anhydrous layer. This melting and the crust growth are weak mainly because of the lower heat flux consisting of the radiogenic heat production in the undifferentiated lower layer and almost not contributed from the secular-cooling heat flux from the core (it is even negative) and the remaining radioactivity in the differentiated layer. An additional consequence of the model is that the magnetic field was never generated in venusian history.

References: [1] Zuber M. T. and Parmentier E. M. (1987) *Proc. LPSC 17th*, in *JGR*, *92*, E541. [2] Zuber M. T. and Parmentier E. M. (1990) *Icarus*, *85*, 290. [3] Grimm R. E. and Solomon S. C. (1988) *JGR*, *93*, 11911. [4] Zharkov V. N. and Solomatov V. S. (1992) In *Venus Geology, Geochemistry, and Geophysics*, 281, Univ. of Arizona, Tucson. [5] Solomon S. C. and Head J. W. (1991) *Science*, *252*, 252. [6] Williams D. R. and Pan V. (1990) *GRL*, *17*, 1397. [7] Kaula W. M. (1990) *Science*, *247*, 1191. [8] Solomatov V. S. (1992) In *Flow and Dynamic Modeling of the Earth and Planets*, Univ. of Alaska, in press.

N93-14382

THE TECTONICS OF VENUS: AN OVERVIEW. Sean C. Solomon, Department of Earth, Atmospheric, and Planetary Sciences, Massachusetts Institute of Technology, Cambridge MA 02139, USA.

Introduction: While the Pioneer Venus altimeter, Earth-based radar observatories, and the Venera 15–16 orbital imaging radars provided views of large-scale tectonic features on Venus at ever-increasing resolution [1–3], the radar images from Magellan constitute an improvement in resolution of at least an order of magnitude over the best previously available [4]. A summary of early Magellan observations of tectonic features on Venus has been published [5], but data available at that time were restricted to the first month of mapping and represented only about 15% of the surface of the planet. Magellan images and altimetry are now available for more than 95% of the Venus surface. Thus a more global perspective may be taken on the styles and distribution of lithospheric deformation on Venus and their implications for the tectonic history of the planet [6].

Generalizations: Tectonic features on Venus are widespread and diverse, and comparatively few regions are undeformed. Areas lacking tectonic features at Magellan resolution are restricted to relatively young volcanic deposits and the younger impact craters and associated ejecta. Most of the surface, during at least some period over approximately the last 500 m.y. [7,8] has experienced horizontal strain sufficient to fault or fold near-surface material.

Tectonic activity on Venus has continued until geologically recent time, and most likely the planet is tectonically active at present. Several arguments support this inference. The great relief and steep slopes of the mountains and plateau scarps of Ishtar Terra and of the equatorial chasm systems are difficult to reconcile with long-term passive support by crustal strength. Because of the high surface temperature on Venus, temperatures at which crustal rocks fail by ductile flow should be reached at much shallower depths than on Earth [9,10]. Numerical models suggest that areas of high relief and steep slope in the Ishtar region should spread under self-gravity by ductile flow of the weak lower crust on time scales less than about 10 m.y. [11]. Thus the processes that build relief and steepen slopes must have been active within the last 10 m.y. Further, a number of features produced by geological processes that have operated more or less steadily during the past 500 m.y. show evidence of subsequent tectonic activity. About one-third of all preserved impact craters on Venus have thoroughgoing faults and fractures, and 1 in 12 are extensively deformed [8]. The longest lava channel on the plains of Venus does not progress monotonically to lower elevations downstream, indicating that differential vertical motions have occurred since the channel was formed [12].

Compared with the Earth, horizontal displacements on Venus over the last 500 m.y. have been limited. Most of the tectonic features require modest strains and horizontal displacements of no more than a few tens to perhaps a few hundreds of kilometers. Plains thousands of kilometers across record horizontal strains of order 10^{-2} or less. The great rift systems of Beta and Atla Regiones need have extended no more than a few tens of kilometers, on the basis of topographic profiles, extended features such as Somerville Crater in Devana Chasma, and analogy with continental rifts on Earth [13]. For compressional features, the amount of crustal thickening can be estimated from topographic relief and isostatic considerations, but this approach provides only a lower bound on horizontal displacements if any crustal material is recycled into the mantle at zones of underthrusting. For ridge belts 100 km in width with up to 1 km of relief, horizontal displacements of no more than 100 km are required for crustal thicknesses of 10–20 km beneath the adjacent plains [14,15]. Mountain belts are exceptional in that greater horizontal displacements are required. For a two- to four-fold thickening of the crust beneath the 500-km width of Maxwell Montes, the implied minimum horizontal displacement is 1000–2000 km.

Unlike the Earth, Venus does not show evidence for a global system of nearly rigid plates with horizontal dimensions of 10^3–10^4 km separated by narrow plate boundary zones a few kilometers to tens of kilometers across. Predictions prior to Magellan that Aphrodite Terra would show features analogous to terrestrial spreading centers and oceanic fracture zones [16] now seem to be incorrect. Evidence for shear is present in the ridge and fracture belts and in the mountain belts, but the shearing tends to be broadly distributed and to accompany horizontal stretching or shortening. Few clear examples have yet been documented of long, large-offset strike-slip faults such as those typical of oceanic and many continental areas on Earth; two such features have been identified in the interior of Artemis Corona [17]. A number of the chasm systems of Venus have arcuate planforms, asymmetric topographic profiles, and high relief [18] and have been likened to deep-sea trenches on Earth [17]. These include Dali and Diana Chasmata [17] and the moat structure of Artemis Corona; such trenches may be the products of limited underthrusting or subduction of lithosphere surrounding large coronae [19]. Elsewhere, however, chasm systems of somewhat lesser relief display more linear segments and

more nearly symmetric topographic profiles, such as Devana Chasma, and on the basis of small-scale morphology are clearly extensional rifts.

Much of the tectonic behavior on Venus appears to be more reminiscent of actively deforming continental regions than of oceanic regions on Earth. In particular, as in tectonically active continental areas, deformation is typically distributed across broad zones one to a few hundred kilometers wide separated by comparatively stronger and less deformed blocks having dimensions of hundreds of kilometers. On Earth, the continental lithosphere in tectonically active areas is weaker than typical oceanic lithosphere because of the greater thickness of more easily deformable crust. As noted above, because of the higher surface temperature on Venus, the likely comparable lithospheric thermal gradients on Venus and Earth [20,21], and the strong temperature dependence of ductile behavior, the lithosphere on Venus should behave in a weak manner for crustal thicknesses less than are typical of continental regions on Earth.

Status of Models: A major challenge in unraveling the tectonic evolution of Venus is to understand the interaction between mantle convection and the lithosphere. The hotspot [22] and coldspot [23] models for the formation and evolution of major highlands on Venus are distinguishable on the basis of the predicted sequence of events and the time-dependent relationship between topography and gravity. Both models face difficulties in their present forms, however, at least partly because both the rheology of the upper crust of Venus and the observed patterns of magmatism and deformation are more complex than current models for the deformation and magmatic response of the crust to mantle flow. Any global tectonic model, of course, must also consider the formation and characteristics of the lowlands, including the large apparent depths of isostatic compensation [22] and relatively recent lowland volcanism [24]. All dynamical models to date require special pleading to explain Ishtar Terra. Both the rifted, volcanically active highlands and at least the larger coronae are generally regarded as sites of upwelling mantle flow and magma generation by pressure-release partial melting of mantle material. These two classes of features, however, have very different tectonic and morphological manifestations at the Venus surface. If both are products of mantle upwelling, then multiple scales of mantle convection are indicated and the different morphologies of the two classes of features must be related to differences in the geometry, buoyancy flux, or duration of flow in the two types of upwelling regions. The assessment of existing dynamical models for the tectonic evolution of Venus and the development of the next generation of models will require an understanding of geological relationships at all scales, from the highest resolution available to global patterns. High-resolution measurements of the global gravity field later in the Magellan mission will provide key data for testing and refining models.

References: [1] Masursky H. et al. (1980) *JGR, 85*, 8232. [2] Campbell D. B. et al. (1983) *Science, 221*, 644. [3] Barsukov V. L. et al. (1986) *Proc. LPSC 16th*, in *JGR, 91*, D378. [4] Pettengill G. H. et al. (1991) *Science, 252*, 260. [5] Solomon S. C. et al. (1991) *Science, 252*, 297. [6] Solomon S. C. et al. (1992) *JGR*, in press. [7] Phillips R. J. et al. (1991) *Science, 252*, 288. [8] Schaber G. G. et al. (1992) *JGR*, in press. [9] Weertman J. (1979) *PEPI, 19*, 197. [10] Solomon S. C. and Head J. W. (1984) *JGR, 89*, 6885. [11] Smrekar S. E. and Solomon S. C. (1992) *JGR*, in press. [12] Baker V. R. et al. (1992) *JGR*, in press. [13] McGill G. E. et al. (1981) *GRL, 8*, 737. [14] Grimm R. E. and Solomon S. C. (1988) *JGR, 93*, 11911. [15] Zuber M. T. and Parmentier E. M. (1990) *Icarus, 85*, 290. [16] Head J. W. and Crumpler L. S. (1987) *Science,* *238*, 1380. [17] McKenzie D. et al. (1992) *JGR*, in press. [18] Ford P. G. and Pettengill G. H. (1992) *JGR*, in press. [19] Sandwell D. T. and Schubert G. (1992) *JGR*, in press. [20] Solomon S. C. and Head J. W. (1982) *JGR, 87*, 9236. [21] Phillips R. J. and Malin M. C. (1984) *Annu. Rev. Earth Planet. Sci., 12*, 411. [22] Phillips R. J. et al. (1991) *Science, 252*, 651. [23] Bindschadler D. L. et al. (1992) *JGR*, in press. [24] Head J. W. et al. (1991) *Science, 252*, 276.

N93-14383

THE SPATIAL DISTRIBUTION OF CORONAE ON VENUS.

S. W. Squyres[1], G. Schubert[2], D. L. Bindschadler[2], D. M. Janes[1], J. E. Moersch[1], W. Moore[2], P. Olson[3], J. T. Ratcliff[2], E. R. Stofan[4], D. L. Turcotte[1], [1]Cornell University, [2]University of California, Los Angeles, [3]Johns Hopkins University, [4]Jet Propulsion Laboratory, USA.

Coronae on Venus are large, generally circular surface features that have distinctive tectonic, volcanic, and topographic expressions. They range in diameter from less than 200 km to at least 1000 km. Data from the Magellan spacecraft have now allowed complete global mapping of the spatial distribution of coronae on the planet. Unlike impact craters, which show a random (i.e., Poisson) spatial distribution [1], the distribution of coronae appears to be nonrandom. We investigate the distribution here in detail, and explore its implications in terms of mantle convection and surface modification processes.

Figure 1 shows the distribution of coronae and corona-related features on Venus, in a simple cylindrical (Plate Carrée) projection. The map gives the locations of 311 features identified in all of the Magellan data taken to date. These features include coronae; they also include radially fractured domes, which are believed to be coronae in an early or arrested stage of development [2]. The map gives the qualitative sense that the distribution is nonrandom, with distinct areas of clustering and sparseness. However, this assertion requires testing, especially because there are some significant gaps in the Magellan data that artificially introduce areas of sparseness in the corona distribution.

In order to test for nonrandomness, we apply a simple nearest-neighbor test. In this test, we measure the distance, r, of each feature from its nearest neighbor on the planet. The percentage of points with a nearest-neighbor distance greater than r is then plotted as a function of r in Fig. 2. The next step is to compare this result to the result expected for a spatially random distribution. There exist theoretical treatments for a nearest-neighbor curve of the sort in
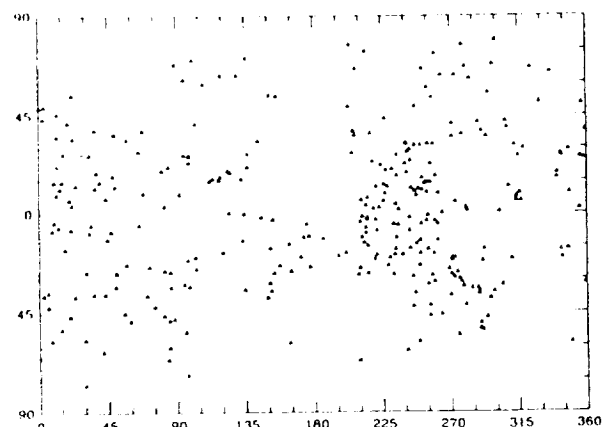

Fig. 1. Map showing the distribution of coronae and related features on Venus.
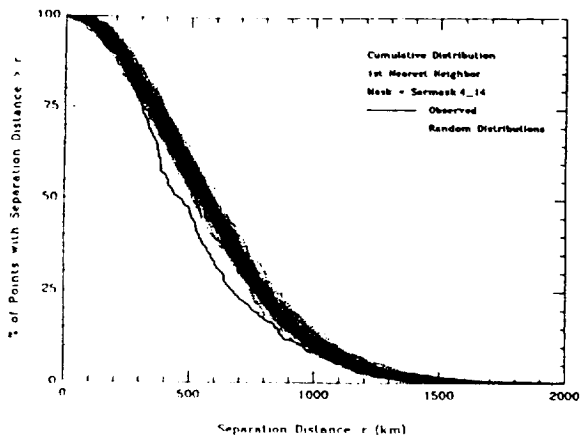
Fig. 2. Nearest-neighbor plots for the observed corona distribution (solid line), and 100 random distributions (dashed lines). Random distributions contain no points in the Magellan data gaps.

Fig. 2 for randomly distributed points on a sphere. Such treatments, however, do not readily allow for inclusion of the effects of data gaps. We therefore take a Monte Carlo approach. We have generated 100 distributions of 311 points on a sphere that are randomly distributed except that they are not allowed to fall within the Magellan data gaps. We then produce nearest-neighbor curves for these distributions, also shown in Fig. 2, and compare them to the observed curve. For separation distances ranging from about 300 to 800 km, the observed curve lies below all 100 of the random curves. We therefore conclude that coronae on Venus are clustered over this range of length scales, with a statistical certainty of >99%.

We next investigate the distribution of coronae as a function of elevation. Again, we take a Monte Carlo approach. For each planetary radius R, we plot the fraction of coronae that lie at an elevation higher than R (Fig. 3). We have also generated such plots for 100 randomly distributed points that fall outside the Magellan data gaps. Interestingly, the observed curve lies above all of the random curves for elevations between about 6050.5 and 6051.7 km, but crosses all the random curves and lies below them between about
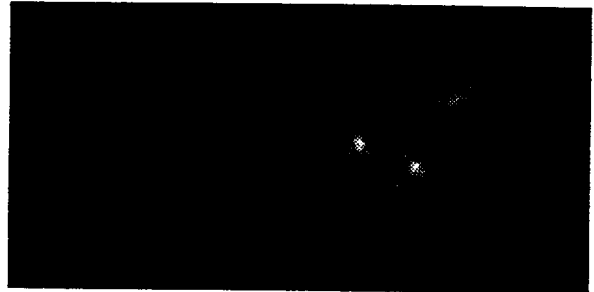
Fig. 4. Grey-scale map of the concentration of coronae and related features on Venus. Latitude limits are ±90°, central longitude is 180°.

6052.4 and 6053.4 km. This shape means that coronae on Venus tend to be concentrated away from both the lowest and highest elevations on the planet, instead clustering around an elevation of roughly 6052 km.

We are exploring several statistical models for the spatial clustering of the coronae on Venus, including clustering along great circles and clustering about a point. The best of these simple models appears to be clustering about a point near the equator at around 240°E longitude. The reason for this is shown by Fig. 4, which is a grey-scale representation of a map (Plate Carrée projection) of corona concentration on Venus. The large cluster of coronae at this location is evident, and our results show that this cluster is significant at a high level of certainty.

Two aspects of the observed corona distribution may have significant geologic and geophysical implications. The clustering at intermediate elevations may reflect preferential preservation of coronae at such elevations. The highest elevations on Venus tend to be the ones that are most tectonically disrupted [3]. With severe tectonic disruption, coronae in these higher regions may be more difficult to recognize amid other forms of tectonic overprinting. The lowest elevations on the planet, on the other hand, might be expected to be regions of preferential accumulation of lavas, covering coronae that lie there. The clustering of coronae around one geographic location we interpret as related to mantle processes. We have argued on the basis of Magellan SAR and altimetry data that coronae form when rising mantle diapirs impinge on the underside of the venusian lithosphere [2,4,5]. If this is correct, then our observations suggest that the deep mantle of Venus is anomalously hot below the large corona cluster, and hence is an especially effective source of the mantle diapirs that we believe produce coronae.

References: [1] Phillips R. J. et al., *JGR*, in press. [2] Squyres S. W. et al., *JGR*, in press. [3] Solomon S. C. et al., *JGR*, in press. [4] Stofan et al. *JGR*, in press. [5] Janes et al., *JGR*. in press.

N93-14384

MICROWAVE SCATTERING AND EMISSION PROPERTIES OF LARGE IMPACT CRATERS ON THE SURFACE OF VENUS.

N. J. S. Stacy, D. B. Campbell, and C. Devries, Department of Astronomy, Cornell University, Ithaca NY 14853, USA.

Many of the impact craters on Venus imaged by the Magellan synthetic aperture radar (SAR) have interior floors with oblique incidence angle backscatter cross sections 2 to 16 times (3 dB to 12 dB) greater than the average scattering properties of the planet's surface. Such high backscatter cross sections are indicative of a high degree of wavelength-scale surface roughness and/or a high intrin-
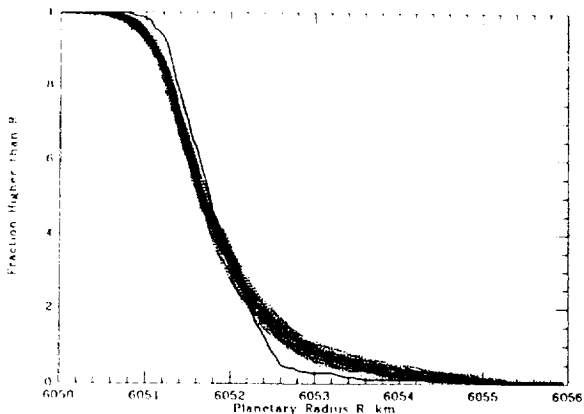

Fig. 3. Fraction of coronae lying at a planetary radius greater than R as a function of R (solid line), and 100 random distributions (dashed lines). Random distributions contain no points in the Magellan data gaps.
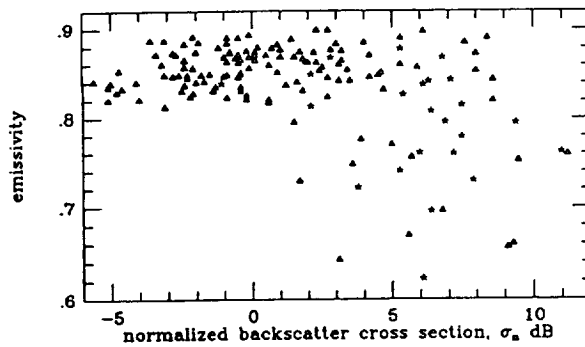
Fig. 1. Microwave emissivity vs. normalized backscatter cross section σ_n of the floors of 158 impact craters with diameters >30 km. Impact craters associated with parabolic-shaped radar-dark halos are shown as ★, craters without an associated parabolic halo are shown as △. σ_n values are dB with respect to the normalizing scattering used in the processing of Magellan SAR data [3].

sic reflectivity of the material forming the crater floors. Fifty-three of these (radar) bright floored craters are associated with 93% of the parabolic-shaped radar-dark features found in the Magellan SAR and emissivity data, features that are thought to be among the youngest on the surface of Venus [1]. It was suggested by Campbell et al. [1] that either the bright floors of the parabolic feature parent craters are indicative of a young impact and the floor properties are modified with time to a lower backscatter cross section or that they result from some property of the surface or subsurface material at the point of impact or from the properties of the impacting object. As a continuation of the work in [1] we have examined all craters with diameters greater than 30 km (except 6 that were outside the available data) so both the backscatter cross section and emissivity of the crater floors could be estimated from the Magellan data.

A plot of the emissivity vs. normalized backscatter cross section of the floors of 158 craters with diameters >30 km (Fig. 1) shows little direct correlation between crater floor backscatter brightness and emissivity. One-third of the measured crater floors have normalized backscatter cross sections greater than 3 dB above average and 36% of these have an associated radar-dark parabolic feature. Most of the crater floors have emissivities near 0.85, the typical value for the venusian surface, but many are slightly higher, which may be due to the slight increase in emissivity observed with

increased surface roughness [2]. Twenty-five (or 16%) of the craters have floor emissivities <0.81. In an attempt to understand if these low emissivities are the result of elevated Fresnel reflectivities and hence compositional differences in the crater floor material, we plotted the measured emissivities vs. incidence angle along with the theoretical emissivity for a smooth surface with dielectric constant ε = 5.0 (Fig. 2). At the highest incidence angle of the cycle 1 Magellan observations the theoretical emissivity drops to ~0.76, indicating that some of the low emissivities measured at the higher incidence angles may not be the result of compositional differences.

References: [1] Campbell D. B. et al. (1992) JGR, in press. [2] Ulaby F. T. et al. (1982) In Microwave Remote Sensing Active and Passive, 2, 949–966, Addison-Wesley. [3] SDPS–101 (1991) NASA/JPL Magellan Project SIS F–BIDR, Appendix F, 31–33.

N93-14385

THE EFFECTS OF VENUSIAN MANTLE CONVECTION WITH MULTIPLE PHASE TRANSITIONS.

V. Steinbach[1], D. A. Yuen[2], and U. R. Christensen[3], [1]Institut für Geophysik u. Meteorologie, Universität zu Köln, Köln, Germany, [2]Minnesota Supercomputer Institute and Department of Geology and Geophysics, University of Minnesota, Minneapolis MN 55415, USA, [3]Max-Planck-Institut für Chemie, Mainz, Germany.

Recently there was a flurry of activities in studying the effects of phase transitions in the Earth's mantle. From petrological and geophysical considerations, phase-transition would also play an important role in venusian dynamics. The basic differences between the two planets are the surface boundary conditions both thermally and mechanically. In this vein we have studied time-dependent mantle convection with multiple phase transitions and depth-dependent thermal expansivity ($\alpha \sim \rho^{-6}$, based on high-pressure and temperature measurements by Chopelas and Boehler [1]). Both the olivine-spinel and spinel-perovskite transitions were simulated by introducing an effective thermal expansivity, as described in [2]. Used together with the extended Boussinesq Approximation [3] this method serves as a powerful tool to examine the effects of phase transitions on convection at relatively low computational costs.

In comparison to models with constant α the decrease of α injects vigor into lower mantle convection and stabilizes long aspect ratio flows. Hence the tendency to layered flows is increased.

Due to its positive Clapeyron slope the olivine-spinel transition increases the effective Rayleigh number in the upper mantle. This effect also stabilizes layered convection. Consequently, layered flows with a third thermal boundary layer at around 700 km depth and very long aspect ratio flows in the upper mantle can be observed (Fig. 1). The amount of exchange of matter between upper and lower mantle depends on the Clapeyron slopes and the "widths" of the
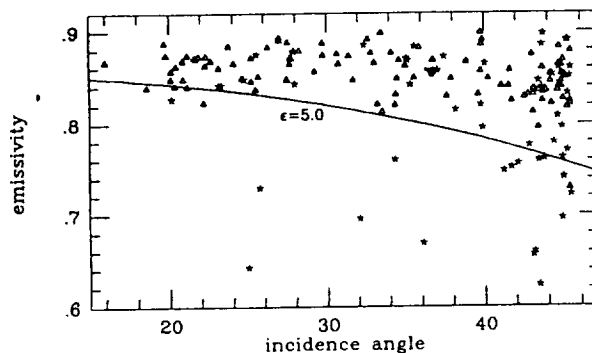

Fig. 2. Microwave emissivity vs. incidence angle of the floors of 158 impact craters with diameters >30 km with the theoretical emissivity for a smooth surface material with dielectric constant ε = 5.0. Impact craters with $\sigma_n \geq 3.0$ dB are shown as ★ and with $\sigma_n < 3.0$ dB as △.

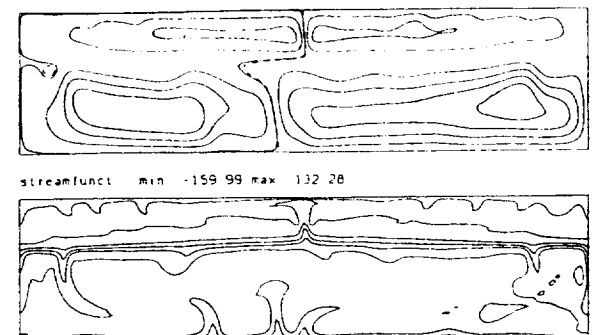streamfunct   min -159 99 max   132 28

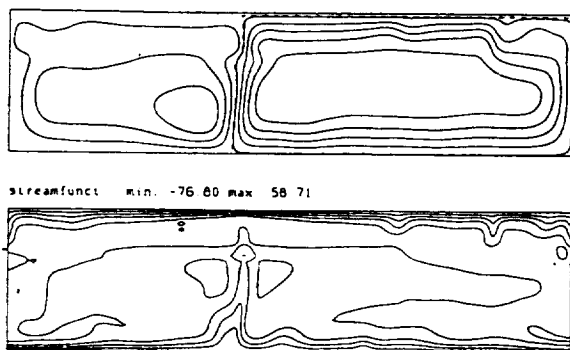Fig. 1. Streamlines (top) and isotherms (bottom) of a flow with two phase transitions. Rayleigh number (Ra) is 10^7.

Fig. 2. Same diagram as Fig. 1, but at lower Rayleigh number (Ra = 2 × 10⁶).

phase transitions. The olivine-spinel transition may give rise to secondary instabilities emanating from the thermal boundary layer, as it can be also observed in flows with both temperature- and pressure-dependent viscosity included.

As argued first by Kaula [4], the venusian mantle may contain much less water than the Earth's, resulting in a higher viscosity and therefore lower Rayleigh number. Our calculations confirm that lower Rayleigh number flows show less tendency to be layered (Fig. 2), as observed by Christensen and Yuen [2]. For terrestrial planets like Venus and Earth this means that the form of convection may undergo several changes during the planet's history. In early stages (characterized by high Rayleigh number) phase transitions act as a barrier to convective flows, resulting in low heat flows and cooling rates.

As the Rayleigh number decreases with time, the flow becomes more and more penetrative, the upper mantle heats up, and the lower mantle and core cool down, while heat flow increases despite the lower Rayleigh number. Due to the high cooling rate in this stage the vigor of convection decreases faster and the flow may undergo another transition from time dependent to steady state.

Thus the combined effects of a relatively dry venusian mantle and phase transition would facilitate the cooling of Venus in spite of its having a higher surface temperature. Venus is therefore in a stage of planetary evolution that is characterized by much less tectonic and volcanic activity. On the other hand, convection models with phase transitions [e.g.,5] and global seismic tomography suggest that the present-day Earth is in an earlier state of layered convection.

References: [1] Chopelas A. and Boehler R. (1989) *GRL, 16,* 1347–1350. [2] Christensen U. R. and Yuen D. A. (1985) *JGR, 90,* 10291–10300. [3] Steinbach V. et al. (1989) *GRL, 16,* 633–636. [4] Kaula W. M. (1990) *Science, 247,* 1191–1196. [5] Machetel P. and Weber P. (1991) *Nature, 350,* 55–57.

N93-14486

EVIDENCE FOR LIGHTNING ON VENUS. R. J. Strangeway, Institute of Geophysics and Planetary Physics, University of California, Los Angeles CA 90024, USA.

Lightning is an interesting phenomenon both for atmospheric and ionospheric science. At the Earth lightning is generated in regions where there is strong convection. Lightning also requires the generation of large charge-separation electric fields. The energy dissipated in a lightning discharge can, for example, result in chemical reactions that would not normally occur. From an ionospheric point of view, lightning generates a broad spectrum of

electromagnetic radiation. This radiation can propagate through the ionosphere as whistler mode waves, and at the Earth the waves propagate to high altitudes in the plasmasphere where they can cause energetic particle precipitation [1]. The atmosphere and ionosphere of Venus are quite different from at the Earth, and the presence of lightning at Venus has important consequences for our knowledge of why lightning occurs and how the energy is dissipated in the atmosphere and ionosphere.

As discussed here, it now appears that lightning occurs in the dusk local time sector at Venus. Since the clouds are at much higher altitudes at Venus than at the Earth, we expect lightning to be primarily an intracloud phenomenon [2]. It is possible, however, that lightning could also propagate upward into the ionosphere, as has been observed recently at the Earth [3]. This may explain the high-frequency VLF bursts detected at low altitudes in the nightside ionosphere by the Pioneer Venus Orbiter, as described below.

Some of the early evidence for lightning on Venus came from the Venera landers, which carried loop antennas to detect electromagnetic radiation in the VLF range [4]. These sensors detected sporadic impulsive signals. Since the detectors were sensitive to magnetic rather than electric field fluctuations, it is highly unlikely that these impulses were generated locally by the interaction of the lander and the atmosphere. An optical sensor was flown on Venera 9, and this instrument also detected occasional impulsive bursts [5].

The largest body of data used as evidence for lightning on Venus comes from the Pioneer Venus Orbiter electric field detector. This is a small plasma wave experiment that measures wave electric fields in the ELF and VLF range. Because of restrictions on power, weight, and telemetry, the instrument has only four frequency channels (100 Hz, 730 Hz, 5.4 kHz, and 30 kHz). Highly impulsive signals were detected at low altitudes in the nightside ionosphere in all four channels [6]. However, the ambient magnetic field at Venus is small, only a few tens of nanoteslas, and the electron gyrofrequency is usually less than 1 kHz, and often less than 500 Hz. Since there is a stop band for electromagnetic wave propagation between the electron gyrofrequency and plasma frequency, bursts detected in the higher channels do not correspond to freely propagating modes. In subsequent studies [7] F. L. Scarf and colleagues adopted a convention that bursts must be detected at only 100 Hz (i.e., below the gyrofrequency) for the bursts to be considered as lightning-generated whistlers. With this definition it was found that the signals tended to cluster over the highland regions [8], and Scarf and Russell speculated that the VLF bursts were whistler mode waves generated by lightning associated with volcanic activity. This was a highly controversial interpretation, which was subsequently criticized by H. A. Taylor and colleagues [9,10]. Among other criticisms, they pointed out that the studies of Scarf and colleagues were not normalized by the spacecraft dwell time, which tended to exaggerate the altitude dependence of the 100-Hz bursts. However, other studies [11] have shown that the burst rate does maximize at lowest altitudes. Nevertheless, it is important to note that the apparent geographic correlation may in fact be a consequence of the restricted longitudinal coverage of the Pioneer Venus Orbiter for each season of nightside periapsis. Periapsis in the early seasons was maintained at low altitudes, but was allowed to rise in later seasons. The periapsis longitude only covered the lowlands in these later seasons, and since the data were acquired at higher altitude, the event rate decreased. However, this decrease was mainly a consequence of the change in altitude, rather than a change in planetary longitude.

Although Scarf et al. only considered 100-Hz bursts as evidence for lightning, since these waves could be whistler mode, Russell et

al. [12] also considered the high-frequency bursts as possible lightning events. They found that while the high-frequency events did show some longitudinal dependence, the data were better ordered by local time, with the peak rates occurring in the dusk local time sector. Consequently, it is now thought that the lightning is not associated with volcanic activity. Rather, it is due to weather processes in an analogous manner to lightning at the Earth, which tends to peak in afternoon local time sector [13].

The evidence for lightning at Venus from the VLF data now falls into two classes. The higher frequency bursts show the local time dependence, and the rate also decreases most quickly as a function of altitude [14]. These bursts are thought be a local response to the lightning discharge, and therefore are best suited for determining planetwide rates. The rates are found to be comparable to terrestrial rates. However, it is still not clear how the high-frequency signals enter the ionosphere. On the other hand, about 50% of the 100-Hz bursts are clearly whistler mode signals, as evidenced by the wave polarization [15]. These signals can propagate some distance in the surface ionosphere waveguide before entering the ionosphere. The 100-Hz bursts are therefore less reliable in determining the light-ning rate, or the main source location.

Perhaps the least ambiguous evidence for lightning on Venus has come from the plasma wave data acquired by the Galileo spacecraft during the Venus flyby [16]. Unlike Pioneer Venus, Galileo was able to measure plasma waves at frequencies up to 500 kHz. The plasma wave experiment detected nine impulsive signals that were several standard deviations above the instrument background while the spacecraft was at a distance of about five planetary radii. Although some of the lower-frequency bursts could possibly have been Langmuir wave harmonics, the higher-frequency bursts were probably due to lightning. The bursts were at sufficiently high frequency to pass through the lower-density nightside ionosphere as freely propagating electromagnetic radiation.

While there is a strong body of evidence for the existence of lightning at Venus, there are still many questions that remain. From an ionospheric physics point of view, it is not clear how high-frequency signals can propagate through the ionosphere. The low-frequency signals do appear to be whistler mode waves, although there is still some doubt [17]. Also, although whistler mode propa-gation may be allowed locally, it is not necessarily certain that the waves can gain access to the ionosphere from below. For example, whistler mode propagation requires that the ambient magnetic field passes through the ionosphere into the atmosphere below. It is possible that the ionosphere completely shields out the magnetic field. With regard to atmospheric science, there are several ques-tions that require further study. First, can charge separation occur in clouds at Venus? Is there sufficient atmospheric circulation to cause a local time dependence as observed in the VLF data? Do Venus clouds discharge to the ionosphere, and so cause strong local electromagnetic or electrostatic signals that could explain the high-frequency VLF bursts? While some of these questions may be answered as low-altitude data are acquired during the final entry phase of the Pioneer Venus Orbiter, many questions will still remain.

References: [1] Inan U. S. and Carpenter D. C. (1987) *JGR, 92*, 3293–3303. [2] Russell C. T. et al. (1989) *Adv. Space Res., 10(5)*, 37–40. [3] Franz R. C. et al. (1990) *Science, 249*, 48–51. [4] Ksanfomaliti L. V. et al. (1983) In *Venus*, 565–603, Univ. of Arizona, Tucson. [5] Krasnopol'sky V. A. (1983) In *Venus*, 459–483, Univ. of Arizona, Tucson. [6] Taylor W. W. L. et al. (1979) *Nature, 279*, 614–616. [7] Scarf F. L. et al. (1980) *JGR, 85*, 8158–8166. [8] Scarf F. L. and Russell C. T. (1983) *GRL, 10*, 1192–1195. [9] Taylor H. A. Jr. et al. (1985) *JGR, 90*, 7415–7426. [10] Taylor H. A. Jr. et al. (1989) *JGR, 94*, 12087–12091. [11] Ho C.-M. et al. (1991) *JGR, 96*, 21361–21369. [12] Russell C. T. et al. (1989) *Icarus, 80*, 390–415. [13] Russell C. T. (1991) *Space Sci. Rev., 55*, 317–356. [14] Ho C.-M. et al. (1992) *JGR*, in press. [15] Strangeway R. J. (1991) *JGR, 96*, 22741–22752. [16] Gurnett D. A. et al. (1991) *Science, 253*, 1522–1525. [17] Grebowsky J. M. et al. (1991) *JGR, 96*, 21347–21359.

N93-14487

VOLCANISM BY MELT-DRIVEN RAYLEIGH-TAYLOR INSTABILITIES AND POSSIBLE CONSEQUENCES OF MELTING FOR ADMITTANCE RATIOS ON VENUS.

P. J. Tackley[1], D. J. Stevenson[1], and D. R. Scott[2], [1]Division of Geological and Planetary Sciences, Caltech, Pasadena CA 91125, USA, [2]Department of Geological Sciences, University of Southern California, Los Angeles CA 90089, USA.

A large number of volcanic features exist on Venus, ranging from tens of thousands of small domes to large shields and coronae. It is difficult to reconcile all these with an explanation involving deep mantle plumes, since a number of separate arguments lead to the conclusion that deep mantle plumes reaching the base of the lithosphere must exceed a certain size. In addition, the fraction of basal heating in Venus' mantle may be significantly lower than in Earth's mantle, reducing the number of strong plumes from the core-mantle boundary. In three-dimensional convection simula-tions with mainly internal heating, weak, distributed upwellings are usually observed.

Description of Instability: We present an alternative mecha-nism for such volcanism, originally proposed for the Earth [1] and for Venus [2], involving Rayleigh-Taylor instabilities driven by melt buoyancy, occurring spontaneously in partially or incipiently molten regions. An adiabatically upwelling element of rock expe-riences pressure-release partial melting, hence increased buoyancy and upwelling velocity. This positive feedback situation can lead to an episode of melt buoyancy driven flow and magma production, with the melt percolating through the solid by Darcy flow. The percolation and loss of partial melt diminishes the buoyancy, leading to a maximum upwelling velocity at which melt percolation flux is equal to the rate of melt production by pressure-release melting.

Application to Venus: The instability has been thoroughly investigated and parameterized using finite-element numerical models, and hence its applicability to Venus can be assessed. Numerical convection simulations and theoretical considerations indicate that Venus' interior temperature is likely hotter than Earth's, hence the depth of intersection of the adiabat with the dry solidus may be appreciably deeper. In the regions of distributed broad-scale upwelling commonly observed in internally-heated convection simulations, partial melt may thus be generated by the adiabatically upwelling material, providing the necessary environ-ment for these instabilities to develop. Scaling to realistic material properties and melting depths, the viscosity at shallow depth must be 10^{19} Pa.s or less, leading to a period of self-perpetuating circulation and magma production lasting ~30 Ma, magma produc-tion rates of ~1000 km^3/Ma, and lengthscales of ~250 km.

Geoid, Topography, and Viscosity Profiles: Partial melt and buoyant residuum represent density anomalies that are of the same
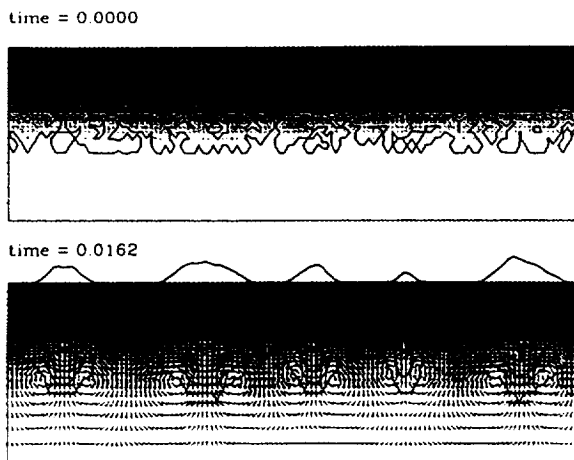
time = 0.0000

time = 0.0162

Fig. 1. Finite-element simulation showing the growth of melt-driven instabilities at the top of the mantle (depth of box ~160 km) from initially small (<0.1%) random partial melt perturbations. Temperature (shaded), velocity (arrows), partial melt distribution (contours, at 0 and intervals of 2.5%), melt production rate per unit area (on top). Time nondimensionalized to D^2/κ.

order as thermal anomalies driving mantle flow. Density anomalies equivalent to 100 K are obtained by only 1% partial melt or buoyant residuum, which is 3% depleted. These density effects are expected to have an effect on geoid and topography caused by one of these instabilities, and possibly the geoid and topography caused by thermal plumes.

Comparison of mantle geotherms for Venus (derived both from numerical simulations and from observations combined with theory) with an experimentally determined dry solidus for peridotite [3] indicate that the average geotherm passes close to or even exceeds the dry solidus at a depth of around 90 km. Thus, for any reasonable viscosity law, such as in [4], a region of lower viscosity is expected at shallow depth. This contradicts several geoid/topography studies based on simple mantle models, which require no low-viscosity zone. We investigate the possibility that the presence of buoyant residuum and partial melt at shallow depth may account for this discrepancy.

Global geoid modeling using the technique described in [5] indicates that a possible way to satisfy the long wavelength admittance data is with an Earth-like viscosity structure and a concentration of mass anomalies close to the surface, compatible with a shallow layer of buoyant residuum and/or partial melt. Geoid and topography signatures for local features, specifically Rayleigh-Taylor instabilities and thermal plumes with partial melting, are currently being evaluated and compared to data.

References: [1] Tackley P. J. and Stevenson D. J. (1990) *Eos, 71*, 1582. [2] Tackley P. J. and Stevenson D. J. (1991) *Eos, 72*, 287. [3] Takahashi E. (1986) *JGR, 91*, 9367–9382. [4] Borch R. S. and Green H. W. (1987) *Nature, 330*, 345. [5] Hager B. H. and Clayton R. W. (1989) In *Mantle Convection*. 657–764.

N93-14388

CAN A TIME-STRATIGRAPHIC CLASSIFICATION SYSTEM BE DEVELOPED FOR VENUS?   K. L. Tanaka and G. G. Schaber, U.S. Geological Survey, 2255 N. Gemini Drive, Flagstaff AZ 86001, USA.

Magellan radar images reveal that Venus' exposed geologic record covers a relatively short and recent time span, as indicated by the low density of impact craters across the planet [1]. Therefore, because impact cratering in itself will not be a useful tool to define

geologic ages on Venus, it has been questioned whether a useful stratigraphic scheme can be developed for the planet. We believe that a venusian stratigraphy is possible and that it can be based on (1) an examination of the rationale and methods that have been used to develop such schemes for the other planets, and (2) what can be gleaned from Magellan and other datasets of Venus.

Time-stratigraphic classification systems or schemes have been derived for all other terrestrial planetary bodies (Earth, Moon, Mars, Mercury) [2–5] because the schemes are useful in determining geologic history and in correlating geologic events across the entire surface of a planet. Such schemes consist of a succession of time-stratigraphic units (such as systems and series) that include all geologic units formed during specified intervals of time. Our terrestrial stratigraphy is largely based on successions of fossil assemblages contained in rock units and the relations of such units with others as determined by their lateral continuity and superposition and intersection relations. To define geologic periods on the other planets, where fossil assemblages cannot be used, major geologic events have been employed (such as the formation of large impact basins on the Moon and Mercury [3,5] or the emplacement of widespread geologic terrains on Mars [4,6]). Furthermore, terrestrial schemes have been supplemented by absolute ages determined by radiometric techniques; on the Moon and Mars, relative ages of stratigraphic units have been defined according to impact cratering statistics [3,4].

Stratigraphies are by nature provisional, and they are commonly revised and refined according to new findings. Boundaries of stratigraphic units are difficult to define precisely on a global scale; refinements such as newly discovered marker beds may require changes in nomenclature or minor adjustments in absolute- or relative-age assignments. Although the martian stratigraphy has been revised only once [4], the lunar stratigraphy is in its fifth major version [3] and continues to be refined in detail [7]. Terrestrial stratigraphy has been revised many times in its development over the past century. Although the Galilean satellites of Jupiter are being mapped geologically, there has been insufficient basis or need for the development of formal stratigraphies for them [8].

Given the current state of stratigraphic methods and their application to the planets, what are the prospects for a stratigraphy for Venus? To address this question, we need to examine two related questions: (1) Has the planet experienced widespread geologic events or processes resulting in the broad distribution of coeval materials (which would form the basis for time-stratigraphic units)? (2) Can we unravel the complex stratigraphic-tectonic sequences apparent on Venus? (Or can superposition relations and relative age be reasonably well established from Magellan radar or other datasets?)

Already a variety of potential venusian stratigraphic markers based on widespread geologic events and activities are emerging (Table 1). First, the global distribution of impact craters indicates that Venus had a global resurfacing event or series of events that ended about 500 ± 300 m.y. ago [1]. Presumably, most of the plains material that covers about 80% of the planet formed during that resurfacing and can be included in a stratigraphic system. Underlying much of the plains material are complex ridged or tesselated terrain materials; they must be older than the plains material, but their structures may in part be contemporary with its emplacement [9]. Postdating the plains material are most of the impact craters, many of the largest volcanic shields, and regional fracture belts [1]. Most of the plains are cut by lineations, narrow grabens, and wrinkle ridges. Perhaps such widespread structures may provide a basis for defining regional or even nearly global stratigraphic markers to

- Relatively pristine lava-flow surfaces as indicated by radar backscatter characteristics
- Preserved crater halos and surface splotches
- Widespread fractures, grabens, and ridges
- Plains material
- Complex ridged terrain (tesserae)

which local volcanic and tectonic features and units may be correlated. Finally, very young time markers may be defined by the degree of weathering or eolian modification of a surface. For example, lavas flows at Maat Mons show a decrease in radar contrast and brightness with increasing age (based on superposition relations) [10]. Also, some impact craters retain radar-dark (less commonly radar-bright) halos perhaps consisting of impact debris; apparently related to the halos are dark and light surface "splotches" that may represent relatively young debris and shock-induced surface roughness produced by impacting bolides of a narrow size range that disintegrated deep down in the dense venusian atmosphere [1]. As these features age, they may become less distinct relative to surrounding terrains.

Initially, superposition relations were difficult to ascertain among various geologic units on Venus because of the general difficulty in perceiving topography on the radar images. (Exceptions, such as thick lava flows or domes, were relatively rare). Still, many stratigraphic relations can be determined in plan view, because overlying materials tend to mute or embay the texture and structure of underlying surfaces. More recently, Magellan has produced repeated radar images of selected areas, which permits stereoradargrammetry [11]. In addition, synthetic-parallax stereo-images (produced from merged Magellan images and altimetry) commonly show the association between geologic/tectonic-terrain units and regional topography.

Magellan radar mapping shows that Venus has had a complex geologic history that can be unraveled to a large extent from available data. Even though exposed rocks apparently record only a small portion of the planet's history, stratigraphic markers are sufficient to permit the development of a useful scheme of time-stratigraphic units. Such a scheme should result from NASA's new Venus Geologic Mapping (VGM) Program, which will cover the entire planet.

References: [1] Schaber G. G. et al., *JGR*, special Magellan issue, in press. [2] Palmer A. R. (1983) *Geology, 11*, 503. [3] Wilhelms D. E. (1987) *USGS Prof. Paper 1348*, Ch. 7. [4] Tanaka K. L. (1986) *Proc. LPSC 17th*, in *JGR, 91*, E139. [5] Spudis P. D. and Guest J. E. (1987) In *Mercury* (F. Vilas et al., eds.), 118, Univ. of Arizona, Tucson. [6] Scott D. H. and Carr M. H. (1978) *USGS I-Map 1083*. [7] Ryder G. et al. (1991) *Geology, 19*, 143. [8] Lucchitta B. K. (1992) personal communication. [9] Squyres S. W. et al., *JGR*, special Magellan issue, in press. [10] Arvidson R. E. et al. (1992) *Eos, 73*, 161. [11] Moore H. G., this volume.

N93-14389

STRUCTURAL CHARACTERISTICS AND TECTONICS OF NORTHEASTERN TELLUS REGIO AND MENI TESSERA.

T. Törmänen, Department of Astronomy, University of Oulu, SF–90570, Oulu, Finland.

Introduction: Tellus Regio-Meni Tessera region is an interesting highland area characterized by large areas of complex ridged

terrain (CRT [1]) or tessera terrain [2]: Tellus Regio and Meni Tessera areas and deformed plains areas between the highland tesserae. The area was previously studied from the Venera 15/16 data and typical characteristics of complex tessera terrain of Tellus Regio were analyzed and a formation mechanism proposed [3]. Apparent depths of compensation of ~30–50 km were calculated from Pioneer Venus gravity and topography data. These values indicate predominant Airy compensation for the area [4,5]. Regional stresses and lithospheric structures were defined from analysis of surface structures, topography, and gravity data [6]. In this work we concentrate on northeastern Tellus Regio and Meni Tessera, which are situated north and west of Tellus Regio. Structural features and relationships are analyzed in order to interpret tectonic history of the area. Study area was divided into three subareas: northeastern Tellus Regio, Meni Tessera, and the deformed plain between them.

Description of Areas and Interpretations of Structures: *Northeastern Tellus Regio.* Northeastern Tellus Regio is defined here as a roughly triangle-shaped area between longitudes 84° and 92°E and latitudes 46° and 53°N. The ridgelike northern end of northeastern Tellus Regio is cut by a fracture belt at 53°N, 85°E, but the overall trend of the CRT is continued by CRT of Dekla Tessera. Together these areas form a >2000-km-long south-concave arc of tesserae, which extends to Kamari Dorsa south of Audra Planitia and west of Laima Tessera.

The northernmost area of northeastern Tellus Regio is characterized by wide, arcuate ridgelike features, which form the major structural element of the CRT in this area. The longest one of these ridgelike features is oriented in a northwest-southeast direction and it forms the curving northeastern edge of the CRT of Tellus Regio ("A" in Fig. 1). It is ~660 km long, 4–40 km wide, and has gentle slopes. The east-facing slope is steeper and more pronounced. The other two ridgelike structures of the CRT are situated southwest of the first one ("B" and "C" in Fig. 1). They are less distinct and shorter: ~40 km wide and 280 km long ("B") and ~30–85 km wide and 230 km long ("C"). Their general orientation is west-northwest/east-southeast. These ridgelike features end abruptly in the northwest, but in the south and southeast they merge to more topographically flat-looking tessera surface. The large ridgelike features of northeastern Tellus Regio are composed of narrower (widths 1–2.5 km), closely spaced, linear, and generally ridges tens of kilometers in length.

The narrow ridges and the larger-scale ridgelike features comprising them appear to be the oldest structural elements of the CRT. In the topography data the widest ridgelike patterns can be distinguished. Their heights are typically several hundred meters below or about the mean planetary radius of 6052 km. The topography and morphology of ridges support compressional origin. There are oval-shaped intratessera plains depressions and troughlike features in between the major ridgelike structures of the CRT in several places (e.g., 49°N, 87°E, "D"). These postdate the ridgelike features of the CRT. The oval plains areas have smooth radar-dark surfaces and are obviously covered by lavas. There are narrow (1–3 km wide) ridges on the edges of the oval-shaped plains, which follow the curvature of the edges of the plains. These ridges appear to have formed in a later episode of compression in the area.

There is a 30-km-wide belt of narrow linear ridges adjacent to the northeastern tessera border. The widths of these ridges are 1–2 km and are several tens of kilometers in length. These ridges apparently formed due to compressional stresses oriented perpendicular to the border of CRT (approx. northeast-southwest). These ridges are not
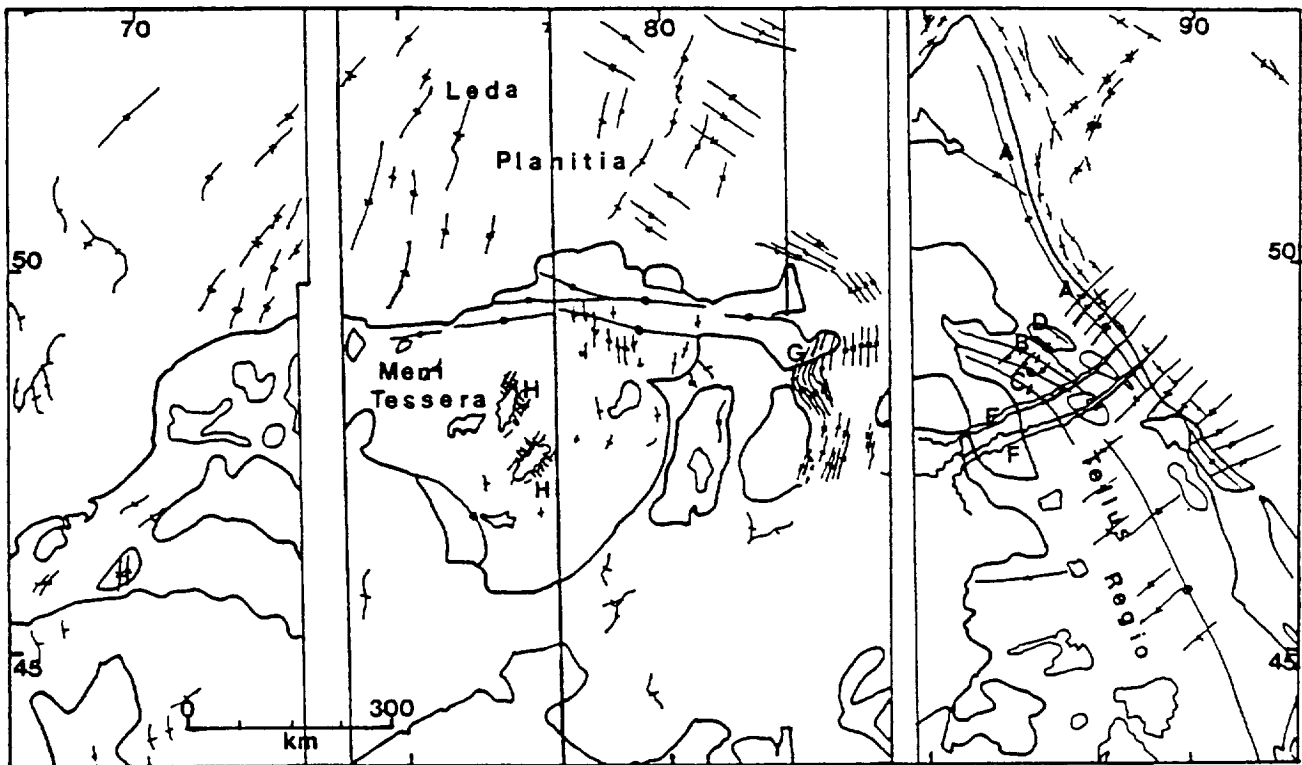
Fig. 1. Sketch of a map of northeastern Tellus Regio and Meni Tessera region. Mercator projection. CRT or tessera areas are outlined by a slightly thicker line. Lines with small cross lines represnt ridges, lines with crosses represent fractures and graben, lines with circles are troughs.

part of the CRT because their spacing is larger and they do not form a similar structural pattern to the ridges of the neighboring CRT.

The ridges of the CRT are extensively cut by northeast-southwest-oriented flat-floored valleys. These features are interpreted to be graben and manifest moderate tensional strain in the area. The graben cut almost orthogonally both the ridges of the CRT and the ridges bordering the CRT but they rarely cut across the intratessera plains. Their typical widths are 1.5–3.5 km with lengths 20–150 km.

Two large, linear depressions in the area follow the strike of the graben ("E" and "F" in Fig. 1). Based on their distinct morphological characteristics (wide scarp-bounded openings on the plain, sinuous edges, widenings along the strike and up to 20 km long orthogonal to the strike-oriented segments) they are classified as valley networks of subtype III [7,8]. Valley networks of Venus resemble sapping valleys of the Earth and are intepreted to have formed by the fluid motion through an underground fracture system [9,10]. These two valley networks of northeastern Tellus Regio cut across the CRT, but are more pronounced on the plains within and adjacent to the CRT than on the CRT itself. They have similar orientation to the graben, which shows that the valley formation probably occurred along two large preexisting graben. The northeastern Tellus Regio is cut by a 560-km-long northwest-southeast-striking linear trough (Medeina Chasma). Most of the northeast-southwest-oriented graben cross-cut it, which shows that the trough formed earlier.

Inferred Sequence of Deformation: (1) The narrow linear ridges and larger ridgelike structures of the CRT form in compressional folding and thrusting. (2) The ridge belt along the northeastern edge of Tellus Regio forms in northeast-southwest compression. (3) Extensional deformation results in widespread graben formation. (4) Formation of intratessera plains and subsequent compres-

sional deformation occurs along the edges. (5) Valley networks and some extensional graben form. Medeina Chasma and other long troughs of the area probably formed during phase 2. This sequence agrees well with both earlier and other recent studies of the area [3,11] and analyses of deformation of many other regions of CRT or tessera [1,12,13].

The Deformed Area Between Northeast Tellus Regio and Meni Tessera: The troughlike area is characterized by several irregular patches of CRT, which seem to be remnants of an earlier continuous CRT connecting Meni Tessera and Northeastern Tellus Regio. The CRT areas near eastern Meni Tessera have very similar structures as adjacent Meni Tessera. Linear, narrow fractures form up to 45-km-wide belts on the plain between the CRT areas. These fractures are oriented northwest-southeast in the northern part of the trough and they follow the dominant strike of fractures to the southeastern corner of northern Leda Planitia. They turn to a north-south direction in the trough. Fractures directed almost perpendicularly against a scarp-like, linear edge of the eastern extension of the Meni Tessera ("G" in Fig. 1) turn near the edge to the north-northeast and form a bend in the fracture pattern. The linear edge appears to be a fault (its strike can be traced also further to the west-southwest) and the bend in the fracture belt can be due to right-lateral shear. Fracture belts also cut into areas of CRT. Fractures are covered in some places by plains material, apparently lava flows. Fractures were probably formed by extensional deformation of the area, but later plains formation has covered them extensively.

Eastern and Central Meni Tessera: Meni Tessera is situated between latitudes 45° and 50°N and longitudes 67° and 83°E. It has narrow, topographically distinct extensions to the southeast and east. Its central part is composed of more equidimensional and topographically lower area of CRT. The northern part of Meni

Tessera is characterized by troughs, which define ~110–370-km-long and ~15–50-km-wide east-west-oriented segments of CRT. These elongated areas have some of the highest topography in the Meni Tessera. One of the segments forms the previously mentioned eastern extension of the CRT ("G" in Fig. 1). Although these elongated parts of the Meni Tessera do not have a similar strike as the ridgelike typography and morphology, and they are not composed of clear individual ridges, they do have a strike similar to the ridgelike components in northeastern Tellus Regio.

Structurally Meni Tessera CRT is more complex than northeastern Tellus Regio. The oldest underlying structures are curvilinear ridges, but they are wider and shorter (2–8 km wide and 10–30 km long) and more widely spaced than in northeastern Tellus. There does appear to be very fine ridgelike structures superposed on these ridges, but they can not always be distinguished from scarps and normal faults. The dominant direction of the ridges is to be north-south/northeast-southwest, but this orientation may be due to more later deformation and the original directions may not be observable any more. Near the eastern edge of central Meni Tessera the ridges follow the curving tessera border. The central parts of Meni Tessera are characterized by areas of orthogonal terrain of intersecting northeast-southwest and northwest-southeast graben ("H" in Fig. 1). This terrain has been partly covered by lavas of intratessera plains in the areas where it is visible. There are also places where graben cut across the border between the CRT and the plain, especially around western and northern edges of Meni Tessera.

The relationships between graben with different orientations is complex: North-south striking graben and individual scarps (probably normal faults) cut other features extensively in the eastern and northern parts of the central Meni Tessera. There are also graben oriented in the northeast-southwest direction, especially near the northwestern and southeastern borders, which cut ridges and northwest-southeast graben. In the central parts of the CRT there are northeast-southwest-oriented graben that cut other features, but these graben are frequently covered by lavas. There are also small areas where graben are not widespread or at least can not be distinguished from small-scale ridges or closely spaced faults. Deformation seems to have followed the same kind of basic sequence as in northeastern Tellus Regio except that there have been several different episodes of graben formation with both spatially and chronologically more complex relationships. Also, differences in orientation and morphology of ridges in Meni Tessera and northeastern Tellus Regio may reflect different original stress regimes. Although no major strike-slip faults were identified in Meni Tessera, there is evidence of probable shear deformation in nearby plains areas.

Discussion and Conclusions: Similarities in the topographic trends, especially the similar types of linear ridgelike features in northeastern Tellus Regio and corresponding elongated segments in northern Meni Tessera, which together form a roughly south-concave arc of topographically higher CRT, as well as some similarities with structures of the CRT of the easternmost Meni Tessera and western edge of northeastern Tellus Regio, indicate that these areas of CRT were probably earlier interconnected. The troughlike plain area between Meni Tessera and Tellus Regio is probably underlain by CRT, which has been disrupted and covered by lavas. The adjacent northern Leda Planitia is deformed by complex intersecting systems of fractures and ridges. Some of this deformation may reflect a presence of a covered basement of CRT. The arclike pattern of tesserae between Kamari Dorsa and northeastern Tellus Regio may also reflect an earlier larger area of tessera. Similar conclusions were earlier presented on the basis of analysis

of Venera data [14,15] and more recently by a comprehensive analysis of distribution and characteristics of tessera from Magellan images [16]. Based on this work, however, it is very hard to define exactly the original extent of the CRT in this region.

Tessera are proposed to form by hot-spot-related volcanism and tectonism [17,18] or by convection-driven tectonics above mantle downwellings [1,12,19]. The results of this work do not conclusively rule out either model. Analysis of structures and deformation shows that the earliest distinguishable deformation was compression, which was followed by widespread extension and volcanism (formation of intratessera plains). This result is in agreement with other studies [e.g., 1,3,11,13] and similar results have been used to support the mantle downwelling model [1,12], but in our opinion they do not leave out other possibilities.

The arclike arrangement of topographically higher ridgelike features in northeastern Tellus Regio and northern Meni Tessera is roughly similar in planform, but smaller than the Dekla Tessera–northeastern Tellus Regio arch in the north. These arcuate patterns of tessera are typical to the area between longitudes 0° and 150°E [16] and could tell us about the scales of deformation of the crust in these areas. Observed complex deformational sequences in the northeastern Tellus Regio–Meni Tessera region do support the idea that the CRT is probably a result of repeated deformation through different mechanisms [20]. We are currently analyzing in more detail structures in Meni Tessera and northern Tellus Regio and their relationships with topography, intratessera volcanism, and the deformation and volcanism on the adjacent plains.

References: [1] Bindschadler D. L. et al. (1992) *JGR,* submitted. [2] Barsukov V. L. et al. (1986) *Proc. LPSC 17th,* in *JGR, 91,* D378–D398. [3] Bindschadler D. L. and Head J. W. (1991) *JGR, 96,* 5889–5907. [4] Smrekar S. and Phillips R. J. (1990) *LPSC XXI,* 1176–1177. [5] Smrekar S. and Phillips R. J. (1992) *EPSL, 107,* 582–597. [6] Williams D. R. and Gaddis L. (1991) *JGR, 96,* 18841–18859. [7] Baker V. R. et al. (1992) *JGR,* submitted. [8] Komatsu G. and Baker V. R. (1992) *LPSC XXIII,* 715–716. [9] Gulick V. C. et al. (1992) *LPSC XXIII,* 465–466. [10] Komatsu G. et al. (1992) *LPSC XXIII,* 719–720. [11] Bindschadler D. L. and Tatsumura M. J. (1992) *LPSC XXIII,* 103–104. [12] Bindschadler D. L. et al. (1992) *JGR,* submitted. [13] DeCharon A. V. and Stofan E. R. (1992) *LPSC XXIII,* 289–290. [14] Sukhanov A. L. (1986) *Geotectonics, 20,* 294–305. [15] Nikishin A. M. (1990) *Earth Moon Planets, 50/51,* 101–125. [16] Ivanov M. A. et al. (1992) *LPSC XXIII,* 581–581. [17] Herrick R. R. and Phillips R. J. (1990) *GRL, 17,* 2129–2132. [18] Phillips R. J. et al. (1991) *Science, 252,* 651–658. [19] Bindschadler D. L. and Parmentier E. M. (1990) *JGR, 95,* 21329–21344. [20] Solomon S. C. et al. (1992) *JGR,* submitted.

N93-14390

EPISODIC PLATE TECTONICS ON VENUS. Donald Turcotte, Department of Geological Sciences, Cornell University, Ithaca NY 14853, USA.

Studies of impact craters on Venus from the Magellan images have placed important constraints on surface volcanism. Some 840 impact craters have been identified with diameters ranging from 2 to 280 km. Correlations of this impact flux with craters on the Moon, Earth, and Mars indicate a mean surface age of 0.5 ± 0.3 Ga. Another important observation is that 52% of the craters are slightly fractured and only 4.5% are embayed by lava flows. These observations led Schaber et al. [7] to hypothesize that a pervasive resurfacing event occurred about 500 m.y. ago and that relatively little surface volcanism has occurred since. An alternative hypothesis has been

proposed by Izenber et al. [3]. They suggested that the observations can be explained by a random distribution of small volcanic events.

Strom et al. [8] have pointed out that a global resurfacing event that ceased about 500 MYBP is consistent with the results given by Arkani-Hamed and Toksoz [1]. These authors carried out a series of numerical calculations of mantle convection in Venus yielding thermal evolution results. Their model 4 considered crustal recycling and gave rapid planetary cooling. They, in fact, suggested that prior to 500 MYBP plate tectonics was active in Venus and since 500 MYBP the lithosphere has stabilized and only hot-spot volcanism has reached the surface. Thus they suggested that the transition to a near pristine lithosphere was the result of the secular cooling of the planet.

In this abstract we propose an alternative hypothesis for the inferred cessation of surface volcanism on Venus. We hypothesize that plate tectonics on Venus is episodic. Periods of rapid plate tectonics result in high rates of subduction that cool the interior resulting in more sluggish mantle convection. With a cool viscous interior the surface lithospheric plate stabilizes and plate tectonics cease. The stable lithosphere thickness increases with time reducing the surface heat flow. As a result the interior temperature increases leading to an increase in the plume flux. Eventually the lithosphere is sufficiently thick and its gravitational instability initiates an episode of global subduction.

This hypothesis is illustrated qualitatively in Fig. 1. During a period of about 500 m.y. the lithosphere is globally stable and no plate tectonics occurs. During this period the lithosphere thickens, the surface heat flow decreases, and the mantle temperature increases. As the lithosphere thickens it becomes gravitationally unstable. Eventually this instability leads to a catastrophic global subduction event. In the model illustrated in Fig. 1 this event occurred 600 MYBP. At the time of the global lithospheric instability the mantle on Venus is expected to be considerably hotter and less viscous than on the Earth so that rapid subduction would occur. Without a lithosphere, vigorous mantle convection would lead to extensive volcanism, vigorous plate tectonics, a high surface heat flow, and a rapid cooling of the mantle. As the mantle cools the mantle convection and its surface manifestation, plate tectonics, become less vigorous. Eventually the global lithosphere stabilizes and plate tectonics ceases. In the model illustrated in Fig. 1 this occurs at 500 MYBP. The lithosphere thickens, the surface heat flow decreases, and the cycle repeats.
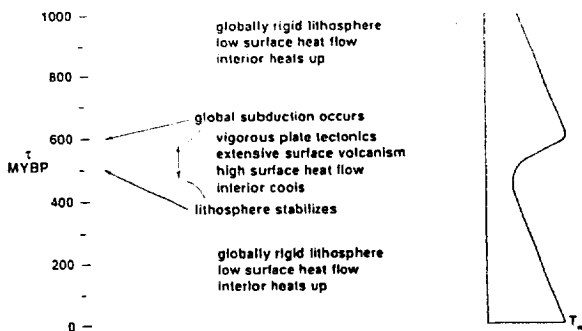

Fig. 1. Illustration of episodic tectonics on Venus for the last 1000 Ga. Also shown is the qualitative behavior of the mean mantle temperature T_m.

Assuming that the venusian lithosphere stabilized 500 MYBP, it is easy to determine its thermal structure, assuming no basal heating from mantle plumes and no partial delamination. After 500 m.y. the depth to the 1475-K isotherm is 290 km, the depth to the 1275-K isotherm is 180 km, and the depth to the 1125-K isotherm is 120 km. The corresponding depths for a venusian lithosphere with steady-state conductive heat transport are 34, 26, and 19 km respectively. The transient cooling of the lithosphere results in much greater thicknesses, almost an order of magnitude. Such a thick lithosphere is consistent with the large observed topographic and gravity anomalies.

McKenzie et al. [4] have argued that the perimeters of several large coronae on Venus, specifically Artemis, Latona, and Eithinoha, resemble terrestrial subduction zones in both platform and topography. Artemis chasma has a radius of curvature similar to that of the South Sandwich subduction zone on the Earth. Sandwell and Schubert [6] have shown that the morphologies of several coronae are in good agreement with the lithosphere flexure models that have been successful in explaining the sea floor morphology at ocean trenches on this planet. Their flexural profiles yield elastic lithosphere thicknesses of 37 km for Artemis, 35 km for Latona, 15 km for Eithinoha, 40 km for Heng-O, and 18 km for Freyja. These values are consistent with a thick conductive lithosphere. The presence of incipient subduction zones may be an indication of the onset of another episode of active plate tectonics.

References: [1] Arkani-Hamed J. and Toksoz M. N. (1984) *PEPI, 34,* 232–250. [2] Ghail R. and Wilson L. (1992) *LPSC XXIII,* 409–410. [3] Izenber N. K. et al. (1992) *LPSC XXIII,* 591–592. [4] McKenzie D. et al. (1992) *JGR,* submitted. [5] Parmentier E. M. and Hess P. C. (1992) *LPSC XXIII,* 1037–1038. [6] Sandwell D. T. and Schubert G. (1992) *LPSC XXIII,* 1209–1210. [7] Schaber G. G. et al. (1992) *LPSC XXIII,* 1213–1214. [8] Strom R. G. et al. (1992) *LPSC XXIII,* 1279–1380.

N93-14391

SCATTERING PROPERTIES OF VENUS' SURFACE.

G. L. Tyler, R. A. Simpson, M. J. Maurer, and E. Holmann, Center for Radar Astronomy, Stanford University, Stanford CA 94305-4055, USA.

Radar backscatter functions $\hat{\sigma}_0(\phi)$ for incidence angles between $0 \leq \phi \leq 4°–10°$ have been derived from Magellan altimetry radar echoes. The procedure includes constrained solution of a system of simultaneous equations for which the echo spectrum and echo time profile are inputs. A practical and workable set of constraints has been applied; optimization and improved results are expected as the analysis matures. The scattering functions yield information on small-scale surface structure (tens of centimeters to tens of meters) but averaged over hundreds of km². RMS surface slopes derived from fits of analytic functions to the $\hat{\sigma}_0(\phi)$ results have been converted to map form and show patterns similar to those reported using other techniques. While all three forms are found on Venus, fit residuals imply that an exponential scattering function matches data better than either the Hagfors or gaussian form in most areas, although the Hagfors function may be a better descriptor at some sites. Limited study of image data indicates that average backscatter cross section, and possibly its slope, can be derived at oblique angles ($17° \leq \phi \leq 45°$). Offsets of the echo peak in altimetry spectra are surprisingly common and are loosely correlated with Venus topography, but no cause for this phenomenon has yet been identified.

LOW-EMISSIVITY IMPACT CRATERS ON VENUS.

C. M. Weitz[1], C. Elachi[1], H. J. Moore[2], A. T. Basilevsky[3], B. A. Ivanov[4], and G. G. Schaber[5], [1]Jet Propulsion Laboratory, California Institute of Technology, Pasadena CA 91109, USA, [2]USGS, Menlo Park CA 94025, USA, [3]Vernadsky Institute of Geochemistry and Analytical Chemistry, Russian Academy of Sciences, Moscow, 117975, Russia, [4]Institute for Dynamics of Geospheres, Russian Academy of Sciences, Moscow, 123810, Russia, [5]USGS, Flagstaff AZ 86001, USA.

The observation that rms slopes obtained from direct inversion of the altimetry data are consistent, at least in a general way, with values derived from template fits [1] provides some confidence that both these procedures are reliable. Since the recovered functions from inversion $\hat{\sigma}_0(\phi)$ do not depend on *a priori* specification of an analytic function, we expect to find differences between our results and those obtained via the template method as our analysis proceeds.

Our result that an exponential scattering function can provide better agreement with data than the widely used Hagfors function is significant in terms of its implications for the surface. Although the difference is not large, it is convincing. A gaussian surface model is derived by assuming that the surface is gently rolling. A Hagfors surface must have at least a few flat segments and some "edges" in order to justify use of an exponential autocorrelation function. The degree to which a fresh planetary surface has been turned over and smoothed may be expressed in the degree to which its scattering is described by gaussian functions rather than Hagfors functions. The exponential function requires that there be more or larger flat-lying segments than even the Hagfors function requires. We note that while the exponential law works best for Venus, just the opposite is the case for the Moon [2]. It seems likely this difference reflects underlying differences in processes of erosion and deposition and of materials on the two bodies.

Our results from SAR image analysis to date are limited. We have found a smooth region (in altimetry data) east of Alpha Regio where SAR backscatter cross section is lower than predicted by the Muhleman function, suggesting that the same scattering mechanisms apply at both nadir and at $\phi \approx 30°$ and 35°. East of Maxwell, SAR backscatter is above average, but our estimates of rms slopes and those derived from template fitting [3] indicate that this is an "average" region in its nadir backscatter. The difference could be accounted for by the presence of small-scale roughness that is not apparent to the altimeter but scatters relatively strongly at oblique angles.

The Doppler offset observations appear to be real and a manifestation of a geophysical or geological state of the surface. They show global patterns that include a great circle at equatorial latitudes (roughly following the band of equatorial highlands that includes Aphrodite Terra, Eistla Regio, and Beta Regio) and at least part of another (constant latitude) circle at 40°–50° N. Large-scale surface slopes from Pioneer Venus topography [4] correlate to some extent, but are inadequate by themselves to cause the displacements observed. Small-scale "shingles" or other asymmetric scattering surfaces (for example, sand dunes [R. A. Arvidson, personal communication]) could contribute, but acquiring independent confirming data will be difficult. Local slopes of 0.3° on kilometer scales may also be important [P.G. Ford, personal communication], but more needs to be learned of their distribution. A concentration of negative offsets between Sapas Mons and Rusalka Planitia, where the large-scale surface gradient is perpendicular to the Magellan track, indicates that this phenomenon need not be associated with large-scale slopes. Global-scale "zones of disruption" [5] may have led to surface modification, which is expressed in small-scale surface features but does not necessarily show up in the large-scale topography.

References: [1] Ford P. G. and Pettengill G. H. (1992) *JGR*, submitted. [2] Simpson R. A. and Tyler G. L. (1982) *IEEE Trans.*, *AP-30*, 438–449. [3] Tyler G. L. et al. (1991) *Science, 252*, 265–270. [4] Sharpton V. L. and Head J. W. (1985) *JGR, 90*, 3733–3740. [5] Schaber G. G. (1982) *GRL, 9*, 499–502.

Procedure: An analysis of 144 impact craters on Venus has shown that 11 of these have floors with average emissivities lower than 0.8. The remaining craters have emissivities between 0.8 and 0.9, independent of the specific backscatter cross section of the crater floors. These 144 impact craters were chosen from a possible 164 craters with diameters greater than 30 km as identified by Schaber et al. [1] for 89% of the surface of Venus. We have only looked at craters below 6053.5 km altitude because a mineralogical change causes high reflectivity/low emissivity above this altitude [2]. We have also excluded all craters with diameters smaller than 30 km because the emissivity footprint at periapsis is 16 × 24 km and becomes larger at the poles [3].

On the SAR images, rectangular boxes were chosen on the crater floor that avoided central peaks and inner rings. Backscatter cross sections were calculated from the average DN values within the boxes for the incidence angle for the crater latitude. Emissivity values were taken from the datasets produced by MIT [3]. A rectangular box was selected inside each crater floor and the average DN was then converted to emissivity. In Fig. 1, while the majority of crater floors lie between 0.8 and 0.9 in average emissivity independent of backscatter cross sections, 11 craters fall below this range.

We also found all craters that had any emissivity values on their floors below or equal to 0.8 because several craters had variations across their floors. After doing this, we found five more crater floors with emissivity values below or equal to 0.8. Table 1 lists the 16 craters and the lowest emissivity values found on their floors. The 16 craters represent a minimum number of craters with low emissivities on Venus because craters with diameters smaller than the footprint of the radiometer may have low emissivities that will not be detected.

Results: A study of backscatter and emissivity for impact craters associated with parabolic-shaped features by Campbell et al. [4] indicates that the majority of these craters have high specific
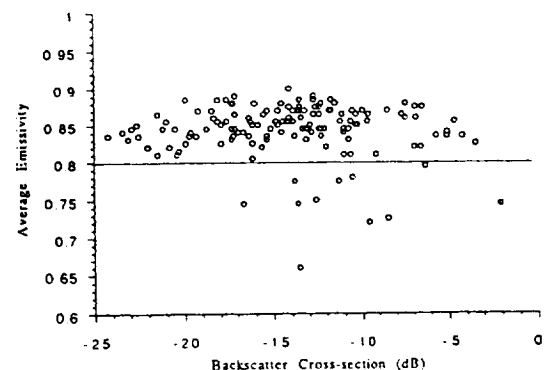

Fig. 1. Emissivity and specific backscatter cross section for 144 craters on Venus.

TABLE 1.　Data on 16 craters with floors that have low emissivities.

Crater	Latitude	Longitude	Diameter (km)	Backscatter cross section (dB)	Emissivity
Boleyn	24.4	219.9	70	-13.52	0.62
Stanton	-23.4	199.9	110	-9.53	0.665
Stuart	-30.75	20.2	71	-8.45	0.69
Mead	12.5	57.2	280	-16.64	0.705
Adivar	8.95	76.1	32	-13.64	0.715
Sitwell	16.68	190.35	37	-12.64	0.72
Stowe	-43.2	233	80	-2.07	0.725
Warren	-11.8	176.5	53	-13.78	0.735
Truth	28.7	287.75	49	-11.25	0.745
Greenaway	22.95	145	92	-10.52	0.755
Boulanger	-26.55	99.3	73	-6.31	0.76
Bonheur	9.8	288.75	109	-13.84	0.775
Aurelia	20.25	331.85	32	-10.98	0.785
Ban Zhao	17.2	146.9	40	-10.64	0.785
O'Keeffe	24.5	228.75	81	-16.12	0.79
Bathsheba	-15.1	49.35	35	-9.1	0.8

radar backscatter cross sections and low emissivities. They suggest that these craters are relatively young and that these radar-bright floors are the result of wavelength scale roughness and high Fresnel reflectivity material. With time, modification processes remove the parabolic deposits and alter the crater floors to lower backscatter cross sections, lower Fresnel reflectivities, and higher emissivities that match those typical of the older craters without parabolic features.

We have plotted the specific backscatter cross sections for the 144 craters used in our analysis (Fig. 2). The dashed line is the Muhleman Law, which is the derived average scattering function based on Pioneer Venus SAR observations and used by the Magellan project to normalize the backscatter cross sections. Because all but one (Mead) of the low-emissivity crater floors have stronger backscatter than most craters, this supports an association between low-emissivity and high-backscatter cross sections for most craters on Venus. Of these 16 low-emissivity craters, 7 are peak ring, 6 are central peak, and 3 have no floor structure. Ten of these craters have associated parabolic features.
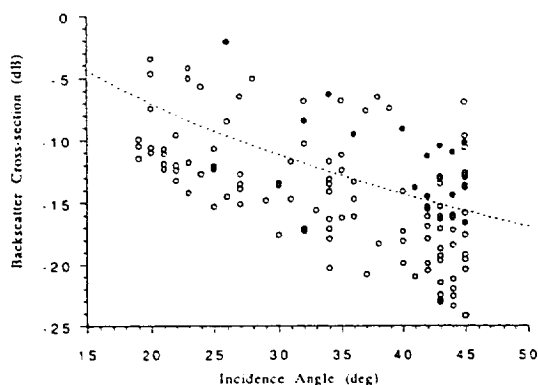

Fig. 2.　Specific backscatter cross section vs. incidence angle for 144 craters on Venus. Dashed line is the Muhleman Law. Filled circles are low-emissivity craters, open circles high-emissivity craters.

Interpretations: To help us interpret the materials in the crater floors, we have used a relation between bulk density and relative dielectric constant for lunar samples of rocks and "soils" [5]. A Fresnel reflectivity near 0.38 can be inferred [3] from the emissivity (0.62) of crater floor materials of Boleyn (Table 1) to yield a calculated dielectric constant of 17.8 [6]. The inferred bulk density, which is 4380 kg/m³ (range: 3880–5090), is much too large for common basaltic rocks. More probable bulk densities of basaltic rocks, which have dielectric constants near 8 to 9 [7], lie in the range of 2600–3000 kg/m³.

Low emissivity values for the venusian highlands can best be explained by the presence of conducting minerals, such as iron pyrite, iron sulfides, or iron oxides [8]. We also suggest that inclusions of conducting minerals or particles in the crater floor materials could account for the low emissivities and high Fresnel reflectivities. Materials containing these particles may have been (1) excavated from depth in the crust during the impact process, (2) derived from the projectile that produced the crater, (3) formed by physical-chemical reactions associated with the impact process (including impact melts), (4) extruded into the crater by volcanic processes, and (5) produced by some combination of these processes. The absence of low-emissivity signatures on the crater flanks and bright outflows suggest that 1, 2, and 3 are unlikely because the low emissivities are confined to crater floors. It may be possible, however, that atmospheric shocks associated with the impacts confine materials or impact metamorphism is confined to the materials of the floors.

Some of the craters are clearly filled with postcrater lavas while others may be filled with impact melts. In the case of the crater Bonheur, the flooded interior basin has a lower emissivity and a smaller backscatter cross section than the outer basin. This observation supports an endogenetic lava flow with low emissivity (possibly high in iron content) that has flooded the interior basin. Two low-emissivity craters reside on the tessera and one of these appears to be partly flooded by lava. This means that low emissivity lavas may erupt from magma sources beneath the tessera as well as the plains. Backscatter cross sections for both the floors and outflows of some craters, such as Stowe, are about the same and this suggests the materials of the floors include impact melts. The next step is to investigate how this low-emissivity material could weather to the

higher emissivity values (0.8–0.9) on the plains and on the other crater floors and to investigate whether young lava flows also exhibit low emissivities. (This work was conducted at the Jet Propulsion Laboratory, California Institute of Technology, under contract with the National Aeronautics and Space Administration.)

References: [1] Schaber et al. (1992) *JGR*, in press. [2] Klose et al. (1992) *JGR*, in press. [3] Pettengill et al. (1991) *Science, 252*, 260–265. [4] Campbell et al. (1992) *JGR*, in press. [5] Olhoeft G. R. and Strangway D. W. (1975) *EPSL, 24*, 394–404. [6] Tyler et al. (1976) *Science, 193*, 812–815. [7] Campbell M. J. and Ulrichs J. (1969) *JGR, 74*, 5867–5881. [8] Pettengill et al. (1988) *JGR, 93*, 14881–14892.

N93-14393

FLOOR-FRACTURED CRATER MODELS FOR IGNEOUS CRATER MODIFICATION ON VENUS.

R. W. Wichman and P. H. Schultz, Department of Geological Sciences, Brown University, Providence RI 02912, USA.

Introduction: Although crater modification on the Earth, Moon, and Mars results from surface erosion and crater infilling, a significant number of craters on the Moon also exhibit distinctive patterns of crater-centered fracturing and volcanism that can be modeled as the result of igneous crater modification [1–5]. Here, we consider the possible effects of Venus surface conditions on this model, describe two examples of such crater modification, and then briefly discuss the constraints these craters may place on conditions at depth.

Floor-fractured Crater Model: On the Moon, most floor-fractured craters occur near the lunar maria [1,6,7] or along basin ring faults [5], and commonly contain ponded mare units and dark mantling deposits [1,8,9]. Fracturing is confined to the crater interior, and, in the more modified craters, uplift of the crater floor as a single coherent unit results in a distinctive moatlike failure zone in the crater wall region [1,4]. In some cases, later volcanism floods this moat structure or buries the entire floor [1,3].

Although viscous relaxation can produce uplift of the crater floor [10–12], shallow, laccolithlike intrusion beneath the crater floor provides a model consistent with observations on the Moon. As discussed elsewhere [1,4,5], intrusions apparently begin in a neutral buoyancy zone near the base of the crater-centered breccia lens through the lateral growth of a sill-like magma body. Both the increased lithostatic pressures and diminished impact brecciation beneath the crater walls, however, enhance resistance to such lateral intrusion growth beyond the crater floor region, thereby evolving into vertical, laccolithic intrusion growth described by [13]. During vertical growth, the crater floor rises through a pistonlike uplift, while ring faulting near the edge of the intrusion produces the moat structures outside this uplift.

For a laccolithic intrusion, crater modification is controlled by parameters that allow assessing conditions at depth [4,5]. Since elastic deformation should not thin the uplifted crater floor section, the amount of floor uplift essentially reflects the intrusion thickness. If the uplifted floor diameter delineates the laccolith size at depth, then the model [13] can be used to estimate both the magma pressure driving deformation and an effective thickness for the crater floor materials overlying the intrusion. The derived magma pressures then help constrain the length of the magma column beneath the intrusion, whereas the inferred floor thickness provides a model for both the intrusion depth and breccia thickness in a given crater [4,5].

Floor-fractured Craters on Venus: The evidence for widespread volcanism on Venus [14] would seem to favor igneous crater modification. Four significant differences between conditions on Venus and on the Moon may modify the processes of crater-centered igneous intrusion. First, where the anorthositic crust on the Moon is apparently equivalent in density or less dense than most mare magmas [15], the basaltic crust on Venus should be denser than basaltic melts and may be thinner than the lunar crust as well. Consequently, basalt magmas on Venus are more likely to rise to the surface than magmas on the Moon, perhaps decreasing the likelihood of crater-centered intrusions at depth [4]. Second, the lunar crust has been extensively fractured by successive, overlapping impact events. The resulting combination of a megaregolith and basin ring faults, therefore, provides a number of conduits through which magma can enter individual crater-centered breccias. In contrast, the crust on Venus appears to be more coherent; hence, magma may not favor breccias beneath craters on Venus. Instead, a crater-centered intrusion may first require deformation by a regional fracture system. Third, the higher surface gravity on Venus should reduce the fracture porosity of an impact breccia, thereby reducing the density contrast required for a shallow zone of crater-centered neutral buoyancy. High surface gravity also should consolidate impact breccias at depth, which may produce thinner breccia lenses on Venus than on the Moon. As a result, the uplifted floor plate on Venus should be thinner than on the Moon, and floor fracturing would then be expected to be more polygonal, i.e., reflecting inhomogeneities in the floor rather than acting as a coherent block. Fourth, since the increased surface temperatures on Venus may allow annealing of impact breccias over time, both the fracture density beneath a Venus crater and the probability of an igneous intrusion also may decrease as a function of crater age.

Most impact craters on Venus do not exhibit floor fractures comparable to examples on the Moon. Instead, either volcanic infilling occurs or craters are simply engulfed rather than participate in surface volcanism. Figures 1 and 2, however, illustrate two craters that closely resemble floor-fractured craters on the Moon. For reference, both craters occur in ridged lowland plains with elevations of approximately –500 m to 500 m, relative to the mean planetary radius. The first of these craters (Fig. 1) is 48 km in diameter and exhibits a scarp-bounded central floor plate 32 km in diameter in which an additional pattern of concentric failure can be

Fig. 1.   Modified crater centered at 52°S, 196°E. Note the wide outer moat structure surrounding the central floor and the bright scarp along the southwest edge of the central floor plate. Scale bar is ~17 km (enlarged section of C1-45S202;1).
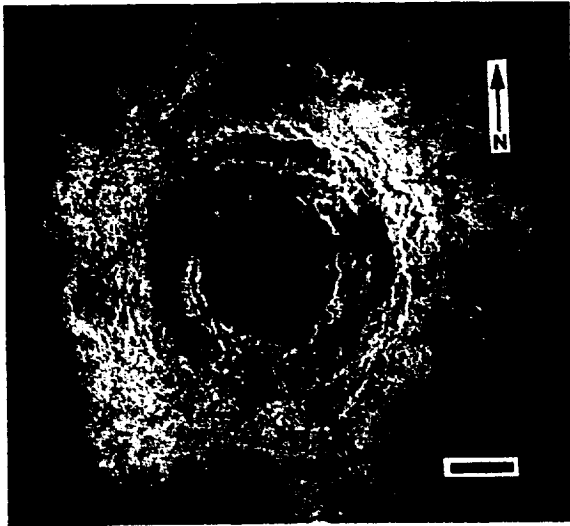
Fig. 2.   Mona Lisa Crater, centered at 25.6°N, 25.2°E near the edge of Eisila Regio. Note partial flooding of outer moat structure and bright fracture pattern in the central floor plate. Scale bar is ~17 km (enlarged section of C1-30N027;1).

recognized. Although transected by a number of later wrinkle ridges, both the outer moat region and the central floor appear to be relatively smooth and may reflect a sequence of crater-centered volcanism after the uplift event, also observed in the lunar crater Posidonius. The second crater (Fig. 2) is larger (~75 km diameter) and somewhat less modified. In this case, a bright ridge nearly surrounds the central floor plate, and volcanism has only flooded the central floor and the northern half of the outer moat structure, allowing identification of the moat fractures in the south. Inside the central floor plate, concentric fractures bound the central floor with a set of radial/polygonal fractures in the center of the floor plate. Both craters occur in ridged lowland plains with elevations close to the mean planetary radius. Since the ejecta pattern and the scalloped southern crater rim indicate an oblique impact from the north [16,17], the northward offset of these central fracture patterns relative to the crater center is consistent with the uprange offset of both central peaks and basin rings in other oblique impact structures [5,16,17], whereas the distribution of moat-filling volcanism is consistent with the enhanced failure uprange proposed by [5,18,19] for cavity collapse in an oblique impact event.

The intrusion parameters derived from the relations of [13] can be related to the local crustal structure. For floor uplift of ~1.5 km (inferred for the craters described above), both craters indicate a magmatic driving pressure of ~375 bar for a basaltic melt. If this pressure then reflects the magmastatic head resulting from the density contrast between a basaltic magma (~2800 kg/m³) and a basaltic crust (3000 kg/m³), a magma column length of 22 km is indicated for both regions. Since the effective thickness of the floor plate is estimated at 2–6 km for crater 1 and 4–8 km for crater 2, this simple model requires a crustal (basaltic) thickness exceeding ~2530 km. Alternatively, if the basaltic crust on Venus is less than 10–20 km, as proposed in [20], the base of the magma column occurs within a denser mantle unit at depths of less than 20–25 km. If the base of the magma column corresponds to a deep, regional magma chamber, these magma column models should indicate either the base of the basaltic crust or rheological boundaries with the crust or lithosphere [21]. Consequently, the implications of floor-fractured

craters on Venus for subsurface density provide an additional test for models of regional crustal structure.

References: [1] Schultz P. H. (1976) *Moon, 15,* 241–273. [2] Schultz P. H. (1978) *GRL, 5,* 457–460. [3] Schultz P. H. (1976) *Moon Morphology.* [4] Wichman R. W. and Schultz P. H. (1991) *LPSC XXII,* 1501–1502. [5] Wichman R. W. (1992) Ph.D. thesis, Brown University. [6] Brennan W. J. (1975) *Moon, 12,* 449–461. [7] Whitford-Stark J. L. (1974) *Nature, 248,* 573–575. [8] Young R. A. (1972) *Apollo 16 Prelim. Sci. Rep.,* NASA SP–315, 29–89 to 29–90. [9] Bryan W. B. et al. (1975) *Proc. LSC 6th,* 2563–2570. [10] Danes Z. F. (1965) *Astrogeol. Stud. Ann. Prog. Rep. A (1964–1965),* 81–100. [11] Scott R. F. (1967) *Icarus, 7,* 139–148. [12] Hall J. L. et al. (1981) *JGR, 86,* 9537–9552. [13] Pollard D. P. and Johnson A. M. (1973) *Tectonophysics, 18,* 261–309. [14] Head J. W. et al. (1992) *Magellan 6 Month Rep.,* in press. [15] Solomon S. C. (1975) *Proc. LSC 6th,* 1021–1042. [16] Schultz P. H. and Gault D. E. (1991) *LPSC XXIII,* 1231–1232. [17] Schultz P. H. (1992) *Magellan 6 Month Rep.,* in press. [18] Wichman R. W. and Schultz P. H. (1992) *LPSC XXIII,* 1521–1523. [19] Schultz P. H., this volume. [20] Grimm R. E. and Solomon S. C. (1988) *JGR, 93,* 11911–11929. [21] Head J. W. and Wilson L. (1992) *JGR, 97,* 3877–3903.

N93-14394

VENUS: GEOCHEMICAL CONCLUSIONS FROM THE MAGELLAN DATA.   J. A. Wood, Harvard-Smithsonian Center for Astrophysics, Cambridge MA 02138, USA.

Though the Magellan mission was not designed to collect geochemical or petrological information, it has done so nonetheless. Since the time of the Pioneer Venus mission it has been known that high-altitude (>2.5–5 km) mountainous areas on Venus exhibit anomalously low radiothermal emissivity (ε < 0.6) [1]. Magellan has greatly refined and extended these observations. The low emissivity requires surface material in the uplands to have a mineralogical composition that gives it a high bulk dielectric constant, >~20. The dielectric constant of dry terrestrial volcanic rocks seldom exceeds 7. The high-dielectric character of high-altitude surface material cannot be a primary property of the local volcanic rock, because there is no reason why rock having the required special mineralogy would erupt only at high altitudes. Therefore it is a secondary property; the primary Venus rock has reacted with the atmosphere to form a mineralogically different surface layer, and the secondary minerals formed are controlled by the ambient temperature, which decreases with altitude on Venus.

Klose et al. [2] showed that, for a plausible assumption of oxygen fugacity in the Venus atmosphere (~10⁻²¹ bar), variation of the equilibrium weathered mineral assemblage with altitude and temperature would create such a situation: above a few kilometers altitude the stable assemblage includes pyrite (FeS_2) in sufficient abundance to create a "loaded dielectric" with a bulk dielectric constant >~20; at lower altitudes the stable Fe mineral is magnetite (Fe_3O_4), and this is present in insufficient abundance to give rise to such a high bulk dielectric constant. Pettengill et al. [3] first concluded that pyrite was the mineral responsible for the high-dielectric materials observed at high altitudes on Venus.

Fegley et al. [4] reject this interpretation. They note that the gas species COS is much less abundant in the Venus atmosphere than the equilibrium concentration, and argue that the reaction

$$3FeS_2 + 2CO + 4CO_2 = 6COS + Fe_3O_4$$
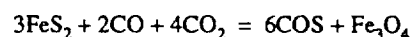
would tend to oxidize pyrite to magnetite at all altitudes, using its S to build up the deficit of atmospheric COS. This argument is specious. Fegley et al. argue from only one reaction and three species abundances in the Venus atmosphere, while [2] used an energy-minimization procedure that effectively considers all possible reactions simultaneously. Klose et al. [2] used as input the bulk elemental composition of the atmosphere, not the abundances of selected gas species in it. They determined the total equilibrium system, including concentrations of gas species in the atmosphere as well as surface minerals. Klose et al. found, as Fegley et al. say, that the equilibrium abundance of COS is greater than the concentration the Venus atmosphere appears to contain (~15 ppm vs. ~0.25 ppm). Apparently kinetic barriers prevent COS from attaining its equilibrium concentration at ground level. Thus the Venus system is not completely at equilibrium. One can debate how badly the system is out of equilibrium, but the nonequilibrium abundance of the minor species COS in the atmosphere by no means requires that the surface mineralogy is completely out of equilibrium; and to be in equilibrium with the atmosphere's concentration of SO_2, ~185 ppm, at the f_{O2} cited above, the mountaintop mineral assemblage must contain pyrite.

Fegley et al. [4] suggest that primary perovskite ($CaTiO_3$) in the rock might be responsible for low-emissivity mountaintops on Venus, since this mineral has a particularly high dielectric constant. They note the occurrence of perovskite in (relatively rare) SiO_2-undersaturated igneous rocks on Earth, but do not examine its thermodynamic stability in more typical basalts, or in Venus basalts having the compositions reported by Soviet landers. In fact, perovskite is not a stable primary mineral at crystallization temperatures in these expected Venus rock types: instead Ti appears as rutile, and most Ca as diopside and anorthite.

With time, the weathering reactions discussed by [2] work deeper and deeper into surface rock on Venus. The timescale of weathering—the time needed to weather rock to a depth sufficient to control the radiothermal emissivity measured by PVO and Magellan—is not known, but is expected to be long. Water is an essential ingredient of terrestrial weathering, and its near absence on Venus must greatly retard the process. To some extent this effect is offset by the much higher temperatures on Venus, but in spite of this it may take tens or even hundreds of millions of years to weather a high-altitude surface to a high-dielectric assemblage.

This is comparable to the timescales of other important processes on Venus, and an interplay between weathering and (e.g.) volcanism and tectonism is to be expected. In other words, it may be possible to use the presence or absence of weathering effects to distinguish between relatively young features on Venus and older landforms.

Volcanism: Klose et al. [2] and Robinson and Wood [5] have drawn attention to large and small flow units high on the volcanos Maat, Sapas, Ozza, and Theia Mons that display relatively high emissivities. They conclude these units are too young to have had time to weather to the high-dielectric pyritic state. This criterion, if confirmed, provides a crude basis for establishing a chronology of volcanism.

Tectonism: Klose et al. [2] and Pathare [6] have explored the complex relationship between altitude (a) and emissivity exhibited by Maxwell Montes. An a/e scatter plot of measurements made over the broad Maxwell landmass shows a well-defined band at e ~ 0.4, which presumably reflects the presence locally of completely weathered surface material; but there is also a broad scatter of points to higher values of e (<~0.6) in the diagram. Pathare [6] found these

latter data points are provided by a belt of mountainous terrain (latitude ~67°, longitude 350°–05°) that defines the northern edge of the Maxwell Montes low-emissivity zone. Pathare [6] attributed the less-than-minimal emissivities in this belt to incomplete weathering, and concluded that this belt was uplifted more recently than other parts of Maxwell. The emissivity increases, and presumably the time of uplift decreases, westward along the belt.

The Magellan emissivity records contain other information of interest. For example, [5] found that some small volcanic domes and clusters of domes near plains level display anomalously low emissivity. At these altitudes, according to the model of [2], magnetite should be the stable Fe mineral, and weathered surface material should not have high-dielectric properties. Robinson and Wood [5] attributed this phenomenon to continued seepage of volcanic gas through the soil covering these domes, and showed that an admixture of only ~0.02% of sulfurous gas of the type emitted by the Kilauea volcano on Earth, with normal Venus atmospheric gas in the pores of the soil, would stabilize pyrite in the soil at plains altitude. They noted a correlation between the presence of apparently unweathered volcanic flows at the summits of volcanos, and nearby low-emissivity domes; both should be manifestations of recent volcanic activity.

Another interesting aspect of weathering and emissivity on Venus is the fact that the mineral reaction boundary separating pyrite (low-emissivity) from magnetite (high-emissivity), which presumably follows an isothermal surface in the Venus atmosphere, does not intersect all highlands at the same altitude. The observed "snowline" varies in altitude from ~2.5 km (Sapas Mons) to ~4.7 km (Maxwell). Curiously, the "snowline" altitude correlates well with the total height of the mountain; the "snowline" occurs at roughly half the peak height. This suggests that the thermal structure of the atmosphere is somehow modulated by topography on Venus, a concept that has not found favor with atmospheric scientists. An alternative explanation has not been forthcoming, and this phenomenon remains to be understood.

References: [1] Pettengill G. H. et al. (1988) *JGR, 93,* 14881–14892. [2] Klose K. B. et al. (1992) *JGR,* submitted. [3] Pettengill G. H. et al. (1982) *Science, 217,* 640–642. [4] Fegley B. Jr. et al. (1992) *Proc. LPSC, Vol . 22,* 3–19. [5] Robinson C. A. and Wood J. A. (1992) in preparation. [6] Pathare A. (1992) B.S. thesis, Harvard University.

N93-14395

FINITE AMPLITUDE GRAVITY WAVES IN THE VENUS ATMOSPHERE GENERATED BY SURFACE TOPOGRAPHY. R. E. Young[1], H. Houben[2], R. L. Walterscheid[3], and G. Schubert[4], [1]NASA Ames Research Center, Moffett Field CA, USA, [2]Space Physics Research Institute, Sunnyvale CA, USA, [3]The Aerospace Corporation, Los Angeles CA, USA, [4]University of California, Los Angeles CA, USA.

A two-dimensional, fully nonlinear, nonhydrostatic, gravity wave model is used to study the evolution of gravity waves generated near the surface of Venus. The model extends from near the surface to well above the cloud layers. Waves are forced by applying a vertical wind at the bottom boundary. The boundary vertical wind is determined by the product of the horizontal wind and the gradient of the surface height. When wave amplitudes are small, the near-surface horizontal wind is the zonally averaged basic-state zonal wind, and the length scales of the forcing that results are characteristic of the surface height variation. When the forcing becomes larger and wave amplitudes affect the near-surface

horizontal wind field, the forcing spectrum becomes more complicated, and a spectrum of waves is generated that is not a direct reflection of the spectrum of the surface height variation. Model spatial resolution required depends on the amplitude of forcing; for very nonlinear cases considered, vertical resolution was 250 m, and horizontal resolution was slightly greater than 1 km. For smaller forcing amplitudes, spatial resolution was much coarser, being 1 km in the vertical and about 10 km in the horizontal. Background static stability and mean wind are typical of those observed in the Venus atmosphere.

Computations to date have considered a periodic sinusoidally varying surface height. Such forcing is relevant to the situation in which surface topography consists of a series of ridges extending over a region largely compared to the dimensions of each individual ridge. Because of the particular variations with altitude of static stability and mean wind in the Venus atmosphere, an evanescent region exists between about 15 km altitude and just below the cloud layer for waves having horizontal wavelengths less than about 100 km. This means waves generated at the surface having short wavelengths do not propagate to cloud levels with significant amplitude. At longer wavelengths (> 100 km), waves easily reach cloud levels and above. With surface wind speeds of several m/s and surface slopes having values in the vicinity of 0.02 (not unreasonable values in the higher mountainous regions of Venus such as Aphrodite), wave amplitudes are large enough to cause considerable nonlinear effects. From the surface to cloud levels and above, wave spatial patterns are relatively complicated and the spectra exhibit much shorter wavelengths than typical of the surface height variation, the dominant wavelength being somewhat less than 100 km for a surface height wavelength of 400 km. For this same case, maximum vertical winds at middle cloud levels associated with the waves are typical of the 2–3 m/s vertical winds observed by the VEGA balloon as it overflew the Aphrodite region. Wave horizontal wind amplitude at middle cloud levels is about 10 m/s. To date, with reasonable values of the surface forcing, we have not been able to generate waves having sufficient amplitude to cause wave breaking. Wave-induced mean winds are largest near the surface, and can become comparable to the low-altitude background wind.

N93-14396

MIDDLE ATMOSPHERE OF VENUS AND ITS CLOUDS: LATITUDE AND SOLAR TIME VARIATIONS.　L. V. Zasova, Space Research Institute, Russian Academy of Sciences, Moscow 117810, Russia.

The structure of the middle atmosphere of Venus and its upper clouds, derived from infrared spectrometry (from 250 to 1650 cm^{-1}) on Venera 15 [1–5] are discussed. Poleward increasing of temperature, monotonous on the average, at altitudes h >70 km changes to poleward decreasing at h <60 km. Temperature inversion at 85–95 km at low latitudes was observed as a half-day wave with two minima near 9:00 a.m. and 9:00 p.m., with a more pronounced morning feature. At high latitudes the inversion with temperature minimum near 64 km exists. There are several minima depending on solar time, but the most pronounced is one on the dayside, where the depth of inversion may reach more than 40 K (near 10:00 a.m.; we have no observations closer to noon). Another minimum is situated symmetrically on the nightside. Usually in the polar region the temperature inversion is situated deeper in the atmosphere (near 62 km). A jet at latitudes 50°–55°N divides Venus into two drastically different latitude zones: pretty homogeneous at 56–95-km zone <50° N with diffuse clouds and daily temperature variations

near cloud tops about several degrees, and zone >55°N (where such dynamic structures as cold collar and hot dipole were observed) with dense low clouds (with the exceptions of the regions at 55°–80°N outside the cold collar).

We separate Venus into four latitudinal zones with approximate latitude boundaries, where the different IR-features were observed. They are characterized by different cloud scale height, H, and observed position of upper boundary of clouds (optical thickness is reached unit): h (1152) is for spectral region with maximal aerosol absorption coefficient (1152 cm^{-1}), and h (365) for the spectral region with minimal aerosol absorption coefficient (365 cm^{-1}). They are

1. l<55 – rather homogeneous, low and mid latitudes, with H_a = 3.5–4 km, and h (1152) = 67–69 km, and h (365) = 57–59 km.

2. 55 <l <75 – the most inhomogeneous latitudes as for aerosol, and for temperature. Two types of areas are found here: (1) cold collar, with H_a ≤ 1 km, h (1152) = 60–62 km, and h (365) = 58–60 km, and (2) inhomogeneous areas outside cold collar with H_a ≥ 4–5 km, h (1152) = 70–72 km, and h (365) = 56–60 km.

3. 75 <l <85 – the hot dipole. The temperature is only several degrees higher in hot dipole than outside it near the upper boundary of the clouds at the same levels in the atmosphere. The clouds are situated lower and have larger scale height. For the hot dipole H_a = 1–1.5 km, h (1152) = 59–63 km, and h (365) = 56–58 km, and outside it, H_a ≤ 1 km, h (1152) = 63–64 km, and h (365) = 61–63 km.

4. l>85 – usually the clouds here have a very sharp upper boundary, with H_a ≤ 0.5 km, h (1152) = 62–64 km, and h (365) = 62–64 km.

References:　[1] Moroz V. I. et al. (1986) *Applied Optics, 25,* N10. [2] Oertel D. et al. (1987) *Adv. Space Res., 5,* 25. [3] Schafer K. et al. (1987) *Adv. Space Res., 7,* 17. [4] Spankuch D. et al. (1990) *Adv. Space Res., 10,* 67. [5] Zasova L. V. and Moroz V. I. (1992) *Adv. Space Res., 12,* 79–90.

N93-14397

SO$_2$ IN THE MIDDLE ATMOSPHERE OF VENUS: IR MEASUREMENTS FROM VENERA 15 AND COMPARISON TO UV.　L. V. Zasova[1], V. I. Moroz[1], L. W. Esposito[2], and C. Y. Na[2], [1]Space Research Institute, Russian Academy of Sciences, Moscow 117810, Russia, [2]Laboratory for Atmospheric and Space Physics, University of Colorado, Boulder CO, USA.

Two sets of measurements of SO$_2$ bands in the Venus spectra are presented and compared: IR spectra obtained on the USSR Venera 15 orbiter [1–3] and UV spectra from the American Pioneer Venus orbiter and sounding rockets [4–6]. The 40-mbar level was chosen as a reference level for comparison. The UV data are referred to this level. There are three SO$_2$ bands in the infrared spectrum: at 519 cm^{-1}, 1150 cm^{-1}, and 1360 cm^{-1}. The levels of their formation in the atmosphere may differ significantly, more than 10 km. In principal, it allows us to obtain the vertical profile of SO$_2$ from 58 to 72 km, in the best case. So the IR data are sensitive to the 40-mbar level (maybe with exception of the cold collar). For low and mid latitudes, both data give a mixing ratio, f, of several tens of ppb and SO$_2$ scale height (H) of 1.5–2.5 km, which is in a good agreement with the photochemically predicted values [7]. This confirms that the photochemical processes dominate in the upper clouds at low and mid latitudes. Both data show an increase of abundance to several hundreds of ppb at high latitudes, but there are differences in scale-height latitudinal behavior. Decreases to 1 km are seen according to UV, but according to the IR the high latitudes of Venus are seen to be strongly inhomogeneous. Dynamic features with low position of

clouds seeing in the IR, such as cold collar, hot dipole, and polar cap, are not observed in UV. The IR data show H = 3–5 km on the average for high latitudes outside the cold collar, and the mixing ratio varies from 100–200 ppb in hot dipole to 1000 ppb in inhomogeneous regions with retrieved high diffuse clouds. We find inside the cold collar f ~ 1–10 ppb and H ~ 1 km. The comparison of IR and UV data shows that the vertical profile of SO_2 may be more complex than our two-parametric model, and H decreases with height at h > 69 km. In this case the differences in H are explained by viewing angle differences between the observations and the differential opacity at UV and IR. Temporal variations may also contribute.

Latitudinal averaged column density at 62 km (near observed upper boundary of clouds at high latitudes) obtained from the IR is about 10^{19} cm^{-2} at low latitudes and it increases to 10^{20} cm^{-2} at high latitudes.

References: [1] Moroz V. I. et al., (1986) *Applied Optics, 25,* N10. [2] Oertel D. et al. (1987) *Adv. Space Res., 5,* 25. [3] Moroz V. I. et al. (1990) *Adv. Space Res., 10,* 77. [4] Esposito L. W. (1980) *JGR, 85,* 8151–8157. [5] Esposito L. W. et al. (1988) *JGR, 93,* 5267. [6] Na C. Y. et al. (1990) *JGR, 95,* 7485. [7] Yung Y. L. and Demore W. B. (1982) *Icarus, 51,* 199.

N93-14398

OUTGASSING HISTORY OF VENUS AND THE ABSENCE OF WATER ON VENUS.

Youxue Zhang[1,2] and Alan Zindler[1], [1]Lamont-Doherty Geological Observatory and Department of Geological Sciences of Columbia University, Palisades NY 10964, USA, [2]Department of Geological Sciences, University of Michigan, Ann Arbor MI 48109-1063, USA.

Similarities in the size and mean density of Earth and Venus encourage the use of Earth-analogue models for the evolution of Venus. However, the amount of water in the present Venus atmosphere is miniscule compared to Earth's oceans [e.g., 1–3]. The "missing" water is thus one of the most significant problems related to the origin and evolution of Venus and has been discussed extensively [e.g., 2–14]. Lewis [4] proposed that Venus accreted with less water, but this has been challenged [10,13]. The high D/H ratio in Venus' atmosphere is consistent with an earlier water mass more than 100 times higher than at present conditions and is often cited to support a "wet" Venus, but this amounts to only 0.01 to 0.1% of the water in terrestrial oceans [5,12,15, and Table 1] and the high D/H ratio on Venus could easily reflect cometary injection [14]. Nevertheless, many authors begin with the premise that Venus once had an oceanlike water mass on its surface, and investigate the many possible mechanisms that might account for its loss [e.g., 2,6–12]. In this paper we propose that Venus degassed to a lower

degree than the Earth and never had an oceanlike surface water mass.

Lower degree of outgassing for Venus and its consequences:

1. ^{40}Ar in the atmosphere of Venus and Earth. ^{40}Ar in Venus' atmosphere is ~1/4 of that in Earth's atmosphere, when normalized by planetary mass and ignoring ^{40}Ar stored in Earth's continental crust [2,16]. Since K/U and Th/U ratios and K contents in venusian crustal rocks are similar to those in terrestrial rocks [17,18], less ^{40}Ar in Venus' atmosphere implies a lower degree of outgassing for ^{40}Ar [16]. ^{40}Ar in Earth's atmosphere represents 62% degassing of the time-integrated ^{40}Ar budget of DM (degassed mantle), but ^{40}Ar in Venus' atmosphere represents only 15% degassing of its DM, if the relative masses of DM in Venus and Earth are similar.

2. Comparison of N_2, CO_2, and H_2O on Earth and Venus. Previous workers noted that the CO_2/N_2 ratio of surface reservoirs on Venus and Earth are nearly identical when CO_2 stored in Earth's continental crust is included [2,9]. However, such comparisons did not take into account the effect of recycling CO_2 back to Earth's DM, which may be a significant part of the Earth's CO_2 budget [19]. The present venusian crust is hot (surface temperature 740 K) and the formation of carbonates requires liquid water, at least on the Earth, hence the venusian crust is probably a poor repository of volatiles. Most of the outgassed volatiles from Venus' DM are, therefore, likely to reside in the atmosphere. Hence, subduction on Venus, if it occurs, should have little effect on surface CO_2 budget, analogous to the case for N_2 on Earth. In this context, the atmospheric composition of Venus can be used to estimate total outgassing from the interior.

Table 1 compares the volatile inventory of Earth, which is corrected for recycling, with that of Venus. Although the atmosphere of Venus has twice as much N_2 as the AC* of Earth, it has only about half as much CO_2, and orders of magnitude less water. This sequence is the inverse of the solubilities of these volatile components in basaltic melts (Table 1). In the context of a solubility-controlled degassing model, the relative difference in N_2, CO_2, and H_2O on Earth and Venus can perhaps be explained by a lower degree of outgassing of Venus compared to Earth.

For solubility-controlled equilibrium outgassing we can write the following equation [20]

$$c_i M + \frac{P_i V_g}{RT_m} = c_i^0 M_0, \quad \Rightarrow \quad \frac{c_i^0}{c_i} = 1 + \frac{V_g}{K_i RT_m M}, \quad \Rightarrow$$

$$K_i\left(\frac{1}{1-F_i}-1\right) = K_j\left(\frac{1}{1-F_j}-1\right)$$

where c_i^0 and c_i are the initial and final concentrations of gas species i in the magma, M_0 and M are the intial and final mass of the magma

TABLE 1. Comparison of volatile inventory of Earth and Venus.

	H_2O	CO_2	N_2
Solubility (in mol g^{-1} bar^{-1})	1.8×10^{-6}	1.8×10^{-8}	$\sim 3.6 \times 10^{-9}$
AC* of Earth (in moles)	8×10^{22}	$\left(2.4^{+0.9}_{-0.6}\right) \times 10^{22}$	$(2.0 \pm 0.2) \times 10^{20}$
Atm of Venus (in moles)	10^{16} to 10^{17}	$(1.1 \pm 0.1) \times 10^{22}$	$(4.3 \pm 0.5) \times 10^{20}$

Solubility data are those in basaltic magma at 1 kbar partial vapor pressure and 1200°C. Source of data: water [21]; CO_2 [22,23]; and N_2 [24], atm of Venus [1–3]. AC* (atm + crust) plus a correction for recycling (recycling of water is ignored since the comparison is not affected by augmenting water on Earth's surface).

$(M \approx M_0)$, P_i is the partial pressure and V_g is the total volume of the gas phase, R is the universal gas constant and T_m is the magma temnperature, $K_i = c_i/P_i$ where K_i is the solubility of i in the melt, and F_i $(=1-c_i/c_i^0)$ is the degree of degassing.

If we assume that the outgassing of Venus can be approximately described by this equilibrium degassing formulation as is the case for Earth [20], then we can estimate the degree of outgassing for different volatile components in Venus by reproducing the present atmospheric CO_2/N_2 ratio from the initial ratio, assumed to be the same as the initial ratio of the Earth. We note that the H_2O/N_2 ratio cannot be reproduced exactly due to loss of water from Venus' atmosphere. Uncertainties in the initial CO_2/N_2 ratio for Earth and the present CO_2/N_2 ratio in Venus' atmosphere (and in the degassing species), combine to permit large ranges in the degrees of outgassing for each of the components. All possible solutions, however, suggest very low degrees of degassing for water (less than 1%), if H_2O is the major degassing species for water. A "best" solution is shown in Table 2 with 0.2% outgassing for H_2O from the DM of Venus. (The total amount of ^{40}Ar in Venus' atmosphere also provides, in principle, a constraint on the degree of degassing, but it is difficult to utilize the constraint in a quantitative way due to the contribution of continental degassing to ^{40}Ar in Venus' atmosphere [16] and the fact that the degree of degassing for ^{40}Ar is not equivalent to that for ^{36}Ar.)

The fractionation effects on volatile-element ratios during outgassing can be likened to that on incompatible and compatible elements during the partial melting process, although we hasten to emphasize that such a comparison should not be taken to imply that inferred low degrees of degassing for Venus are equivalent to, or a result of, lower degrees of melting. At low degrees of partial melting, large proportions of incompatible elements (such as K), and only very small proportions of the compatible elements (such as Ni), partition into the melt. At high degrees of melting, large proportions of both compatible and incompatible elements go into the melt. Similar effects are produced during different degrees of degassing. The degree of outgassing for Earth is very high, so that even water has been outgassed to ~50%. The degree of outgassing for Venus is low, hence only incompatible volatiles have outgassed significantly, while H_2O, a very compatible volatile in silicate melts (100 times more soluble than CO_2 and ~500 times more soluble than N_2 [21–24]), remains predominantly within the mantle.

To illustrate the implication of the solubility-controlled outgassing model for Venus, we first assume that Venus accreted the same amount of water as the Earth although lower or higher amounts of initial water are possible and consistent with the model. Taking the "best" solution shown in Table 2, only ~0.2% of this water has been outgassed from the Venus' mantle to its atmosphere. The total amount of outgassed water is ~3 × 10²⁰ mol or ~0.4% of the water mass now present in terrestrial oceans, enough to generate 13 m of water on the surface of Venus if it were all present at the same time. This estimate is similar to an independent estimate of 8 m of water [15]. There is now 10¹⁶ to 10¹⁷ mol of water in Venus' atmosphere, which requires a time-integrated escaping rate of 7 × 10¹⁰ mol/yr, ~30 times the present loss rate [7,14]. Such losses are capable of generating a 100-fold enrichment in the D/H ratio over Venus' history [5]. The important point is that Venus never had much water at its surface, and the absence of a globe-encircling ocean on Venus must have had profound effects on its geological evolution, making it very different from that of Earth.

Discussion: It is difficult to explain why Venus outgassed to a lower degree than the Earth. One possibility is that a lower degree of degassing reflects the lack of plate tectonics on Venus [16]. It is

TABLE 2. Calcualted degree of outgassing from DM of Earth (corrected for recycling) and Venus.

	H_2O	CO_2	N_2
Earth	0.45	0.98	0.997
Venus	0.002	0.15	0.50

often suggested that present heat losses on Venus are mostly via hot spots [e.g., 25,26], as opposed to spreading ridges. The degree of melting at hot spots may be higher on average than that at normal ocean ridges, at least for the Earth [27]. The elevated surface temperatures on Venus, if it is more than a very recent phenomenon, also serves to elevate the geotherm and hence increase the degrees of melting. If so, the average degree of melting on Venus may be higher than on Earth, leading to lower volatile concentrations in the undegassed magma. If the rates of magma production or heat dissipation on Venus and the Earth are the same, the lower initial concentration of volatiles results in a decreased level of degassing on average because a column of magmas must ascend closer to the surface before it reaches saturation and begins to degas.

The slow outgassing is probably a positive-feedback process. If the initial outgassing is slow, very little water is outgassed. The deposition of carbonates requires water as a medium, so CO_2 quickly accumulates in the atmosphere. The surface temperature then rises due to the greenhouse effect, which then impedes subduction by increasing the buoyancy of the lithosphere [25,26,28–30]. This results in even slower outgassing, and hence higher surface temperatures.

In summary, there are two major lines of evidence to support our contention that Venus outgassed to a lower degree than did the Earth. (1) There is less ^{40}Ar in Venus' atmosphere than in the terrestrial atmosphere. This implies that the time-integrated degree of degassing for Venus is lower than that for Earth. (2) When recycling effects are corrected for, the major volatiles of both planets show a relationship between solubility and mass on the surface. This relationship is consistent with outgassing on both planets being controlled by melt-vapor partitioning, provided that Venus outgassed to a lower degree. In the context of this scenario, the absence of water on Venus' surface is just the most conspicuous expression of a lower degree of outgassing than Earth. We note that our model can be tested in the future for other volatile components that have solubilities between those of CO_2 and water, or higher than that of water. Venus probably never had much water on its surface, even if Venus and Earth accreted the same amount of water. Therefore, there is no compelling need to explain the loss of massive water quantities from Venus' atmosphere.

References: [1] Hoffman J. H. et al. (1980) *JGR*, *85*, 7871–7881. [2] Donahue T. M. and Pollack J. B. (1983) In *Venus* (D. M. Hunten et al., eds.), 1036. [3] von Zahn U. et al. (1983) In *Venus* (D. M. Hunten et al., eds.), 299–430. [4] Lewis J. S. (1972) *EPSL*, *15*, 286–290. [5] Donahue T. M. et al. (1982) *Science, 216*, 630–633. [6] Kasting J. F. and Pollack J. B. (1983) *Icarus, 53*, 479–508. [7] Kumar S. et al. (1983) *Icarus, 55*, 369–389. [8] Kasting J. F. et al. (1984) *Icarus, 57*, 335–355. [9] Krasnopolsky V. A. (1985) *Icarus, 62*, 221–229. [10] Kasting J. F. (1988) *Icarus, 74*, 472–494. [11] Zahnle K. J. and Kasting J. F. (1986) *Icarus, 68*, 462–480. [12] Hunten (1990) *Icarus, 85*, 1–20. [13] Wetherill G. W. (1985) *Science, 228*, 877–879. [14] Grinspoon D. H. and Lewis J. S. (1988) *Icarus, 74*, 21–35. [15] McElroy M. B. et al. (1982) *Science, 215*, 1614–1615. [16] Turcotte D. L. and Schubert G. (1988) *Icarus, 74*, 36–46. [17] Surkov Yu. A. (1977) *Proc. LPSC 8th*, 2665–2689.

[18] Surkov Yu. A. (1983) In *Venus* (D. M. Hunten et al., eds.), 154–158. [19] Zhang Y. and Zindler A. (1988) *Chem. Geol., 70,* 43; Zhang Y. and Zindler A., in preparation. [20] Zhang Y. and Zindler A. (1989) *JGR, 94,* 13719–13737. [21] Hamilton D. L. et al. (1964) *J. Petrol., 5,* 21–39. [22] Stolper E. M. and Holloway J. R. (1988) *EPSL, 87,* 397–408. [23] Pan V. et al. (1991) *GCA, 55,* 1587–1595. [24] Javoy M. et al. (1986) *Chem. Geol., 57,* 41–62; Javoy M., personal communication. [25] McGill G. E. et al. (1983) In *Venus* (D. M. Hunten et al., eds.). 69–130. [26] Phillips R. J. (1983) In *Venus* (D. M. Hunten et al., eds.). 159–214. [27] Klein E. M. and Langmuir C. H. (1987) *JGR, 92,* 8089–8115. [28] Anderson D. L. (1981) *GRL, 7,* 101–102. [29] Phillips R. J. et al. (1981) *Science, 212,* 879–887. [30] Turcotte D. L. (1989) *JGR, 94,* 2779–2785.